UNIVERSITY OF THESSALY
DEPARTMENT OF ECONOMICS

Doctor of Philosophy Dissertation

Complex Population Dynamics and Economic Repercussions: Predator-Prey Interactions, Infectious Disease Transmission and Solar Magnetic Activity

by

AMALIA GKANA

Diploma in Economics, Department of Economics, UPatras (2009)
Master of Science in Applied Economics, Department of Economics, UTH (2011)

Supervisor: Prof. Loukas Zachilas, Assistant Professor

Submitted in partial fulfilment
of the requirements for the degree
of Doctor of Philosophy

Volos

Genesis hides in chaos.

Acknowledgements

I would like to start by giving credit to the people who have contributed to this PhD thesis. First I want to thank my supervisor Prof. Loukas Zachilas for his support, patience, advices and for giving me the freedom to pursue various projects without objection during these years. I would like to express my sincere gratitude to Prof. L. Magafas for sharing his knowledge about data analysis and his constructive suggestions. I would like to thank Prof. J.H. Seiradakis for introducing me to Hoyt and Schatten's (1998) solar-activity reconstruction and for his constructive suggestions. I would also like to thank Prof. J.M. Pasachoff for providing the Maunder (1922) paper and for his fruitful suggestions. I am grateful for the time spent with Prof. Iakovos Psarianos, for all the lovely conversations we had and all his advices. This PhD thesis interpolates material from six published research papers by the author; I would like to thank all the editors and anonymous referees for their detailed constructive comments and helpful recommendations towards the improvement of the first versions of these manuscripts. I would like to thank the members of my thesis review committee as well, for their detailed insightful comments, reviews and suggestions. Lastly, I would like to thank my parents, my partner and my best friend for their support and encouragement to complete this thesis, for being patient with me and for their unconditional love.

Complex Population Dynamics and Economic Repercussions: Predator-Prey Interactions, Infectious Disease Transmission and Solar Magnetic Activity

AMALIA GKANA

University of Thessaly, Department of Economics

Supervisor: Prof. Loukas Zachilas, Assistant Professor

Abstract

This thesis contributes to the understanding of the complex population dynamics. In the first part of this thesis deterministic models describing predator-prey interactions and the spread of an infectious disease are investigated under new assumptions; the economic impacts of the outbreaks and infectious disease epidemics corresponding to the prey populations studied in this part are examined as well. We start with a predator-prey model with Holling type I functional response by incorporating prey refuge in the system; it is shown that refuge in some cases exhibits random-like dynamics leading to prey population outbreaks. Following, a dynamical system suitable for species having no overlap between successive generations is investigated; assuming that population evolves in discrete-time steps we investigate the prey refuge effect on predator-prey interactions. We show that reproduction in certain intervals is important and should be taken into account since it could help in the identification of pest population outbreaks. Finally, a deterministic epidemic model for the spread of gonorrhea is investigated by taking into account the interval between successive clinical cases; our modified model exhibits a wider array of dynamics. Moreover, chaos control is obtained in order to see how the male latex condom use during sexual intercourse affects the incidence of gonorrhea.

In the second part of this thesis we investigate the solar magnetic activity using the sunspot numbers. We analyze the monthly and yearly mean sunspot-number data; we perform future predictions trying to forecast the solar activity during the next months and decades by using a neural network-type core algorithm. In order to test the predictive accuracy of our proposed models we perform several monthly

and yearly *post-facto* predictions comparing them with the actual sunspot numbers. We provide evidence that the yearly sunspot-number data can be used for long-term predictions. Our yearly predictions indicate that the level of solar activity is likely to be reduced significantly during the next 90 years. Finally, we re-evaluate our proposed models for predicting solar activity in the light of the recently revised sunspot-number data, indicating that there is no significant degradation in their performance.

The third and last part of this thesis connects all the topics studied in the previous parts; we investigate the existence of terrestrial and extraterrestrial relationships. We start by providing some background review of the existing literature on the possible connection between solar activity and terrestrial (biological and economic) phenomena. Finally, we attempt to find a correlation between solar activity and agricultural economy by studying the wheat prices in Early Modern Britain. The results of our study suggest the existence of a link between solar activity and wheat market. However, an inconsistency is observed in the wheat prices between two solar minima (Maunder and Dalton Minima). We suggest that the rapid transformation in farming techniques taken during the Maunder Minimum leading to grain-output increase, could be a response to the radical climate change of the coldest phase of the Little Ice Age, resulting to this inconsistency.

Περίληψη

Η συγκεκριμένη διατριβή συμβάλλει στην κατανόηση των πολύπλοκων πληθυσμιακών δυναμικών συστημάτων. Στο πρώτο μέρος της διατριβής ντετερμινιστικά μοντέλα που περιγράφουν αλληλεπιδράσεις αρπακτικών-θηραμάτων και τη μετάδοση μιας μολυσματικής ασθένειας εξετάζονται υπό το φως νέων υποθέσεων˙ οι οικονομικές επιπτώσεις των πληθυσμιακών εξάρσεων και επιδημιών των μολυσματικών ασθενειών που αντιστοιχούν στους πληθυσμούς των θηραμάτων που μελετώνται σε αυτό το πρώτο μέρος εξετάζονται επίσης. Αρχικά, ένα μοντέλο αρπακτικού-θηράματος με συνάρτηση αντίδρασης Holling Τύπου I μελετάται, εισάγοντας στο σύστημα δυνατότητα προστασίας των θηραμάτων από τα αρπακτικά˙ η προστασία των θηράματων σε ορισμένες περιπτώσεις οδηγεί σε φαινομενικά τυχαίες δυναμικές συμπεριφορές και πληθυσμιακές εξάρσεις θηραμάτων εμφανίζονται το σύστημα. Στη συνέχεια, ένα δυναμικό σύστημα κατάλληλο για είδη πληθυσμών δίχως επικάλυψη διαδοχικών γενεών μελετάται˙ υποθέτοντας ότι οι πληθυσμοί εξελίσσονται διαχρονικά σε διακριτά βήματα, εξετάζεται η επίδραση της δυνατότητας προστασίας των θηραμάτων στις αλληλεπιδράσεις αρπακτικού-θηράματος. Δείχνουμε ότι η αναπαραγωγή σε συγκεκριμένα χρονικά διαστήματα είναι σημαντική και θα έπρεπε να λαμβάνεται υπόψη, καθώς θα

μπορούσε να συμβάλλει στην αναγνώριση των εξάρσεων που εμφανίζονται σε πληθυσμούς βλαβερών εντόμων. Τέλος, ένα ντετερμινιστικό επιδημιολογικό μοντέλο για την μετάδοση της γονόρροιας μελετάται, λαμβάνοντας υπόψη το διάστημα που μεσολαβεί ανάμεσα σε διαδοχικές μολύνσεις˙ το τροποποιημένο προτεινόμενο μοντέλο εκδηλώνει ένα ευρύτερο φάσμα δυναμικών συμπεριφορών. Επιπλέον, έλεγχος χάους πραγματοποιείται για να εξετάσουμε πως η χρήση ανδρικού προφυλακτικού κατά τη διάρκεια σεξουαλικής επαφής επηρεάζει τα περιστατικά γονόρροιας.

Το δεύτερο μέρος της διατριβής ασχολείται με τη μελέτη της ηλιακής μαγνητικής δραστηριότητας μέσω του αριθμού ηλιακών κηλίδων. Διεξάγεται ανάλυση των μηνιαίων και ετήσιων δεδομένων του αριθμού ηλιακών κηλίδων˙ επιπρόσθετα, μελλοντικές προβλέψεις πραγματοποιούνται για την πρόγνωση ηλιακής δραστηριότητας μέσα στους επόμενους μήνες και δεκαετίες κάνοντας χρήση αλγόριθμου νευρονικών δικτύων. Για τον έλεγχο ακρίβειας των μελλοντικών προβλέψεων των προτεινόμενων μοντέλων μας, μηνιαίες και ετήσιες παρελθοντικές προβλέψεις διεξάγονται και συγκρίνονται με τους αντίστοιχους πραγματικούς αριθμούς ηλιακών κηλίδων. Δείχνεται ότι τα ετήσια δεδομένα ηλιακών κηλίδων μπορούν να χρησιμοποιηθούν για μακροπρόθεσμες προβλέψεις. Οι ετήσιες προβλέψεις μας δείχνουν ότι το επίπεδο ηλιακής δραστηριότητας αναμένεται να μειωθεί σημαντικά κατά τη διάρκεια των επόμενων 90 ετών. Τέλος, διεξάγεται επαναξιολόγηση των προτεινόμενων μοντέλων μας για την πρόβλεψη ηλιακής δραστηριότητας, υπό το φως των πρόσφατα αναθεωρημένων δεδομένων του αριθμού ηλιακών κηλίδων, δείχνοντας ότι δεν υπάρχει σημαντική επίδραση στην απόδοσή τους.

Το τρίτο και τελευταίο μέρος συνδέει όλα τα θέματα που μελετώνται στα προηγούμενα μέρη της διατριβής. Εξετάζεται η ύπαρξη συσχέτισης ανάμεσα σε γήινα και εξωγήινα φαινόμενα, ξεκινώντας με μία ανασκόπηση της υπάρχουσας βιβλιογραφίας σχετικά με την πιθανή σύνδεση μεταξύ ηλιακής δραστηριότητας και γήινων (βιολογικών και οικονομικών) φαινομένων. Στη συνέχεια, προσπάθεια εύρεσης πιθανής συσχέτισης μεταξύ ηλιακής δραστηριότητας και αγροτικής οικονομίας πραγματοποιείται, μελετώντας τις τιμές των σιτηρών στην Βρετανία των Πρώιμων Νεότερων χρόνων. Τα αποτελέσματα της μελέτης μας υποδεικνύουν πιθανή σύνδεση μεταξύ ηλιακής δραστηριότητας και αγοράς σιτηρών. Μία ασυνέπεια παρατηρείται ωστόσο στις τιμές των σιτηρών μεταξύ δύο ηλιακών ελαχίστων (Maunder και Dalton Ελάχιστα). Προτείνουμε ότι η ραγδαία μεταβολή στις αγροτικές τεχνικές που έλαβε μέρος κατά τη διάρκεια του Maunder Ελαχίστου οδηγώντας σε αυξημένη παραγωγή σιτηρών, θα μπορούσε να είναι μία αντίδραση στην μεγάλη κλιματική αλλαγή της πιο ψυχρής περιόδου της Μικρής Εποχής Παγετώνων, οδηγώντας σε αυτήν την ασυνέπεια.

Contents

Chapter 1

Introduction

This thesis contributes to the understanding of the complex population dynamics. The dissertation is developed in six chapters and interpolates material from six published research papers by the author (Gkana and Zachilas, 2013, Gkana and Zachilas, 2015a; Gkana and Zachilas, 2015b; Gkana and Zachilas, 2015c; Zachilas and Gkana, 2015; Gkana and Zachilas, 2016). Some material from each of these papers has been also incorporated into this introductory chapter. In Chapter 1 we present all the analytic, qualitative, and numerical techniques that we use to investigate the complex dynamical systems studied in this thesis. Chapters 2 and 3 start by providing some background review of the existing literature on dynamical systems describing predator-prey interactions and epidemics of infectious diseases. In these chapters we focus on the research of predator-prey interactions and transmission of infectious diseases by further modifications of various population models in order to make them more realistic. In Chapter 2 we start by investigating the effect of refugia on a predator-prey dynamical system with passive predators. Further, we examine the effect of prey refuge on the evolution of populations which have no overlap between successive generations. Finally, the economic repercussions of the outbreaks and infectious disease epidemics corresponding to the prey populations studied in this chapter are also examined. In Chapter 3, we investigate the transmission dynamics of an infection disease by taking into account the time interval length between successive clinical cases. Sections 2.1 and 2.2 use material from Gkana and Zachilas (2013) and Gkana and Zachilas (2015a), respectively. Section 3.1 is based on Gkana and Zachilas (2015b).

In Chapter 4 we investigate the solar magnetic activity using the sunspot numbers. We start by providing some basic information on solar magnetic activity; a brief introduction to neural networks that we use in Sections 4.1 – 4.3 to perform sunspot-number predictions is also given. In Sections 4.1 and 4.2 we analyze the monthly and yearly sunspot numbers in order to study whether they come from a stochastic or a deterministic chaotic process. We also propose monthly and yearly neural network models; we test their predictive accuracy by performing various *post-facto* reconstructions. Further, we perform future sunspot-number predictions in order to forecast the solar activity during the next months and decades. In Section 4.3 we re-evaluate the performance of our proposed neural network models in the light of the recently revised sunspot-number data. Sections 4.1, 4.2, and 4.3 are based on Gkana and Zachilas (2015c), Zachilas and Gkana (2015), and Gkana and Zachilas (2016), respectively. In the last part of this thesis, Chapter 5, we investigate the existence of solar-terrestrial

connection. A summary of the existing literature on the possible link between extraterrestrial (solar activity) and terrestrial (biological and economic) phenomena is provided. Based on the studies of solar-agricultural connection, we investigate the existence of relationship between solar activity and London & Southern England wheat market in Early Modern Britain. In Chapter 6 an overall summary of the main findings of the studies presented in this thesis, discussion and suggestions for future research are given.

1.1 Dynamical Systems

In this thesis we study mathematical models of systems that evolve in time (*i.e.* dynamical systems). The models consist of the following three elements: the *independent* variable, the *dependent* variables, and the *parameters*. The independent variable is the time. The dependent variables are functions of the time. The parameters do not depend on time but can be adjusted by natural causes or by a scientist running the experiment depending on the specifics of the application at hand. However in many models only approximate values are known for the parameters. Determining how the behavior of the dependent variables changes when one adjusts the parameters is the most important aspect of the study of a model (Blanchard *et al.*, 2006).

The notion of a dynamical system includes the following (Boccara, 2010): (i) a phase space S whose elements represent all the possible states of the system, (ii) the time t which may be discrete or continuous, (iii) and an evolution law that allows the determination of the state at time t from the knowledge of the states at all previous times. Dynamical systems may be divided into two brand categories according to whether the time variable may be considered as continuous or discrete. Thus the dynamics of a given one-dimensional system is described by (i) differential equations or (ii) finite difference equations:

(i) $\dot{x} \equiv \frac{dx}{dt} = f\left(x\right)$

(ii) $x_{t+1} = f\left(x_t\right)$

In this thesis we study systems describing the evolution of phenomena occurring at discrete time intervals (*e.g.* the growth process of a species that breed at specific time). Discrete dynamical systems are also known as *iterated maps*. Moreover, we study only time-invariant systems known as *autonomous*. Autonomous systems evolve according to equations that are determined entirely by the values of the dependent variables (Blanchard *et al.*, 2006). *One-dimensional* (1D) maps have the form

$x_{n+1} = f(x_n)$ where $x_n \in \mathbb{R}$. Starting from a point x_0 one may generate a sequence that is the iterative procedure of a discrete dynamical system (Elaydi, 2005): $x_0, f(x_0), f(f(x_0)), f(f(f(x_0))),...$ where $f^2(x_0) = f(f(x_0))$, $f^3(x_0) = f(f(f(x_0)))$, …, etc.

$f(x_0)$ is the known as the 1st iterate of x_0 under *f*, $f^2(x_0)$ is the known as the 2nd iterate of x_0 under *f*, and $f^n(x_0)$ is the nth iterate of x_0 under *f*. The set of all iterates $\{f^n(x_0) : n \geq 0\}$, where $f^0(x_0) = x_0$ by definition, is called the *orbit of* x_0 (Elaydi, 2005).

We focus on systems of nonlinear difference equations that involve more than one dependent variable; *i.e. two-dimensional* (2D) maps. Nonlinear 2D maps have the form:

$$\begin{aligned} x_{n+1} &= f(x_n, y_n) \\ y_{n+1} &= g(x_n, y_n) \end{aligned} \tag{1}$$

f and g are nonlinear functions of x_n, y_n (*e.g.* quadratic)

While *n-dimensional* (ND) maps have the form:

$$\begin{aligned} x_{n+1}^1 &= f_1(x_n^1, x_n^2, ..., x_n^N) \\ x_{n+1}^2 &= f_2(x_n^1, x_n^2, ..., x_n^N) \\ &\vdots \\ x_{n+1}^N &= f_N(x_n^1, x_n^2, ..., x_n^N) \end{aligned}$$

Since in this thesis we study only two-dimensional maps we will stick to 2D. Hence, suppose we have the above nonlinear 2D map (Equation (1)). A *solution* to a system of two equations is a pair of functions that describe the dependent variables as functions of time. To determine these functions we must solve both equations $f(x_n, y_n)$, $g(x_n, y_n)$ simultaneously (Blanchard *et al.*, 2006). Unfortunately, finding the exact solutions of discrete maps is rarely possible. Hence, there is a combination of three different methods one can use to study the solutions of a system (Blanchard *et al.*, 2006): (i) the *analytic* approach where one searches for explicit formulas that describe the behavior of solutions, (ii) the *qualitative* approach which involves using geometry to give an overview of the behavior of solutions, (iii) and the *numerical* approach where the computer approximates the solution we seek. However, even with these techniques, it is unable for one to describe even 1D nonlinear

iterations completely. The reason is that many discrete nonlinear maps behave in a complex and unpredictable manner (Blanchard *et al.*, 2006).

Overall, the dynamics of the proposed and modified models of the following chapters are investigated as follows (Blanchard *et al.*, 2006): (i) the meaning of the variables and parameters is described, (ii) explanation is given on why each system is the way it is, (iii) analytic, qualitative, and numerical techniques are used in order to describe the dynamics of each model, (iv) justifications for the specific values chosen for the parameters are given, concluding with (v) discussion on which model (basic vs. modified) describes better the real-world system.

1.1.1 Discretization of continuous-time dynamical systems

Discrete-time models are often directly applicable to time-series data and may represent contacts which are restricted to a specific time or time period more accurately (Allen *et al.*, 2004). Therefore, it may be easier to compare the output of discrete-time models with statistical real-world data. Moreover, parameters in discrete time models can be more easily related to data that have been collated over discrete time interval (Getz and Lloyd-Smith, 2006). Discretizing a continuous-time model has the following advantages (Ramani *et al.*, 2004):

1. The epidemic statistics are collected from given time intervals, not continuously. This makes discrete-time models more realistic than the continuous ones.
2. The discrete-time models provide natural simulators for the continuous-time models. Thus, one can not only study with good accuracy the behavior of the continuous-time model, but also evaluate the effect of larger time steps.
3. With discrete-time models one can use the entire arsenal of methods that have been developed for the study of mappings and lattice equations, either from integrability and/or chaos points of view.

There are several ways to discretize a continuous-time model. However, the approach of discretizing the differential equations of a dynamical system has the advantage that can keep track of the known properties of the continuous time system (Hadeler and Gerstmann, 1990). In Sections 2.2 and 3.1 we use the *Euler's algorithm* to discretize two continuous-time dynamical systems describing the predator-prey interactions and the transmission of an infectious disease. The *Euler's method* is a numerical scheme that can be used to discretize the differential equations of a continuous-time dynamical system. Consider the first-order differential equation (Elaydi, 2005): $\dot{x} = f\left(t, x\left(t\right)\right)$ with $x\left(t_0\right) = x_0$ and $t_0 \le t \le b$. Dividing the interval $\left[t_0, b\right]$ into N equal subintervals, the size of each

subinterval is called the *step size* of the method and is denoted by $\delta = (b - t_0)/N$. This step size defines the *nodes* $t_0, t_1, t_2, ..., t_N$, where $t_j = t_0 + j\delta$. The Euler's method approximates $\dot{x}$ by $\left(x(t+\delta) - x(t)\right)/\delta$. Substituting this values into the differential equation gives $x(t+\delta) = x(t) + \delta g\left(t, x(t)\right)$.

And for $t = t_0 + n\delta$ we obtain $x\left[t_0 + (n+1)\delta\right] = x(t_0 + n\delta) + \delta g\left[t_0 + n\delta, x(t_0 + n\delta)\right]$ for $n = 0, 1, 2, ..., N-1$. Adapting the difference equation notation and replacing $x(t_0 + n\delta)$ by $x(n)$ gives the *Euler's algorithm* (Elaydi, 2005):

$$x(n+1) = x(n) + \delta f\left[n, x(n)\right] \tag{2}$$

1.1.2 Fixed points and stability criteria in two-dimensional maps

Equilibrium solutions or *equilibrium points* or *fixed points* are the simplest orbits for dynamical systems (Blanchard *et al.*, 2006). In 1D discrete dynamical systems a point x^* in the domain of *f* is said to be fixed point if it is a constant solution of *f*: $f(x^*) = x^*$ (Elaydi, 2005). Accordingly, in 2D systems the fixed point is a pair of constant functions in which the system is at rest; *i.e.* solution curves where x_n and y_n never vary. Hence, the orbit of a fixed point is a constant sequence $x^*, x^*, x^*, ...$ and $y^*, y^*, y^*, ...$. By solving the equations $f(x^*, y^*) = x^*$ and $g(x^*, y^*) = y^*$ we find the fixed points of a 2D discrete dynamical system. Another basic type of orbit for discrete dynamical systems is the stable periodic solution or *periodic cycle*. The orbit of a periodic cycle is a sequence of *k* distinct points which under the iterated action are repeatedly visited by the system always in the same order. The resulting sequence is known as "*k-period* cycle" (Barnett *et al.*, 2006). Hence, the orbit of a cycle of period *k* is the repeating sequence $(x_1, y_1), (x_2, y_2), ..., (x_k, y_k)$.

Suppose the 2D map (Equation (1)) has a fixed point at (x^*, y^*). A fixed point (x^*, y^*) of a 2D system is called *attracting* if there is an interval around (x^*, y^*) having the property that every initial point in this interval has an orbit that remains in the interval and tends to (x^*, y^*) under iteration of the map. The fixed point is called *repelling* if there is an interval around (x^*, y^*) having the property that every initial point in this interval – except (x^*, y^*) – has an orbit that leaves the interval under iteration of the map. A fixed point that is neither attracting nor repelling is called *neutral* or *indifferent* (Blanchard

et al., 2006). Analytic techniques can be used to study the behavior of solutions around a fixed point. In Chapters 2 and 3 analytical stability analysis[1] is obtained in each section in order to investigate the local stability properties of the fixed points and the several local bifurcations our modified models undergo as well. In order to study the local behavior around a fixed point $\left(x^*, y^*\right)$ we calculate the Jacobian matrix at $\left(x^*, y^*\right)$. If we perturb around the fixed point $\left(x^*, y^*\right)$ by some small amount $\hat{x}_n, \hat{y}_n$ then (McKane, 2007):

$$x_n = x^* + \hat{x}_n \qquad x_{n+1} = x^* + \hat{x}_{n+1}$$
$$y_n = y^* + \hat{y}_n \qquad y_{n+1} = y^* + \hat{y}_{n+1}$$

The nonlinear terms can be discarded after using Taylor series expansions around the fixed point:

$$x^* + \hat{x}_{n+1} = f\left(x^*, y^*\right) + \left.\frac{\partial f}{\partial x}\right|_{\left(x^*, y^*\right)} \hat{x}_n + \left.\frac{\partial f}{\partial y}\right|_{\left(x^*, y^*\right)} \hat{y}_n + \ldots$$
$$y^* + \hat{y}_{n+1} = g\left(x^*, y^*\right) + \left.\frac{\partial g}{\partial x}\right|_{\left(x^*, y^*\right)} \hat{x}_n + \left.\frac{\partial g}{\partial y}\right|_{\left(x^*, y^*\right)} \hat{y}_n + \ldots$$

Notice that $x^* = f\left(x^*, y^*\right)$ and $y^* = g\left(x^*, y^*\right)$ by definition, so that they cancel. This then leaves us to write this in matrix (McKane, 2007):

$$\begin{pmatrix} \hat{x}_{n+1} \\ \hat{y}_{n+1} \end{pmatrix} = \left.\begin{pmatrix} \frac{\partial f}{\partial x} & \frac{\partial f}{\partial y} \\ \frac{\partial g}{\partial x} & \frac{\partial g}{\partial y} \end{pmatrix}\right|_{\left(x^*, y^*\right)} \begin{pmatrix} \hat{x}_n \\ \hat{y}_n \end{pmatrix}$$

That is, the *Jacobian* where the elements have been evaluated at the fixed point:

$$J\left(x^*, y^*\right) = \begin{pmatrix} \frac{\partial f\left(x^*, y^*\right)}{\partial x_n} & \frac{\partial f\left(x^*, y^*\right)}{\partial y_n} \\ \frac{\partial g\left(x^*, y^*\right)}{\partial x_n} & \frac{\partial g\left(x^*, y^*\right)}{\partial y_n} \end{pmatrix} = \begin{pmatrix} J_{11} & J_{12} \\ J_{21} & J_{22} \end{pmatrix}$$

The *eigenvalues* of the Jacobian matrix *J* determine the stability of the equilibrium point $\left(x^*, y^*\right)$. Suppose that λ_1, λ_2 are the eigenvalues of the Jacobian. The eigenvalues are the roots of the

[1] The stability analysis results of the 2D maps studied in this thesis have been exhibited by using the software package *Maxima* (Available at: http://maxima.sourceforge.net/).

characteristic equation; hence, to find the eigenvalues, we need to derive the characteristic polynomial of the Jacobian matrix (Hirsch *et al.*, 2004):

$$det\left(J-\lambda I\right)=det\begin{pmatrix}J_{11}-\lambda & J_{12}\\ J_{21} & J_{22}-\lambda\end{pmatrix}=\lambda^2-\left(J_{11}+J_{22}\right)\lambda+\left(J_{11}J_{22}-J_{12}J_{21}\right)$$

The quantity $J_{11}+J_{22}$ in this equation is the sum of the diagonal elements of the Jacobian matrix. This quantity is called the *trace* of the Jacobian and is denoted by $trJ=J_{11}+J_{22}$. The constant term $detJ=J_{11}J_{22}-J_{12}J_{21}$ is the *determinant* of the Jacobian. Hence, the characteristic polynomial is $det\left(J-\lambda I\right)=\lambda^2-trJ\lambda+detJ$. It has a nonzero solution if and only if $det\left(J-\lambda\mathrm{I}\right)=0$; hence, solving this equation the two eigenvalues of the Jacobian matrix are given by:

$$\lambda_{1,2}=\frac{trJ\pm\sqrt{tr^2J-4detJ}}{2}$$

Moreover, applying *Vieta's formula* (Viète, 1646) to the quadratic characteristic polynomial then the trace of the Jacobian matrix is the sum of the eigenvalues and the determinant is the product of the eigenvalues; *i.e.* if λ_1 and λ_2 the roots of $\lambda^2-trJ\lambda+detJ=\left(\lambda-\lambda_1\right)\left(\lambda-\lambda_2\right)=0$ then:

$\lambda_1+\lambda_2=trJ$ and $\lambda_1\cdot\lambda_2=detJ$

By using Vieta's equations $\lambda_1+\lambda_2=trJ$, $\lambda_1\cdot\lambda_2=detJ$ and applying *Jury's conditions* (1974) the fixed point is linearly asymptotically stable if and only if the trace and the determinant of the Jacobian satisfy the condition $\left|trJ\right|<1+detJ<2$ or, equivalently (Boccara, 2010):

$$\begin{aligned}&1+trJ+detJ>0\\&1-detJ>0\\&1-trJ+detJ>0\end{aligned}\qquad(3)$$

Hence, knowing trJ and $detJ$ tells us the eigenvalues of the Jacobian matrix and therefore everything about the geometry of solutions of the system.

1.1.3 Classification of fixed points and local bifurcations

The eigenvalues λ_1,λ_2 of the Jacobian matrix yield the information about stability of the system. There are three cases (Elaydi, 2005): (a) distinct real eigenvalues λ_1,λ_2, (b) repeated real eigenvalues λ, (c) complex conjugate eigenvalues $\lambda=\alpha\pm i\beta$. In case (a) the fixed point $\left(x^*,y^*\right)$ is locally

asymptotically stable if both the eigenvalues lie inside the unit disk $|\lambda_1|<1$ and $|\lambda_2|<1$. If they both lie outside the unit disk $|\lambda_1|>1$ and $|\lambda_2|>1$ the fixed point (x^*, y^*) is locally unstable. In particular: (i) if $0<\lambda_1<\lambda_2<1$ the fixed point is an asymptotically *stable node*, (ii) if $\lambda_1>\lambda_2>1$ the fixed point is an *unstable node*, (iii) if $0<\lambda_1<1$ and $\lambda_2>1$ the fixed point is a *saddle*, (iv) if $\lambda_1=1$ and $\lambda_2<\lambda_1$ the fixed point is a *stable degenerate node* – all the points on the vertical axis y in phase space (x, y) are equilibrium points. In case (b) with two repeated eigenvalues: (i) if $\lambda_1=\lambda_2<1$ fixed point is asymptotically *stable*, (ii) if $\lambda_1=\lambda_2=1$ all the points on the horizontal axis x in phase space (x, y) are equilibrium points – *unstable degenerated* case. In case (c) the Jacobian matrix has two complex conjugate eigenvalues $\lambda_1=\alpha+i\beta$ and $\lambda_2=\alpha+i\beta$ with $\beta\neq 0$ and $tr^2J-4detJ<0$. In this case: (i) if $detJ<1$ the fixed point is an asymptotically *stable focus* and there are two complex eigenvalues with real parts $|\alpha|<1$, (ii) if $detJ>1$ the fixed point is an *unstable focus* and there are two complex eigenvalues with real parts $|\alpha|>1$, if $detJ=1$ and $-2<trJ<+2$ the fixed point is a (*stable*) *center* and there are two complex eigenvalues with real parts $|\alpha|=1$.

In order for a model to be useful one must know how the variations in the control parameter values change the orbit structure of the system. When a small change in a parameter value *a* leads to a drastic change in the long-term behavior of solutions, then this change is known as a *bifurcation*. These changes may include the birth or death of fixed points and periodic cycles or changes in the type of these orbits. The parameter value $a=a_0$ where the change occurs is known as the *bifurcation point* and is the threshold value above which the behavior of solutions alter significantly (Blanchard *et al.*, 2006).

A fixed point is *hyperbolic* if none of the eigenvalues of the Jacobian matrix has unit modulus (*i.e.* $|\lambda_1|\neq 1$ and $|\lambda_2|\neq 1$). If a fixed point is hyperbolic then for values of a varied parameter *a* sufficiently close to the bifurcation value a_0 the stability of the fixed point is not affected. If the fixed point is *non-hyperbolic* – at least one eigenvalue has unit modulus (*i.e.* either $|\lambda_1|=1$ or $|\lambda_2|=1$) – then for values of *a* close to a_0 a totally new dynamical behavior can occur. Hence, *non-hyperbolic* points on maps are usually bifurcation points (Boccara, 2010). The types of local bifurcations we will meet in the 2D maps studied in this thesis are the *Fold bifurcation*, the *Flip bifurcation*, and the *Neimark-Sacker bifurcation*. Considering a 2D map $f_a(x, y), g_a(x, y)$ that depends on a parameter a:

1. In a *Fold* or *Tangent* or *Saddle-node bifurcation* fixed or periodic orbits suddenly appear or disappear; *i.e.* as the parameter passes through the bifurcation value $a = a_0$, the birth of a fixed point $\left(x^*, y^*\right)$ occurs which then splits into two fixed points $\left(x_1^*, y_1^*\right), \left(x_2^*, y_2^*\right)$, and vice versa. Hence, there is an interval about the bifurcation value a_0 and another interval *I* in which the system has (Hirsch *et al.*, 2004): (i) two hyperbolic fixed points – one asymptotically stable and one unstable – in *I* if $a < a_0$, (ii) one non-hyperbolic fixed point in *I* if $a = a_0$, (iii) no fixed points in *I* if $a > a_0$.
2. The *Neimark-Sacker* or *Hopf bifurcation* is an interesting transition for iterated maps where, as the varied parameter *a* passes through the bifurcation value a_0 the attracting fixed point $\left(x^*, y^*\right)$ loses stability and an invariant curve (*i.e.* closed curve densely filled up by *quasi-periodic*[2] motion) is born (Hirsch *et al.*, 2004): (i) a stable fixed point if $a < a_0$, (ii) a non-hyperbolic fixed point with the modulus of a pair of complex eigenvalues equal to one if $a = a_0$, (iii) an unstable fixed point and all nonzero solutions spiral toward an isolated closed invariant curve as $n \to \infty$ if $a > a_0$; all the orbits outside and inside the invariant curve approach the attracting curve under iterations of the map.
3. *Flip or period-doubling bifurcation* is one of the most important types of bifurcations for discrete dynamical systems. This bifurcation produces a new periodic cycle having twice the period of the original cycle. In particular, the original orbit of period 2^{n-1} changes from attracting to repelling (or vice versa) and is accompanied by the birth of a new orbit of period 2^n (Blanchard *et al.*, 2006). *Reverse flip* or *period-halving bifurcation* is also possible with the new cycle having half the period of the original cycle. Hence, as the varied parameter *a* passes through the bifurcation value a_0: (i) one asymptotically stable fixed point if $a < a_0$, (ii) one non-hyperbolic fixed point if $a = a_0$, (iii) the original stable fixed point becomes unstable and a stable cycle of period 2 appears in the system if $a > a_0$.

Moreover, the stability conditions (Equation (3)) are associated with these three local bifurcations in the following way (Agliari *et al.*, 2009): (i) the first condition $-trJ = 1 + detJ$ is associated with a *Flip bifurcation* and one real eigenvalue equal to -1, (ii) the second condition $detJ = 1$ is associated with

[2] *Quasi-periodic* orbits are another type of attractors that look quite complicated since the motion never exactly repeats itself but the motion is never chaotic. The dynamics of a quasi-periodic attractor can be described as a mechanism consisting of two or more independent periodic motions (Barnett *et al.*, 2006).

a *Neimark-Sacker* bifurcation and two complex eigenvalues crossing the unit circle (*i.e.* a pair of complex eigenvalues with unit modulus), (iii) the third condition $trJ = 1 + detJ$ is associated with a *Fold bifurcation* and one real eigenvalue equal to $+1$.

1.2 Chaos

The period-doubling process may occur repeatedly leading to an *infinite sequence of period-doubling bifurcations*. In this case, as the parameter continues to vary, the successive births of attracting cycles give rise to a new type of behavior – chaos – where we cannot fully explain what is happening to the orbits for values in this regime (Blanchard *et al.*, 2006). The term "chaotic" seems to have been used for the first time by Li and York (1975) to qualify the apparently random behavior of deterministic non-periodic orbits of 1D maps. Moreover, May (1976) introduced the term "deterministic chaotic behavior" in his work where he studied the complex dynamics of a simple 1D population model. Roughly speaking, *chaos* is the aperiodic long-term behavior in a deterministic system that exhibits sensitive dependence on initial conditions (Strogatz, 1994). Hence, when a system exhibits chaos there are no regular cycles of any period (fixed points, periodic orbits, or quasi-periodic orbits); a chaotic orbit, although generated by a deterministic[3] system, has all the characteristics of random behavior.

Attractors[4] with orbit structure more complicated than that of periodic or quasi-periodic motions are called strange attractors (Barnett *et al.*, 2006). In particular, a *strange attractor* is defined to be an attractor that exhibits sensitive dependence on initial conditions (Eckmann and Ruelle, 1985). According to Ruelle (Ruelle, 1980; Ruelle and Takens, 1971), a bounded set $A \subset \mathbb{R}^k$ is a *strange attractor* for a map $\boldsymbol{f}$ if there is a *k*-dimensional neighborhood *N* of *A* such that for all $t \in \mathbb{N}$, $\boldsymbol{f}^t(N) \subset N$, and if, for all initial points of *N*, the map $\boldsymbol{f}$ has sensitive dependence on initial conditions. The mechanisms that are responsible for the existence of a strange attractor are the (Gilmore, 1993): (i) *stretching* and (ii) *compressing*. The stretching is responsible for sensitive dependence on initial conditions. The compressing is responsible for the recurrent[5] behavior exhibited by all chaotic systems. Each strange attractor contains a large number of unstable dense periodic orbits of many periodicities (Gilmore, 1993). However, when studying a dynamical system on a computer one needs an operational

[3] *Deterministic* means that a system has no random or noisy inputs or parameters. The irregular behavior arises from the system's nonlinearity, rather than from noisy driving forces (Strogatz, 1994).
[4] Roughly speaking an *attractor* is an invariant set with the property that nearby orbits are drawn to it asymptotically (Aronson *et al.*, 1982).
[5] The *compressing* mechanism is responsible for patterns which almost repeat themselves throughout a chaotic data set ensuring that trajectories do not run off to infinity and return to a bounded region of phase space (Gilmore, 1993).

definition for strange attractor (Aronson *et al.*, 1982): a dynamical system is said to have a strange attractor if there is an orbit which when followed for a long time does not appear to converge to a fixed point, a periodic orbit, or a quasi-periodic orbit.

The scenario in which a parameter-dependent system that has a simple deterministic time evolution becomes chaotic as a parameter changes is known as "route to chaos" (Boccara, 2010). Hence, one route to chaos is the *period-doubling route to chaos*; *i.e.* as the parameter varies the infinite sequence of period-doubling bifurcations gives rise to a range that exhibit chaotic dynamics. Another one is the *intermittency route to chaos* discovered by Pomeau and Manneville (1980) where as the varying parameter passes through a critical value, long-time intervals with periodic oscillations (*i.e.* laminar phases) seems to be abruptly and randomly disrupted by strong chaotic bursts – named "intermittences" – of finite duration. These bursts occur at seemingly random times, much larger than – and not correlated with – the period of the underlying oscillations. As the parameter continues to vary the chaotic bursts become more frequent and regular oscillations are no longer apparent; *i.e.* fully developed chaos is attained.

1.2.1 Lyapunov exponent

One necessary condition for a system's behavior to be chaotic is the *sensitive dependence on initial conditions*[6]. In real life the seed of an orbit is rarely known with complete accuracy. If a system exhibits chaos then this inaccuracy is really important; *i.e.* chaotic dynamical systems are exceptionally sensitive to small observation errors. In such a case, if one plot the time series for orbits initially very close, it is observed that after very few iterations they separate and thereafter bear little resemblance to one another. Hence, the small numerical errors that are always introduced in such numerical procedures are amplified by the action of the map making the predictions about the fate of orbits totally distrusted (Blanchard *et al.*, 2006).

However the "sensitive dependence on initial conditions" alone is not a sufficient condition for a system to be chaotic. Another indication is the *Lyapunov Exponent* which can be used to measure the "sensitive dependence on initial conditions" of a chaotic system (Boccara, 2010). In particular, if *f* is a map on $\mathbb{R}$ and $\{x_0, x_1, ...\}$ is a bounded orbit, then the orbit is called *chaotic* if (Alligood *et al.*, 1996): (i) it is not asymptotically periodic, and (ii) its Lyapunov exponent is positive $(\lambda > 0)$. The Lyapunov

[6] An *initial condition* for a 2D system yields a solution which consists of two functions x_n, y_n that, taken together, satisfy the system of the equations. Using an initial value for each dependent variable (x_0, y_0) one can determine the way in which they evolve in time (Blanchard *et al.*, 2006).

exponents for the dynamical systems studied in Chapters 2 and 3 were calculated using the algorithm introduced by Wolf *et al.* (1985). Considering two neighboring initial points x_0 and $x_0+\varepsilon$ (where ε is the infinitesimally small difference between the two points; *i.e.* the error between the estimated and the actual initial value), if after *n* iterations of the map *f* the distance between the two nearby points $\left|f^n(x_0+\varepsilon)-f^n(x_0)\right|$ grows exponentially, the Lyapunov exponent $\lambda(x_0)$ can be defined by $\left|f^n(x_0+\varepsilon)-f^n(x_0)\right| \sim \varepsilon e^{n\lambda(x_0)}$ (Boccara, 2010). In particular, by taking the logarithm and solving for $\lambda(x_0)$ the Lyapunov exponent is given by:

$$\lambda(x_0)=\lim_{n\to\infty}\lim_{\varepsilon\to\infty}\frac{1}{n}\log\left|\frac{f^n(x_0+\varepsilon)-f^n(x_0)}{\varepsilon}\right|=\lim_{n\to\infty}\frac{1}{n}\log\left|\frac{df^n(x_0)}{dx}\right|$$

$\lambda(x_0)$ is the Lyapunov Exponent for an orbit with initial point x_0 and $e^{\lambda(x_0)}$ is the average factor by which the distance between two neighboring points becomes stretched after one iteration. Moreover, applying the chain rule, $df^n/dx\big|_{x=x_0}=f'(x_{n-1})\,f'(x_{n-2})\ldots f'(x_0)=\sum_{i=0}^{n-1}f'(x_i)$ where $f'(x_i)\neq 0$ for all *i*, the Lyapunov exponent can be also expressed as (Boccara, 2010):

$$L=\lim_{n\to\infty}\frac{1}{n}\log\left|\sum_{i=0}^{n-1}f'(x_i)\right|=\lim_{n\to\infty}\frac{1}{n}\sum_{i=0}^{n-1}\log\left|f'(x_i)\right|$$

where, $x_i=f^i(x_0)$, for $i=0,1,2,\ldots,n-1$

Hence, the method of Lyapunov exponents measures the asymptotic exponential rate of convergence or divergence of infinitesimally nearby orbits, since it is evaluated in the limit of an indefinitely large numbers of iterations as $n\to\infty$, assuming that the limit exists (Barnett *et al.*, 2006). The sign of the Lyapunov exponent classifies the different types of a system's dynamical behavior as follows (Wolf *et al.*, 1985): (i) a positive Lyapunov exponent $L>0$ indicates chaos (diverged neighbouring orbits), (ii) a negative Lyapunov exponent $L<0$ defines a periodic orbit (converged neighbouring orbits), and (iii) a zero Lyapunov exponent $L=0$ represents an orbit with marginal stability. Often only the largest Lyapunov exponent [λ_{max}] is calculated since it yields the greatest insight into the dynamics of the system (McCue and Troesch, 2011). A positive[7] largest Lyapunov exponent indicates that nearby

[7] A strictly positive largest Lyapunov exponent is often considers as a definition of "deterministic chaos" (Pikovsky and Politi, 2016).

orbits diverge exponentially in the corresponding direction and is intimately related to the lack of predictability; thus $\lambda_{\max} > 0$ defines the chaotic behavior of a dynamical system (Barnett *et al.*, 2006).

Calculating the largest Lyapunov exponent from time series

In Chapter 4 we investigate the presence of chaos in the monthly and yearly actual sunspot-number data by calculating the largest Lyapunov exponent [$\lambda_{\max}$]. We use the two methods developed by Rosenstein *et al.* (1993) and Kantz (1994) for calculating the largest Lyapunov exponent from time series directly. The two methods are similar; they calculate the largest Lyapunov exponent by searching for all neighbors within a neighborhood of the reference trajectory and compute the average distance between neighbors and the reference trajectory as a function of time (Rosenstein *et al.*, 1993; Kantz, 1994). In particular, they developed independently an algorithm which calculates the largest Lyapunov exponent from time series directly as follows:

$$S(\tau) = \frac{1}{T}\sum_{t=1}^{T} \ln\left(\frac{1}{|U_t|}\sum_{i\in U_t}|x_{t+\tau} - x_{i+\tau}|\right)$$

x_t is the arbitrary point in time series, U_t is the neighborhood of x_t, x_i is the neighbor of x_t, τ is the relative time scaled by sampling rate, T is the length of time series, $S(\tau)$ is the stretching factor with region of robust linear increase showing slope equal to Lyapunov exponent (Kantz, 1994).

As mentioned above, chaos means unpredictability; an important factor in performing accurate predictions is the upper limit of predictability. The predictability of a system is essentially determined by the Lyapunov exponents. In particular, the magnitude of the largest Lyapunov exponent is an indicator of the time scale on which chaotic behavior can be predicted (Wolf, 1986). Hence, when a system has positive largest Lyapunov exponent, there is a "time horizon" beyond which prediction breaks down (Strogatz, 1994). Specifically, the inverse of the largest Lyapunov exponent $\left(T_{\text{pr}} \approx 1/\lambda_{\max}\right)$, known as the *Lyapunov time*, is the characteristic time of instability (the perturbation doubles within such time interval) and identifies the *predictability time* (Pikovsky *et al.*, 2001; Pikovsky and Politi, 2016); that is, the length of the time horizon on which predictions are effective.

1.2.2 Chaos control in two-dimensional maps

Although predictions in deterministic chaotic systems are distrusted, later studies showed that chaotic behaviors are controllable via small perturbations to the control phase trajectories of the systems. Plapp and Hübler (1990) proposed a method which control chaos by applying large perturbations to system parameters. Ott, Grebogi, and Yorke (1990) proposed a chaos control method known as the *OGY*

algorithm, showing that it is possible to convert the chaotic behavior of a dynamical system to periodic behavior by making small time-dependent perturbations in an accessible system parameter. They applied successfully their control method to the Henon map by creating a large variety of attracting periodic motions and choosing the most desirable amongst them. Their method relies on a large class of chaotic attractors having embedded within it an infinite number of unstable periodic orbits (Grebogi *et al.*, 1988). The OGY algorithm has been applied to control various experimental systems (Ditto *et al.*, 1990; Singer *et al.*, 1991).

Another interesting method to gain control over deterministic chaotic behavior has been proposed by Güémez and Matias (1993) known as the *G.M. algorithm* which stabilizes a given unstable periodic orbit by performing a feedback to the variable of the iterated map every Δn iterations. In contrast to the OGY algorithm the G.M. algorithm does not change system parameters. Suppose we have the nonlinear two-dimensional map (Equation (1)). The G.M. control algorithm consists of the application of a proportional feedback (γ_1, γ_2) to the variables of the system x, y in the form of pulses, every Δn iterations (Güémez and Matias, 1993):

$$\begin{aligned} x_n &\to x_n(1+\gamma_1) \\ y_n &\to y_n(1+\gamma_2) \end{aligned} \tag{4}$$

γ_1, γ_2 represent the strength of the feedback for x_n, y_n. Depending on the sign of γ_1, γ_2, some part of the system variables x, y is injected or withdrawn from Equation (4), which depends on the value of the variables x, y at the moment n; a new dynamical system is created based on the original one (Güémez and Matias, 1993; Codreanu and Danca, 1997b). By appropriately choosing Δn and γ_1, γ_2 it is possible to stabilize different unstable periodic orbits (Codreanu and Danca, 1997b).

Güémez and Matias (1993) applied the G.M algorithm to the logistic map and the exponential map for various values of the parameters. Later, they also applied their algorithm in the case of a chemical system (Matias and Güémez, 1994); they considered that this method can be applied to biological systems as well. In addition, Codreanu and Danca (1997a) applied the G.M. method to a predator-prey model supporting its use in biological systems. In this thesis we apply the G.M. algorithm to an epidemic model which describes the transmission of an infection disease (Chapter 3).

1.3 Numerical Simulation Tools

Considering the behavior of solutions away from the fixed points, the only way to study their behavior is via numerical simulations. In Chapters 2 and 3 various numerical simulation tools (Figure 1), such as parametric basins of attraction, bifurcation diagrams, phase plots, time series and largest Lyapunov exponent diagrams, are used in order to illustrate the stability analysis results and study further the complex dynamics of our systems. All numerical simulation results have been exhibited using the software package *E&F Chaos* (Diks *et al.*, 2008; Available at: http://cendef.uva.nl/software/ef-chaos/ef-chaos.html).

- The *phase plot* (x, y) is a diagram which illustrates the trajectories of a system that correspond to various initial conditions (Figure 1(a)). It can be used in order to investigate further the dynamical behavior and plot the attractors of the system (Diks *et al.*, 2008). The set of all solution curves is known as the *phase portrait* of the system. All phase plot figures illustrate each system's behavior for 1000 steps and for about 500000 iterations after a transient of 1000 iterations.
- The *parametric basins of attraction* (a, b) match different colors for periodic cycles of different period in a two-dimensional parametric space (Diks *et al.*, 2008). The different colors in all parametric planes (a, m) constructed in this thesis correspond to the following stable states (Figure 1(b)): light-blue for attracting fixed point, dark-blue for two-period cycle, yellow for three-period cycle, pink for four-period cycle, orange for five-period cycle, red for six-period cycle, light-green for seven-period cycle, dark-green for eight-period cycle, grey for nine-period cycle and purple for ten-period cycle. The white area corresponds to those values of parameters for which the behavior of solutions may be quasi-periodic (invariant curves) or aperiodic (chaos; strange attractors). The black area is the set of parameters for which every orbit diverges to infinity. We plot this diagram for 500 transient iterations, 450×450 resolution and convergence distance epsilon 0.001.
- The *bifurcation diagram* $(x^*, a), (y^*, a)$ is an extremely helpful numerical simulation tool to understand the qualitative changes occurring in the orbits of solutions as a system parameter varies (Figure 1(c)). In particular it highlights how the characteristics of the stable orbits change as the value of varying parameter increases/decreases in a specific interval (Blanchard *et al.*, 2006). The bifurcation diagrams constructed in this thesis illustrate the long run dynamical behavior 1000 iterations after a transient of 1000 iterations. Describing the qualitative changes in the orbit structure of the system which take place when the control parameters are varied we obtain not only a snapshot of chaotic dynamics but also a description of its emergence.

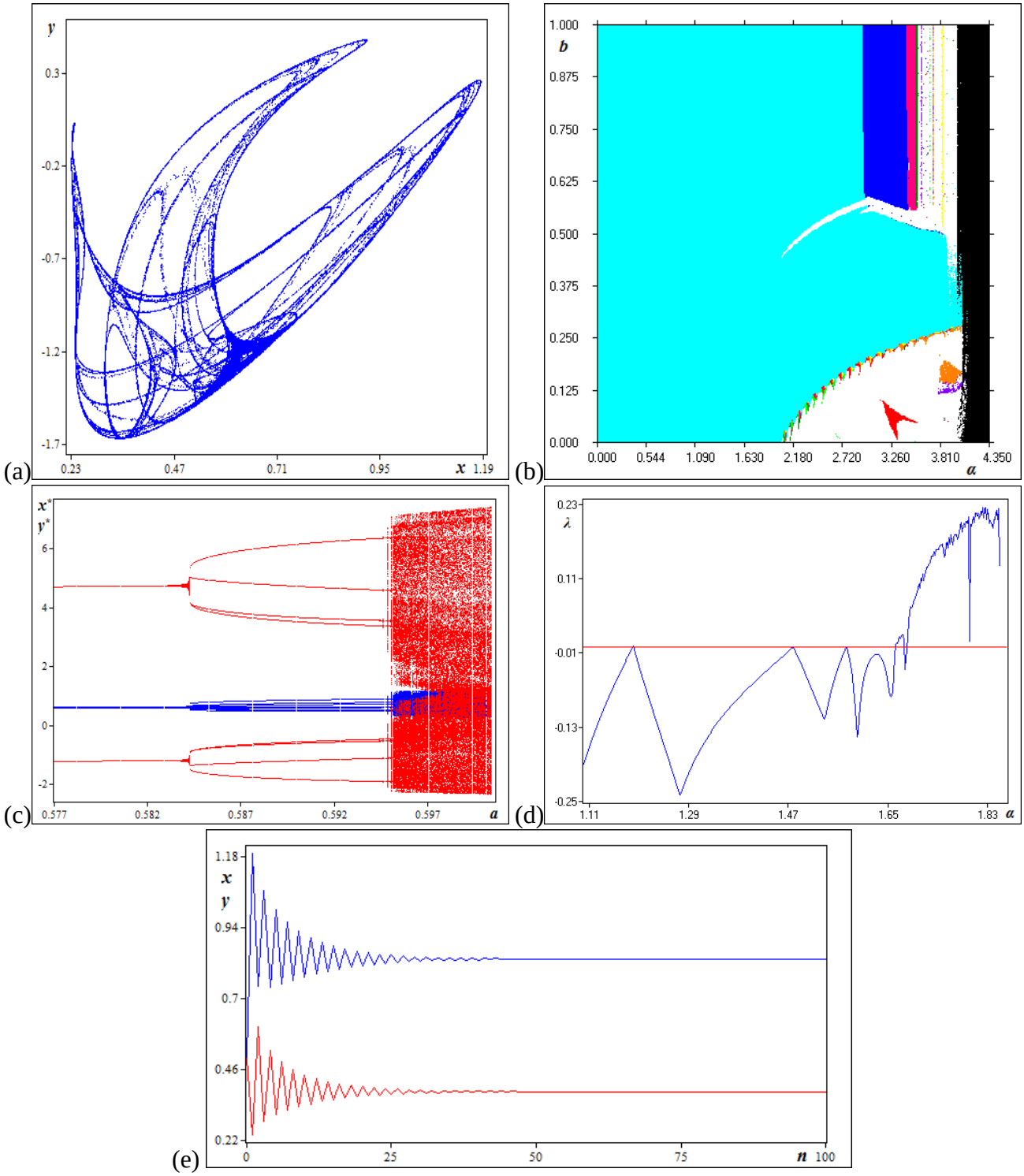

Figure 1 Numerical Simulation Tools. (a) Phase plot (x, y), (b) Parametric basins of attraction (a, b), (c) Bifurcation diagram $(x^*, a), (y^*, a)$, (d) Lyapunov exponent diagram (λ, α), (e) Time series diagrams $(x_n, n), (y_n, n)$.

- The *Lyapunov exponent diagram* (λ, a) as a function of one of the model parameters a is a numerical simulation tool that can be used to investigate the behavior of nonlinear dynamical

systems (Figure 1(d)). The plot illustrates for which values of the varying parameter two orbits with neighbouring initial conditions converge or diverge from one another exponentially, depending on the sign of the Lyapunov exponents. In this thesis we plot each Lyapunov exponent diagram for 5000 iterations after a transient of 300 iterations.

- The *times series* diagrams $(x_n, n), (y_n, n)$ is the best way to get information about the time variable *t*; they illustrate how fast the solutions traverses the curve (Figure 1(e)). The iteration count is plotted on the horizontal axis while the numerical values of the orbit on the vertical axis (Blanchard *et al.*, 2006).

1.4 Dynamical Analysis of Single Time Series

In Sections 4.1 and 4.2 we analyze[8] the monthly and yearly sunspot-number data in order to study whether they come from a stochastic or a deterministic chaotic process. Our data analysis is based on the method developed by Takens and Ruelle (1971) that shows how to reconstruct the *m*-dimensional phase space of a dynamical system from a single-variable observed times series, using the method of time delay coordinates. This method fills the other dimensions with lagged versions of one dynamical variable; for sufficient large *m* the reconstructed high-dimension system will be geometrically equivalent to the original system, producing an attractor of dimension *D*, $m = 2D+1$ (Takens, 1981). The property of the attractor will not change, therefore the *m*-dimensional system can be used to study the dynamical behavior of the original system (Zhang, 1996).

Packard *et al.* (1980) outline a simple method (time lag) developed by Ruelle and Takens (1971) for reconstructing a phase space from one dynamical variable denoted as $\{x(t_i)\}$, where $i = 1, 2..., N$; let $x(t_1), x(t_2), ..., x(t_N)$ be measurements of a physical variable of length *N* in discrete time. From this sequence one can construct a set of *m*-dimensional vectors $\mathbf{X}(t_i) = 1, 2, ..., N-(m-1)\tau$, of the form:

$$\mathbf{X}(t_i) = \{x(t_i), x(t_i+\tau), x(t_i+2\tau), ..., x(t_i+(m-1)\tau)\} \quad (5)$$

$x(t_i)$ is the *i*th element of the time series and the time delay (time lag) τ is an integer multiple of Δt. In order to investigate the dynamics of our system in a space defined by delayed vectors of dimension

[8] The sunspot-number data analysis has been integrated by using the software package *Auguri* (Available at: http://aag-auguri.com/index.html).

[m], we first have to estimate the embedding parameters; *i.e.* the suitable time delay [τ] and the embedding dimension [m].

1.4.1 Embedding parameters: Time delay and embedding dimension

In order to estimate the suitable *time delay*, we use the Average Mutual Information (AMI) introduced by Fraser and Swinney (1986) as a method to determine a reasonable time delay for nonlinear systems. The AMI is a generalization from the correlation function, which measures the linear correlations, to the case of nonlinear correlations between measurements. Fraser and Swinney (1986) suggested a method to estimate the value of τ by estimating the first minimum of the mutual information between the embedded vectors. A measure of a mutual information between the elements of the time series $x(t_i)$, $i=1,2,...,N$ is:

$$I(T)=\sum_{x(t_i),x(t_i+T)} P\left(x(t_i),x(t_i+T)\right)\times\log_2\left[\frac{P\left(x(t_i),x(t_i+T)\right)}{P\left(x(t_i)\right)P\left(x(t_i+T)\right)}\right]$$

$T=k\Delta t$ $(k=1,2,...,k_{\max})$, $P\left(x(t_i)\right)$ is the probability density at $x(t_i)$, $P\left(x(t_i),x(t_i+T)\right)$ is the joint probability density at the pair $x(t_i),x(t_i+T)$. Hence, the delay (T_m) of the first minimum of the AMI is chosen as a delay time τ for time-delay reconstruction of a phase space (Fraser and Swinney, 1986).

Further, in order to find the suitable *embedding dimension* [m], we use the False Nearest Neighbors (FNN) which has been first introduced by Kennel *et al.* (1992) as a convenient method to determine the minimal sufficient embedding dimension. This method uses the time-delay reconstruction of a phase space (Macek and Strumik, 2006); from the time series $x(t_i)$, $i=1,2,...,N$, a collection of m-dimensional vectors $\mathbf{X}(t_i)$ are constructed to trace out an orbit of a dynamical system for a given time delay τ (Equation (4)). Any element of the time series can be predicted as a function involving time-delayed elements of the same series $x(t_i+m\tau)=G\left[\mathbf{X}(t_i)\right]$. If the dimension m of time-delay coordinates is too small, then there are many nearest neighbors $\mathbf{X}(t_i),\mathbf{X}(t_j)$ that are close in the reconstructed space, but their images $x(t_i+m\tau),x(t_j+m\tau)$ are very distant. When this is the case, points close to each other may have very different time evolution, and actually belong to different parts of the underlying attractor (Aittokallio *et al.*, 1999).

In order to determine the sufficient number m of time-delay coordinates one next looks at the nearest neighbor of each vector with respect to the Euclidean metric. Comparing the "$(m\tau+1)$"st coordinates

of $\mathbf{X}(t_i)$ and $\mathbf{X}(t_j)$ – *e.g.* $x(t_i + m\tau)$ and $x(t_j + m\tau)$ – if the distance $\left|x(t_i + m\tau) - x(t_j + m\tau)\right|$ is large the points $\mathbf{X}(t_i)$ and $\mathbf{X}(t_j)$ are close just by projection. They are false nearest neighbors and they will be pulled apart by increasing the dimension *m*. If the distances $\left|x(t_i + m\tau) - x(t_j + m\tau)\right|$ are predominantly small, then only a small portion of the neighbors are false and *m* can be considered a sufficient embedding dimension. In the FNN algorithm (Kennel *et al.*, 1992) the neighbor is declared false if (Aittokallio *et al.*, 1999):

$$\frac{\left|x(t_i + m\tau) - x(t_j + m\tau)\right|}{\left\|\mathbf{X}(t_i) - \mathbf{X}(t_j)\right\|} > R_{tol} \tag{6}$$

or if

$$\frac{\left\|\mathbf{X}(t_i) - \mathbf{X}(t_j)\right\|^2 + \left[x(t_i + m\tau) - x(t_j + m\tau)\right]^2}{R_A^2} > A_{tol}^2 \tag{7}$$

$R_A^2 = \frac{1}{N}\sum_{i=1}^{N}\left[x(t_i) - \bar{x}\right]^2$ and $\bar{x}$ is the mean of all points. The parameter R_{tol} in the first threshold test (Equation (5)) is fixed beforehand and in most studies it has been set to 10 – 20. The second criterion (Equation (7)) was proposed in order to provide correct diagnostics for noise and usually one takes $A_{tol}^2 \approx 2$. If this test fails, then even the ($m\tau$ + 1-dimensional) nearest neighbors themselves are far apart in the extended $m\tau$ + 1 dimensional space and should be considered false neighbors. Using the above tests (Equations (6), (7)) one can check all *m*-dimensional vectors in the data set, and compute the percentage of false nearest neighbors. By increasing the dimension *m* this percentage should drop to zero or to some acceptable small number. In that case the embedding dimension is large enough to represent the dynamics.

1.4.2 Correlation dimension

For an orbit $x(t_1), x(t_2), x(t_3)..., x(t_N)$ of the map f on $\mathbb{R}^m$ the correlation dimension can be defined as follows (Alligood *et al.*, 1996): if the orbit converges to an attractor, the correlation dimension of that orbit is also regarded as the correlation dimension of the attractor. The correlation dimension measures the probability that two points randomly chosen will be within a certain distance of each other, and can be computed using the correlation integral (Al-Shameri, 2012). Packard *et al.* (1980) showed that the geometrical form of the attractor can be reconstructed from the set of vectors $\mathbf{X}(t_i)$,

provided that *m* is greater than *D*; if an attractor exists, the vectors $\mathbf{X}(t_i)$ will lie on a *D*-dimensional subset of the embedding space R^m. A lower limit on the dimension *D* of the attractor can be calculated by computing the correlation integral introduced by Grassberger and Procaccia (1983a) defined as

$$C^{(m)}(r)=\frac{1}{N^2}\sum_{\substack{i,j=1\\ j\neq i}}^{N}\theta\left(r-\left|\mathbf{X}(t_i)-\mathbf{X}(t_j)\right|\right),\quad \text{where } \theta\left(r-\left|\mathbf{X}(t_i)-\mathbf{X}(t_j)\right|\right)=\begin{cases}1, & \left(r-\left|\mathbf{X}(t_i)-\mathbf{X}(t_j)\right|\right)\geq 0\\ 0, & \left(r-\left|\mathbf{X}(t_i)-\mathbf{X}(t_j)\right|\right)<0\end{cases}$$

$\theta\left(r-\left|\mathbf{X}(t_i)-\mathbf{X}(t_j)\right|\right)$ is the Heavyside function, *N* is the number of observations, *r* is the distance in phase space, and $C^{(m)}$ is the correlation integral for dimension *m*; the correlation integral is the probability that two points chosen at random are less than *r* units apart (Nesis *et al*., 2001). Grassberger and Procaccia (1983a) suggested that, for a system with behavior governed by a *D*-dimensional attractor, when *r* is less than the overall size of the attractor, then $C^{(m)}(r)\propto r^{\nu}$, where *v* is called the correlation dimension. They showed that $D_c\geq\nu$; moreover, for several model systems they found that $\nu\simeq D_c$ (D_c is the dimension of the attractor) so that *v* is expected to be a good estimate of the exact dimensionality D_c (Nesis *et al*., 2001):

$$C^{(m)}(r)\propto\lim_{r\to 0}r^{D_c(m)}\ \text{ or }\ D_c(m)\propto\lim_{r\to 0}\frac{\ln C^{(m)}(r)}{\ln r}$$

$\ln C^{(m)}(r)$ is the logarithm of the correlation integral for *m*-dimension; $\ln r$ is the logarithm of the distance in phase space. For a dimension *m* we can calculate $C^{(m)}(r)$ for increasing values of *r*. By finding the slope of a graph of the $\ln C^{(m)}(r)$ with increasing values of $\ln r$, through a linear regression, we can estimate the correlation dimension $D_c(m)$ for every embedding dimension *m*. By increasing *m*, $D_c(m)$ will eventually converge to its true value (Nesis *et al*., 2001).

1.5 Recurrence Plots and Recurrence Quantification Analysis

In Section 4.1 we use the Recurrence Plot and Recurrence Quantification Analysis to exploit and quantify the recurrent patterns that exist within the time series of a solar magnetic activity index (actual monthly sunspot-number data). The Recurrence Plots (RP) and the Recurrence Quantification Analysis (RQA) are numerical analysis methodologies that can be used in order to exploit and quantify the dynamic properties of a time series (Fabretti and Ausloos, 2005). Recurrence is a characteristic of

many dynamical systems introduced by Poincaré (1890). According to the Recurrence Theorem, the motion of a point is stable if it returns infinitely often to positions arbitrarily close to its initial position (Poincaré, 1890). The Recurrence Plots (RPs) are 2D graphs which are based on the phase space reconstruction introduced by Eckmann *et al*. (1987) in order to visualize the recurrences of trajectories of dynamical systems. The RQA is a statistical quantification of RP introduced later by Zbilut and Webber (1992) and Webber and Zbilut (1994) in order to quantify the diagonal (and vertical) line structures in RPs.

The RP is a qualitative analysis tool that detects[9] whether a time series $x(t)$ exhibits chaotic behavior by searching for evidence of the unstable periodic orbits embedded in a chaotic system (Gilmore, 1993). The points of the phase space of a dynamical system represent possible states of the system. Assuming that the state of the system at a fixed time t can be specified by d components, they can be considered to form a vector (Marwan *et al.*, 2007): $\vec{x}(t) = \left(x_1(t), x_2(t), ..., x_d(t)\right)^T$ in the d-dimensional phase space of the system. The time evolution is given by $\dot{\vec{x}}(t) = d\,\vec{x}(t)/dt = \vec{F}\left(\vec{x}(t)\right)$, $F : \mathbb{R}^d \to \mathbb{R}^d$ where the vectors $\vec{x}(t)$ define a trajectory in phase space. However not all relevant components to construct the state vector are known or can be measured and we are confronted with a time-discrete measurement of only one observable. This yields a scalar and discrete time series $u_i = u(i\Delta t)$, where $i = 1, \ldots, N$ and Δt is the sampling rate of the measurement. In this case the phase space needs to be reconstructed (Takens, 1981). In order to reconstruct the phase space the time delay method is used (Marwan *et al.*, 2007):

$$\hat{\vec{x}} = \sum_{j=1}^{m} u_{i+(j-1)\tau}\vec{e}_j$$

m is the embedding dimension and τ is the time delay. The vectors $\vec{e}_i$ are unit vectors and span an orthogonal coordinate system $(\vec{e}_i \cdot \vec{e}_j = \delta_{i,j})$. In order to analyze the time series the embedding dimension m and the time delay τ needs to be chosen appropriately. The RP measures recurrences of the trajectory $\vec{x}_i \in \mathbb{R}^d$ in phase space and can be formally expressed by the matrix (Marwan *et al.*, 2007):

$$\mathbf{R}_{i,j}(\varepsilon) = \theta\left(\varepsilon - \left\|\vec{x}_i - \vec{x}_j\right\|\right), \qquad i, j = 1, ..., N \tag{8}$$

[9] The RP reconstructs completely the stretching and compressing mechanisms which are responsible for generating the strange attractor and therefore can detect if a time series exhibit chaotic behavior (Gilmore, 1993).

N is the number of measured points $\vec{x}_i$, ε is a threshold distance, $\theta(\cdot)$ the Heaviside function (*i.e.* $\theta(x)=0$, if $x < 0$, and $\theta(x)=1$ otherwise) and $\|\cdot\|$ is a norm. For ε-recurrent states (in an ε-neighborhood) the following notion is introduced: $\vec{x}_i \approx \vec{x}_j \Leftrightarrow \mathbf{R}_{i,j} \equiv 1$. The RP is obtained by plotting the recurrence matrix (Equation (8)) using different colors for its binary entries (*e.g.* a black dot at the coordinates (*i*, *j*) if $\mathbf{R}_{i,j} \equiv 1$ and a white dot if $\mathbf{R}_{i,j} \equiv 0$). Both axes of the RP are time axes and show rightwards and upwards. Since $\mathbf{R}_{i,j} \equiv 1|_{i=1}^{N}$ by definition, the RP has always a black main diagonal line, known as the *Line of Identity* (LOI). Moreover, the RP is symmetric by definition with respect to the main diagonal, *i.e.* $\mathbf{R}_{i,j} \equiv \mathbf{R}_{j,i}$.

One of the strengths of the RPs is that they can capture dynamics in shorter time series than what is required to calculate Lyapunov exponents (Zou *et al.*, 2007b). Typical patterns in RPs are linked to specific systems' behaviors (Marwan *et al.*, 2007). Various RP structures can be interpreted as follows (Belaire-Franch *et al.*, 2002): (i) *short line segments* parallel to the main diagonal indicate that the time series is deterministic and the system's attractor will be revisited by the trajectory sometime in the future (*e.g.* recurrent points forming distinct diagonals parallel to the main diagonal among scattered recurrent points), (ii) *absence of structure* corresponds to time series with purely random dynamics (*e.g.* uniformly scattered recurrent points). Finally, *straight horizontal* or *vertical lines* indicate a motion constant in time; *i.e.* a state that is not changing or changes very slowly (Marwan and Kurths, 2005). In case of *periodic* dynamics the RP consists of very long diagonal lines (Kyrtsou *et al.*, 2009). Moreover, in case of *quasi-periodic* dynamics the RP will show continuous diagonal lines besides regular dashed lines, while the RP of *chaotic* dynamics consists of many random lines of short length (Zou *et al.*, 2007a). *Abrupt changes* in the dynamics of the system cause white areas or bands in the RP (Marwan *et al.*, 2007). The RP from purely *stochastic* systems consist of a uniform array of points with no apparent structure (Aparicio *et al.*, 2008); *i.e.* no diagonal lines at all.

However, because the RPs can be difficult to interpret, several measures based on the RP structure can be used; that is, the RQA. The RQA is based on the quantification of the structures found in the RPs (*i.e.* the number and distributions of the recurrence point density and the diagonal and vertical line structures) by computing several variables (Marwan *et al.*, 2007). In this thesis we use five of the most important RQA measures based on the recurrence density and diagonal lines: *Recurrence Rate, Determinism, Maxline, Entropy, and Trend*.

- The *Recurrence Rate* (RR) is defined as the ratio of the number of recurrent points to the total number of recurrent points of a RP; it measures the recurrence density (Marwan *et al.*, 2007). The

RR exclude the upward central diagonal which represents the distance between each embedded vector and itself (Belaire-Franch *et al.*, 2002).

$$RR(\varepsilon) = \frac{1}{N^2}\sum_{i,j=1}^{N} R_{i,j}(\varepsilon) \quad \text{where } R_{i,j} = \begin{cases} 1, & (i,j): recurrent \\ 0, & otherwise \end{cases}$$

Embedded processes which are periodic have higher RR than processes which exhibit aperiodic dynamics.

- *Determinism* (DET) is defined as the ratio of the number of recurrent points, which form the parallel diagonal lines of at least length $l_{\min}$ with respect to the main diagonal, to the total number of the recurrent points. The DET allows to distinguish between dispersed recurrent points and those that are organized in diagonal patterns (Belaire-Franch *et al.*, 2002).

$$DET = \frac{\sum_{l=l_{\min}}^{N} lP(l)}{\sum_{l=1}^{N} lP(l)}$$

$P(l) = P(\varepsilon, l) = \sum_{i,j=1}^{N}\left(1-\mathbf{R}_{i-1,j-1}(\varepsilon)\right)\left(1-\mathbf{R}_{i+l,j+l}(\varepsilon)\right)\prod_{k=0}^{l-1}\mathbf{R}_{i+k,j+k}(\varepsilon)$ the histogram of diagonal lines of length l (Marwan *et al.*, 2007). The upward diagonal that DET quantifies are the signature of determinism since they represent strings of vectors repeating themselves in the future (Belaire-Franch *et al.*, 2002). For purely stochastic processes the DET is close to zero, while deterministic processes correspond to DET significantly greater than zero (Aparicio *et al.*, 2008).

- *Maxline* ($L_{\max}$) is defined as the length of the longest diagonal line parallel to the main diagonal found in the RP (excluding the main diagonal). These measure is related to the exponential divergence of the phase space trajectory. The faster the trajectory segments diverge, the shorter are the diagonal lines (Marwan *et al.*, 2007).

$$L_{\max} = \max\left(\{l_i\}_{i=1}^{N_l}\right)$$

$N_l = \sum_{l \geq l_{\min}} P(l)$ is the total number of diagonal lines. Moreover, according to Eckmann *et al*. (1987) the length of the diagonal lines is related to the largest positive Lyapunov exponent. Trulla *et al.* (1996) suggested an approach to estimate the largest Lyapunov exponent; *i.e.* the Maxline is proportional to the inverse of the largest Lyapunov exponent.

- The *Entropy* (ENTR) refers to the Shannon entropy of the probability $p(l) = P(l)/N_l$ to find a diagonal line of exactly length *l* in the RP (Marwan *et al.*, 2007).

$$ENTR = -\sum_{l=l_{\min}}^{N} p(l) \ln p(l)$$

ENTR reflects the complexity of the RP in respect of the diagonal lines (*e.g.* for uncorrelated noise the value of ENTR is rather small, indicating its low complexity) (Marwan *et al.*, 2007). A high ENTR value indicates that much information are required in order to identify the system (Fabretti and Ausloos, 2005).

- The *Trend* is a linear regression coefficient over the recurrence point density RR_τ[10] of the diagonals parallel to the main diagonal line as a function of the time distance between these diagonals and the main diagonal line (Marwan *et al.*, 2007).

$$TREND = \frac{\sum_{\tau=1}^{\tilde{N}} \left(\tau - \tilde{N}/2\right)\left(RR_\tau - \langle RR_\tau \rangle\right)}{\sum_{\tau=1}^{\tilde{N}} \left(\tau - \tilde{N}/2\right)^2}$$

TREND provides information about the non-stationarity of the time series (Marwan *et al.*, 2007). High values of TREND are associated with a non-stationary process having strong trend (Fabretti and Ausloos, 2005).

[10] It is the τ-recurrence rate for the diagonal lines with distance τ from the main diagonal line; it can be interpreted as the probability that a state recurs to its ε-neighborhood after τ time steps (Marwan *et al.*, 2007).

Chapter 2

Predator-Prey Interactions and Prey Refuge

Predation is one variety of biological interactions between species where a predator feeds on its prey (Begon *et al.*, 2006). According to the way predators feed on their prey, various categories of predators may be distinguished (Thompson, 1982): (i) parasites; they live throughout a major period of their life in a single host – their attack is harmful but rarely lethal (*e.g.* tapeworms, tuberculosis bacteria), (ii) grazers; they also consume only parts of their prey without causing immediate death – however, they attack large numbers of prey during their lifetime (*e.g.* sheep, biting flies), (iii) true predators; they also attack many prey during their lifetime – however, they quickly kill their prey (*e.g.* wolves, plankton-eating aquatic animals). In this chapter we study the population dynamics of predator-prey systems with true predators only.

The simplest population model in continuous-time was firstly introduced by Verhulst (1838) and describes the growth rate of the population of a single species. This model is known as the logistic differential equation. Lotka (1925) and Volterra (1926) later were the first who proposed the simplest predator-prey model with two species; they described the predator-prey interaction by introducing the known Lotka-Volterra predator-prey continuous-time model. A drawback of Lotka-Volterra model, which makes this model unrealistic, is that the predator never becomes saturated, while in the absence of predator the prey population grows exponentially. A somewhat realistic 2D predator-prey model should at least take into account the following features (Boccara, 2010): (i) intraspecific competition; *i.e.* competition between individuals belonging to the same species, (ii) predator's functional response; *i.e.* the relation between the predator's consumption rate and the prey density, (iii) predator's numerical response; *i.e.* the efficiency with which extra food is transformed into extra predation.

The functional response problem in the Lotka-Volterra model was solved by Holling (1959, 1965). He suggested three kinds of functional responses for different species of predator, which are called Holling type I, II and III. The function indicates the number of prey killed by one predator at various prey densities. According to Holling (1959, 1965) the functional response at low prey density depends upon the predator: (i) if the predator eats one type of prey the functional response should be linear, (ii) if the predator eats different types of prey the functional response should increase as a power greater than one of prey density. Thus, Rosenzweig and MacArthur (1963) later studied the Lotka-Volterra model with logistic growth rate of prey, while the saturation of the predator has been taken into account by a

Holling type II functional response. The Rosenzweig-MacArthur's model is one of the basic models since the predator-prey coexistence is not limited to a stable equilibrium; a limit cycle appears when the stable equilibrium undergoes the Hopf bifurcation.

The research of the predator-prey interactions for many years focused mainly on continuous predator-prey models, where the dynamics could produce only stable equilibrium or limit cycles. However, in recent years the research has turned to discrete-time predator-prey models, where it seems that their dynamics may include a much richer set of patterns. Maynard Smith (1968) firstly studied the Lotka-Volterra predator-prey model with logistic growth rate of prey in discrete time. Hadeler and Gerstmann (1990) studied the discrete-time version of the Rosenzweig-MacArthur model. Danca *et al.* (1997) later studied a simple discrete-time predator-prey model with Holling type I taking place and showed that such a simple discrete model can exhibit chaotic dynamics. Later, Liu and Xiao (2007) studied the Rosenzweig-MacArthur predator-prey model with Holling type I, proving once again that the discrete system exhibits far richer dynamics compared to the continuous model. He and Lai (2011) also reached to the same conclusion, investigating another Lotka-Volterra type predator-prey system with Holling type III functional response (Murray, 1993) in discrete time, showing that the discrete-time model exhibits more complicated dynamics. A discrete-time version of the Leslie-Gower predator-prey model have been studied by Huo and Li (2004).

However, since many prey populations incorporate some form of refuge available, a prey refuge provides a more realistic predator-prey model. Maynard Smith (1974) showed that a constant proportion refuge did not alter the dynamics of the neutrally stable Lotka-Volterra model, while a constant number refuge of any size replaced the neutrally stable behavior with a stable equilibrium. Also, Hassel (1978) showed that a large refuge to a model, which in the absence of a refuge exhibits divergent oscillations, replaces the oscillatory behavior with a stable equilibrium. Later, Kar (2005) studied a predator-prey model with Holling type II functional response incorporating a prey refuge, proving that when the positive equilibrium point is unstable, one stable limit cycle appears in the system. Huang *et al.* (2006) extended Chen and Zhang's (1986) model and studied the case of the predator-prey model with Holling type III functional response incorporating prey refuge. They also concluded that refuge had a stabilizing effect on predator-prey interactions. Finally, Zhuang and Wen (2011) studied a discrete-time version of Leslie's (1948, 1958) predator-prey system with a prey refuge. Thus, we observe that many studies have shown that refugia have a stabilizing effect on predator-prey interactions. However, as Taylor (1984) mentioned, it would be an oversimplification to assume this is always the case.

2.1 Prey Refuge in a Predator-Prey Model with Holling Type I Functional Response[11]

In this section we extend Danca's *et al.* (1997) Lotka-Volterra model with Holling type I functional response by incorporating prey refuge. The Holling type I functional response mainly refers to passive predators like spiders which wait for their prey to come close in order to capture them (Holling, 1959). Spiders are the main predators of insects. A single spider eats one hundred insects at least in a year and therefore it is estimated that in temperate countries the annual total weight of insects the spiders eat is larger than the weight of the human population (Pollock, 1993). So from this perspective, spiders in the role of predators, which prey on vectors, can be really useful to humans. However, by incorporating a prey refuge into Danca's *et al.* (1997) model, we assume that insects are able to protect themselves from spiders and escape from predation in some way. Does prey refuge stabilizes the predator-prey interactions as many studies have shown or leads eventually to population outbreaks? This is the main question we try to answer in this section.

2.1.1 Extending the basic model by incorporating prey refuge

Danca *et al.* (1997) studied the following discrete predator-prey model with Holling type I[12] functional response taking place:

$$\begin{cases} x_{n+1} = ax_n\left(1-x_n\right) - bx_n y_n \\ y_{n+1} = dx_n y_n \end{cases} \tag{9}$$

They showed that as the rate growth of prey increases, chaotic dynamics appear in the system and the predator-prey interactions become irregular. Particularly, they showed that for the parameter values $b = 0.2,\ d = 3.5$, as parameter *a* varies in the interval $0 < a < 4$, the dynamical system (Equation (9)) exhibits a strange attractor (Figure 2).

[11] This section is based on the publication "Incorporating prey refuge in a prey-predator model with Holling type I functional response: Random dynamics and population outbreaks" (Gkana, A., Zachilas, L.: 2013, Incorporating prey refuge in a prey-predator model with Holling type I functional response: Random dynamics and population outbreaks, *Journal of Biological Physics* **39**(4), 587-606.).

[12] The shape of the Holling type I functional response is linear. So if the predators are spiders and the preys are biting flies, the number of flies killed by one spider is proportional to the flies' density (Holling, 1959).

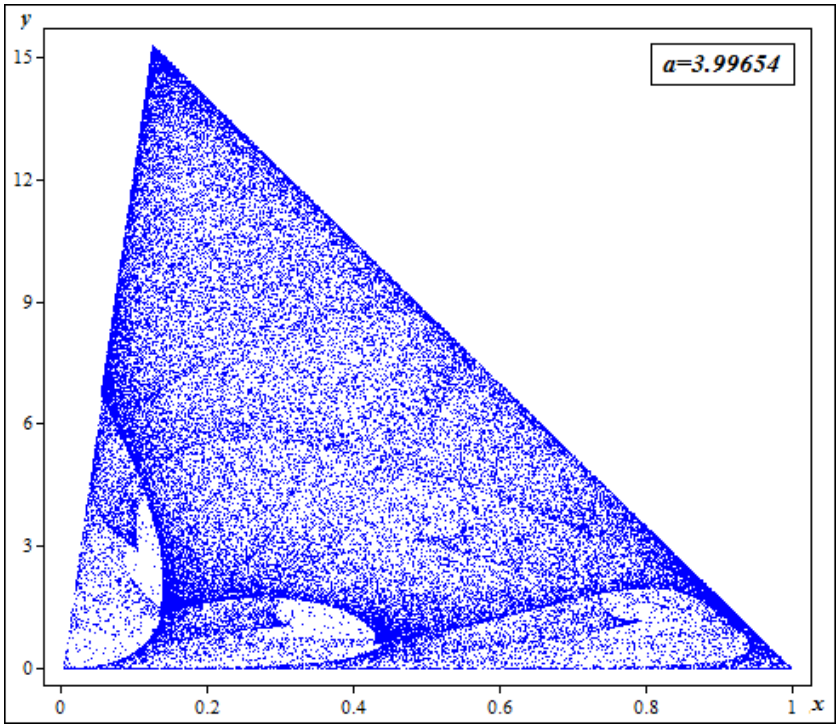

Figure 2 The strange attractor without prey refuge (m = 0) for a = 3.99654.

Extending Danca's *et al.* (1997) Lotka-Volterra model by incorporating prey refuge, we take the following predator-prey system:

$$\begin{cases} x_{n+1} = a x_n (1 - x_n) - b(1-m) x_n y_n \\ y_{n+1} = d(1-m) x_n y_n \end{cases} \tag{10}$$

x_n is the prey population after n generations with $0 < x_n < 1$ and y_n is the predator population after n generations; $a > 0$ is the rate growth of the prey in the absence of predators, in the presence of plenty food and all other requirements; $b > 0$ is the foraging efficiency of the predator – it measures the intensity of the predator's negative impact on the prey population's growth; $d > 0$ is the rate growth of the predator; mx is a refuge protecting the prey from the predator and $(1-m)x$ is the prey available to the predator, where $m \in [0,1)$. Thus, we extend the basic model (Equation (9)) by adding the new terms $(+bmx_n y_n)$ and $(-dmx_n y_n)$ associated with a refuge protecting the prey from the predator.

2.1.2 *Fold, flip* and *Neimark-Sacker* bifurcations

The dynamical system (Equation (10)) has the following three fixed points, the origin (E_1), a boundary fixed point (E_2) and a fixed point for which both populations survive (E_3):

$$E_1 : \left(x^*, y^*\right) = (0,0)$$
$$E_2 : \left(x^*, y^*\right) = \left(\frac{a-1}{a}, 0\right)$$
$$E_3 : \left(x^*, y^*\right) = \left(-\frac{1}{dm-d}, -\frac{(a-1)dm+(1-a)d+a}{bdm^2-2bdm+bd}\right)$$

The Jacobian matrix at any point (x, y) is:

$$J(x,y) = \begin{pmatrix} \frac{\partial x_{n+1}}{\partial x_n} & \frac{\partial x_{n+1}}{\partial y_n} \\ \frac{\partial y_{n+1}}{\partial x_n} & \frac{\partial y_{n+1}}{\partial y_n} \end{pmatrix} = \begin{pmatrix} (bm-b)y_n - 2ax_n + a & (bm-b)x_n \\ (d-dm)y_n & (d-dm)x_n \end{pmatrix}$$

The determinant of the Jacobian matrix is:

$$detJ(x,y) = (2adm-2ad)x_n^2 + (ad-adm)x_n$$

According to the stability criteria of fixed points for 2D maps (Subsection 1.1.2), in order to study the local behavior around each of the three fixed points we calculate the Jacobian matrix at E_1, E_2, E_3. Each fixed point is asymptotically stable (*i.e.* the eigenvalues λ_1, λ_2, either real or complex, have a modulus less than one) if the determinant and the trace of the Jacobian at E_1, E_2, E_3 satisfy the condition $|trJ| < 1 + detJ < 2$ (Equation (3)).

Local stability of the fixed point E_1

The Jacobian matrix at $E_1 : \left(x^*, y^*\right) = (0,0)$ is:

$$J(E_1) = \begin{pmatrix} a & 0 \\ 0 & 0 \end{pmatrix}$$

With eigenvalues $\lambda_1 = a, \lambda_2 = 0$, determinant $detJ(E_1) = 0$ and trace $trJ(E_1) = a$. For $a < 1$ both eigenvalues lie inside the unit circle $(\lambda_1, \lambda_2 < 1)$ and the origin is a *stable node*, For $a > 1$ one eigenvalue lies outside the unit circle and the other inside $(\lambda_1 > 1, \lambda_2 < 1)$ and the origin is a *saddle*. For $a = 1$ the fixed point is a *stable degenerate node* $(\lambda_1 = 1, \lambda_2 < 1)$; the fixed point is non-hyperbolic and this parameter value is associated with the stability condition $trJ = 1 + detJ$ (Equation (3)) and a

real eigenvalue crossing the unit circle at +1. So $a=1$ is a bifurcation point at which a *Fold bifurcation* occurs.

Local stability of the fixed point E_2

The Jacobian matrix at $E_2:\left(x^*,y^*\right)=\left(\frac{a-1}{a},0\right)$ is:

$$J\left(E_2\right)=\begin{pmatrix}2-a & \frac{\left(a-1\right)bm+\left(1-a\right)b}{a}\\ 0 & -\frac{\left(a-1\right)dm+\left(1-a\right)d}{a}\end{pmatrix}$$

The eigenvalues of the Jacobian matrix at E_2 are given by $\lambda_1=-\frac{\left(a-1\right)dm+\left(1-a\right)d}{a}$ and $\lambda_2=2-a$.

The determinant and the trace are: $detJ\left(E_2\right)=\frac{\left(a^2-3a+2\right)dm+\left(-a^2+3a-2\right)d}{a}$ and $trJ\left(E_2\right)=-\frac{\left(a-1\right)dm+\left(1-a\right)d+a^2-2a}{a}$.

Using the stability conditions (Equation (3)) we obtain the following:

1. If $m<\frac{\left(a-1\right)d-a}{\left(a-1\right)d}$ and $a<1$ then E_2 is an *unstable node*; both eigenvalues lie outside the unit circle $\left(|\lambda_1|,|\lambda_2|>1\right)$
2. If $m>\frac{\left(a-1\right)d-a}{\left(a-1\right)d}$ and $\begin{cases}\frac{dm-d}{dm-d-1}<a<1\\ \frac{dm-d}{dm-d+1}<a<3\end{cases}$ then E_2 is a *saddle*; one eigenvalue lies outside the unit circle and the other inside $\begin{matrix}\left(|\lambda_1|<1,|\lambda_2|>1\right)\\ \left(|\lambda_1|>1,|\lambda_2|<1\right)\end{matrix}$
3. If $\frac{dm-d}{dm-d-1}<a<\frac{dm-d}{dm-d+1}$ then E_2 is a *stable node*; both eigenvalues lie inside the unit circle $\left(|\lambda_1|,|\lambda_2|<1\right)$

4. If $a=\frac{dm-d}{dm-d+1}$ then E_2 is *non-hyperbolic* $(\lambda_1=1)$; this parameter value is associated with the stability condition $trJ=1+detJ$ (Equation (3)) and a real eigenvalue crossing the unit circle at +1. So this is another bifurcation point at which a *Fold bifurcation* occurs in the system.

Local stability of the fixed point E_3

The Jacobian matrix at $E_3:(x^*,y^*)=\left(-\frac{1}{dm-d},-\frac{(a-1)dm+(1-a)d+a}{bdm^2-2bdm+bd}\right)$ is:

$$J(E_3)=\begin{pmatrix}\frac{dm-d+a}{dm-d} & -\frac{b}{d}\\ \frac{(a-1)dm+(1-a)d+a}{bm-b} & 1\end{pmatrix}$$

With eigenvalues

$$\lambda_1=-\frac{\sqrt{(4-4a)d^2m^2+((8a-8)d^2-4ad)m+(4-4a)d^2+4ad+a^2}-2dm+2d-a}{2dm-2d}$$

$$\lambda_2=\frac{\sqrt{(4-4a)d^2m^2+((8a-8)d^2-4ad)m+(4-4a)d^2+4ad+a^2}+2dm-2d+a}{2dm-2d}$$

determinant $detJ(E_3)=\frac{adm-ad+2a}{dm-d}$ and trace $trJ(E_3)=\frac{2dm-2d+a}{dm-d}$.

And using the stability conditions (Equation (3)) we obtain the following:

1. If $a<\frac{dm-d}{dm-d+1}$ and $\frac{(a+3)d-3a}{(a+3)d}<m<\frac{(a-1)d-a}{(a-1)d}$ then E_3 is a *saddle*; one eigenvalue lies outside the unit circle and the other inside $(|\lambda_1|<1,|\lambda_2|>1)$

2. If $\frac{dm-d}{dm-d+1}<a<\frac{dm-d}{dm-d+2}$ and $\frac{(a-1)d-2a}{(a-1)d}<m<\frac{(a+3)d-3a}{(a+3)d}$ then E_3 is a *stable focus* (complex eigenvalues with real parts $|\alpha_1|=|\alpha_2|<1$ and $detJ(E_3)<1$) or a *stable node* (both eigenvalues lie inside the unit circle; *i.e.* $|\lambda_1|,|\lambda_2|<1$).

3. If $a>\frac{dm-d}{dm-d+2}$ and $m<\frac{(a-1)d-2a}{(a-1)d}$ then E_3 is an *unstable focus*; complex eigenvalues with real parts $|\alpha_1|=|\alpha_2|>1$ and $detJ(E_3)>1$.

4. If $m > \frac{(a-1)d - a}{(a-1)d}$ then E_3 is an *unstable node*; both eigenvalues lie outside the unit circle $(|\lambda_1|, |\lambda_2| > 1)$.

5. If $a = \frac{dm - d}{dm - d + 1}$ then E_3 is *non-hyperbolic* $(\lambda_2 = 1)$; this parameter value is associated with the stability condition $trJ = 1 + detJ$ (Equation (3)) and a real eigenvalue crossing the unit circle at +1. So this is a bifurcation point at which a *Fold bifurcation* occurs in the system.

6. If $m = \frac{(a-1)d - 2a}{(a-1)d}$ and $a = \frac{dm - d}{dm - d + 2}$ then E_3 is a *center* (*i.e.* complex eigenvalues with real parts $|\alpha_1| = |\alpha_2| = 1$ and $detJ(E_3) = 1$, $-2 < trJ(E_3) < +2$); this parameter value is associated with the stability condition $DetJ = 1$ (Equation (3)) and two complex eigenvalues crossing the unit circle simultaneously. So this is a bifurcation point at which a *Neimark-Sacker bifurcation* occurs in the system.

7. If $m = \frac{(a+3)d - 3a}{(a+3)d}$ then E_3 is *non-hyperbolic* $(\lambda_1 = -1)$; this parameter value is associated with the first stability condition $-trJ = 1 + detJ$ (Equation (3)) and one real eigenvalue crossing the unit circle at –1. Hence, this parameter value corresponds to a bifurcation point at which a *Flip bifurcation* occurs in the system.

2.1.3 Stabilization of chaotic dynamics, routes to chaos and random-like dynamics

We use various numerical simulation tools (Section 1.3) to study the complex dynamics of the dynamical system (Equation (10)). In order to see the effect of refuge on predator-prey interactions, we choose the initial conditions $x_0 = 0.83$ and $y_0 = 0.55$. We also assume $b < d$ since observational studies of spiders have shown that, while many species have very low capture rates of prey (parameter *b*) (Edgar, 1969; Nyffeler and Breene, 1990), they produce many offspring (parameter *d*) (*i.e.* female spiders lay up to 3,000 eggs in one or more silk egg sacks (Ruppert *et al.*, 2004)). This paradox "low foraging efficiency – high offspring production" is likely related with the fact that spiders have very low metabolic rates compared to other animals. On average, the resting metabolic rate of spiders is 70% of that of comparable ectothermic arthropods[13] (Anderson, 1970). This is ecologically an important factor that allows spiders to survive extended periods of time (which are sometimes in excess

[13] This low resting metabolic rate may be due to the fact that they use hydrostatic pressure for extending their appendages (Anderson and Prestwich, 1975).

of 200 or 300 days) without food[14] (Anderson, 1974). Furthermore, even when spiders elevate their metabolic rate during activities (such as searching for food[15], producing webs[16], producing eggs[17], courtship[18]), the increase in respiration and metabolic rate is relatively low to other animals; two to six times resting rates (Anderson and Prestwich, 1982). Hence, the general low metabolic rates make them very efficient in their use of energy, so that despite their low foraging efficiency, they have high reproduction rates. Thus, the parameters $b = 0.2$ and $d = 3.5$ (Danca *et al.*, 1997) are fixed[19] and we vary the parameters of the growth rate of prey *a* and refuge *m*.

Simultaneous variation of rate growth of prey and refuge parameters

We plot the parametric basins of attraction for the parameter values $a \in [0, 4.35]$ and $m \in [0,1]$ to see how the dynamics of the system change as refuge increases (Figure 3). Observing the 2D parameter space we point out the following:

- For small values of prey refuge $0 < m < 0.254$ as the rate growth of prey a increases, the stable fixed point (light blue area) is giving rise to *non-periodic* behavior (white area). So, adding a small refuge does not seem to alter significantly the dynamics of the basic model (Equation (9)).
- For slightly higher values of refuge $0.254 < m < 0.467$, we see that as a increases, the aperiodic dynamics is being replaced by a *stable* equilibrium. So, by adding more prey refuge, the refuge stabilizes the predator-prey interactions.
- However, for even higher values of prey refuge $0.467 < m < 1$, the stabilizing effect of refuge is not the case anymore. Now, as a takes higher values, the stable fixed point, through successive *period-doubling bifurcations*, 2-period cycle (dark blue area), 4-period cycle (pink area), 8-period cycle (dark green area), is giving rise to *non-periodic* behavior (white area). So, adding a large refuge makes the system unstable once again.

[14] In addition, spiders can further reduce their metabolic rate below their already low levels, when they experience periods of food limitation (Anderson, 1974).
[15] Many spiders, including both web building and wandering spiders are sit-and-wait predators that spend very little time in active locomotion (Prestwich, 1977). For example, the wolf spider *Pardosa amentata*, the daily energy loss attributed to locomotion was estimated to be only 1% of the daily energy usage of spiders (Ford, 1977).
[16] The energetic costs of web production are relatively small because web building is often a short process and some spiders are able to recycle web proteins, which can substantially reduce the metabolic cost of silk production (Ford, 1977).
[17] For example the wolf spider *Pardosa lugubris*, the females invest 26% in reproduction and males invest only 16% (Edgar, 1971).
[18] Male spiders invest 81% of their ingested energy in respiration, while females invest 73% (Edgar, 1971). This difference in respiration rate between the sexes is likely related to the high energetic needs of males for agonistic encounters with competing males and for courting females (Kotiaho *et al.*, 1998).
[19] We use the same parameter values that are also used in Danca's *et al.* (1997) paper, so that our results to be comparable with those of the basic model (Equation (9)).

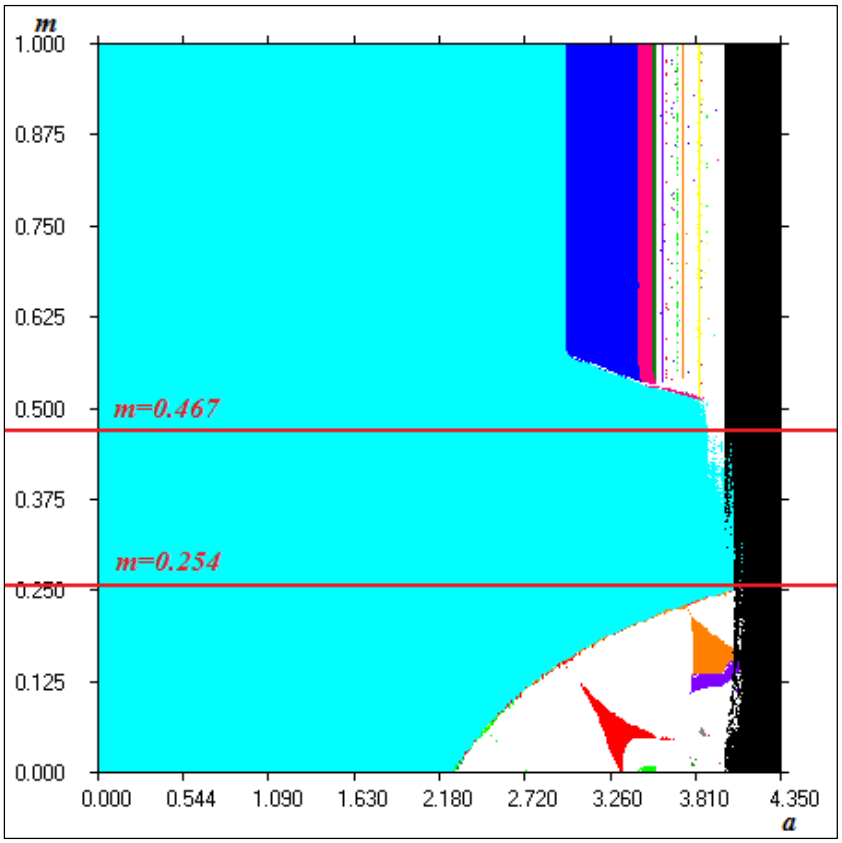

Figure 3 The parametric basins of attraction (*a, m*).

- Higher values of the refuge parameter $m>1$ do not correspond to positive equilibrium and therefore it has no realistic ecological significance.

Predator-prey interactions as the prey refuge increases for various rate growth of prey values

In order to see in detail what happens in both populations' species, as the refuge parameter increases, we use the bifurcation diagrams. We plot the bifurcation diagram, as the system's parameter increases in the interval $m\in[0,1]$ for various values of parameter *a* and we distinguish the following cases (Figure 4):

1. For low growth rate of prey $0<a<1.45$, as refuge increases in $m\in[0,1]$ the prey population survives in a small quantity, because of the low reproduction rate, while the predators cannot survive because of refuge. As we see in Figure 4(a), with such low birth rate of prey $a=1.1$ all preys are able to find refuge and the food is enough to feed them all, while predators cannot find food at all and become extinct immediately. So in this case the system has a *stable* boundary equilibrium point $(x^*,y^*)=(0.091,0)$ where both populations are fixed in time.

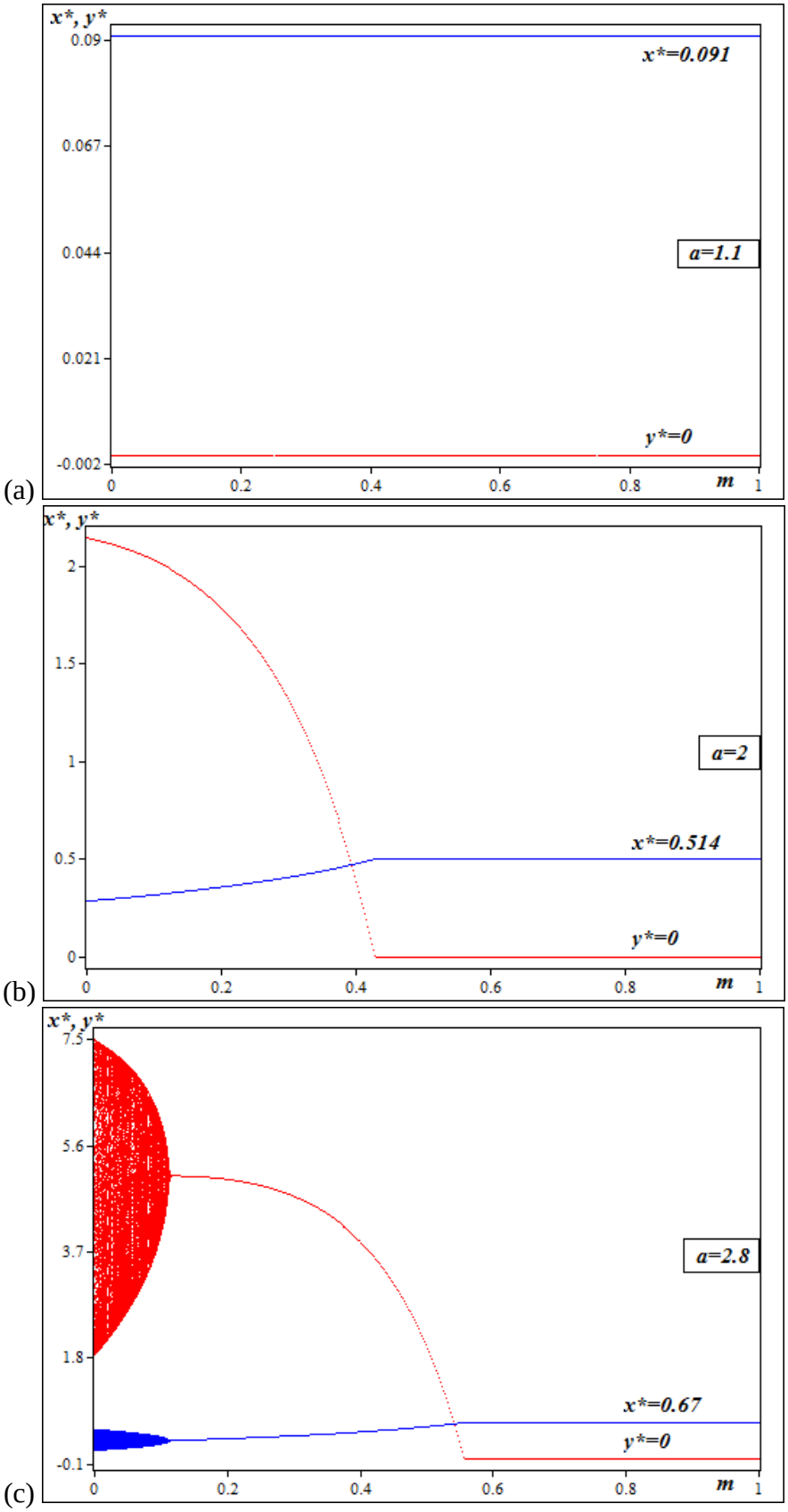

Figure 4 (*Continued.*)

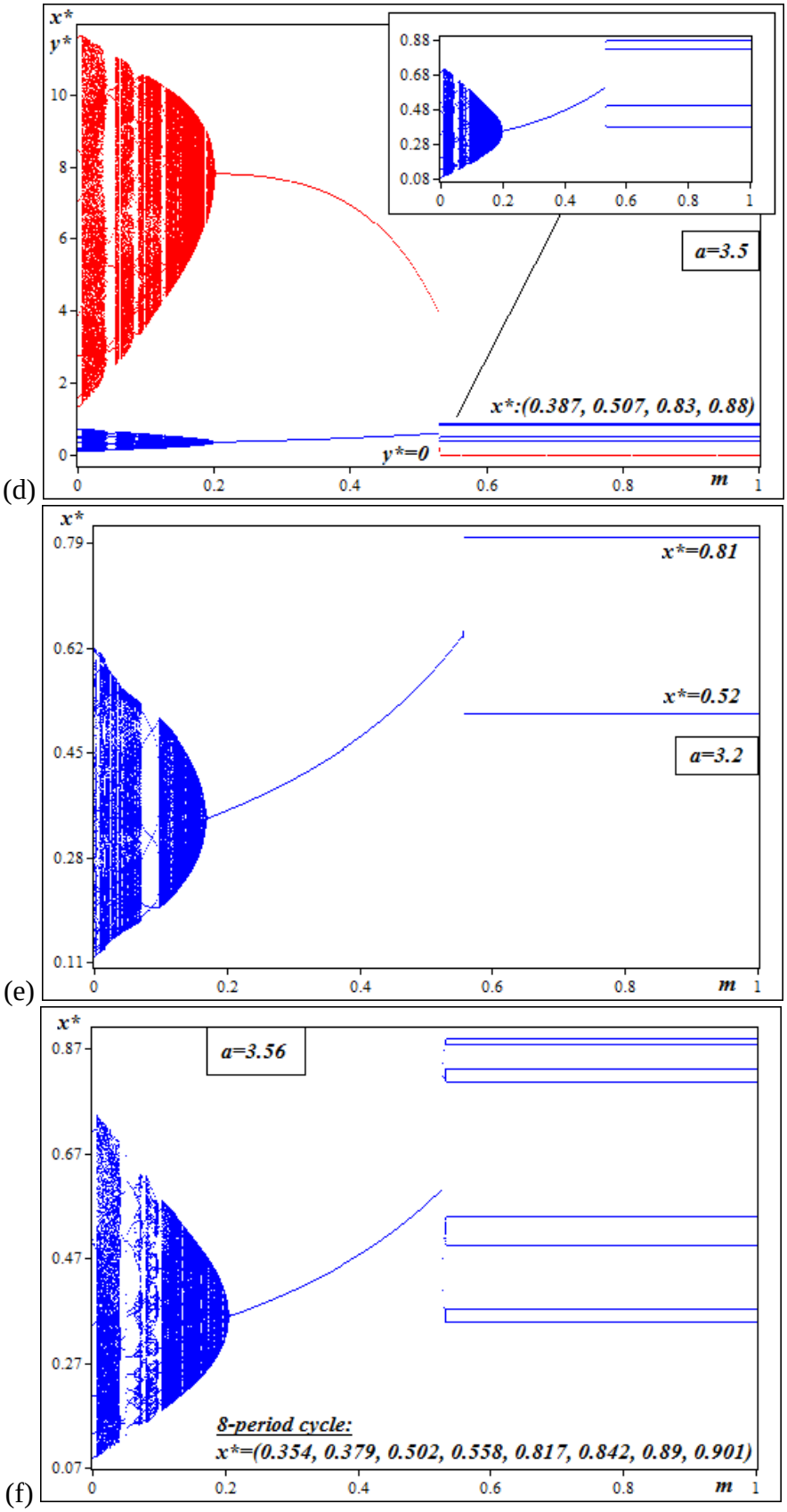

Figure 4 (*Continued.*)

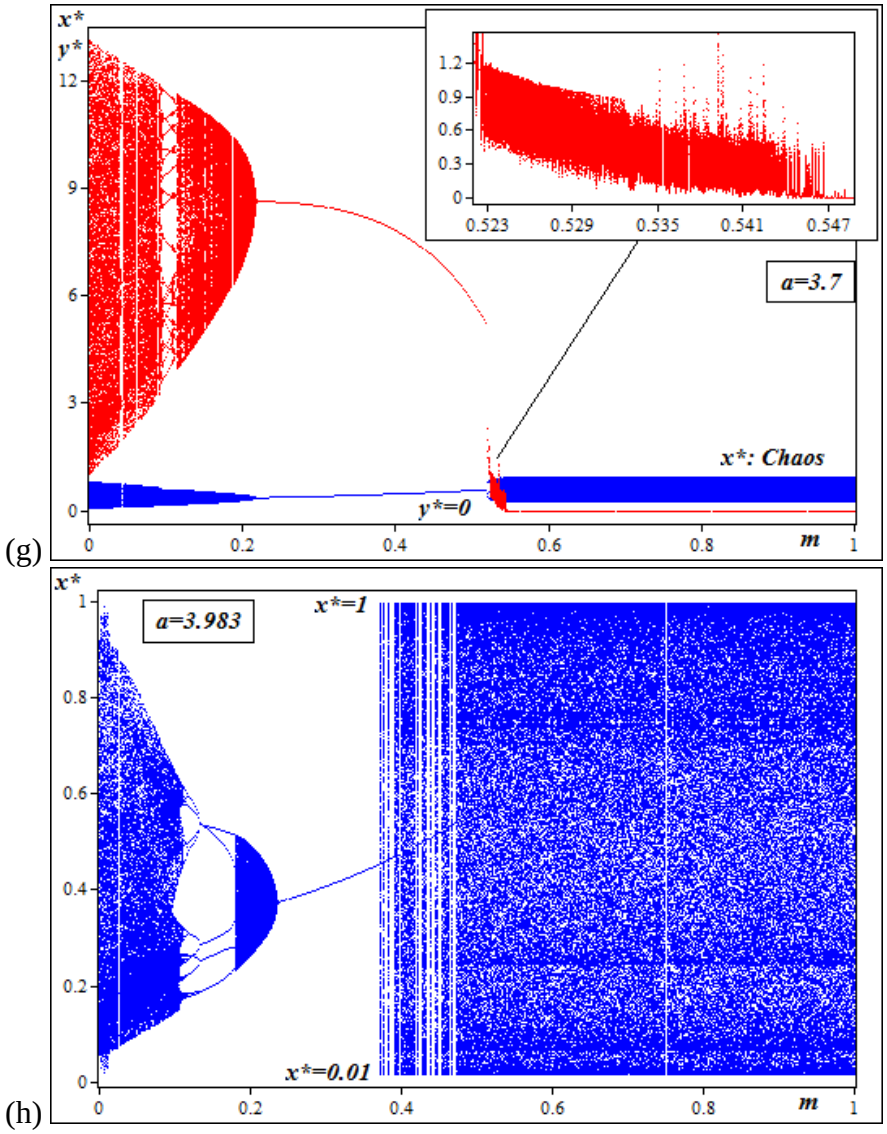

Figure 4 The bifurcation diagrams (m, x^*) and (m, y^*) as m varies in the interval [0, 1] for the parameter values: (a) a = 1.1, (b) a = 2, (c) a = 2.8, (d) a = 3.5, (e) a = 3.2, (f) a = 3.56, (g) a = 3.7 and (h) a = 3.983.

2. For average birth rate of prey $1.45 < a < 2.3$ and small prey refuge $m < 0.45$ both populations survive $\left(x^* > 0, y^* > 0\right)$ temporarily (Figure 4(b)). This happens because for such growth rate $a = 2$ the prey density is larger than the amount of refuge. Therefore, the predators are able to find preys to eat and since their population increases faster than the prey population $d = 3.5 > a = 2$ the predator population survives in a higher quantity than the prey population $\left(y^* > x^*\right)$ temporarily. As prey refuge increases, more and more preys find refuge and therefore the prey population increases, while the predator population decreases. When the amount of refuge is $m > 0.45$ all preys are able to find refuge and since the food is enough to feed them all, they survive in larger density $\left(x^* = 0.514\right)$ due to their higher birth rate. On the other hand, predators cannot find food

anymore and become extinct $\left(y^* = 0\right)$. Moreover, this qualitative change in the behavior of solutions, as the refuge parameter increases, is associated with a local bifurcation. For $a = 2$ (Figure 4(b)) in particular and $m < 0.4286$, the fixed point $E_3 : \left(x^* > 0, y^* > 0\right)$ is a stable node and the boundary fixed point $E_2 : \left(x^*, y^*\right) = \left(0.5, 0\right)$ is a saddle (the origin $E_1 : \left(x^*, y^*\right) = \left(0, 0\right)$ is always a saddle since $a = 2 > 1$). For $m = 0.4286$ both fixed points become non-hyperbolic; the eigenvalues of the Jacobian matrix at E_3 are $\left(\lambda_1 = -0.0001, \lambda_2 = 1\right)$ and the eigenvalues at E_2 are $\left(\lambda_1 = 1, \lambda_2 = 0\right)$. For $m > 0.4286$, E_3 becomes a saddle and E_2 becomes a stable node. Hence, as the varying parameter passes through the critical value $m = 0.4286$ both fixed points undergo a *Fold bifurcation*.

3. For high birth rate of prey $2.3 < a < 3$ and exceptionally small values of refuge $m < 0.11$, we observe *aperiodic* dynamics in both populations' species (Figure 4(c)). This happens because the high reproduction rate of prey $a = 2.8$, combined with the exceptionally small amount of refuge, have as a result that a large number of preys are not able to find refuge and to protect themselves from predators. The high birth rate of predators has as a result that both populations will appear irregular oscillations. However, for $m > 0.11$ refuge stabilizes the system to a positive fixed point $\left(x^*, y^* > 0\right)$, while the predator population is temporarily higher than the prey population $\left(y^* > x^*\right)$ again. For even higher values of prey refuge $m > 0.56$, all preys are able to find refuge and food, and because of their higher birth rate, they survive in an even larger density $\left(x^* = 0.67\right)$. The predators cannot find preys; they do not have food and become extinct $\left(y^* = 0\right)$ once again.
4. However, for higher growth rate of prey $3 < a < 3.57$, the increase of the amount of refuge does not always stabilize the system. As we see in Figure 4(d), for $m < 0.53$ refuge replaces the chaotic regimes with a stable positive equilibrium in both populations $\left(y^* > x^* > 0\right)$. However, once the prey refuge exceeds the threshold $m \approx 0.53$, the system loses stability and all orbits in prey population lie on an attracting four-period cycle $x^* : \left(0.387, 0.507, 0.83, 0.88\right)$. At the same time, the predator population decreases up to extinction $\left(y^* = 0\right)$, once again. Particularly, as parameter *a* increases in the interval $\left(3, 3.57\right)$ and for an amount of refuge $m > 0.5$, successive *period-doubling bifurcations* appear in prey population; 2-period cycle (Figure 4(e)), 4-period cycle (Figure 4(d)) and 8-period cycle (Figure 4(f)). This is because, once predators become extinct and since the birth rate of preys is significantly high, the available food is not enough to feed the large

prey density. Therefore, the prey population becomes slowly unstable, as their birth rate increases continuously.

5. Finally, for even higher birth rate of prey $a > 3.57$, as refuge takes higher values $m > 0.523$, the successive cycles of higher periods in prey's population lead to chaotic behavior; *period-doubling route to chaos* (Figure 4(g)). Thus, once predators become extinct, the exceptionally high reproduction rate of prey and the resource limitation compete with each other, leading sometimes the prey population to extinction $\left(x^* = 0.01\right)$ and sometimes to excessive growth $\left(x^* = 1\right)$ once again (Figure 4(h)). However, now, the chaotic dynamics in prey population looks like random. Particularly, observing both chaotic regimes in Figure 4(h), we see that for small prey refuge $m < 0.237$, the system alternates between chaotic behavior and periodic behavior, while for higher values of prey refuge $m < 0.372$, the system produces dynamics, which seems to have lost almost all its determinism. So, we observe that for such high reproduction rate $a = 3.983$, refuge not only destabilizes the system, but moreover makes the prey's population behavior almost random.
6. Moreover, observing the behavior of predator's population for $a = 3.7$, just before predators become extinct (Figure 4(g)), we see a small chaotic region. This chaotic regime could be also a result of the competition between the reproduction rate of prey and their resource limitation. Particularly, because of the resource limitation, many preys are not able to find food and die. But the piles of dead preys are food for the predators. While due to the high growth rate of prey, preys die in irregular frequencies. So maybe these two facts lead eventually to the appearance of chaotic behavior in predator's population too.

Predator-prey interactions for high rate growth of prey and small refuge

Another useful numerical simulation tool that can be used to investigate the predator-prey interactions is the phase diagram (x, y). The strange attractor (Figure 2) appears in the system for high rate growth of prey. In order to see how refuge replaces the chaotic strange attractor with a stable equilibrium point (*i.e.* stabilizes the predator-prey interactions), we plot the phase diagrams for the parameter value $a = 3.986$, as refuge varies in the interval $m \in [0, 0.24]$ (Figure 5).

- For $m = 0$ the origin $E_1 : \left(x^*, y^*\right) = (0,0)$ is a *saddle* (with eigenvalues $\left(\lambda_1 = 3.986, \lambda_2 = 0\right)$; it remains saddle for every value of the varying parameter m since $a = 3.986 > 1$), the boundary fixed point $E_2 : \left(x^*, y^*\right) = (0.7491, 0)$ is an *unstable node* (with eigenvalues $\left(\lambda_1 = 2.6219, \lambda_2 = -1.986\right)$ it remains unstable node as m increases), the fixed point

$E_3 : \left(x^*, y^*\right) = \left(0.2857, 9.2357\right)$ is an *unstable focus* (with eigenvalues $\lambda_{1,2} = 0.4306 \pm 1.2341i$, determinant $detJ\left(E_3\right) = 1.7083 > 1$ and trace $trJ\left(E_3\right) = 0.8611$) and all solutions converge to the strange attractor (Figure 5(a)).

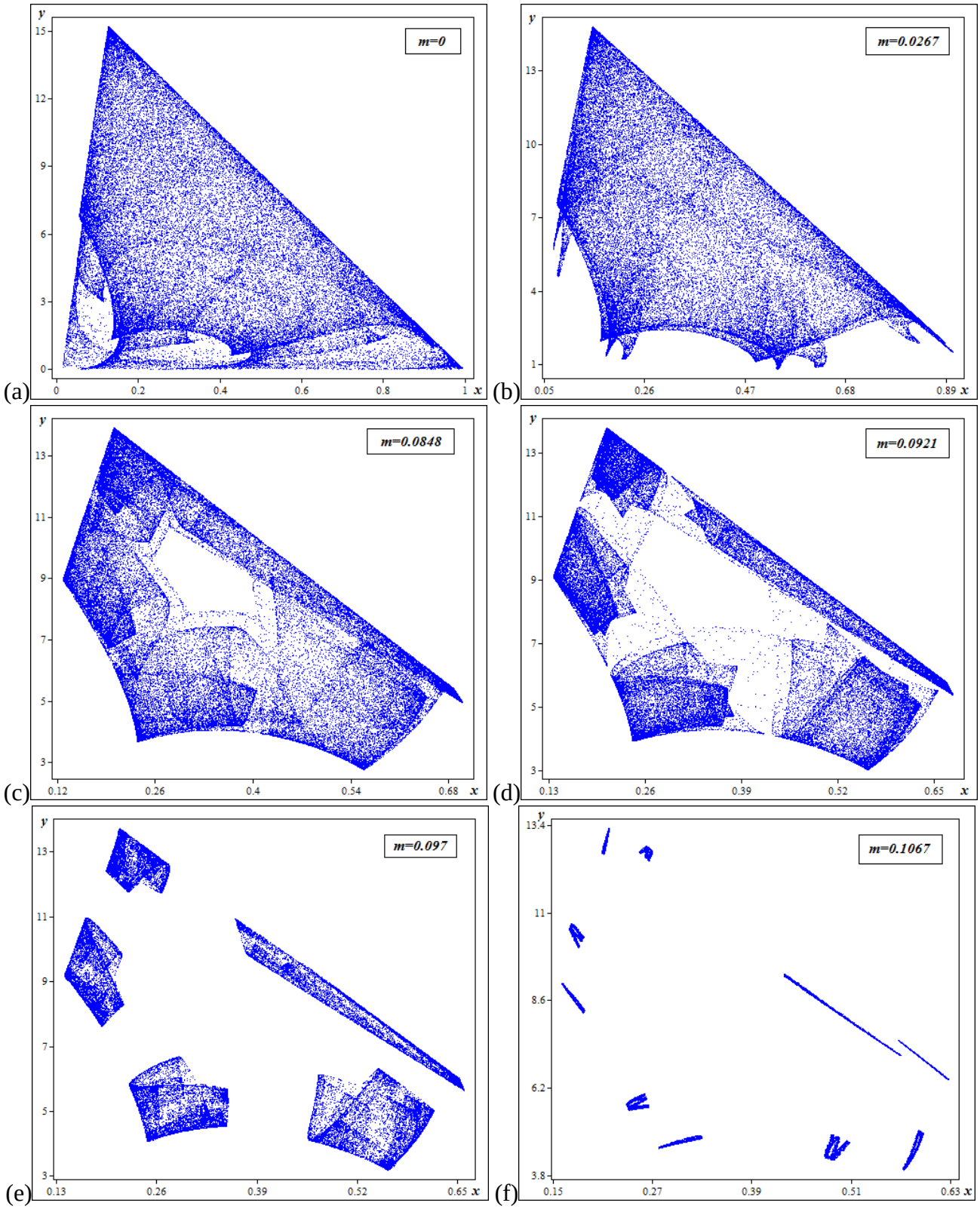

Figure 5 (*Continued.*)

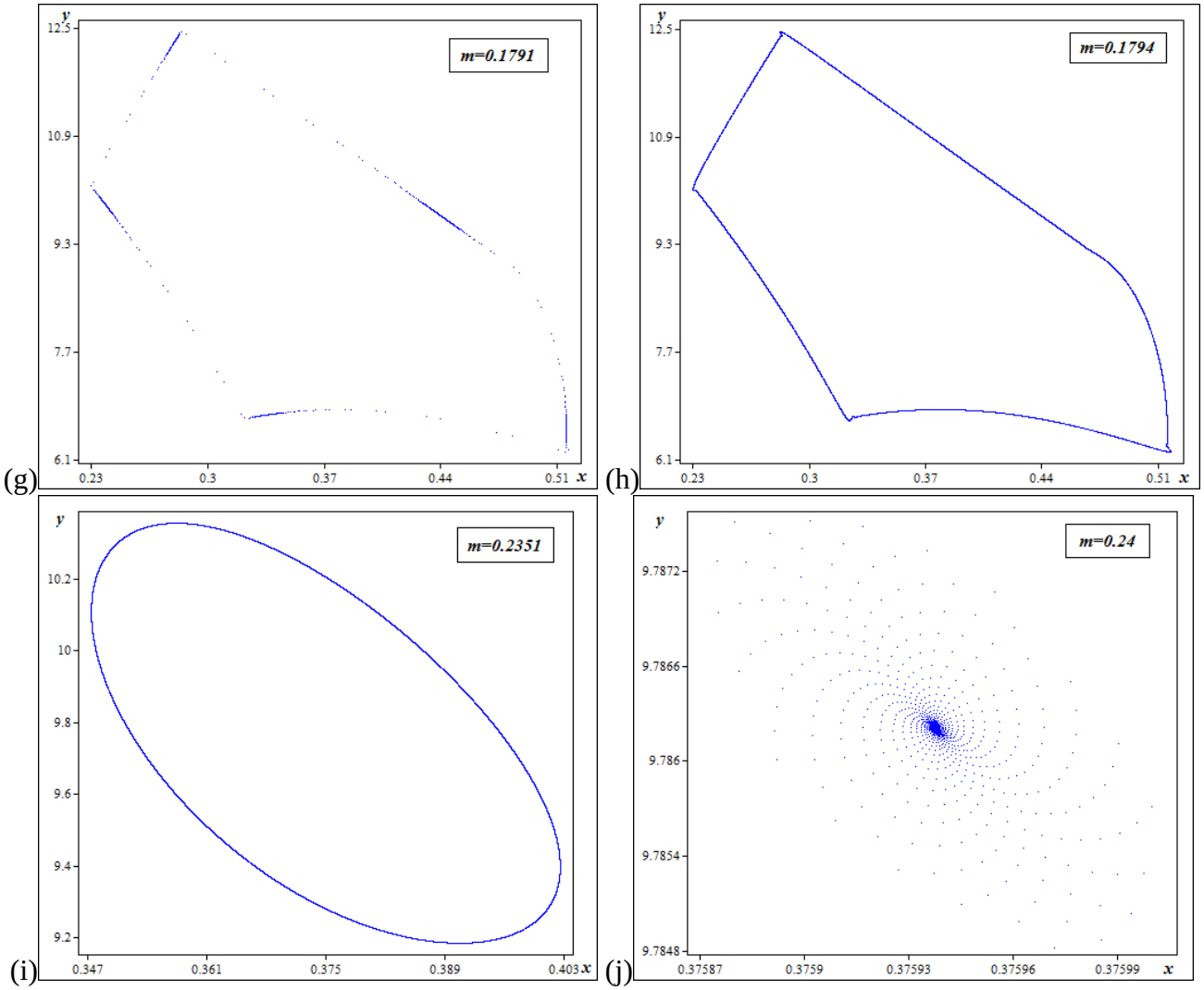

Figure 5 The phase plots (*x*, *y*) for growth rate of prey $a = 3.986$ and refuge parameter values: (a) $m = 0$, (b) $m = 0.0267$, (c) $m = 0.0848$, (d) $m = 0.0921$, (e) $m = 0.097$, (f) $m = 0.1067$, (g) $m = 0.1791$, (h) $m = 0.1794$, (i) $m = 0.2351$ and (j) $m = 0.24$.

- As the refuge parameter increases in the range $0 < m < 0.0286$, the *strange attractor* deforms and becomes less complicated. The strange attractor splits, locks into a stable 4-period cycle and near the value $m \approx 0.02868$, reappears more deformed (Figure 5(b)).
- For the refuge parameter values $0.029 < m < 0.092$, the strange attractor becomes less and less complicated. Particularly, near the value $m \approx 0.065$, the strange attractor evolves into a *strange contiguous band* (Figures 5(c), 5(d)).
- The contiguous strange band breaks apart into a *motion of period 5* near the value $m \approx 0.0926$ (Figure 5(e)) and then it splits again into a *motion of period 10* at $m \approx 0.1067$ (Figure 5(f)).

- For higher values of the parameter $0.11 < m < 0.1777$, a series of *period-halving bifurcations* takes place in both populations (20-period cycle at $m \approx 0.112$, 10-period cycle at $m \approx 0.1164$, and a 5-period cycle at $m \approx 0.133$). The system has an *ordered* behavior (Figure 5(g)).
- For even higher values of the refuge parameter $0.1777 < m < 0.235$, the locally stable orbit of period 5 gives rise to a *kinked curve* at $m \approx 0.179$ (Figure 5(h)). The kinked curve loses and gains stability consecutively, deforms and becomes an *invariant circle* near the value $m \approx 0.22$ (Figure 5(i)). At this point the prey coexists with the predator population and both oscillate among all the states of the invariant circle.
- Eventually, the invariant circle diminishes in size and near the value $m \approx 0.2372$ the fixed point $E_3 : \left(x^*, y^*\right) = \left(0.3746, 9.7863\right)$ undergoes a *subcritical Neimark-Sacker bifurcation* becoming a *center* ($detJ\left(E_3\right) = 1$ and $trJ\left(E_3\right) = 0.507 < +2$). For $0.2372 < m < 0.443$, E_3 becomes a *stable focus* fixed point (with complex eigenvalues and $detJ\left(E_3\right) < 1$), where both populations settle down (Figure 5(j)).

In Figure 6 we plot the phase diagram for growth rate of prey $a = 3.7$ as the refuge parameter increases in the interval $m \in [0.515, 0.55]$ – the small chaotic region (Figure 4(g)). We can observe the *fountain* phenomenon (Hadeler and Gerstmann, 1990) just before predators become extinct.

- For the parameter value $m = 0.515$ the origin $E_1 : \left(x^*, y^*\right) = \left(0, 0\right)$ is a *saddle* fixed point $\left(a = 3.7 > 1\right)$, the boundary fixed point $E_2 : \left(x^*, y^*\right) = \left(0.7297, 0\right)$ is an *unstable node* (with eigenvalues $\left(\lambda_1 = 1.2387, \lambda_2 = -1.7\right)$; it remains unstable node as m increases) and all solutions converge to the fixed point $E_3 : \left(x^*, y^*\right) = \left(0.5891, 5.3642\right)$, which is a *stable node* (with eigenvalues $\lambda_1 = -0.9068,\ \lambda_2 = 0.7271$).
- As the refuge parameter increases in the range $0.515 < m < 0.522$, the attracting fixed point $E_3 : \left(y^* > x^* > 0\right)$ near the value $m \approx 0.52$ undergoes a *Flip bifurcation* $\left(\lambda_1 = -1\right)$, becomes a saddle and a 2-period cycle appears surrounding it. The attracting cycle of period 2 loses stability via another period-doubling bifurcation giving rise to a stable orbit of period 4 at $m \approx 0.522$ (Figure 6(a)).
- Close to the value $m \approx 0.5224$, we observe a *period-doubling route to chaos* and the trajectory mimics the Feigenbaum bifurcation diagram (Figure 6(b)).

- Chaos appears in both populations and as refuge increases in the interval $0.5224 < m < 0.5364$, the trajectory is pushing upward (Figure 6(c)).

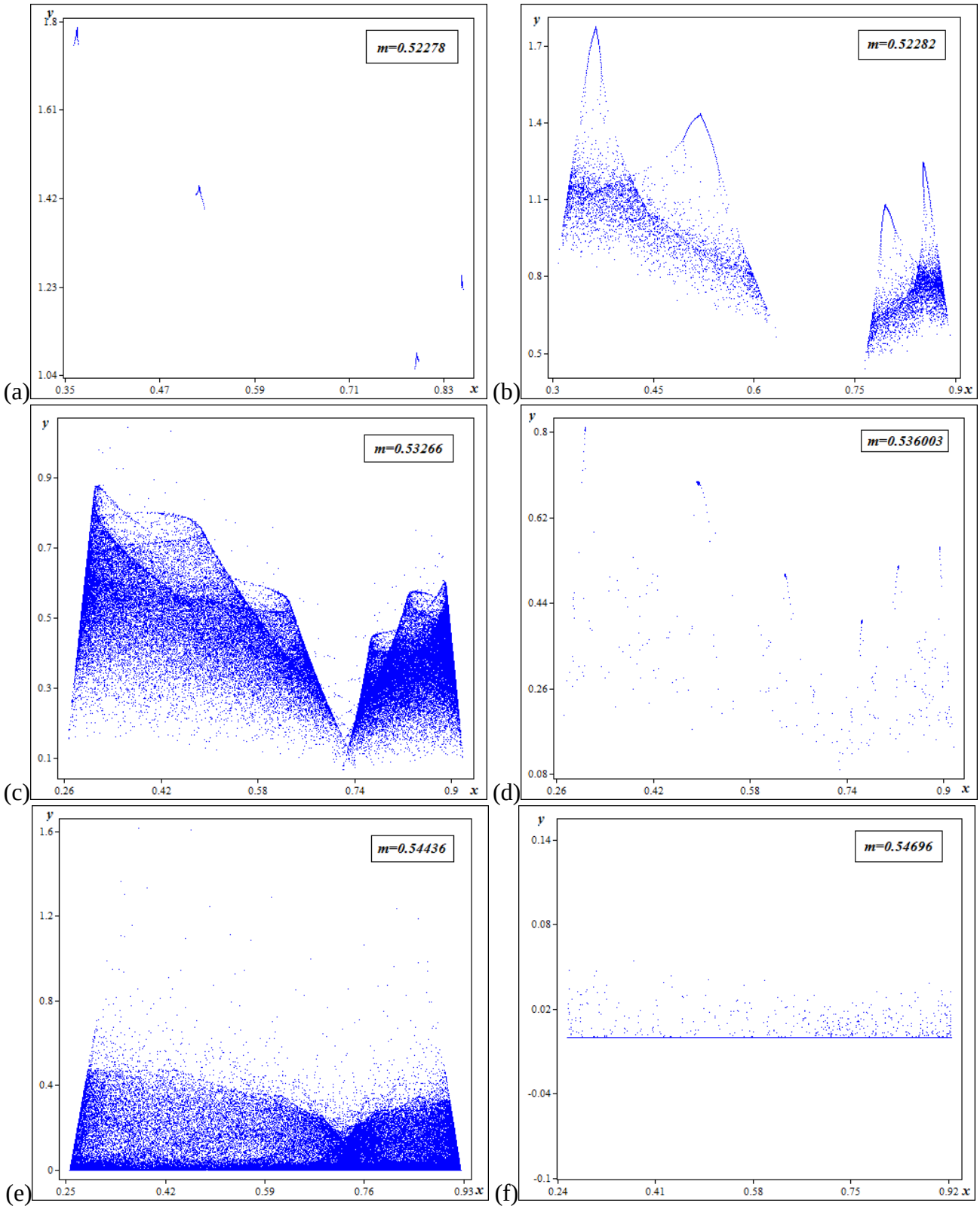

Figure 6 The phase plots (x, y) for growth rate of prey a = 3.7 and refuge parameter values: (a) m = 0.52278, (b) m = 0.52282, (c) m = 0.53266, (d) m = 0.536003, (e) m = 0.54436 and (f) m = 0.54696.

- Near the value $m \approx 0.53647$, the chaotic motion is being replaced by a 6-period cycle (Figure 6(d)).
- For higher values of the refuge parameter $0.5365 < m < 0.55$, chaos reappears in the system (Figure 6(e)) and the predator population decreases continuously until, finally, it becomes extinct (Figure 6(f)).

Small versus large prey refuge

We plot the Lyapunov exponent diagram (a, λ) as the growth rate of prey increases in the interval $a \in [2.2, 4.1]$ for three cases of the refuge parameter: (a) if there is no prey refuge $(m = 0)$ (Figure 7), (b) if we have small refuge $(m = 0.1)$ (Figure 8), and (c) if we have large refuge $(m = 0.783)$ (Figure 9). If there is no prey refuge $(m = 0)$, for low birth rate of prey $2.329 < a < 3.195$, the populations oscillate between quasi-periodic and periodic behavior and the Lyapunov exponents vary among negative and exceptionally small positive values $\lambda_i \leq 0.001$. For average to high birth rate of prey $3.195 < a < 3.578$, the system alternates between chaotic and high-periodical behavior and the Lyapunov exponents vary among negative and rather higher positive values $\lambda_i \leq 0.086$, in compare to the previous interval of birth rate of prey. For exceptionally high birth rate of prey $3.578 < a < 4$, chaotic dynamics appear in both populations and the Lyapunov exponent reaches its maximum value $\lambda_{\max} \approx 0.296364$, for growth rate of prey $a \approx 4.002179$.

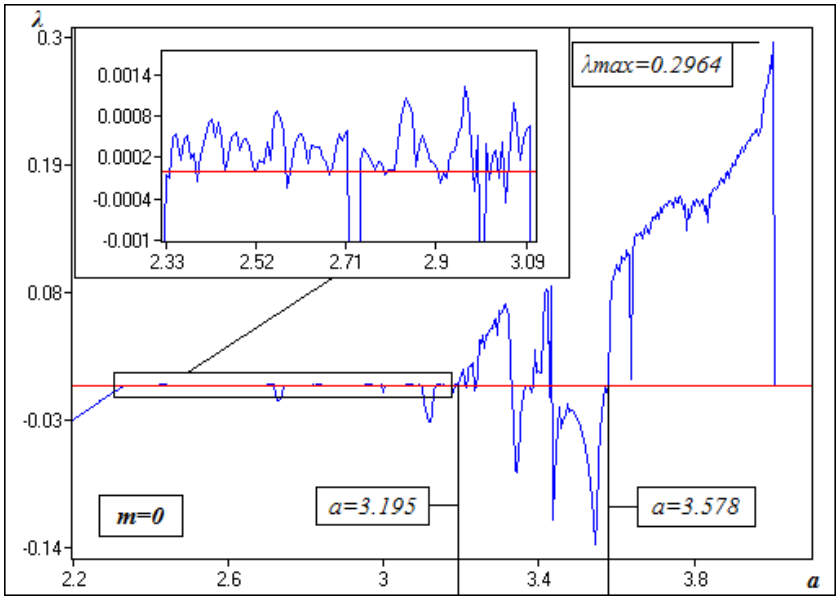

Figure 7 The Lyapunov exponent diagram (a, λ) without refuge $m = 0$.

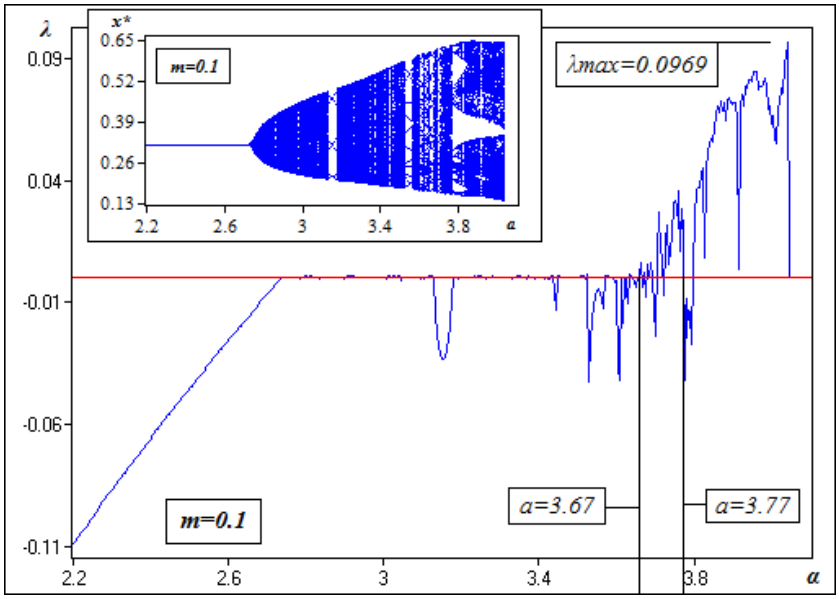

Figure 8 The Lyapunov exponent diagram (a, λ) along with the bifurcation diagram (a, x^*) with small refuge $m = 0.1$.

For small prey refuge $(m = 0.1)$, periodic and quasi-periodic dynamics along with exceptionally small Lyapunov exponent values $\lambda_i \leq 0.002$ appear for average to high birth rate of prey $2.738 < a < 3.67$. For high birth rate of prey $3.67 < a < 3.77$, the populations oscillate among chaotic and periodic behavior, while the Lyapunov exponents vary among negative and small positive values $\lambda_i \leq 0.037$. For higher birth rate of prey $3.77 < a < 4.047$, the period-doubling route to an order of chaotic bands and the largest value of the Lyapunov exponent, which corresponds to rate growth of prey $a \approx 4.043010$, is remarkably low $\lambda_{\max} \approx 0.096923$.

For large prey refuge $(m = 0.783)$, for which predators inevitably become extinct, the dynamical system (Equation (10)) becomes the well-known discrete-time logistic map. For average to high birth rate of prey $3 < a < 3.57$, the system goes through successive period-doubling bifurcations and the Lyapunov exponents take only negative values $\lambda_i < 0$. For high birth rate of prey $3.57 < a < 3.83$, the period-doubling route to chaos and the Lyapunov exponents vary among negative and significantly high positive values $\lambda_i \leq 0.4434$. For exceptionally high birth rate of prey $3.83 < a < 4.002$, another series of period-doubling $(3 \cdot 2^n)$ routes to chaos and the largest Lyapunov exponent reaches the remarkably high value $\lambda_{\max} \approx 0.673651$, for growth rate of prey $a \approx 3.998271$.

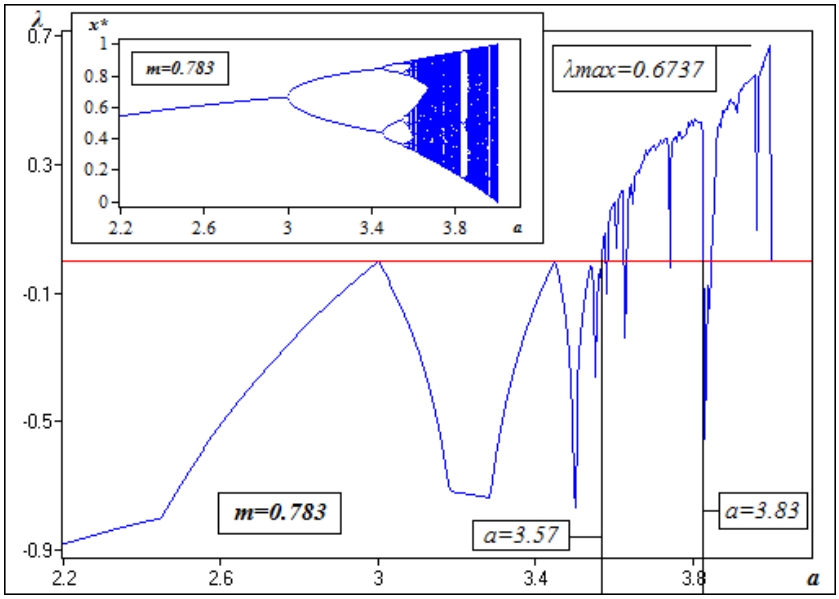

Figure 9 The Lyapunov exponent diagram (a, λ) along with the bifurcation diagram (a, x^*) with large refuge m = 0.783.

Comparing the Lyapunov exponent diagrams without prey refuge to those with small refuge and large refuge, we point out the following:

1. The minimal addition of a small refuge gives rise to periodic and quasi-periodic dynamics, even for high birth rate of prey $a \approx 3.67$, while chaotic dynamics appears only for exceptionally higher birth rates. Moreover, the maximum value of the Lyapunov exponent is considerably lower than the corresponding one without prey refuge $\lambda_{\max} \approx 0.0969 < 0.2964$ (Figures 7, 8). Thus, a small prey refuge stabilizes the system for high birth rates of prey, while for exceptionally even higher birth rates, the predator-prey interactions become much less chaotic. Consequently, the oscillations of prey's population are much smaller $x^* \in (0.14, 0.65)$ and preys do not tend anymore neither to extinction nor to overgrowth (Figure 8).
2. However, by adding a large refuge the system has a lot of similarities as if we would have only a single species with limited resources, while the situation changes drastically for high birth rate of prey $a > 3.57$. For such high birth rate, the dynamics of the system looks like random and therefore the prey population tends to extinction or to overgrowth $x^* \in (0,1)$ with almost random changes (Figure 4(h)). The maximum Lyapunov exponent is higher than in the corresponding case without refuge $\lambda_{\max} \approx 0.6737 > 0.2964$ (Figures 7, 9), the system is extremely chaotic and because of its dependence on initial conditions, it is almost impossible to predict the behavior of the prey's population.

2.1.4 Prey refuge and population outbreaks: Mosquito outbreaks and escape anti-predator strategy

We have shown that although the addition of a small prey refuge stabilizes the predator-prey interactions, however the addition of a large refuge makes the prey population to behave even more chaotic than without refuge. While a small refuge could control the prey population, a large refuge leads to almost unpredictability (*i.e.* random-like prey population outbreaks). Therefore, by taking into consideration that the prey population could be biting insects which feed with human blood and that they were able to protect themselves effectively from passive predators like spiders, we may conclude that a pandemic could be possible. In real world pest insects are one of those insects which show population outbreaks (plagues), indeed (Pollock, 1993). Moreover, a huge number of many infectious diseases are usually transmitted into the human's blood by insects (vectors) which feed on blood, such as mosquitoes (the best known disease vector) which spiders also eat (Last, 2001).

Moreover, regarding our prey-refuge assumption, experiments with mosquito larvae and pupae have shown that mosquitoes exhibit predator-avoidance behavior. Mosquito pupae respond to physical disturbances[20] (passing shadows, predators, hydrodynamic micro-disturbances) by diving down; it has been suggested that mosquito pupae use diving as an escape strategy to avoid predation (Rodriguez-Preito *et al.*, 2006). Rodríguez-Prieto *et al.* (2006) studied the anti-predator responses of *Culex pipiens* (vector of Japanese encephalitis, meningitis, and urticarial) to predation and found that pupae dive and remain below when a shadow repeatedly crosses the surface, suggesting that the diving behavior of *Culex pipiens* plays a role in escaping from aerial or terrestrial predators. Futami *et al*. (2008) also tested this mosquito-diving behavior using immature *Anopheles gambiae*[21] (the major malaria vector in Africa) and the wolf spider *Pardosa messingerae*[22]. Their results showed that mosquito larvae avoided the spider by diving more frequently and for longer periods; this diving behavior allows mosquitoes (*Anopheles gambiae*) to escape predation by terrestrial predators (wolf spiders) providing evidence to support further the predator-avoidance hypothesis. Hence, this predator-avoidance behavior could increase further the probability of having mosquito outbreaks leading to infectious disease outbreaks.

[20] Mosquito pupae detect threats in the environment through hydrodynamic disturbances and by visual stimuli (Rodriguez-Preito *et al*., 2006).
[21] *Anopheles gambiae* is a surface feeder and is thus much more vulnerable to terrestrial and aerial predators (Futami *et al*., 2008).
[22] *Pardosa messingerae* is often observed on the water surface at breeding sites of *Anopheles gambiae* in Western Kenya (Futami *et al*., 2008).

Of course this is just a simple mathematical predator-prey model and in real world there are other predators, which prey on insects like biting insects too. So, even if spiders would become extinct, other predators could control the biting insects' population (biological control) (Pollock, 1993). Moreover, humans have developed various chemical methods in order to control pest populations. However, history has shown that despite of any kind of vector control, significant pandemics have been recorded over the years. According to WHO (2014), one sixth of the illness and disability suffered worldwide is due to vector-borne diseases (malaria, dengue, yellow fever, etc…), with more than half the world's population currently estimated to be at risk. Hence, our modified proposed model seems to be more appropriate for describing the real world pest population outbreaks (such as mosquito outbreaks) than the original predator-prey model.

2.2 Non-overlapping Generation Species and Prey Refuge[23]

As mentioned above, discrete-time models often produce more complex predator-prey dynamics than those observed in continuous-time models and therefore they are considered as more realistic. Moreover, many species of insects have no overlap between successive generations and therefore population evolves in discrete time steps (Liu and Xiao, 2007). In this section we use Huang *et al.* (2006) dynamical system as our basic model and we try to describe the predator-prey interactions in a more realistic way, by taking into account the fact that species reproduce in certain intervals. We investigate whether prey refuge stabilizes the predator-prey interactions as it does in Huang *et al.* (2006) model. In Subsection 2.2.1 we present the dynamical system Huang *et al.* (2006) studied in continuous time, and we introduce our modified model assuming that population evolves in discrete time steps. In Subsection 2.2.2 we investigate the stability properties of the fixed points of our discrete-time dynamical system. In Subsection 2.2.3 we use various numerical simulation tools in order to study the complex dynamics of our system for average and large values of the refuge parameter. Finally, in Subsection 2.2.4 we end up with some concluding remarks, discussion and recommendations about the interpretation of the results of our study.

[23] This section is based on the publication "Non-overlapping Generation Species: Complex Prey-Predator Interactions" (Gkana, A., Zachilas, L.: 2015, Non-overlapping Generation Species: Complex Prey-Predator Interactions, *International Journal of Nonlinear Sciences and Numerical Simulation* **16**(5), 207-219.).

2.2.1 Modification of the basic model for species having no overlap between successive generations

Huang *et al.* (2006) studied the following continuous-time predator-prey model with Holling type III[24] functional response by incorporating prey refuge:

$$\begin{cases} \dfrac{dx}{dt} = ax - bx^2 - \dfrac{\alpha(1-m)^2 x^2 y}{\beta^2 + (1-m)^2 x^2} \\ \dfrac{dy}{dt} = -cy + \dfrac{k\alpha(1-m)^2 x^2 y}{\beta^2 + (1-m)^2 x^2} \end{cases} \tag{11}$$

x is the prey population and y is the predator population at any time t; $c > 0$ is the death rate of predator; $b > 0$ is the intrinsic growth rate of prey; $k > 0$ is the conversion factor denoting the number of newly born predators for each captured prey. The term $\alpha x^2 / \left(\beta^2 + x^2\right)$ denotes the Holling type III functional response according to which the predator consumes the prey, with $\alpha, \beta > 0$. The term mx is the refuge protecting the prey from the predator; this leaves $(1 - m)\,x$ of the prey available to the predator, where $m \in [0,1)$. It was showed that as the refuge parameter m increases (for large refuge), the limit cycle is being replaced with a stable equilibrium, where both populations settle down (Huang *et al.*, 2006).

Assuming that species reproduce in certain intervals, we use the Euler's algorithm to discretize the Huang *et al.* (2006) model. As described above (Subsection 1.1.1), we discretize the differential equations of the basic dynamical system (Equation (11)) by replacing dx/dt, dy/dt with the difference quotients $(\tilde{x} - x)/\delta, (\tilde{y} - y)/\delta$. Thus, we obtain the discrete-time predator-prey dynamical system as follows:

$$\begin{cases} \tilde{x} = x + \delta\left[ax - bx^2 - \dfrac{\alpha(1-m)^2 x^2 y}{\beta^2 + (1-m)^2 x^2} \right] \\ \tilde{y} = y + \delta\left[-cy + \dfrac{k\alpha(1-m)^2 x^2 y}{\beta^2 + (1-m)^2 x^2} \right] \end{cases} \tag{12}$$

$\delta > 0$ is the length of each time step size where the density of both populations grows by the addition of the newly born preys and predators – the fixed interval between generations; x, y are the prey and

[24] The shape of the Holling type III functional response is S-shaped and corresponds to predators that increase their search activity with increasing prey density. Moreover, as the prey density increases, the prey mortality first increases and then decreases (Holling, 1959).

predator population in one generation and $\tilde{x}, \tilde{y}$ are the prey and predator population at the next time step.

The number of individuals at the next generation depends only on the number of individuals at the preceding generation. Hence, generations do not overlap at any point (*i.e.* non-overlapping generations); they are distinct and the number of individuals in one time step is the offspring of individuals at the previous time step.

2.2.2 *Fold, Flip* and *Neimark-Sacker* bifurcations

In this subsection we investigate the stability properties of the fixed points of our system. System (12) has the following three fixed points:

$$E_1 : (x^*, y^*) = (0,0)$$

$$E_2 : (x^*, y^*) = \left(\frac{a}{b}, 0 \right)$$

$$E_3 : (x^*, y^*) = \left[\frac{\beta\sqrt{\frac{c}{\alpha k - c}}}{m-1}, \frac{\sqrt{\alpha ck - c^2}(\beta km - \beta k)a - bc\beta^2 k}{(\alpha ck - c^2)m^2 + (2c^2 - 2\alpha ck)m + \alpha ck - c^2} \right]$$

The Jacobian matrix at any point (*x*, *y*) is

$$J(x,y) = \begin{pmatrix} \frac{\partial \tilde{x}}{\partial x} & \frac{\partial \tilde{x}}{\partial y} \\ \frac{\partial \tilde{y}}{\partial x} & \frac{\partial \tilde{y}}{\partial y} \end{pmatrix} = \begin{pmatrix} \delta\left(-\frac{2\alpha\beta^2(1-m)^2 xy}{\left((1-m)^2 x^2 + \beta^2\right)^2} - 2bx + a \right) + 1 & -\frac{\alpha\delta(1-m)^2 x^2}{(1-m)^2 x^2 + \beta^2} \\ \frac{2\alpha\delta\beta^2 k(1-m)^2 xy}{\left((1-m)^2 x^2 + \beta^2\right)^2} & \delta\left(\frac{\alpha k(1-m)^2 x^2}{(1-m)^2 x^2 + \beta^2} - c \right) + 1 \end{pmatrix}$$

The determinant of the Jacobian matrix is

$$detJ = \left(\delta\left(\frac{\alpha k(1-m)^2 x^2}{(1-m)^2 x^2 + \beta^2} - c \right) + 1 \right) \cdot \left(\delta\left(\frac{2\alpha\beta^2(1-m)^2 xy}{\left((1-m)^2 x^2 + \beta^2\right)^2} - 2bx + a \right) + 1 \right) + \frac{2\alpha^2\delta^2\beta^2 k(1-m)^4 x^3 y}{\left((1-m)^2 x^2 + \beta^2\right)^3}$$

Once again, in order to study the local behavior around each of the three fixed points we calculate the Jacobian matrix at E_1, E_2, E_3 (Subsection 1.1.2). Using the determinant and the trace of the Jacobian, each fixed point is asymptotically stable if $|trJ| < 1 + detJ < 2$ (Equation (3)).

Stability at the fixed point E_1

The Jacobian matrix at $E_1:(x^*,y^*)=(0,0)$ is $J(E_1)=\begin{pmatrix}\delta a+1 & 0\\ 0 & 1-c\delta\end{pmatrix}$.

The Jacobian's eigenvalues are $\lambda_1=\delta a+1, \lambda_2=1-c\delta$, the determinant is $detJ(E_1)=(1-c\delta)(\delta a+1)$ and the trace is $trJ(E_1)=\delta a-c\delta+2$.

So, using the three stability conditions (Equation (3)), we get

1. If $\delta>\frac{2}{c}$, the fixed point $E_1:(x^*,y^*)=(0,0)$ is an *unstable node*; both eigenvalues lie outside the unit circle $\left(|\lambda_1|>1, \lambda_2>1\right)$.
2. If $\delta<\frac{2}{c}$, the fixed point $E_1:(x^*,y^*)=(0,0)$ is a *saddle*; one eigenvalue lies outside the unit circle and the other inside $\left(|\lambda_1|<1, \lambda_2>1\right)$.
3. If $\delta=\frac{2}{c}$, the fixed point $E_1:(x^*,y^*)=(0,0)$ is *non-hyperbolic* $\left(\lambda_1=-1, \lambda_2>1\right)$; this parameter value is associated with the first stability condition $-trJ=1+detJ$ (Equation (3)) and one real eigenvalue crossing the unit circle at –1. So this is a bifurcation point at which the system undergoes a *Flip bifurcation* at E_1.

Stability at the fixed point E_2

The Jacobian matrix at E_2 is $J(E_2)=\begin{pmatrix}1-\delta a & -\dfrac{\alpha\delta(1-m)^2a^2}{(1-m)^2a^2+b^2\beta^2}\\ 0 & \delta\left(\dfrac{\alpha k(1-m)^2a^2}{(1-m)^2a^2+b^2\beta^2}-c\right)+1\end{pmatrix}$

The eigenvalues of the Jacobian matrix are

$$\lambda_1=\frac{\left((\alpha\delta k-c\delta+1)m^2+(-2\alpha\delta k+2c\delta-2)m+\alpha\delta k-c\delta+1\right)a^2+(b^2-b^2c\delta)\beta^2}{(m^2-2m+1)a^2+b^2\beta^2},\ \lambda_2=1-\delta a$$

The determinant is $detJ(E_2)=(1-\delta a)\left(\delta\left(\dfrac{\alpha k(1-m)^2a^2}{(1-m)^2a^2+b^2\beta^2}-c\right)+1\right)$.

And the trace is $trJ(E_2)=\delta\left(\frac{\alpha k(1-m)^2a^2}{\left((1-m)^2a^2+b^2\beta^2\right)}-c\right)-\delta a+2$.

Using the stability conditions (Equation (3)) and let $F_1=1-\frac{b\beta\sqrt{\alpha ck-c^2}}{(\alpha k-c)a}$ we obtain the following:

1. If $m>F_1$ then the fixed point E_2 is a *stable node*; both eigenvalues lie inside the unit circle $(\lambda_1<1,\lambda_2<1)$.
2. If $\begin{cases} m=F_1 \\ \delta=\frac{2}{a} \end{cases}$, then the fixed point E_2 is *non-hyperbolic* $\begin{matrix}(\lambda_1<1,\lambda_2=+1)\\(\lambda_1>1,\lambda_2=-1)\end{matrix}$; the parameter value $m=F_1$ is associated with the stability condition $trJ=1+detJ$ (Equation (3)) and a real eigenvalue crossing the unit circle at +1. So this is a bifurcation point at which the system undergoes a *Fold bifurcation* at E_2.
3. If $m<F_1$ and $\delta<\frac{2}{a}$ then the fixed point E_2 is a *saddle*; one eigenvalue lies outside the unit circle and the other inside $(\lambda_1>1,\ |\lambda_2|<1)$.
4. If $\delta>\frac{2}{a}$ then the fixed point E_2 is an *unstable node*; both eigenvalues lie outside the unit circle $(\lambda_1>1,|\lambda_2|>1)$.

Stability of the fixed point E_3

The Jacobian matrix at E_3 is

$$J(E_3)=\begin{pmatrix} \frac{\sqrt{\alpha k-c}\left(((\alpha k-2c)m-\alpha k+2c)a\delta-\alpha km+\alpha k\right)+2bc^{3/2}\delta\beta}{\alpha k(m-1)\sqrt{\alpha k-c}} & -\frac{c\delta}{k} \\ \frac{\sqrt{\alpha k-c}\left((2\alpha k-2c)m-2\alpha k+2c\right)a\delta+\sqrt{c}(2bc\delta\beta-2\alpha b\delta\beta k)}{\alpha(m-1)\sqrt{\alpha k-c}} & 1 \end{pmatrix}$$

With determinant $detJ(E_3)=$

$$1+\frac{\sqrt{\alpha k-c}\left(\left(\left((m-1)(2c\delta-1)\right)\alpha k-\left((c\delta+1)m+(c\delta-1)\right)2c\right)\delta a\right)+\sqrt{c}\left(c\delta-1-\alpha\delta k\right)2bc\delta\beta}{\alpha k(m-1)\sqrt{\alpha k-c}}$$

And trace $trJ(E_3) = -\dfrac{\sqrt{\alpha k - c}\left(((\alpha k - 2c)m - \alpha k + 2c)\delta a - 2\alpha k m + 2\alpha k\right) + 2bc^{3/2}\delta\beta}{\alpha k(m-1)\sqrt{\alpha k - c}}$

Using the stability conditions (Equation (3)) and let $F_2 = 1 + \dfrac{\sqrt{c}\left(\alpha\delta k + 1 - c\delta\right)2bc\delta\beta}{\sqrt{\alpha k - c}\left((2c\delta - 1)\alpha k - 2c^2\delta + 2c\right)a}$ and $F_3 = 1 + \dfrac{\sqrt{c}\left(\alpha\delta k + 2 - c\delta\right)bc\delta\beta}{\sqrt{\alpha k - c}\left(\left(\alpha\delta k - c\delta + 2\right)c\delta a - \left(\delta a - 2\right)\alpha k\right)}$ we get

1. If $m < 1 + \dfrac{bc\beta}{a\sqrt{\alpha ck - c^2}}$ then the fixed point *E3* is an *unstable node*; both eigenvalues lie outside the unit circle $\left(|\lambda_1| > 1, \lambda_2 > 1\right)$.

2. If $1 + \dfrac{bc\beta}{a\sqrt{\alpha ck - c^2}} < m < F_3$ then the fixed point *E3* is a *saddle*; one eigenvalue lies outside the unit circle and the other inside $\left(|\lambda_1| > 1, \lambda_2 < 1\right)$.

3. If $\begin{cases} m = 1 + \dfrac{bc\beta}{a\sqrt{\alpha ck - c^2}} \\ m = F_3 \end{cases}$, then the fixed point *E3* is *non-hyperbolic* $\begin{matrix} \left(|\lambda_1| > 1, \lambda_2 = +1\right) \\ \left(\lambda_1 = -1, \lambda_2 < 1\right) \end{matrix}$; the parameter value $m = F_3$ is associated with the stability condition $-trJ = 1 + detJ$ (Equation (3)) and a real eigenvalue crossing the unit circle at –1. So this is a bifurcation point at which the system undergoes a *Flip bifurcation* at *E3*. The parameter value $m = 1 + \dfrac{bc\beta}{a\sqrt{\alpha ck - c^2}}$ is associated with the stability condition $trJ = 1 + detJ$ (Equation (3)) and a real eigenvalue crossing the unit circle at +1; hence, this is a bifurcation point at which the system undergoes a *Fold bifurcation* at *E3*.

4. If $F_3 < m < F_2$ then the fixed point *E3* is a *stable node* (*i.e.* both eigenvalues lie inside the unit circle $|\lambda_1| < 1, \lambda_2 < 1$ or a *stable focus* (complex eigenvalues with real parts $|\alpha_1| = |\alpha_2| < 1$ and $detJ\left(E_3\right) < 1$).

5. If $m = F_2$ then the fixed point *E3* is *center* (*i.e.* complex eigenvalues with real parts $|\alpha_1| = |\alpha_2| = 1$ and $detJ\left(E_3\right) = 1$, $-2 < trJ\left(E_3\right) < 2$); this parameter value is associated with the stability condition $detJ = 1$ (Equation (3)) and two complex eigenvalues crossing the unit circle simultaneously. So this is a bifurcation point at which a *Neimark-Sacker bifurcation* occurs in the system.

6. If $m > F_2$ then the fixed point E_3 is an *unstable focus*; complex eigenvalues with real parts $|\alpha_1| = |\alpha_2| > 1$ and $detJ(E_3) > 1$).

2.2.3 Routes to chaos, strange attractors and prey population outbreaks

In order to study the complex dynamics of system (Equation (12)) we use the numerical simulation tools: parametric basins of attraction, bifurcation diagrams, phase plots and Lyapunov exponent diagrams. We fix the parameters $a = 1, b = 0.1, \alpha = 0.5, k = 0.2, c = 0.09, \beta = 0.5$, we use for initial conditions the values $(x(0), y(0)) = (0.5, 0.8)$ (Huang *et al.*, 2006), and let the values of the refuge parameter and the step size vary.

Simultaneous variation of step size and refuge parameters

In order to have a first picture on the dependence of the dynamics of the system to the increase of the step size for various values of the refuge parameter, we plot the basins of attraction diagram for the parameter values $m \in [0,1]$ and $\delta \in [0, 3.5]$ (Figure 10).

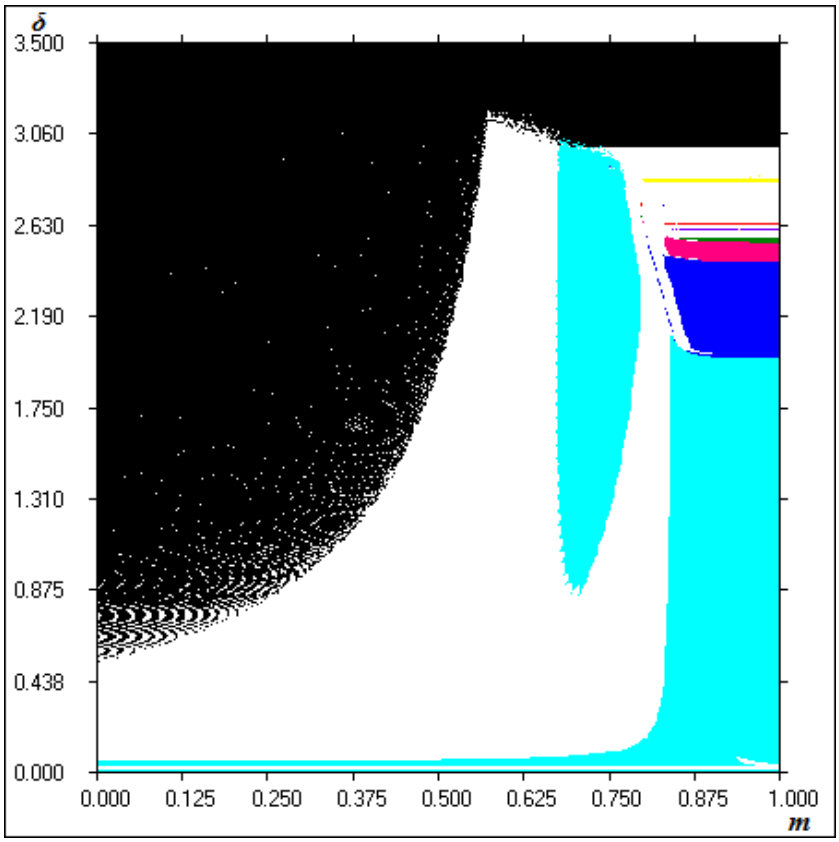

Figure 10 The parametric basins of attraction (m, δ).

From the basins of attraction diagram we observe the following:

1. For small and average refuge ($0 < m < 0.676$) the system's behavior is *non-periodic*. As the step size increases the white area is being replaced by the black area. All initial conditions give rise to extinction of both species.
2. For the values of the refuge parameter ($0.676 < m < 0.797$), as the step size increases, the non-periodic behavior is being replaced with an *attracting* fixed point (light blue area).
3. For large refuge ($0.797 < m < 1$), as the step size takes larger values, the attracting fixed point goes through period-doubling bifurcations (2-period cycle, 4-period cycle, 8-period cycle) giving rise to *non-periodic* behavior (white area).

Thus, adding a large refuge in the 2D map (Equation (12)) does not stabilize the predator-prey interactions anymore as it does in the continuous-time dynamical system (Equation (11)).

Increasing the step size for average refuge

We plot the phase diagram (x, y) for the average value of the refuge parameter $m = 0.57$ as the step size increases in the interval $\delta \in [0, 3.1]$. We observe that the limit cycle of the continuous-time model develops a strange chaotic region (Figure 11).

- As the step size increases in range $0 < \delta < 2$, the diameter of the stable limit cycle of the continuous-time model (Figure 11(a)) increases and near to the value $\delta \approx 0.19$ becomes a *closed invariant curve* (Figure 11(b)).
- The diameter of the closed curve increases continuously. Near to the value $\delta \approx 1.9$ the invariant curve interacts with the saddle fixed point $E_2\left(x^*, y^*\right) = (10, 0)$ and develops a first *kink* (Figure 11(c)).
- As δ passes through the value $\delta \approx 2$, the saddle fixed point $E_2\left(x^*, y^*\right) = (10, 0)$ goes through a bifurcation, where it loses stability and becomes a *source*. For $\delta = 1.5 < 2$, the Jacobian matrix at $E_2\left(x^*, y^*\right) = (10, 0)$ has real eigenvalues $(\lambda_1, \lambda_2) = (1.013, -0.5)$ (*i.e.* one eigenvalue lying outside the unit circle and the other inside (saddle)), while for , the real eigenvalues of the Jacobian matrix are (*i.e.* both eigenvalues lying outside the unit circle (unstable node)).
- As the step size increases in the range $2 < \delta < 2.6$, the closed curve develops more kinks (Figure 11(d)).
- As the step size takes larger values, $\delta > 2.6$, and after many *period-doubling bifurcations*, the invariant curve develops a strange chaotic region (Figure 11(e)), becomes more complicated forming finally into a *strange attractor* (Figure 11(f)).

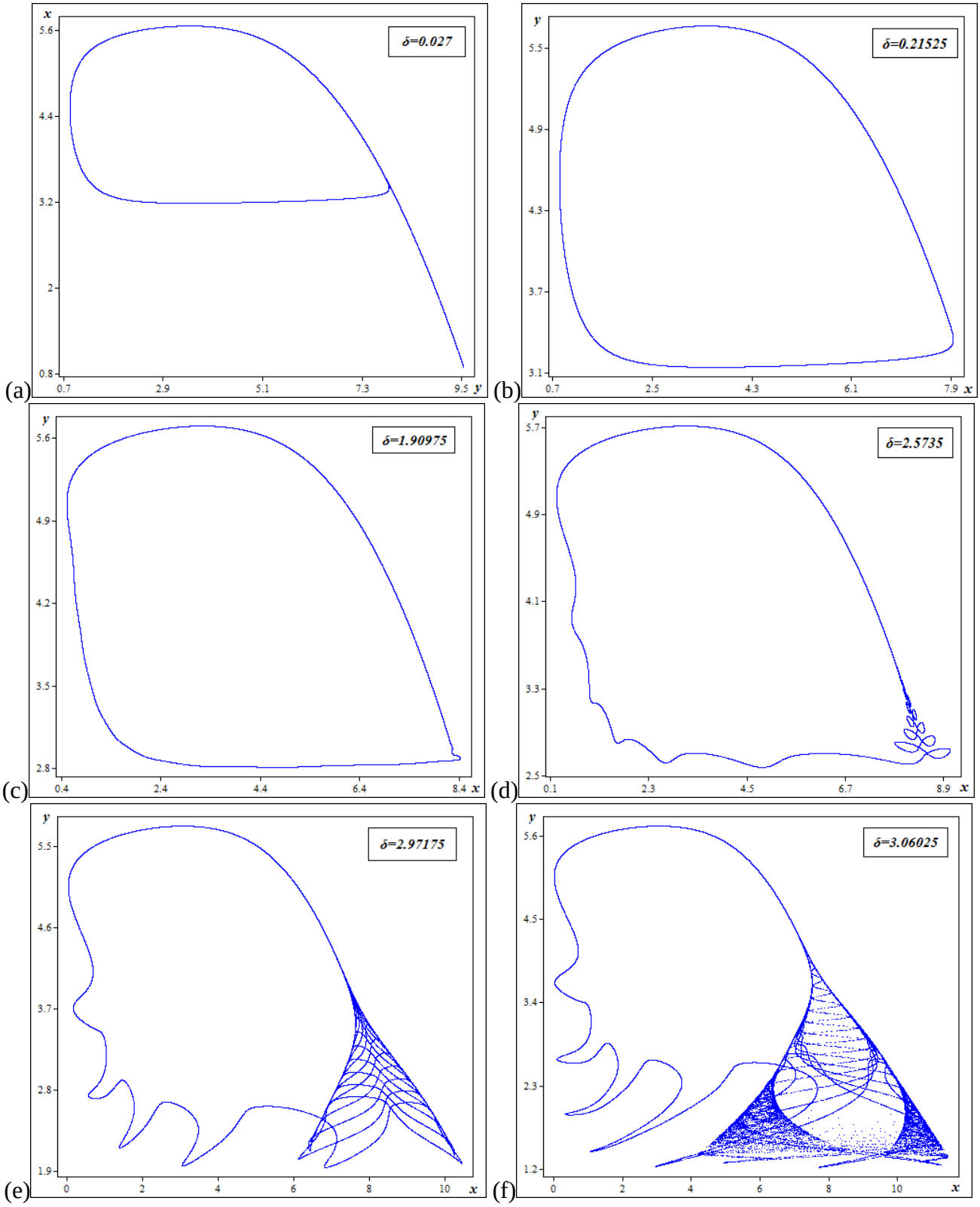

Figure 11 The phase plot (x, y) for $m = 0.57$, as the step size increases in the range $0 < \delta < 3.1$. (a) The limit cycle of the continuous-time model ($\delta = 0.027$), (b) the invariant curve grows in size ($\delta = 0.21525$), (c) the invariant curve develops a first kink ($\delta = 1.90975$), (d) the invariant curve develops more kinks ($\delta = 2.5735$), (e) the invariant curve develops a strange region ($\delta = 2.97175$) and (f) the invariant curve becomes a strange attractor ($\delta = 3.06025$).

The corresponding bifurcation diagram for both population species (δ, x^*), (δ, y^*) and the Lyapunov exponent diagram (δ, λ) for the average value of the refuge parameter m = 0.57, as the step size increases in the range $0 < \delta < 3.05$ are illustrated in Figure 12. In Figure 12(b) we see in magnification how the characteristics of the fixed point in prey population change as the step size increases in range $2.17 < \delta < 2.57$. Particularly, we observe that in this range, where the closed invariant curve develops more kinks (Figure 11(d)), the system undergoes several period-doubling and period-halving bifurcations and alternates between chaotic and periodic behavior of high periods. From the Lyapunov exponent diagram (Figure 12(c)) we observe that:

- In the range $0 < \delta < 2$, where both populations coexist and oscillate between all the states of the closed invariant curve, the Lyapunov exponents vary among negative and exceptionally small positive values $\lambda_i < 0.001$.

(a)

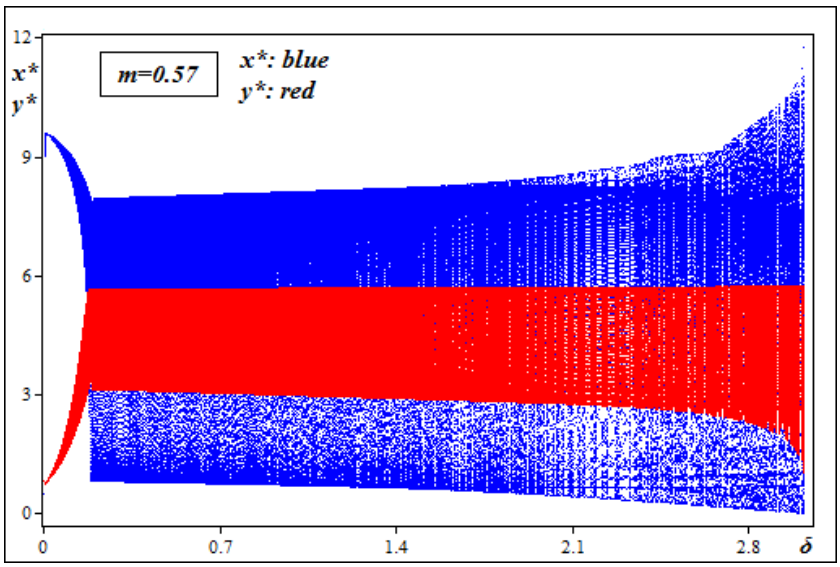

(b)

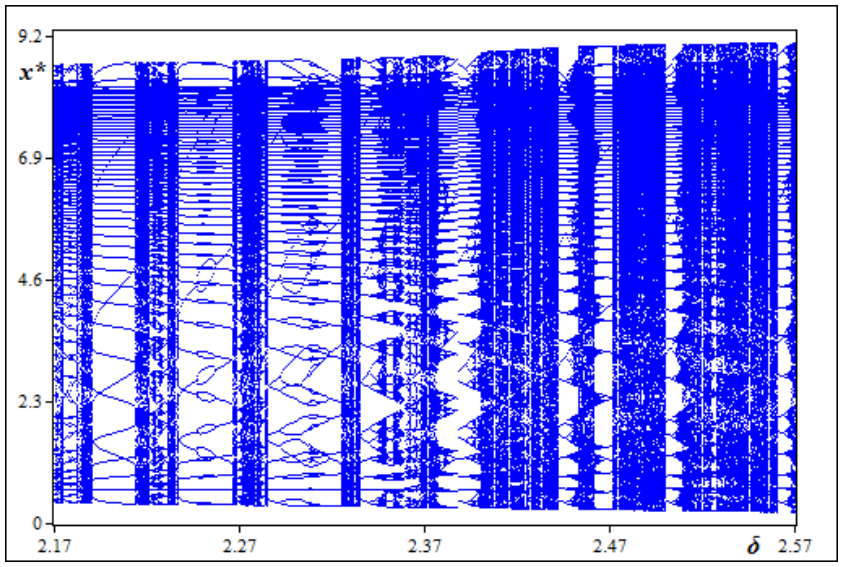

Figure 12 (*Continued.*)

(c)

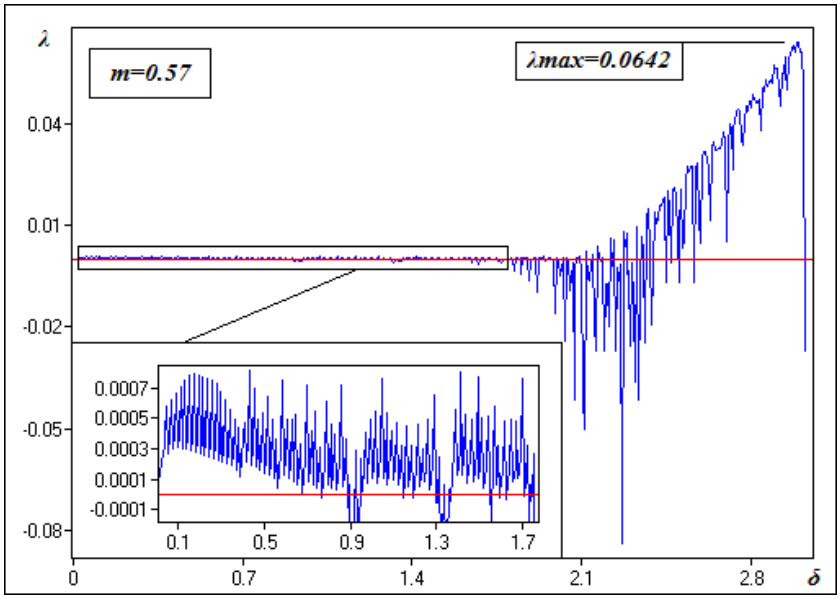

Figure 12 The bifurcation diagrams (δ, x^*), (δ, y^*) and the Lyapunov exponent diagram (δ, λ) for m = 0.57, as the step size increases in the range $0 < \delta < 3.05$. (a) The bifurcation diagrams (δ, x^*) and (δ, y^*), (b) magnification of the bifurcation diagram (δ, x^*) and (c) the Lyapunov exponent diagram (δ, λ).

- In the range $2 < \delta < 2.6$, where the system undergoes several period-halving and period-doubling bifurcations, the Lyapunov exponents vary among negative and higher positive values $0.001 < \lambda_i < 0.03$.
- While for $\delta > 2.6$, where the system undergoes many period-doubling bifurcations, the Lyapunov exponents vary among even higher positive values. For $\delta = 2.9979$ we have the maximum value $\lambda_{\max} \approx 0.0642$ for which the predator-prey interactions are the least predictable.

Decreasing β for average refuge and large step size

For the average value of the refuge parameter $m = 0.57$, for large step size $\delta = 3.08$ and small number of newly born predators for each captured prey $k = 0.3$ (all the other parameters are fixed), we plot the phase diagram (x, y) as the value of β decreases in the range $0.77 < \beta < 1.07$. We observe that the attracting fixed point via a Neimark-Sacker bifurcation gives rise to an invariant curve, which finally evolves into a strange attractor as the value of β decreases further (Figure 13).

- As β decreases, a *supercritical Neimark-Sacker bifurcation* takes place near the value $\beta \approx 1.06$. The stable focus fixed point $(x^*, y^*) \approx (3,7)$ (Figure 13(a)) corresponding to coexistence loses stability, becomes an unstable focus and all trajectories approach a stable *closed invariant curve* (Figure 13(b)).

- The invariant curve grows in size as the value of β decreases and deforms (Figure 13(c)). Close to the value $\beta \approx 0.83006$, the invariant curve splits and locks into a *stable orbit of period 19* (Figure 13(d)).

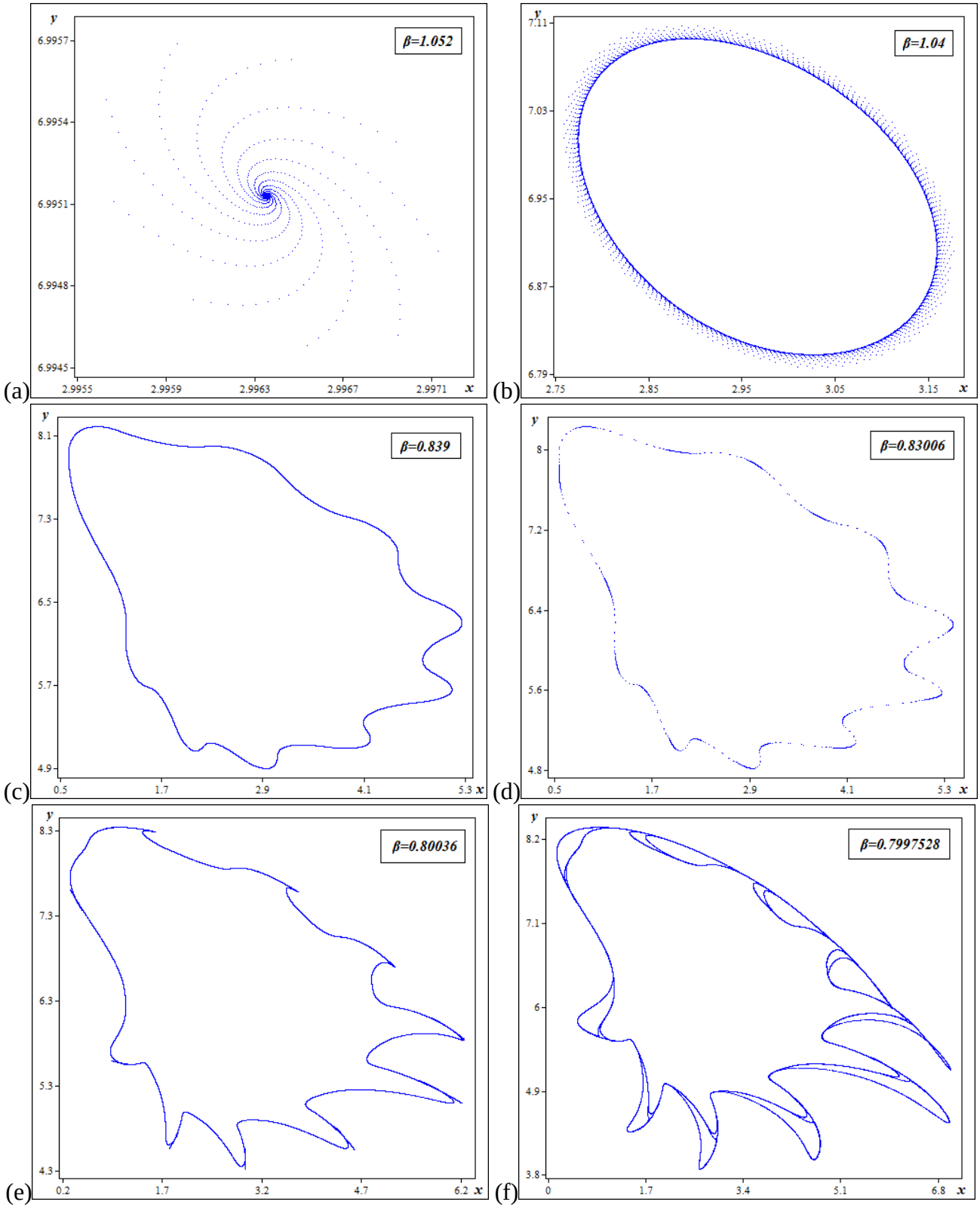

Figure 13 (*Continued.*)

(g) 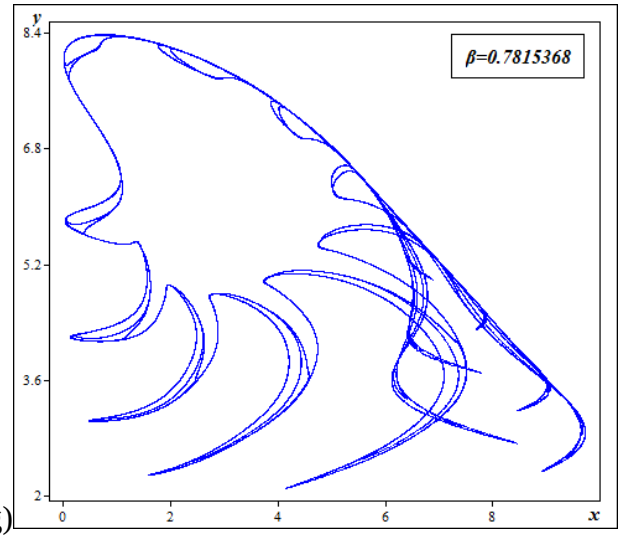

(h) 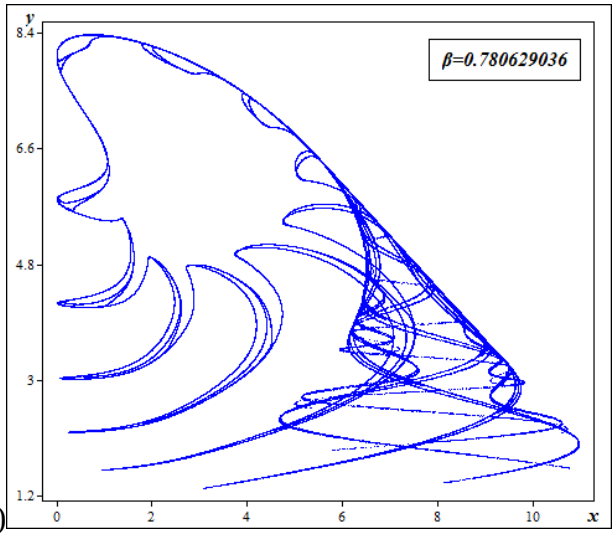

Figure 13 The phase plot (x, y) for m = 0.57 and δ = 3.08, k = 0.3, as β decreases in the range 0.77 < β < 1.07. (a) The attracting fixed point (β = 1.052), (b) the closed invariant curve born (β =1.04), (c) the invariant curve slightly deformed (β = 0.839), (d) the invariant curve has a split (β = 0.83006), (e) the toothed wheel appearance (β = 0.80036), (f) the invariant curve becomes a contiguous ring (β = 0.7997528), (g) the contiguous band more complicated (β = 0.7815368) and (h) the strange attractor (β = 0.780629036).

- The invariant curve reappears slightly deformed (Figure 13(e)), appearing like a *toothed wheel*, which has been investigated by Aronson *et al.* (1982).
- The invariant curve becomes a *contiguous ring* (Figure 13(f)), which as the varying parameter decreases further becomes even more complicated (Figure 13(g)).
- Eventually the strange contiguous band evolves into a *strange attractor* (Figure 13(h)).

By plotting the parametric basins of attraction diagram for 0 < β < 2.3 and 0.15 < k < 1.75, we can see for which values of the parameters (β, k) the supercritical Neimark-Sacker bifurcation takes place (Figure 14). We keep again fixed the parameters δ = 3.08 and m = 0.57. From the basins of attraction diagram we observe the following:

1. For small number of newly born predators for each captured prey (0.2 < k < 0.38), as the value of β decreases, the light blue area (attracting fixed point) is being replaced with the white area (invariant curve and strange attractor) via the supercritical Neimark-Sacker bifurcation. As β decreases further the white area is being replaced with the black area (divergence to infinity) through some kind of catastrophe and any initial condition gives rise to extinction of both population species.

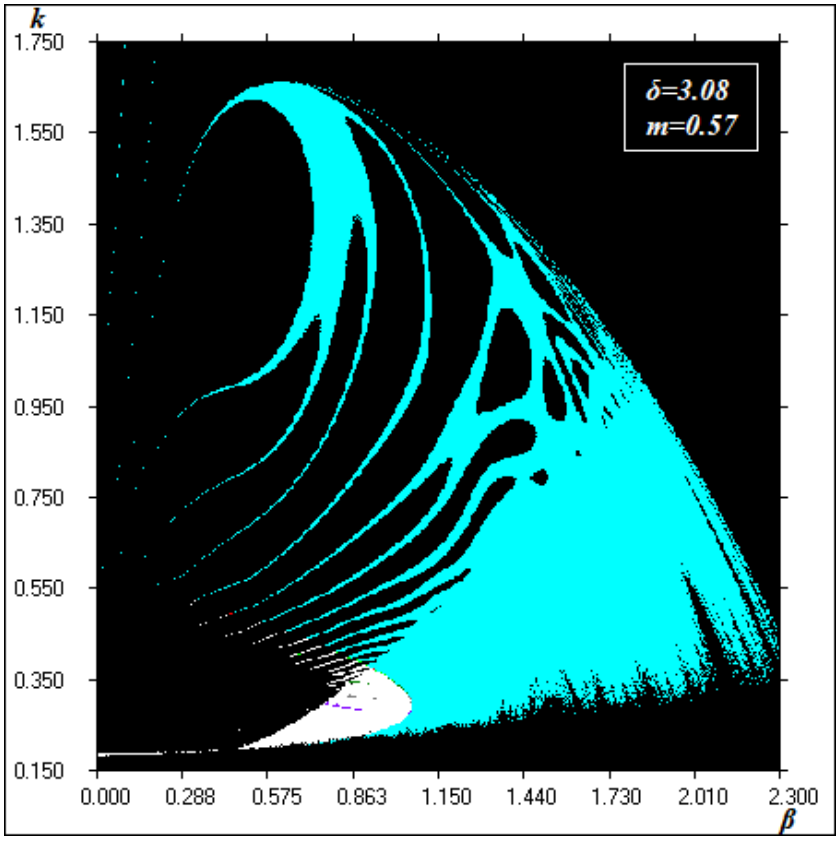

Figure 14 The parametric basins of attraction (β, k) for average refuge (m = 0.57) and large step size (δ = 3.08).

2. For higher number of newly born predators for each captured prey (k > 0.38), we observe that scattered black areas appear inside the light blue areas. So, for the parameter values for which solutions converge to attracting fixed point, as β decreases, iterations suddenly evolve toward infinity and both populations become extinct.

We also plot the corresponding bifurcation diagrams (β, x^*) and (β, y^*), along with the Lyapunov exponent diagram (β, λ) as the varying parameter decreases in the interval 0.7807 < β < 1.07. We keep again fixed the parameters $\delta = 3.08, m = 0.57, k = 0.3$ (Figure 15). In Figure 15(b) we see in magnification a part of the bifurcation diagram in prey population (Figure 15(a)). We observe that the system's behavior alternates between chaotic and periodic of high periods. Particularly:

1. In range 0.8229 < β < 0.8292 both populations settle down on a *19-period cycle*.
2. Near to the value $\beta \approx 0.8129$, as the value of β decreases, a series of *period-doubling bifurcation* $(10 \cdot 2^n)$: (10-period cycle, 20-period cycle, 40-period cycle, *etc.*) lead to chaos.

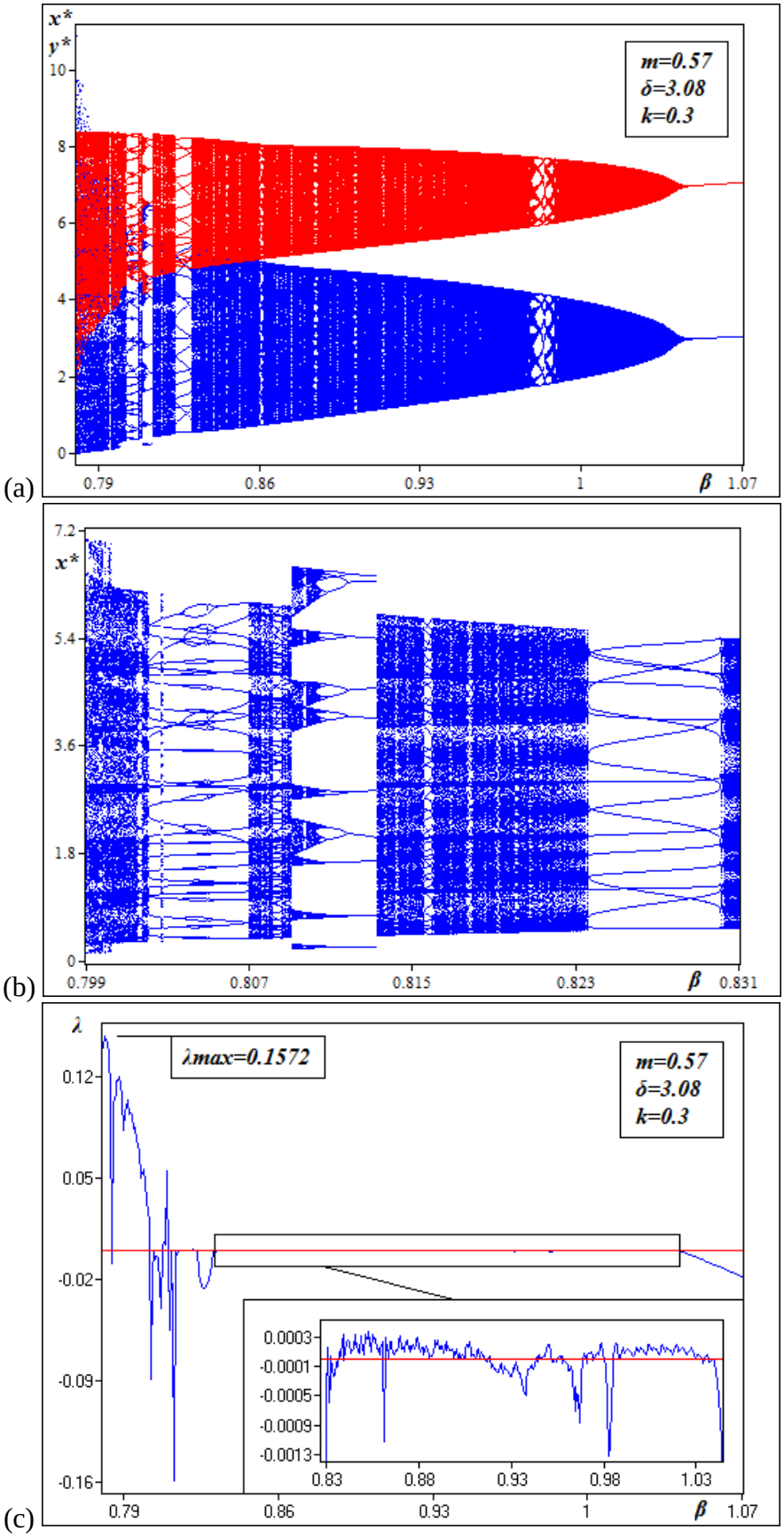

Figure 15 The bifurcation and the Lyapunov exponent diagrams for m = 0.57 and δ = 3.08, k = 0.3, as β decreases in the range 0.7807 < β < 1.07. (a) The bifurcation diagrams (β, x^*) and (β, y^*), (b) magnification of the bifurcation diagram (β, x^*) and (c) the Lyapunov exponent diagram (β, λ).

3. For the values $0.8021 < \beta < 0.8068$, another series of period-doubling and period-halving bifurcations $(29 \cdot 2^n)$: (a 29-period cycle to a 58-period cycle and back to a 29-period cycle) lead to *chaos* once again.

Respectively to the bifurcation diagram, from the Lyapunov exponent diagram (Figure 15(c)) we observe the following:

1. As the value of β decreases in the range $0.83 < \beta < 1.07$ the Lyapunov exponents vary among negative and small positive values $\lambda_i < 0.0004$, as we see in magnification.
2. For smaller values $0.807 < \beta < 0.83$, where period-doubling bifurcations occur in both populations, the Lyapunov exponents vary among negative and higher positive values $\lambda_i < 0.06$.
3. As β takes even smaller values in the range $0.7807 < \beta < 0.807$, the Lyapunov exponents vary among even larger positive values and reach the maximum value $\lambda_{\max} \approx 0.1572$ for $\beta \approx 0.7809$.

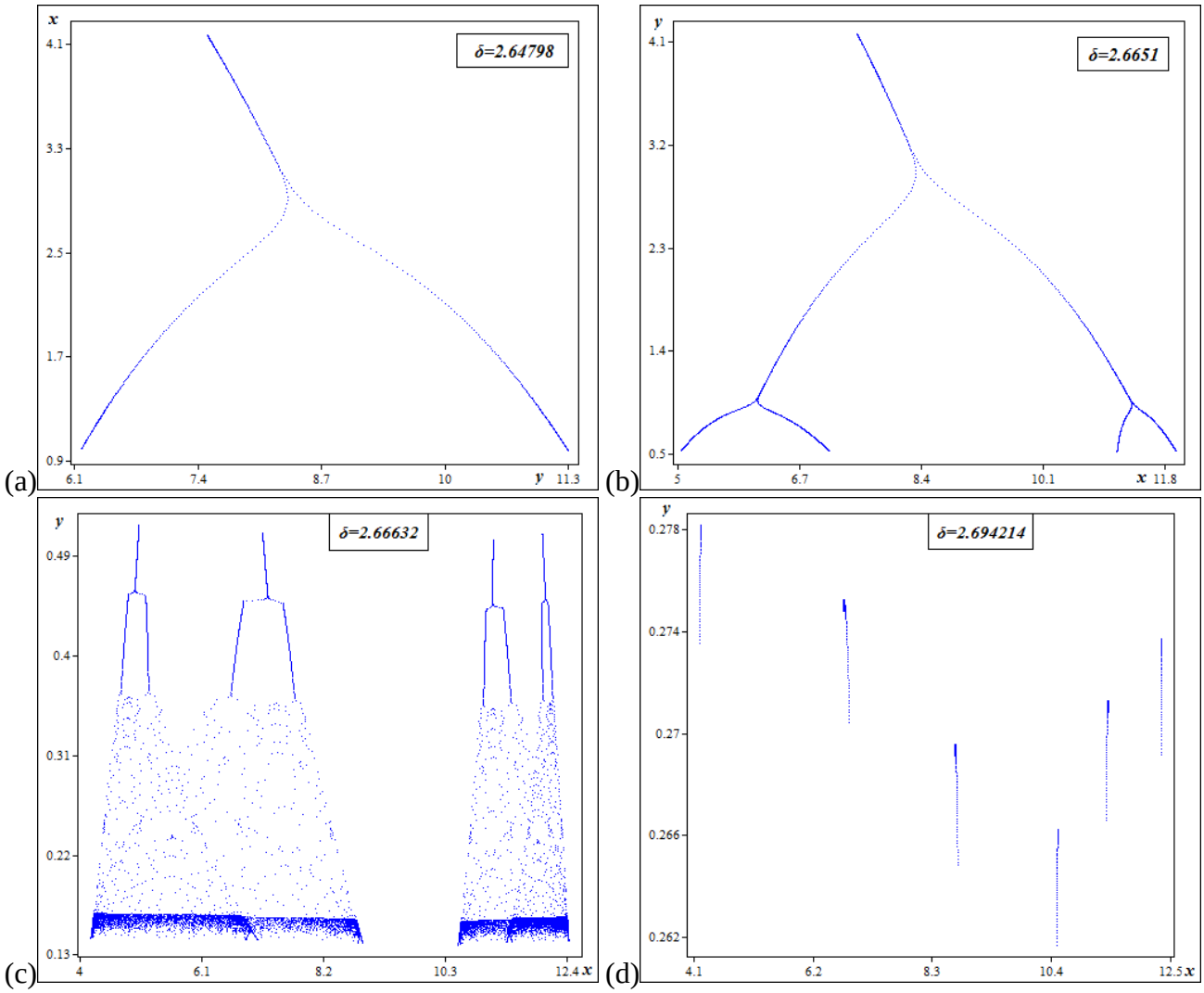

Figure 16 (*Continued.*)

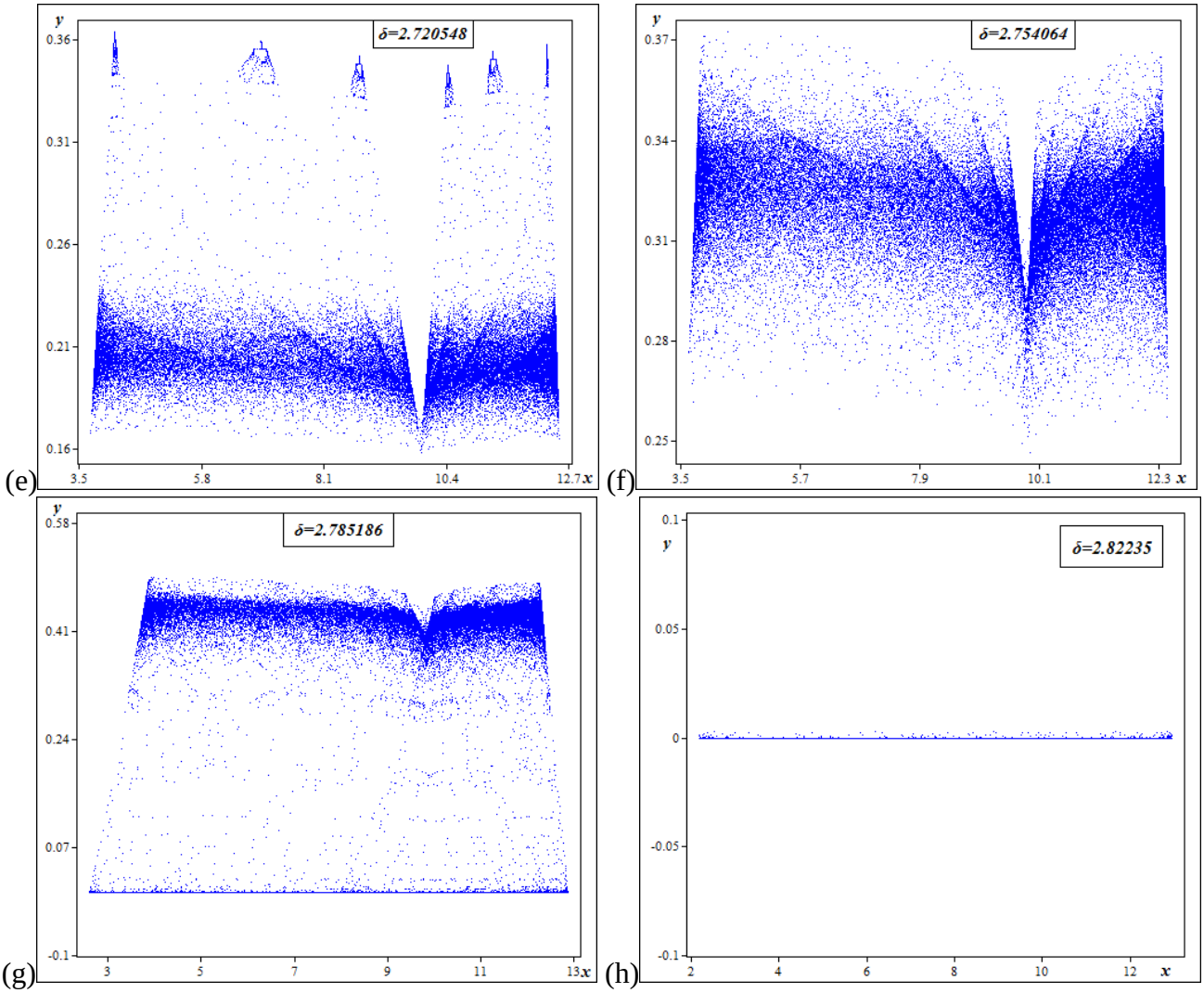

Figure 16 The phase plot (x, y) for large refuge (m = 0.8) and k = 0.2, β = 0.5, as δ increases in the range 2.63 < δ < 2.83. (a) Stable orbit of period 2 (δ = 2.64798), (b) stable orbit of period 4 (δ = 2.6651), (c) period-doubling route to chaos (δ = 2.66632), (d) stable orbit of period 6 (δ = 2.694214), (e) chaos in both population species (δ = 2.720548), (f) trajectory is pushing upward (δ = 2.754064), (g) predator population decreases (δ = 2.785186) and (h) predators become extinct (δ = 2.82235).

Increasing the step size for large refuge

We keep fixed the parameters k = 0.2, β = 0.5 and plot the phase diagram (x, y) for large refuge (m = 0.8), as the step size increases in the interval 2.63 < δ < 2.83 (Figure 16).

- In the range 0 < δ < 2.65 both populations survive ($x^* > y^*$). All trajectories converge to the attracting fixed point (x^*, y^*) = (7.02, 4.27), where both populations are fixed in time.
- As the step size increases, the two-period cycle x^*: (6.174, 11.296) (Figure 16(a)) undergoes a period-doubling bifurcation and near the value $\delta \approx 2.65$ a stable four-period cycle appears in prey population x^*: (5.051, 7.114, 11.135, 11.959) (Figure 16(b)).

- Close to the value $\delta \approx 2.666$, the period-doubling route to chaos and the trajectory mimics the Feigenbaum bifurcation diagram (Figure 16(c)). This is the so-called *fountain* phenomenon, which has been investigated by Hadeler and Gerstmann (1990).
- In the range $2.69 < \delta < 2.72$, the chaotic behavior in prey population is replaced by a stable orbit of period six x^*: (4.24, 6.77, 8.71, 10.48, 11.34, 12.28) (Figure 16(d)).
- As the step size increases further in the range $2.72 < \delta < 2.83$, chaos appear in both population species (Figure 16(e)) and the trajectory is pushed upward (Figure 16(f)).
- The predator population decreases continuously (Figure 16(g)) until the extinction ($y^* = 0$) and only the prey population survives (x^*: chaos) (Figure 16(h)).

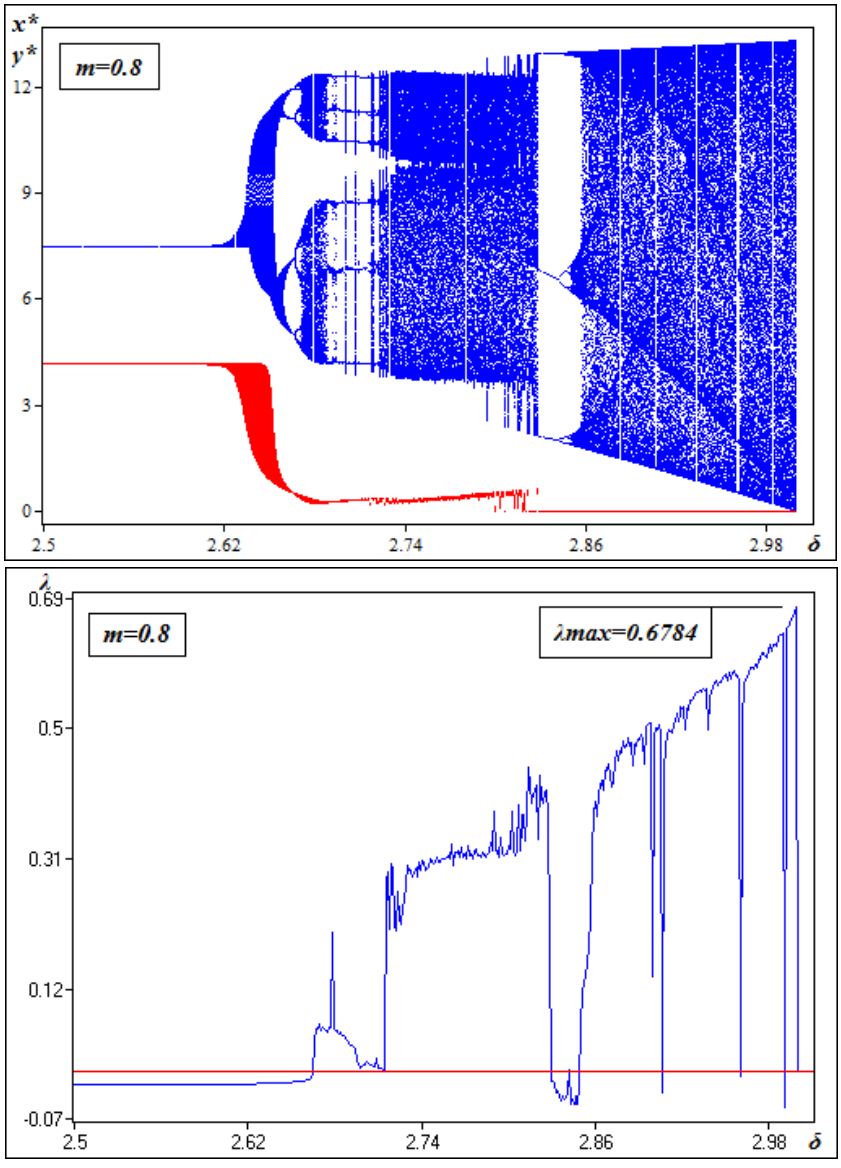

Figure 17 The bifurcation and the Lyapunov exponent diagrams for $m = 0.8$ and $k = 0.2$, $\beta = 0.5$ as δ increases in the range $2.5 < \delta < 3.01$. (a) The bifurcation diagrams (δ, x^*), (δ, y^*), (b) the Lyapunov exponent diagram (δ, λ).

We also plot the corresponding bifurcation and Lyapunov exponent diagrams $(\delta, x^*), (\delta, y^*), (\delta, \lambda)$ for the large value of the refuge parameter $m = 0.8$, as the step size increases in the interval $2.5 < \delta < 3.01$ (Figure 17). In bifurcation diagram (Figure 17(a)), we observe that for values of the step size $\delta > 2.83$ for which predators become extinct, a 3-period orbit appears in prey population and a series of period-doubling bifurcations $(3 \cdot 2^n)$ lead to chaos once again. Once the predators become extinct, we have only a single species with limited resources. So for exceptionally large step size ($\delta \approx 3$), the reproduction rate of prey and the resource limitation compete each other, leading in some cases the prey population to extinction ($x^* \approx 0.01$) and in other cases to overgrowth ($x^* \approx 13.34$). Thus, adding a large refuge leads to the extinction of the predator population and exhibits *prey population outbreaks*.

From the Lyapunov exponent diagram (Figure 17(b)), we observe the following:

1. For values of the step size $\delta < 2.666$, where the period-doubling phenomenon takes place, the Lyapunov exponents take only negative values $(\lambda_i < 0)$.
2. As the step size increases in the range $2.666 < \delta < 2.69$, where the period-doubling route to chaos appears, the Lyapunov exponents vary among positive values $(\lambda_i < 0.1559)$. In the range $2.72 < \delta < 2.83$, where the 6-period cycle is being replaced by chaotic behavior, Lyapunov exponents vary among larger positive values $(\lambda_i < 0.4401)$.
3. For larger step size $\delta > 2.83$, where only the prey population survives, Lyapunov exponents vary among even larger positive values. For $\delta \approx 2.9991$ we get the maximum value $\lambda_{\max} \approx 0.6784$.

The maximum Lyapunov exponent (MLE) for large refuge is remarkably higher than that for average refuge $\lambda_{m=0.8}^{\max} \approx 0.6784 > \lambda_{m=0.57}^{\max} \approx 0.0642$. Hence, adding a large refuge not only exhibits prey population outbreaks, but also makes the prey's population dynamics extremely chaotic as well. Furthermore, once predators become extinct our modified model (Equation (12)) follows approximately the dynamics of the logistic map, which is well known for producing time series that look like random[25]. Therefore, although our system is deterministic, its behavior seems to be stochastic and because of its dependence on initial conditions it is almost impossible to predict the prey population outbreaks.

[25] The logistic map $x_{n+1} = r x_n (1 - x_n)$ for $r = 4$ defines a dynamical system with seemingly random or stochastic behavior (Takens, 1993).

2.2.4 Prey refuge and population outbreaks: Locust plagues and aposematic anti-predator strategy

The results of our study show that the discrete-time model we suggest produces far more complex dynamics compared to the continuous-time version. In particular, we observe the following:

1. Adding an average refuge in the continuous-time model results in the appearance of a stable limit cycle. On the other hand, adding an average refuge in the discrete-time version results in the appearance of a strange chaotic region developed on the invariant curve after many period-doubling bifurcations. Moreover, for large step size and small number of newly born predators for each captured prey, the attracting fixed point is being replaced by a strange attractor via a Neimark-Sacker bifurcation.
2. Adding a large refuge in the continuous-time model stabilizes the predator-prey interactions and both populations settle down in a stable equilibrium point. On the other hand, adding a large refuge in the discrete-time version, the attracting fixed point is being replaced by chaotic behavior via period-doubling bifurcations. Moreover, as the step size increases, the predator population becomes extinct, while prey population outbreaks and random-like dynamics appear.

The Holling type III functional response mainly refers to polyphagous vertebrate predators, like birds (Holling, 1959). Many species of birds prey on pest insects and therefore they are considered beneficial for humanity (Reid, 2006). For instance, many species of birds prey on locusts. Locusts are crop pest insects which show population outbreaks (locust plagues) regularly in real world. Rain allows the female to lay eggs in the sandy soil and because of the vegetation growth and the population outbreak, locusts devour all the vegetation (Pollock, 1993). Desert locusts (*Schistocerca Gregaria*) and the African migratory locust (*Locusta Migratoria*) are the most dangerous of the locust pests causing famines worldwide; they regularly cover vast areas of Northern Africa, Middle East, and Southwestern Asia (Uvarov, 1977). Concerning our assumption (reproduction in certain intervals), the population of desert locusts evolves in discrete time steps; they have two to five generations per year (Topaz *et al*., 2008; Topaz *et al*., 2012) with every generation lasting from two to six months (Symmons and Cressman, 2001). Hence, our study indicates that reproduction in certain intervals is important and should be taken into account since it could help in the identification of insect pest population outbreaks, such as locust outbreaks.

Moreover, the results of our study showed that increasing the amount of refuge leads to almost unpredictable increases in prey population density. So, if desert locusts are able to protect themselves from predation in some way, then population outbreaks of locusts could have devastating effects

worldwide. This could be considered as a rather realistic scenario since desert locusts present changes in their diet while shifting from solitary to gregarious phase in order to protect themselves from predation, indeed. Lab experiments and computer simulation showed that solitarious locusts were deterred at first contact with hyoscyamine – a plant compound that protects against predators – since they would not benefit from consuming the compound, because they escape predation by avoiding detection; by contrary, for high-density gregarious and transiens locusts, for whom crypsis is no longer an option, acquiring toxicity by feeding readily on the compound dramatically decreases predation risk (Despland, 2005).

Concluding, once again, our modified proposed model seems to be more appropriate for describing the real world pest population outbreaks (such as locust plagues) than the original predator-prey model.

2.3 Global Economic Repercussions: Pest Population Outbreaks and Vector-Borne Diseases

2.3.1 Economic and food security impacts of locust plagues

In Section 2.2 we showed that reproduction in certain intervals is important and should be taken into account since it could help in the identification of insect pest population outbreaks, such as locust outbreaks. As already mentioned, desert locusts (*Schistocerca Gregaria*) and the African migratory locust (*Locusta Migratoria*) are the most dangerous of the locust pests causing famines worldwide. Moreover, the results of our study showed that increasing the amount of refuge leads to almost unpredictable increases in prey population density. Hence, considering that desert locusts are able to protect themselves from predation by changing their diet while shifting from solitary to gregarious phase (as mentioned in Subsection 2.2.4), then locust outbreaks could have disastrous effects on global food security.

A locust swarm can travel hundred kilometers per day, stripping most of the vegetation in its path (Kennedy, 1951). In particular, billions of locusts form swarms containing up to 1,010 members covering cross-sectional areas of up to 1000 km^2 and traveling up to 102 km per day for a period of days or weeks as they feed (Uvarov, 1977). In 1999 the Locust Plague in Central Asia resulted in the devastation of millions of hectares (Thomas *et al.*, 2000): (i) 7 million ha (70,000 km^2) of land were devastated in Kazakhstan, (ii) 300,000 ha (3,000 km^2) were destroyed in Uzbekistan, (iii) 2 million ha (20,000 km^2) of land were infected with locust eggs in Pavlodar; the latter resulted in a severe locust outbreak in 2000 in China (930,000 ha (9,300 km^2) of crops were affected in North-Central China,

more than 2 million ha (20,000 km^2) of farmland were damaged in North-Western China, while 1.3 million ha (13,000 km^2) of farmland was predicted that would be further damaged). 2000 Locust Plague in Latin America (Nothern Peru) was one of the largest plagues; at least 15 million Peruvian Locusts (*Scistocerra Piceifrons Peruviana*) were recorded covering an estimated area of 50 square miles (130 km^2) (Thomas *et al.*, 2000). Brazil had several large locust outbreaks in the decade 1990 – 2000; during the 1993 locust outbreak 2 million ha (20,000 km^2) approximately were infested in Mato Grosso (Barrientos, 1995).

The significant crop loss[26] exacerbates problems of food storage and is a threat to food security and therefore it may cause famine (Pollock, 1993). For instance, the 1917 Locust Plague[27] resulted in several increases to the price of food[28] (New York Times, 1915b). The locust plague was also responsible for death and disbursement, due to diseases that were brought by the locusts (University of Utah, 2012). Another locust plague (2003 – 2005) in West and North Africa destroyed $ 2.5 billion in crops (Bell, 2005). This desert locust plague was the worst occurred since 1987-88; locust swarms migrated extensively and over very long distances covering all vegetation over thousands or hundreds of hectares reaching the Cape Verde Islands, the Canary Islands, Southern Portugal, Egypt, Cyprus, and Israel (Lecoq, 2005).

Pest control officials perform several operations (ground control methods using pesticides and biological agents, airborne control methods using aircrafts) to reduce the frequency and duration of locust emergencies. However, locust plagues persist and swarms invade other areas. Moreover, control measures cost a lot resulting in extensive economic damage. In 2004-05 the Australian Plague Locust Commission (APLC) undertook its largest control operation since 1976, treating 450,000 hectares for locust bands and swarms; the costs of the control operations (pesticide expenses and aircraft hire) varied from zero in 2002-03 to $ 3.7 million in 2004-05 (Love and Riwoe, 2005). The Commission's total expenditure (costs related to control operations along with costs on staffing, field operations office and other expenses[29]) over the six year period, from 1999 – 2000 to 2004 – 2005, amounted to $ 27.2 million (Love and Riwoe, 2005). During the desert locust plague in Africa (2003 – 2005), despite control efforts totaling $ 400 million, loss rates exceeded 50% in certain regions (Bell, 2005). Since

[26] A medium-sized locust swarm can consume 80,000 tons of green vegetation or crops per day, enough to feed a population of 100,000 persons for a year (Desert Locust Control Organization-Eastern Africa).
[27] 1917 Locust Plague lasted from March to October 1915 and stripped areas in and around Palestine of almost all vegetation (Library of Congress, 1915).
[28] On 10 April 25, 1915, flour costs $ 15 per sack, potatoes were six times the ordinary price, sugar and petroleum were unprocurable, money has ceased to circulate (New York Times, 1915a).
[29] The Commission's expenditure on staffing, field operations office and other expenses from 1999 – 2000 to 2004 – 2005 ranged between $ 2.6 and $ 3.1 million a year (Love and Riwoe, 2005).

1997 until 2000, more than $ 35 million were spent on pesticides for control of the migratory locust swarms (*Locusta Migratoria*) in Madagascar (Thomas *et al.*, 2000). Thus, from this perspective birds as predators (as mentioned in Section 2.2, our modified model refers to polyphagous vertebrate predators like birds), which prey on desert locusts, encourage the locust biological control programs. However, studies indicate that global warming threatens bird species with extinction[30], while at the same time provide optimum conditions for locusts to multiply and spread[31].

All of the above mentioned facts indicate that locust plagues need to be addressed by finding better ways to predict and control them in order to ensure global food security.

2.3.2 Burden of vector-borne diseases on public health and economy

In Section 2.1 we showed that while a small refuge could control the prey population, a large refuge leads to almost unpredictability (*i.e.* random-like prey population outbreaks). As mentioned above (Subsection 2.1.4), by taking into consideration that the prey population could be biting insects (*e.g.* mosquitoes) and that they were able to protect themselves effectively from passive predators like spiders (by using diving as an escape strategy to avoid predation), then the results of our study suggest that serious infectious diseases, which pests may carry, could spread through human populations across a large region and a pandemic could be a possible scenario.

For instance, the viral disease "yellow fever" (viral haemorrhagic fever) is a mosquito-borne disease (Oldstone, 1998) transmitted by the *Haemagogus* and *Aedes aegypti* mosquito species (WHO, 2014); the parasitic disease "malaria"[32] can be transmitted by female mosquitoes of the genus *Anopheles*, and has been also associated with causing brain tumors (Lehrer, 2010); the viral disease "dengue" is transmitted primarily by the *Aedes aegypti* female mosquito (WHO, 2014); the "Zika" virus can be transmitted primarily by the *Aedes aegypti* and *Aedes albopictus* mosquitoes (WHO, 2016d). All these mosquito-borne infectious diseases have significant direct and indirect costs (Tables 1 and 2) which affect the economic development of many countries globally.

[30] Şekercioğlu (University of Utah, 2012) indicates that 100 – 2,500 land bird species may go extinct due to climate change according to the Intergovernmental Panel on Climate Change, which has predicted 1.1 – 6.4°C of global warming of the Earth's surface by the year 2100.

[31] Yu *et al.* (2009) have found that over the last 100 years severe locust outbreaks generally happen in warm years. Their data suggest that locust outbreaks may become more common as the climate becomes warmer and drier.

[32] Malaria transmission occurs in 97 countries putting about 3.4 billion people – nearly half of the world's population – at risk (WHO, 2014).

Malaria

Malaria contributes to the poor health situation in Africa; according to the latest estimates from WHO, the disease is concentrated in Sub-Saharan Africa accounting for 88% of the world's 214 million (range: 149 – 303 million) malaria cases and 90% of the world's 438,000 (range: 236,000 – 635,000) malaria deaths[33] annually (WHO, 2015). Malaria affects the national income in endemic African countries; Gallup and Sachs (2001) estimated that the economic impact of malaria (costs of health care, absenteeism, days lost in education, decreased productivity due to brain damage from cerebral malaria, and loss of investment and tourism) is estimated to cost Africa $ 12 billion[34] every year. The total cost (sum of direct and indirect costs) of controlling malaria only in Ghana for 2002 was US$ 50.05 million (Asante and Asenso-Okyere, 2003); the direct cost of treatment and prevention (by households and health services) was US$ 26.16 million – represented 52% of the total cost, while the indirect cost in the form of workdays lost to the illness (malaria morbidity and mortality) was US$ 23.89 million – represented 48% of the total cost.

Malaria is also a major cause of health-related absenteeism from school in endemic countries affecting intellectual development; malaria in Uganda impairs as much as 60% of children's learning and cognitive ability affecting primary and secondary education programs (Ministry of Health, 2014). Moreover, malaria negatively affects a country's productivity due to time lost by sick adults and carers of sick children. Cropper *et al.* (2000) found that sick adults in Ethiopia lost up to 21 days per malaria episode, while the time adults lost from caring for sick children was up to 12 days off work (per episode).

Greece was the most malarial country in Europe in the early 1930s with vectors *Anopheles elutus*, *Anopheles maculipennis* and *Anopheles superpictus*; over a million cases (of a population of 6 or 7 millions) of malaria and 5,000 deaths per year (Vine, 1948). Malaria-control efforts in Greece began in 1944 with the introduction of the insecticide "4-4′dichloro-diphenyl-drichloroethane" (DDT), while Government raised its budgetary figure for malaria control from some £ 60,000 to £ 300,000 in 1946 (Vine, 1948). Today, spending on malaria control commodities (ACTs, ITNs, insecticides and spraying equipment for IRS, and RDTs) is estimated to have increased over the past 11 years, from US$ 40 million in 2004 to US$ 1.6 billion in 2014, globally (WHO, 2015).

[33] Children under five are particularly susceptible to malaria death; in 2015 malaria killed an estimated 306,000 (range: 219,000 – 421,000) under-fives globally, including 292,000 children in the African Region (WHO, 2015).
[34] The average cost of management alone since 2000 is estimated to be US$ 300 million annually (WHO, 2015).

Global financing for malaria control increased from an estimated US$ 960 million in 2005 to US$ 2.5 billion in 2014; international funding for malaria control in 2014 was estimated at US$ 1.9 billion, while domestic funding for National Malaria Control Programs (NMCPs) was estimated at US$ 550 million (WHO, 2015).

Dengue

Dengue is the most rapidly spreading mosquito-borne viral disease globally, having significant socio-economic impacts in endemic countries. The disease is now endemic in more than 100 countries[35] in the WHO regions of Africa, the Americas, the Eastern Mediterranean, South-East Asia and the Western Pacific and is becoming more severe over the years; the Americas, South-East Asia and Western Pacific regions are the most seriously affected (WHO, 2016a). Dengue cases worldwide have increased dramatically in recent decades; in three WHO regions the number of dengue cases reported has increased from 2.2 million in 2010 to 3.2 million in 2015 (WHO, 2016a). There are about 390 million (range: 284 – 528 million) dengue infections (Bhatt *et al*., 2013) and 22,000 dengue deaths (Guzman and Isturiz, 2010) globally (per year). Large dengue outbreaks occurred globally the year 2015; 169,000 cases in Philippines, over 111,000 cases in Malaysia, over 1.5 million cases in Brazil (approximately 3 times higher than in 2014), over 15,000 cases in Delhi, India (the worst outbreak since 2006) (WHO, 2016a).

In the Americas alone 2.35 million dengue cases were reported in 2015 (WHO, 2016a); Shepard *et al*. (2011) estimated that the total economic cost of dengue illness in the Americas is US$ 2.1 billion per year. Later, Shepard *et al.* (2013) estimated the annual economic and disease burden of dengue illness in 12 countries in Southeast Asia (Cambodia, Malaysia, Thailand, Singapore, Viet Nam, Myanmar, Bhutan, Brunei, East Timor, Indonesia, Laos, and Philippines) over the decade of 2001 – 2010; the annual dengue-illness cost was US$ 950 million[36] – ranged from US$ 610 million to US$ 1,384 million – with an annual average of 2.9 million dengue episodes and 5,906 deaths. About 52% of the total economic costs resulted from productivity lost (indirect costs) including non-fatal and fatal cases; the average annual direct costs amounted to US$ 451 million – ranged from US$ 289 million to US$ 716 million – and the indirect costs were US$ 499 million – ranged from US$ 290 million to US$ 688 million.

[35] Brady *et al*. (2012) estimated that 3.9 billion people, in 128 countries, are at risk of infection with dengue.
[36] The annual dengue-illness costs in each of the twelve countries were: US$ 16.5 million in Cambodia, US$ 128 million in Malaysia, US$ 290 million in Thailand, US$ 67.1 million in Singapore, US$ 23.5 million in Viet Nam, US$ 14.5 million in Myanmar, US$ 295 million in Bhutan, US$ 636 million in Brunei, US$ 363 million in East Timor, US$ 323.2 million in Indonesia, US$ 5.1 million in Laos, and US$ 81 million in Philippines (Shepard *et al.,* 2013).

Table 1 Burden of vector-borne diseases (Malaria and Dengue) in different regions globally.

Infections	Absenteeism	Economic Cost
Malaria: 97 endemic countries – 3.4 billion people at risk (WHO, 2014)		
Worldwide: 214 million cases and 438,000 (WHO, 2015) Greece (early 1930s): over 1 million cases and 5,000 deaths (Vine, 1948)	Uganda: affects 60% of children's learning and cognitive ability (Ministry of Health, 2014) Ethiopia: sick adults – 21 days lost; carers of sick children – 12 days lost (off work per episode) (Cropper *et al*., 2000)	Africa: US$ 12 billion (Gallup and Sachs, 2001) Ghana (2002): US$ 50.05 million (Asante and Asenso-Okyere, 2003) Africa (since 2000): US$ 300 million – management cost; Global financing (2014): US$ 2.5 billion; International funding (2014): US$ 1.9 billion; Domestic funding for NMCPs (2014): US$ 550 million (WHO, 2015) Worldwide (2014): US$ 1.6 billion for control commodities (WHO, 2015) Greece (1946): £ 300,000 for vector control (Vine, 1948)
Dengue: 128 endemic countries – 3.9 billion people at risk (Brady *et al*., 2012)		
Worldwide: 390 million cases (Bhatt *et al*., 2013) and 22,000 deaths (Guzman and Isturiz, 2010) Southeast Asia (2001 – 2010): 2.9 million cases and 5,906 deaths (Shepard *et al*., 2013) In 2015: 2.35 million cases in the Americas, 169,000 cases in Philippines, over 111,000 cases in Malaysia, over 1.5 million cases in Brazil, over 15,000 cases in Delhi, India (WHO, 2016)	Surat, India (June – December 2006): patient and their caretakers – 50 days lost (per household) (Bhavsar *et al*., 2010) Cambodia: sick children – 6.6 days off school; sick adults – 14.2 days off work and 2.6 days off other activities (Suaya *et al*., 2010) Puerto Rico (2002 – 2010): patient and their caretakers – 30.5 days lost (per episode) (Halasa *et al*., 2012) 8 American and Asian countries: sick children – 5.6 days off school; sick adults – 9.9 days off work (per episode) (Suaya *et al*., 2009)	The Americas: US$ 2.1 billion (Shepard *et al*., 2011) 12 countries in Southeast Asia (2001 – 2010): US$ 950 million (Shepard *et al*., 2013) Puerto Rico (2002 – 2010): $ 46.4 million (Halasa *et al*. 2012) 8 countries in the Americas and Asia (2005 – 2006): Health sector cost – US$ 440 million (Suaya *et al*., 2009)

Halasa *et al*. (2012) estimated the annual average economic cost of dengue cases in Puerto Rico during the period 2002 – 2010; the annual cost averaged $ 38.7 million, while combining this with costs associated with dengue surveillance and vector control activities increased the total economic cost of dengue illness to $ 46.4 million. Finally, Suaya *et al.* (2009) estimated the health sector cost of dengue in eight countries (five in the Americas – Brazil, El Salvador, Guatemala, Panama, Venezuela – and three in Asia – Cambodia, Malaysia, Thailand) in 2005 – 2006; an average dengue episode represented 14.8 lost days for ambulatory patients and 18.9 days for hospitalized patients giving a cost of US$ 440 million.

Moreover, dengue prevention through vector control activities has significant economic impacts. Brazil in 1997 budgeted US$ 0.6 billion for vector control (Pérez-Guerra *et al*., 2010). Pérez-Guerra *et al*. (2010) estimated the economic cost of dengue prevention through vector control activities in Puerto Rico for the years 2002 to 2007. The cost of dengue vector control in the public sector was US$ 46.22 million; the Puerto Rico Department of Health spent an average US$ 1.29 million per year, while 12 municipalities spent on average US$ 6.41 million per year. The average economic cost of dengue illness in Singapore from 2000 to 2009 ranged between $ 0.85 billion and $ 1.15 billion, of which control costs constitute 42% – 59% (Carrasco *et al*., 2011). Finally, several studies have shown that dengue illness is one of the leading causes of health-related absenteeism from school, work, and other activities. Bhavsar *et al*. (2010) estimated the indirect costs of dengue illness in Surat, India, during the 2006 dengue season (June 2006 – December 2006) by analyzing a total of 40 patients; an average of 50 days were lost from school[37], work, and other activities by the patient and their caretakers in a household. Suaya *et al*. (2010) estimated the socioeconomic impact of hospitalized dengue in Cambodia; on average, a hospitalized dengue episode, resulted in a loss of 23.4 days[38] (including both patient and other household members). In Puerto Rico, for the years 2002 – 2010, the average days of a patient's school and work absenteeism were 7.2 days per dengue episode, while time lost because of caregiving raised the number of affected days to 30.5 days (Halasa *et al.*, 2012). Suaya *et al*. (2009) estimated the indirect costs of dengue cases in eight American and Asian countries; students lost 5.6 days of school, while those working lost 9.9 work days (per average dengue episode).

[37] The mean days of total school absence in all household members were 11.4 days (Bhavsar *et al*., 2010).
[38] Of these days, an average of 6.6 days corresponded to school absenteeism, 14.2 days to work lost and 2.6 to other days lost (Suaya *et al*., 2010).

Yellow Fever and Zika Virus

Yellow Fever originated in Africa (Carrington and Auguste, 2013), posing the greatest threat in 45 endemic countries (32 in Africa, 13 in Central and South America) with almost 900 million people at risk (WHO, 2010). Between 1980 and 2012, 150 yellow fever outbreaks in 26 African countries were reported to WHO (Garske *et al*., 2014). Despite vector control and vaccination programs, the number of yellow fever cases remains high during the past two decades. The burden of yellow fever in Africa for the years 1995, 2005, and 2013 were estimated to be: 1.5 (range: 1.1 – 2.2) million number of infections with 95,000 (range: 24,000 – 220,000) number of deaths, 1.8 (range: 1.2 – 2.5) million number of infections with 110,000 (range: 27,000 – 250,000) number of deaths, and 1.3 million (range: 850,000 – 1.8 million) number of infections with 78,000 (range: 19,000 – 180,000) number of deaths, respectively (Garske *et al*., 2014).

Table 2 Burden of vector-borne diseases (Yellow fever and Zika virus) in different regions globally.

Infections	Economic Cost
Yellow Fever: 45 endemic countries – 900 million people at risk (WHO, 2010)	
Africa: 1.5 million cases and 95,000 deaths in 1995; 1.8 million cases and 110,000 deaths in 2005; 1.3 million cases and 78,000 deaths in 2013 (Garske *et al*., 2014)	Kenya (1992 – 1994): US$ 104 million – indirect cost (Marine Medical Systems, 1997) Angola (2016): US$ 24.3 million for WHO's work in Angola and DRC (WHO, 2016c)
Zika Virus: 67 endemic countries (WHO, 2016e) – 93.4 million people at risk in the Americas (Perkins *et al*., 2016)	
Brazil: up to 1,500,000 cases (WHO, 2016d) Colombia: over 25,000 cases; Cape Verde: over 7,000 cases (WHO, 2016f)	Worldwide: US$ 8.9 billion (Pandey, 2016) Latin America and Caribbean: US$ 3.5 billion – impact of 2016 Zika outbreak (World Bank, 2016a) WHO strategic plan (2016 Zika outbreak): US$ 56 million (McCarthy, 2016) CDC response (2016 Zika oubreak): $ 194 million (Tavernise, 2016) Zika Strategic Plan (July 2016 – December 2017): US$ 122.1 million (WHO, 2016e)

Yellow fever outbreaks have significant economic impacts. The yellow fever outbreak in Kenya (1992 – 1993) led to an estimated loss of US$ 104 million due to poor publicity which resulted in 101,000 less British tourists to Kenya in 1992 – 1994 (Marine Medical Systems, 1997). Recently, a yellow

fever outbreak occurred in Angola. Since the first identified yellow fever case (late December 2015) in Luanda, it has spread to all the 18 provinces of Angola; cases of yellow fever have also been exported from Angola to the Democratic Republic of Congo (DRC), China and Kenya (WHO, 2016b). WHO and 54 partner organizations launched a joint Strategic Response Plan for yellow fever with a total budget of US$ 94.1 million for the activities of all partners involved in the response; of this, US$ 24.3 million is for WHO's work in Angola and DRC (WHO, 2016c).

Zika virus outbreaks were reported for the first time from the Pacific in 2007 and 2013 in Yap Island (Federated States of Micronesia) and French Polynesia, respectively (WHO, 2016d). The Zika virus has been spread to other countries ever since; it is now reported to be circulating in 26 countries and territories in Latin America and the Caribbean (McCarthy, 2016). Currently, there is an ongoing Zika virus epidemic in Latin America and the Caribbean; as of 12 February 2016, 39 countries have reported local circulation of Zika virus, and there is evidence of local transmission in six additional countries (WHO, 2016d). Perkins *et al.* (2016) estimated that 93.4 million (range: 81.6 – 117.1 million) people are at risk of infection with Zika virus in the Americas. From 2015 onwards Zika virus has expanded rapidly in 67 countries – mainly in the Americas Region but more recently spreading to Europe and countries in Africa, Asia and the Pacific (WHO, 2016e; WHO, 2016d). Today, the Brazilian national authorities estimate that up to 1,500,000 cases of Zika virus infection have occurred since the outbreak began (WHO, 2016d). According to WHO (2016f), after Brazil, Colombia has been the most-affected country, with over 25,000 suspected cases reported, while Cape Verde has reported more than 7,000 suspected cases of Zika virus.

The Zika virus has significant economic impact for the countries suffering from outbreaks. It has been estimated that the Zika virus cost the global economy a total of US$ 8.9 billion (Pandey, 2016). The World Bank (2016) estimated the short-term economic impact of the Zika Virus epidemic for 2016 in the Latin American and the Caribbean region to be a total of US$ 3.5 billion. Further, World Bank (2016) estimated that health care for infants infected with Zika virus over their lifetimes will exceed hundreds of billions of dollars. On February 16, 2016 the World Health Organization released a report outlining a US$ 56 million[39] strategic plan to respond to the ongoing outbreaks of Zika virus disease in the Americas (McCarthy, 2016). Moreover, the US Centers for Disease Control and Prevention, by August 30, 2016, had spent $ 194 million to respond to the Zika outbreak in Latin America and Caribbean (Tavernise, 2016). Currently, WHO/Pan American Health Organization (PAHO) and

[39] 7.1 million for surveillance, 15.4 million for community engagement and risk communication, 6.4 million for vector control and personal protection, 14.2 million for care for those affected, 6.4 million for research, and 6.1 million for coordination (conducted by partners across sectors and services at the global, regional, and national levels) (WHO, 2016d).

partners have set out a strategic response to Zika that focuses on preventing and managing medical complications caused by Zika virus infection WHO (2016e); a total of US$ 122.1 million is necessary to effectively apply the Zika Strategic Response Plan (July 2016 – December 2017).

Overall, we observe that despite all efforts, vector-borne diseases often burst into outbreaks causing devastating socioeconomic breakdowns. Hence, more research on mosquito outbreaks needs to be done to find better ways to predict and control them, in order to reduce the considerable health and economic burdens they inflict.

Chapter 3

Infectious Disease Transmission and Serial Interval

Mathematical models have been widely used from epidemiologists over the years to predict epidemics of infectious diseases. They have been used to develop a basic understanding of the relevant epidemiological patterns as well as to quantify the likely effects of different intervention strategies (policy development) (Hethcote and Yorke, 1984). The spread of an infection within a population divides the population into three disjoint groups (Kermack and McKendrick, 1927): (i) susceptible individuals; *i.e.* they contract the disease and become infective, (ii) infective individuals; *i.e.* they transmit the disease to others, (iii) removed individuals; *i.e.* they had the disease and are dead/permanently immune/isolated. This type of epidemic models with recovering and permanently immunity are known as SIR models. In case of infections that do not confer protective immunity, individuals become susceptible to the disease again as soon as they recover from the infection; this type of models are known as SIS models (Boccara, 2010). In this case there are no removed individuals. The SIS models have been widely used to describe sexually transmitted diseases (Hethcote and Yorke, 1984).

Continuous-time epidemic models have been widely used over the years in the investigation of the transmission of infectious diseases due to their mathematical tractability. Méndez and Fort (2000) studied a discrete deterministic epidemic model taking into account an incubation period. They showed how small outbreaks of the disease may be catastrophic to the population after the first evolution of the epidemic. Enatsu *et al.* (2012) proposed a discrete-time version of an SIS epidemic continuous-time model with immigration of infectives, using the backward Euler method. Applying Lyapunov function techniques they established the global asymptotic stability of the disease-free and the endemic equilibrium. Li *et al.* (2008) established SI and SIS epidemic models with vital dynamics corresponding to the case that the infectives can recover from a disease or not. They showed that their behavior is the same as their corresponding continuous ones; below a threshold the disease dies out, while above the threshold the disease becomes endemic.

However, discrete-time SIS epidemic models sometimes are capable of generating complex dynamics such as period-doubling and chaotic behavior, in contrast with continuous-time epidemic models. Allen (1994) considered discrete-time models of some well-known SI, SIR and SIS models and found that the discrete-time SI and SIR models have similar dynamical behavior with their continuous

analogues. However, for the SIS discrete-time model found that for some parameter values can exhibit period-doubling and chaotic behavior. Castillo-Chavez and Yakubu (2001) studied the role of various types of reproductive or recruitment regimes including contest and scramble competition on disease dynamics in a discrete-time SIS epidemic model. Another important aspect of modeling epidemics is the formulation of the incidence function. Li *et al.* (2010) discretized a continuous-time epidemic model with nonlinear incidence rate applying Euler scheme. Using qualitative analysis and numerical simulations they showed that the discrete-time model can result in a much richer set of patterns than the corresponding continuous-time model.

3.1 A Gonorrhea Transmission Model: Time Interval between Successive Clinical Cases[40]

3.1.1 The organism *Neisseria gonorrhoeae*

Gonorrhea is one of the oldest known human illnesses. The organism *Neisseria gonorrhoeae* was first described by Neisser in 1879 and cultivated in 1982 (Marrazzo *et al.*, 2010). Neisseria gonorrhoeae causes an estimated 62 million cases of gonorrhea worldwide each year (Gerbase *et al.*, 1998). Gonorrhea is the second most commonly-reported notifiable disease in the United States. Approximately 700,000 new cases of gonorrhea occur in the United States each year (Weinstock *et al.*, 2004). Furthermore, the financial impact of gonorrhea is high. Only the direct medical cost for gonorrhea treatment in the Unites States is estimated at $ 1,051,000,000 annually (Centers for Disease Control and Prevention, 2000).

Infections due to Neisseria gonorrhoeae are a major cause of Pelvic Inflammatory Disease (PID) in the United States. PID can lead to serious outcomes in women such as tubal infertility, ectopic pregnancy, and chronic pelvic pain. In addition epidemiologic and biologic studies provide strong evidence that gonococcal infections facilitate the transmission of HIV infection (Fleming and Wasserheit, 1999). In men gonorrhea can cause a painful condition called epididymitis in the tubes attached to the testicles (Berger *et al.*, 1979). Further, if left untreated, gonorrhea can also spread to the blood and cause Disseminated Gonococcal Infection (DGI), a condition that can be life threatening. DGI is usually characterized by arthritis, tenosynovitis, and/or dermatitis (Holmes *et al.*, 1971). Moreover, the organism Neisseria gonorrhoeae has the ability to develop resistance against all clinically useful

[40] This section is based on the publication "Bifurcations and chaos in discrete-time gonorrhea model" (Gkana, A., Zachilas, L.: 2015b, Bifurcations and chaos in discrete-time gonorrhea model, *Chaotic Modeling and Simulation* **1**, 51-64.).

antibiotics. William Smith (2010) suggests that we are on the verge of a highly untreatable gonorrhea epidemic. Although gonorrhea was easily cured with antibiotics years ago, however bacteria develop resistance to treatments.

Furthermore, the World Health Organization (WHO) recently put out an alert with regards to the reported cases of resistance to cephalosporin antibiotics – the last treatment option against gonorrhea – in several countries including Australia, France, Japan, Norway, Sweden and the United Kingdom (WHO, 2012). According to Dr. Manjula Lusti-Narasimhan from the Department of Reproductive Health and Research at WHO, gonorrhea is becoming a major public health challenge due to the high incidence of infections accompanied by dwindling treatment options. And after the failure from this last effective treatment, as there are no new therapeutic drugs in development, if gonococcal infections become untreatable the health implications will be significant.

The first gonorrhea model, an integral equation model with time delays representing variation in the infectious period, was formulated by Cooke and Yorke (1973). They investigated the solutions' behavior for a single homogeneous population. Reynolds and Chan (1974) studied a linear differential equation model for gonorrhea. They estimated the parameters and projected the prevalence for males and females, both with and without terms modeling control procedures. The drawback of this model is that, due to linearity, the prevalence can grow exponentially without saturating the populations. Bailey (1975) showed how Susceptible-Infected-Susceptible (SIS) models developed for other diseases can be used for gonorrhea.

Lajmanovich and Yorke (1976) formulated and investigated the asymptotic stability properties of a gonorrhea model with an arbitrary number of interesting groups. Aronsson and Mellander (1980) modified Lajmanovich and Yorke model including seasonal variation in the contact and removal rates. They showed that in the endemic case there is a nontrivial solution which is global asymptotically stable. Nallaswamy and Shukla (1982) modified Lajmanovich and Yorke model including spatial diffusion and analyzed the stability of the endemic equilibrium state. Thieme (1982) modified Lajmanovich and Yorke model assuming short periods of incubation or immunity and showed that the same global stability results still hold for this case. Finally, Hirsch (1984) investigated the global stability of a more general version of Lajmanovich and Yorke model.

Moreover, Hethcote and Yorke (1984) monograph is an excellent work in the context of gonorrhea transmission dynamics and control. They used nonlinear differential equations to model the transmission dynamics of gonorrhea in a heterosexually-active population with two distinct levels of sexual activity. Mushayabasa (2012) formulated a deterministic model of non-linear differential

equations in order to analyze the epidemiological consequences of chlamydia and gonorrhea co-infection. In this section we study a discrete-time version of Hethcote and Yorke (1984) gonorrhea model using discrete time steps based on the duration of the serial interval of gonorrhea infection. In Subsection 3.1.2 we present the basic continuous-time gonorrhea model (Hethcote and Yorke, 1984) and in Subsection 3.1.3 we discretize their model. The local stability properties of the fixed points of our discrete-time gonorrhea model are investigated in Subsection 3.1.4, while in Subsection 3.1.5 we use various numerical simulation tools to study the complex dynamics of our system. In Subsection 3.1.6 we proceed to chaos control applying the G.M. method (Güémez and Matias, 1993) in order to obtain regular behavior. Finally (Subsection 3.1.7), we conclude with some remarks and discussion about the consequences of our results.

3.1.2 The basic gonorrhea model

Any gonorrhea model must incorporate the following three characteristics due to three strictly epidemiological characteristics of the disease: (a) it cannot include a removed class since recovery from gonorrhea does not give permanent immunity[41], so that individuals that are cured are immediately susceptible to the disease again; (b) it is not necessary to include an exposed class (E) due to the short[42] latent period of gonorrhea; (c) constant parameter values should be incorporated since gonorrhea incidence do not vary seasonally[43]. As a result, any gonorrhea model considers only susceptible and infective individuals.

Hethcote and Yorke (1984) studied a continuous-time dynamical system for the spread of gonorrhea. They divided population into two groups, *females at risk* $\left(N_f\right)$ and *males at risk* $\left(N_m\right)$; and each group into two subgroups, *susceptible females* $\left(N_f S_f\right)$ & and *infective females* $\left(N_f I_f\right)$ and *susceptible males* $\left(N_m S_m\right)$ & *infective males* $\left(N_m I_m\right)$.

They modeled the dynamics of the spread of gonorrhea by the 4-dimensional system:

[41] Gonococcal infection does not confer protective immunity, and this particular characteristic is what makes gonorrhea very different from other diseases such as measles, mumps, rubella, chickenpox, poliomyelitis, diphtheria, whooping cough, and tetanus (Hethcote and Yorke, 1984).
[42] Individuals who acquire gonorrhea become infectious within a day or two, so that the latent period is very short compared to the latent period of about 12 days for measles, 15 days for chickenpox, and 18 days for mumps (Hethcote and Yorke, 1984).
[43] The seasonal oscillations in gonorrhea incidence are very small (less than 10%). In contrast, the incidences of diseases such as influenza, measles, mumps and chickenpox often vary seasonally by factors of 5 to 50 or more (Hethcote and Yorke, 1984).

$$
\begin{aligned}
N_f \dot{S}_f &= -\lambda_f \cdot S_f \cdot N_m I_m + N_f I_f / d_f \\
N_f \dot{I}_f &= \lambda_f \cdot S_f \cdot N_m I_m - N_f I_f / d_f \\
N_m \dot{S}_m &= -\lambda_m \cdot S_m \cdot N_f I_f + N_m I_m / d_m \\
N_m \dot{I}_m &= \lambda_m \cdot S_m \cdot N_f I_f - N_m I_m / d_m
\end{aligned}
\tag{13}
$$

The sexually active population N_f and N_m is constant and equals the number of susceptible plus the number of infective individuals ($N_f = S_f + I_f$ and $N_m = S_m + I_m$); λ_f and λ_m indicate the transmission rate of infection of susceptible females and males respectively; d_f and d_m indicate the average duration of infection for females and males respectively.

Since the population is constant, the system (Equation (13)) reduces to the 2-dimensional dynamical system:

$$
\begin{cases}
\dfrac{dI_f}{dt} = \dfrac{\lambda_f}{r}\left(1 - I_f\right) I_m - \dfrac{I_f}{d_f} \\
\dfrac{dI_m}{dt} = r\lambda_m \left(1 - I_m\right) I_f - \dfrac{I_m}{d_m}
\end{cases}
\tag{14}
$$

where, $S_f = 1 - I_f$ and $S_m = 1 - I_m$ since the total population size remains constant and $r = N_f / N_m$.

The limiting system (Equation (14)) has 2 equilibrium points, a trivial and a nontrivial:

$$\left(I_f^*, I_m^*\right) = (0,0)$$

$$\left(I_f^*, I_m^*\right) = \left(\frac{\lambda_f \lambda_m d_f d_m - 1}{\lambda_m d_m r + \lambda_f \lambda_m d_f d_m}, \frac{\left(\lambda_f \lambda_m d_f d_m - 1\right) r}{\lambda_f \lambda_m d_f d_m r + \lambda_f d_f} \right)$$

If the trivial equilibrium point exists it is asymptotically stable and gonorrhea dies out. If the trivial equilibrium point does not exist, then the nontrivial equilibrium point is asymptotically stable and gonorrhea remains endemic.

3.1.3 Modification of the basic model by taking into account the *serial interval*

Once again, we use the Euler's algorithm (Subsection 1.1.1) to discretize the Hethcote and Yorke (1984) model; we discretize the differential equations of the basic dynamical system (Equation (14)) by replacing $dI_f / dt, dI_m / dt$ with the difference quotients $\left(I_{n+1}^f - I_n^f\right)/\delta$, $\left(I_{n+1}^m - I_n^m\right)/\delta$. Time is

measured in generations and we obtain a deterministic discrete-time gonorrhea model defined by the 2D map as follows:

$$\begin{cases} I_{n+1}^{f} = I_{n}^{f} + \delta\left(\dfrac{\lambda_f}{r}\left(1-I_{n}^{f}\right)I_{n}^{m} - \dfrac{I_{n}^{f}}{d_f}\right) \\ I_{n+1}^{m} = I_{n}^{m} + \delta\left(r\lambda_m\left(1-I_{n}^{m}\right)I_{n}^{f} - \dfrac{I_{n}^{m}}{d_m}\right) \end{cases} \tag{15}$$

δ is the length of each discrete-time step where the number of infective individuals grow by the addition of the newly infective individuals; I_n^f, I_n^m is the number of infective females and males in one time step; I_{n+1}^f, I_{n+1}^m is the number of infective females and males at the next time step; the infection rates of susceptible males and females $\left(\lambda_f, \lambda_m\right)$ indicate the average number of individuals with whom an infectious individual makes adequate contact[44] during a unit time interval (Hethcote, 1976; Allen *et al.*, 1991). The discrete time step δ corresponds to the generation time of gonorrhea, that is, the time from the moment one person becomes infected until that person infects another person (Scalia *et al.*, 2010). This time interval is well-known as the *serial interval*[45]; *i.e.* the time period between successive clinical cases (Fine, 2003).

3.1.4 *Fold* and *Flip* bifurcations

The map (Equation (15)) has the following two fixed points, which are the same as the equilibrium points of the analogous continuous model (Equation (14)), a disease-free equilibrium E_1 and an endemic equilibrium E_2:

$$E_1 : \left(I_f^*, I_m^*\right) = (0,0)$$

$$E_2 : \left(I_f^*, I_m^*\right) = \left(\frac{\lambda_f\lambda_m d_f d_m - 1}{\lambda_m d_m r + \lambda_f\lambda_m d_f d_m}, \frac{\left(\lambda_f\lambda_m d_f d_m - 1\right)r}{\lambda_f\lambda_m d_f d_m r + \lambda_f d_f}\right)$$

The Jacobian matrix at any point $\left(I_n^f, I_n^m\right)$ is:

[44] Adequate contact is a direct or indirect contact that is sufficient for transmission of infection if the individual contacted is susceptible. The concept of a sufficient contact is necessary since transmission of infection sometimes does not occur during sexual intercourse between an infective and a susceptible (Hethcote and Yorke, 1984).

[45] The serial interval is important in the interpretation of infectious disease surveillance and trend data, in the identification of outbreaks, and in the optimization of quarantine and contact tracing (Fine, 2003).

$$J\left(I_n^f, I_n^m\right)=\begin{pmatrix}\frac{\partial I_{n+1}^f}{\partial I_n^f} & \frac{\partial I_{n+1}^f}{\partial I_n^m}\\ \frac{\partial I_{n+1}^m}{\partial I_n^f} & \frac{\partial I_{n+1}^m}{\partial I_n^m}\end{pmatrix}=\begin{pmatrix}\delta\left(-\frac{\lambda_f I_n^m}{r}-\frac{1}{d_f}\right)+1 & \frac{\lambda_f\delta\left(1-I_n^f\right)}{r}\\ \lambda_m\delta r\left(1-I_n^m\right) & \delta\left(-\lambda_m r I_n^f-\frac{1}{d_m}\right)+1\end{pmatrix}$$

The determinant of the Jacobian matrix is:

$$detJ=\left(\delta\left(-\lambda_m r I_n^f-\frac{1}{d_m}\right)+1\right)\cdot\left(\delta\left(-\frac{\lambda_f I_n^m}{r}-\frac{1}{d_f}\right)+1\right)-\lambda_f\lambda_m\delta^2\left(1-I_n^f\right)\left(1-I_n^m\right)$$

Once again, in order to study the local behavior around each of the two fixed points we calculate the Jacobian matrix at E_1, E_2:

$$J\left(I_f^*, I_m^*\right)=\begin{pmatrix}\frac{\partial I_{n+1}^f\left(I_f^*, I_m^*\right)}{\partial I_n^f} & \frac{\partial I_{n+1}^f\left(I_f^*, I_m^*\right)}{\partial I_n^m}\\ \frac{\partial I_{n+1}^m\left(I_f^*, I_m^*\right)}{\partial I_n^f} & \frac{\partial I_{n+1}^m\left(I_f^*, I_m^*\right)}{\partial I_n^m}\end{pmatrix}$$

Calculating the determinant and the trace of the Jacobian, each fixed point is asymptotically stable if $\left|trJ\right|<1+detJ<2$ (Equation (3)).

Local stability of the disease-free fixed point

The Jacobian matrix at $E_1:\left(I_f^*, I_m^*\right)=\left(0,0\right)$ is:

$$J\left(E_1\right)=\begin{pmatrix}1-\frac{\delta}{d_f} & \frac{\lambda_f\delta}{r}\\ \lambda_m\delta r & 1-\frac{\delta}{d_m}\end{pmatrix}$$

with eigenvalues

$$\lambda_1=-\frac{\sqrt{\left(4\lambda_f\lambda_m d_f^2+1\right)d_m^2-2d_f d_m+d_f^2}\,\delta+\left(d_m+d_f\right)\delta-2d_f d_m}{2d_f d_m}$$

$$\lambda_2=\frac{\sqrt{\left(4\lambda_f\lambda_m d_f^2+1\right)d_m^2-2d_f d_m+d_f^2}\,\delta+\left(-d_m-d_f\right)\delta+2d_f d_m}{2d_f d_m}$$

determinant $detJ\left(E_1\right)=\left(1-\frac{\delta}{d_f}\right)\cdot\left(1-\frac{\delta}{d_m}\right)-\lambda_f\lambda_m\delta^2$ and trace $trJ\left(E_1\right)=-\frac{\delta}{d_m}-\frac{\delta}{d_f}+2$.

Using the three stability conditions (Equation (3)) and let $F_1=\frac{\left(\delta-2d_f\right)\left(\delta-2d_m\right)}{\lambda_m d_f d_m \delta^2}$ and $F_2=\frac{\sqrt{\left(4\lambda_f\lambda_m d_f^2+1\right)d_m^2-2d_f d_m+d_f^2}-d_m-d_f}{\lambda_f\lambda_m d_f d_m-1}$:

1. If $\lambda_f<\frac{1}{\lambda_m d_f d_m}$ the trivial fixed point E_1 is a *stable node*; both eigenvalues lie inside the unit circle $\left(|\lambda_1|<1,\lambda_2<1\right)$.
2. If $\frac{1}{\lambda_m d_f d_m}<\lambda_f<F_1$ and $\delta<F_2$ the trivial fixed point E_1 is a *saddle*; one eigenvalue lies outside the unit circle and the other inside $\left(|\lambda_1|<1,\lambda_2>1\right)$.
3. If $\lambda_f>F_1$ and $\delta>F_2$ the trivial fixed point E_1 is an *unstable node*; both eigenvalues lie outside the unit circle $\left(|\lambda_1|>1,\lambda_2>1\right)$.
4. If $\lambda_f=\frac{1}{\lambda_m d_f d_m}$ the trivial fixed point E_1 is *non-hyperbolic* $\left(\lambda_1=1\right)$; this parameter value is associated with the stability condition $trJ=1+detJ$ (Equation (3)) and a real eigenvalue crossing the unit circle at +1. So this is a bifurcation point at which the system undergoes a *Fold bifurcation* at E_1.

Local stability of the endemic fixed point

The Jacobian matrix at $E_2:\left(I_f^*,I_m^*\right)=\left(\frac{\lambda_f\lambda_m d_f d_m-1}{\lambda_m d_m\left(r+\lambda_f d_f\right)},\frac{\left(\lambda_f\lambda_m d_f d_m-1\right)r}{\lambda_f d_f\left(\lambda_m d_m r+1\right)}\right)$ is:

$$J\left(E_2\right)=\begin{pmatrix}\delta\left(-\frac{\lambda_m d_m\left(\lambda_f d_f-r\right)-2}{d_f\left(\lambda_m d_m r+1\right)}\right)+1 & \frac{\lambda_f\delta\left(\lambda_m d_m r+1\right)}{r\lambda_m d_m\left(r+\lambda_f d_f\right)}\\ \lambda_m\delta r\left(\frac{\lambda_f d_f+r}{\lambda_f d_f\left(\lambda_m d_m r+1\right)}\right) & \delta\left(\frac{\lambda_f d_f\left(1-\lambda_m d_m r\right)}{d_m\left(r+\lambda_f d_f\right)}\right)+1\end{pmatrix}$$

with determinant $detJ\left(E_2\right)=\left(1-\frac{\lambda_f d_f\left(\lambda_m d_m r+1\right)\delta}{d_m\left(r+\lambda_f d_f\right)}\right)\cdot\left(1-\frac{\lambda_m d_m\left(\lambda_f d_f+r\right)\delta}{d_f\left(\lambda_m d_m r+1\right)}\right)-\frac{\delta^2}{d_f d_m}$

and trace $trJ\left(E_2\right)=-\delta\left(\frac{\lambda_m d_m\left(\lambda_f d_f+r\right)}{d_f\left(\lambda_m d_m r+1\right)}+\frac{\lambda_f d_f\left(\lambda_m d_m r+1\right)}{d_m\left(r+\lambda_f d_f\right)}\right)+2$

Using the three stability conditions (Equation (3)) we obtain the following (see Appendix):

1. If $\begin{cases}\lambda_f<\frac{1}{\lambda_m d_f d_m}\\ \lambda_f>F_3\end{cases}$ and $F_4<\delta<F_5$ the nontrivial fixed point E_2 is a *saddle*; one eigenvalue lies outside the unit circle and the other inside $\begin{matrix}\left(\left|\lambda_1\right|<1,\lambda_2>1\right)\\ \left(\left|\lambda_1\right|>1,\left|\lambda_2\right|<1\right)\end{matrix}$.

2. If $\frac{1}{\lambda_m d_f d_m}<\lambda_f<F_3$ and $\delta<F_4$ the nontrivial fixed point E_2 is a *stable node*; both eigenvalues lie inside the unit circle $\left(\left|\lambda_1\right|<1,\left|\lambda_2\right|<1\right)$.

3. If $\delta>F_5$ the nontrivial fixed point E_2 is an *unstable node*; both eigenvalues lie outside the unit circle $\left(\left|\lambda_1\right|>1,\left|\lambda_2\right|>1\right)$.

4. If $\lambda_f=\frac{1}{\lambda_m d_f d_m}$ the nontrivial fixed point E_2 is *non-hyperbolic* $\left(\lambda_2=1\right)$; this parameter value is associated with the stability condition $trJ=1+detJ$ (Equation (3)) and a real eigenvalue crossing the unit circle at +1. So this is a bifurcation point at which the system undergoes a *Fold bifurcation* at E_2.

5. If $\lambda_f=F_3$ and $\delta=F_4$ the nontrivial fixed point E_2 is *non-hyperbolic* $\left(\lambda_1=-1\right)$; these parameter values are associated with the first stability condition $-trJ=1+detJ$ (Equation (3)) and one real eigenvalue crossing the unit circle at -1. Hence, these are bifurcation points at which the system undergoes a *Flip bifurcation* at E_2 with stable periodic two points bifurcating from the fixed point.

3.1.5 Gonorrhea outbreaks: Routes to chaos and strange attractor

Once again, a series of numerical simulations (Section 1.3) are introduced so that to illustrate the results of the analytical stability analysis (Subsection 3.1.4) and for finding some new qualitative dynamics of the discrete-time model (Equation (15)) as the parameters vary.

The rates of infection λ_m and λ_f should be different because transmission efficiency is gender dependent. The average probability of transmission of gonococcal infection during a single sexual exposure (a) from an infectious woman to a susceptible man in estimated to be about 0.2 – 0.3, while (b) from an infectious man to a susceptible woman is about 0.5 – 0.7 (Wiesner and Thompson, 1980). Hence, we use the following values for the rate of infection parameters: $\lambda_f = 0.6$ and $\lambda_m = 0.25$. However, the probability of transmission of gonococcal infection is increased for individuals who have ever had gonorrhea or other STI, for individuals who are street-involved youth, and for individuals having sex with many partners, with sex workers, or with a partner coming from a country where gonorrhea is frequent (Government of New Brunswick, 2010).

The average durations of infection d_m and d_f have also to be different because: (a) 90% of all the men who have gonococcal infection notice symptoms within a few days after exposure and promptly seek medical treatment, while (b) up to 75% of women with gonorrhea fail to have symptoms and remain untreated for some time (National Institute of Allergy and Infectious Diseases, 1980). In particular, when symptoms occur in men, they usually occur 3-5 days after sexual contact with an infected individual; while women who develop symptoms usually experience them within 10 days of sexual contact with an infected individual (Wisconsin Division of Public Health, 2015). So we fix the average duration of infection for females and males at $d_f = 10$ and $d_m = 3$ respectively.

Gonorrhea affects males and females almost equally[46]. So we assume that the number of males and females at risk $\left(N_m, N_f\right)$ is equal with ratio $r = 1$. We also assume that the initial number of infective individuals is the same both for males and females. Therefore we use for initial conditions the values $\left(I_0^f, I_0^m\right) = \left(0.5, 0.5\right)$.

Finally, in order to describe accurate the gonorrhea transmission dynamics, the size of the discrete time step should match the epidemiology of the disease (Trottier and Philippe, 2001); that is, whether the dynamic of infection is a matter of days or hours. The serial interval (*i.e.* the time period between successive clinical cases) is the average time between the observation of symptoms of gonorrhea in one person and the observation of symptoms in another person that has been infected from the first (Figure 18). Furthermore, the symptoms of gonorrhea usually appear two to five days after infection (*i.e.* incubation period) (Marrazzo *et al.*, 2010). Thus, since an infected individual remain infectious

[46] Global estimated incidence of gonorrhea, occurred in 1999, is 62.35 million infected people annually. Particularly gonorrhea affected 33.65 women and 28.70 men (WHO, 2001).

until he/she receives treatment, we assume that infections occur during the infectious period (Figure 18). Moreover, although a range of values for the serial interval is possible, the average serial interval can be estimated as: average incubation period + half the average infectious period, assuming that the maximum infectiousness occurs at the middle of the infectious period (Shil *et al.*, 2011). So the serial interval could be estimated by the incubation period. Therefore we define the length of the discrete time step between infection and subsequent transmission as $2 < \delta < 5$ days.

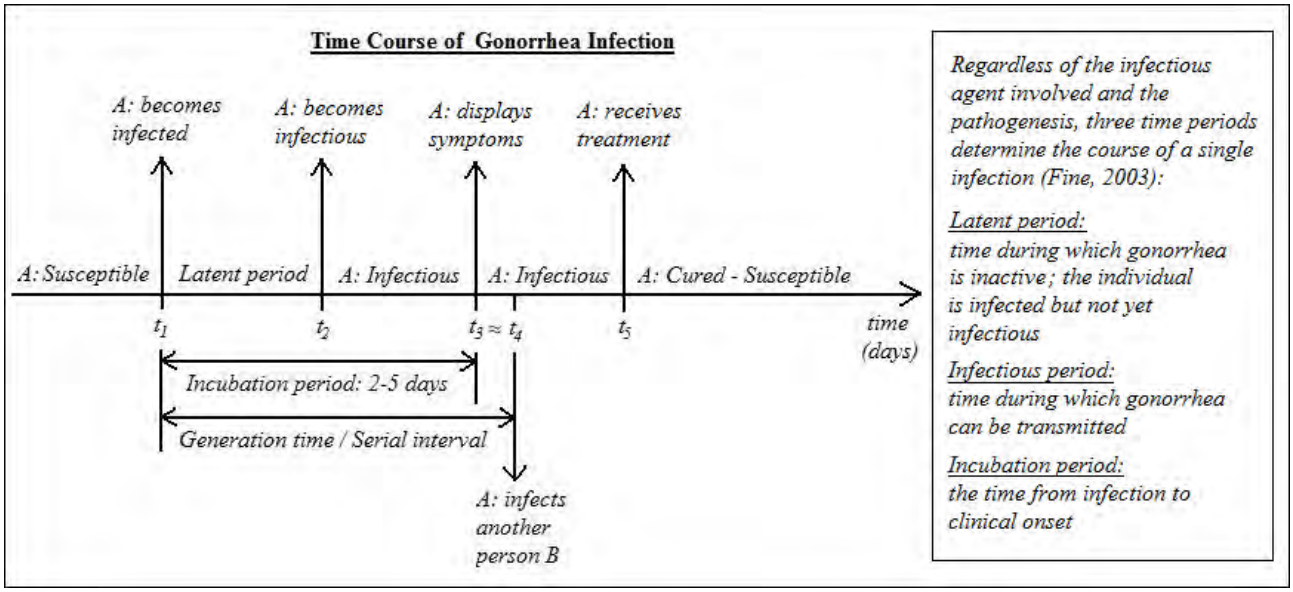

Figure 18 Time course of a single gonorrhea infection. Individual A becomes infected, transmits the infection to individual B and receives treatment.

Using these values for parameters we observe that the dynamics of the basic model (Equation (14)) alter significantly in discrete time for time interval length between successive clinical cases $(2 < \delta < 4)$ days, as the rate of infection of susceptible females increases (Figure 19).

- For small values of the infection rate parameter $(0 < \lambda_f < 0.4)$ the solutions converge either to a disease-free fixed point or to an endemic fixed point (light-blue area) for every value of time interval between clinical cases.
- For average values of the infection rate parameter $(0.4 < \lambda_f < 1.46)$ as λ_f increases the light-blue area is being replaced with the dark-blue area and the solutions converge to an attracting cycle of period 2. Moreover, for specific step size values $(2.25 < \delta < 3)$, further increase in the infection rate parameter λ_f gives rise to *non-periodic* behavior (white area).

- For large values of the infection rate parameter $\left(\lambda_f > 1.85\right)$ as the value of λ_f increases any periodic and non-periodic behavior is being replaced with divergence to infinity (black area). This abrupt behavior is not meaningful but it could be taken as some kind of catastrophe causing the extinction of the infected population.

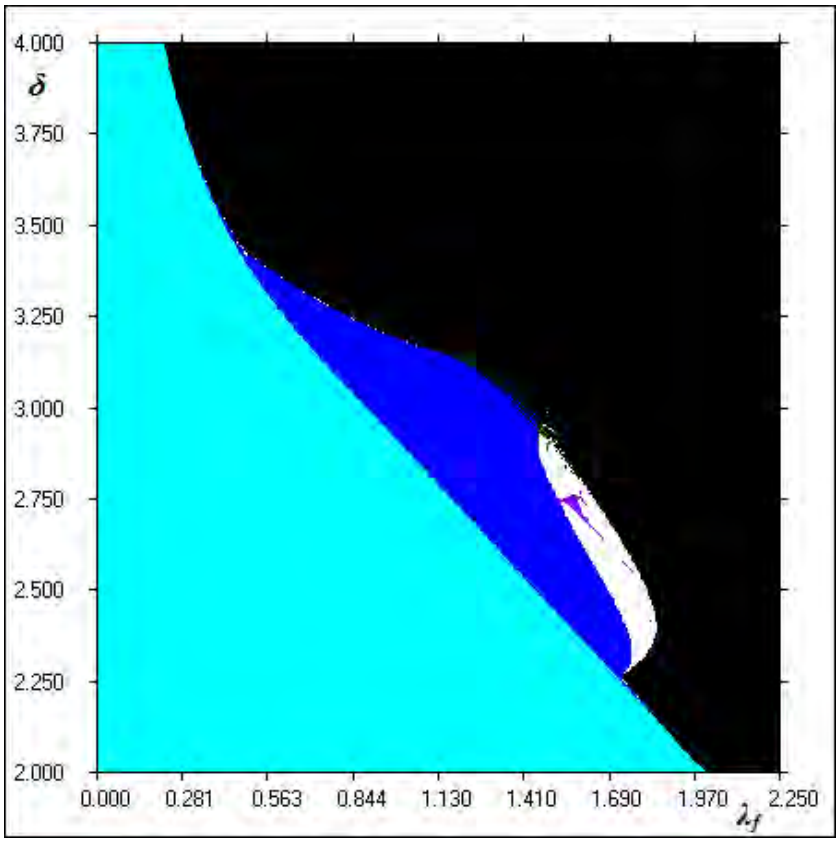

Figure 19 The basins of attraction diagram for the parameter values $\delta \in [2, 4]$ and $\lambda_f \in [0, 2.25]$.

Thus, for sufficiently low infection rate of susceptible females the behavior of solutions of the discrete-time model is qualitatively the same with the basic model. However, as the infection rate increases the discrete-time model exhibits the same behavior as the continuous-time model only for certain short time interval between successive clinical cases of gonorrhea $\left(\delta < 2.25\right)$.

Fixing the time period between clinical cases at the value $\delta = 2.65$ ($2 < \delta < 4$ days) and let the rate of infection of susceptible females parameter increasing in the interval $\lambda_f \in [0,1.59]$ we observe bifurcations occur in the system (Figure 20). The value $\lambda_f \approx 0.1333$ is a bifurcation point at which a *Fold bifurcation* occurs:

1. For exceptionally small values of the varying parameter $\left(\lambda_f < 0.1333\right)$ the disease-free fixed point $E_1 : (0,0)$ is locally asymptotically stable (*stable node*) and the endemic (negative) fixed point $E_2 : \left(I_f^*, I_m^*\right)$ is unstable (*saddle*). Some solutions converge to the attracting disease-free fixed point; there are no infective individuals and gonorrhea dies out. Hence, the initial infective population sizes $\left(I_0^f, I_0^m\right) = (0.5, 0.5)$ lead to the extinction of the disease due to the low probability of infection.

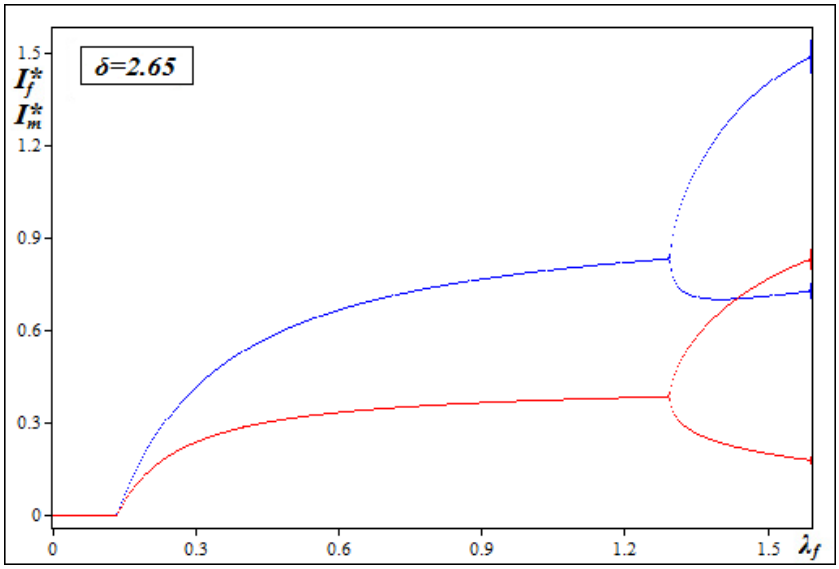

Figure 20 The bifurcation diagrams $\left(\lambda_f, I_f^*\right)$ and $\left(\lambda_f, I_m^*\right)$ for step size value δ = 2.65 as λ_f increases in the interval $\lambda_f \in [0, 1.59]$.

2. Near the value $\lambda_f \approx 0.1333$ both fixed points $E_1 : (0,0)$ and $E_2 : (-0.0001, -0.0001)$ undergo a *Fold bifurcation* and become non-hyperbolic with eigenvalues of the Jacobian matrix $\left(\lambda_1 = -0.1483, \lambda_2 = 0.9999 \approx +1\right)$ and $\left(\lambda_1 = -0.1483, \lambda_2 = 1.0001 \approx +1\right)$ respectively. Hence, for this critical value, the system has only one non-hyperbolic fixed point $E_1 \approx E_2 : (0,0)$.
3. For $0.1333 < \lambda_f < 1.1035$ the system has again two fixed points, the trivial and a non-trivial positive fixed point. The fixed points have exchange their stability, so that, the disease-free fixed point E_1 is now unstable (*saddle*) while the endemic fixed point E_2 is locally asymptotically stable (*stable node*). The initial infective population sizes $\left(I_0^f, I_0^m\right) = (0.5, 0.5)$ converge to the attracting endemic fixed point where both infected males and females are fixed in time. Moreover, the number of infective females is larger than the number of infective males $\left(I_f^* > I_m^*\right)$ likely due to the fact that the infection rate of females is larger than the infection rate of males $\left(\lambda_f > \lambda_m\right)$ and the duration of infection is

larger in females than in males $\left(d_f > d_m\right)$. As the parameter λ_f increases in this interval the number of infective individuals $\left(I_f^*, I_m^*\right)$ increases continuously and gonorrhea remains endemic.

Near the value $\lambda_f \approx 1.1035$ the saddle disease-free fixed point $E_1 : (0,0)$ becomes non-hyperbolic $\left(\lambda_1 = -0.9999, \lambda_2 = 1.8516\right)$ and for $\lambda_f > 1.1035$ it is an unstable node. The value $\lambda_f \approx 1.2961$ is a bifurcation point at which a *Flip bifurcation* occurs:

1. At $\lambda_f \approx 1.2961$ the endemic fixed point $E_2 : (0.8329, 0.3845)$ undergoes a *Flip bifurcation* and becomes non-hyperbolic with eigenvalues of the Jacobian matrix $\left(\lambda_1 = -0.9999 \approx -1, \lambda_2 = -0.0207\right)$.
2. For $1.2961 < \lambda_f < 1.59$ the endemic fixed point E_2 becomes unstable (*saddle*) and a stable cycle of period 2 appears in the system. Both infective males and females now converge to different 2-period cycles, while both periodic cycles become wider as the parameter increases at this particular interval.

For higher values of the rate of infection of susceptible females $\lambda_f \in [1.59, 1.72]$ we come across the phenomenon of *intermittency route to chaos* which according to Manneville and Pomeau (1980) is characterized by regular (laminar) phases alternating with irregular bursts. In particular, as the varying parameter increases the endemic fixed point remains unstable (saddle), while periodic behavior of high periods, cascades of period-doubling bifurcations and deterministic chaos appear eventually in both infected males and females (Figure 21).

- For $1.59 < \lambda_f < 1.6402$ the Lyapunov exponents vary among negative and exceptionally small positive values $\lambda_i^+ < 0.001$ and the behavior of solutions appears to be slightly chaotic.
- For $1.6402 < \lambda_f < 1.6544$ the map exhibits the familiar infinite sequence of period-doubling bifurcations $\left(32 \cdot 2^n\right)$: (32-period cycle, 64-period cycle, 128-period cycle, *etc.*) followed by chaotic oscillations where the Lyapunov exponents take higher positive values $\lambda_i^+ < 0.05$.
- At $\lambda_f \approx 1.6544$ a second series of period-doubling bifurcations $\left(10 \cdot 2^n\right)$: (10-period cycle, 20-period cycle, 40-period cycle, *etc.*) route to chaos once again, while the Lyapunov exponents at this parameter interval $\left(1.6544 < \lambda_f < 1.6763\right)$ vary among larger positive values $\lambda_i^+ < 0.1$.

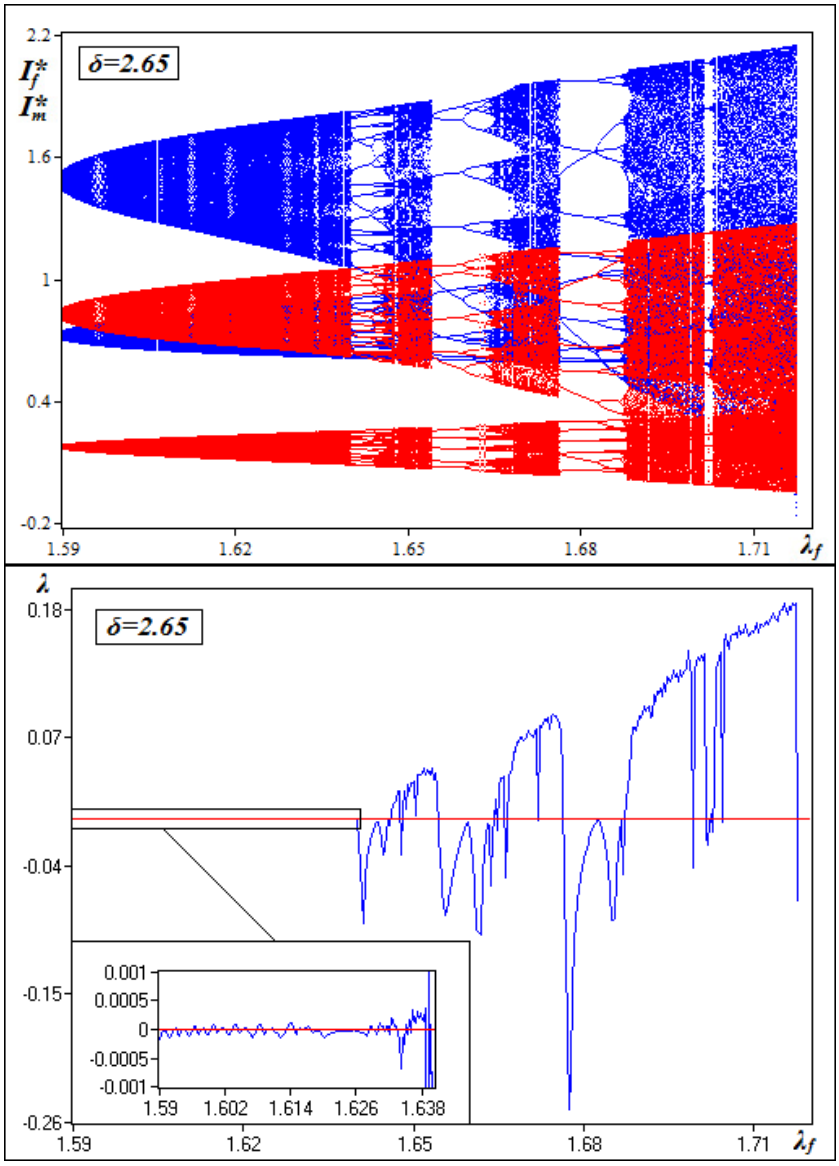

Figure 21 The bifurcation diagrams $\left(\lambda_f, I_f^*\right), \left(\lambda_f, I_m^*\right)$ and the Lyapunov exponent diagram $\left(\lambda_f, \lambda\right)$ as the varying parameter increases in the interval $\lambda_f \in [1.59, 1.72]$ for step size value $\delta = 2.65$.

- At $\lambda_f \approx 1.6763$ another series of period-doubling bifurcations $\left(12 \cdot 2^n\right)$: (12-period cycle, 24-period cycle, 48-period cycle, *etc.*) lead to even more chaotic behavior where the oscillations in the density of infected individuals can be hard to predict. The Lyapunov exponents take even larger positive values and reach the maximum value $\lambda_{\max} \approx 0.1849$ for the parameter value $\lambda_f \approx 1.7172$ for which the variations in the number of gonorrhea cases are the less predictable (fully developed chaos). At this point, the exceptionally high infection rate of susceptible females leads the number of infected individuals sometimes close to extinction and other times close to overgrowth (*i.e.* gonorrhea outbreaks).

Furthermore, as the rate of infection of susceptible females increases in the interval $\lambda_f \in [1.59, 1.72]$ for the same time interval between clinical cases $(\delta = 2.65)$, the system goes through quasi-periodicity and a strange attractor appears in the system (Figure 22).

- The stable period-two orbit (Figure 22(a)) near the value $\lambda_f \approx 1.59$ loses stability via a *supercritical Neimark-Sacker bifurcation* giving rise to two attracting closed invariant curves (Figure 22(b)). At this point the number of infected males and females oscillates between all the states of the two invariant curves. The invariant curves grow in size (*i.e.* the amplitudes of oscillations in the number of infected individuals are increasing), interact with the saddle non-trivial fixed point $\left(I_f^*, I_m^*\right) \approx (0.86, 0.39)$ and near the value $\lambda_f \approx 1.6375$ become noticeably kinked (Figure 22(c)).

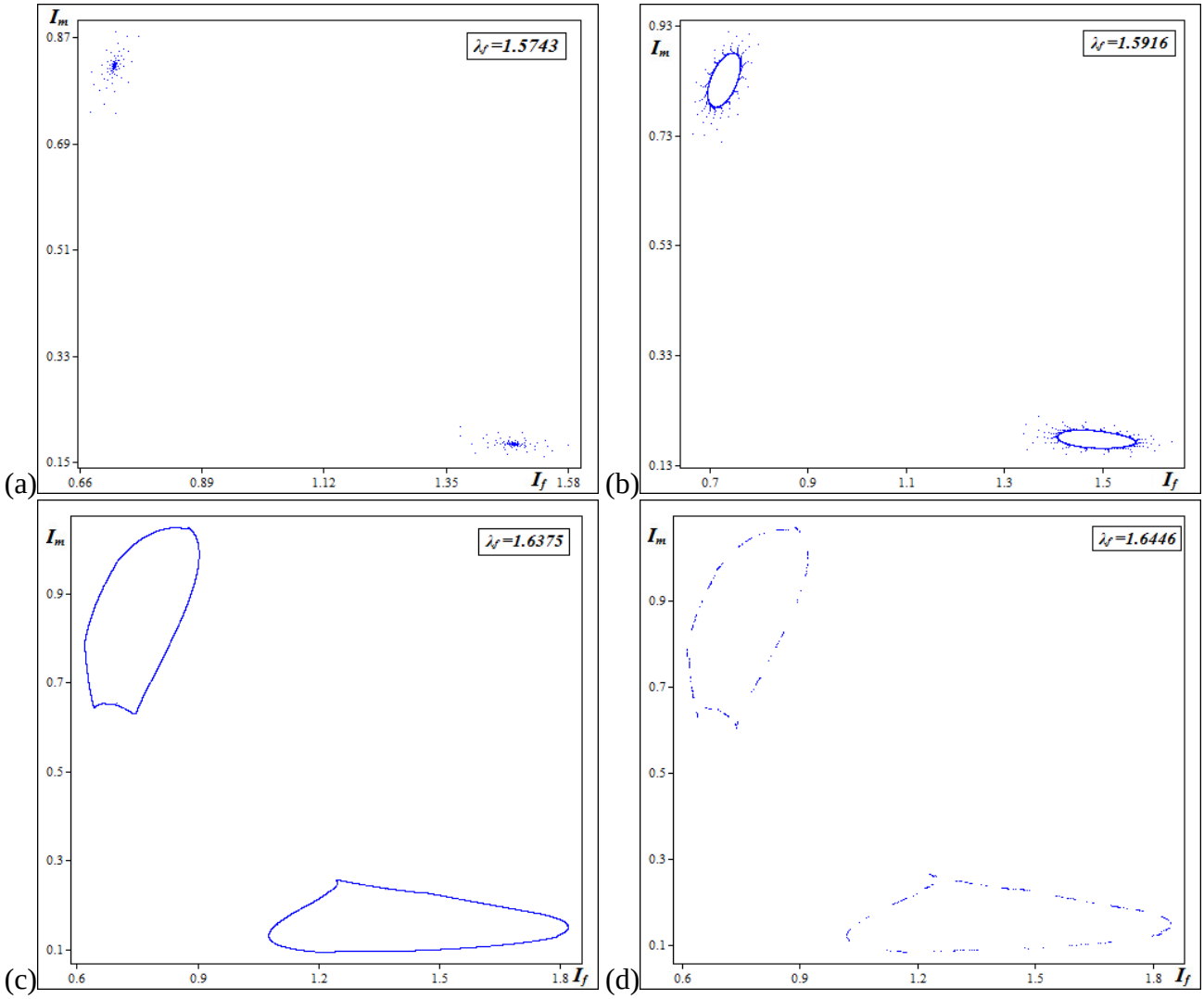

Figure 22 (*Continued.*)

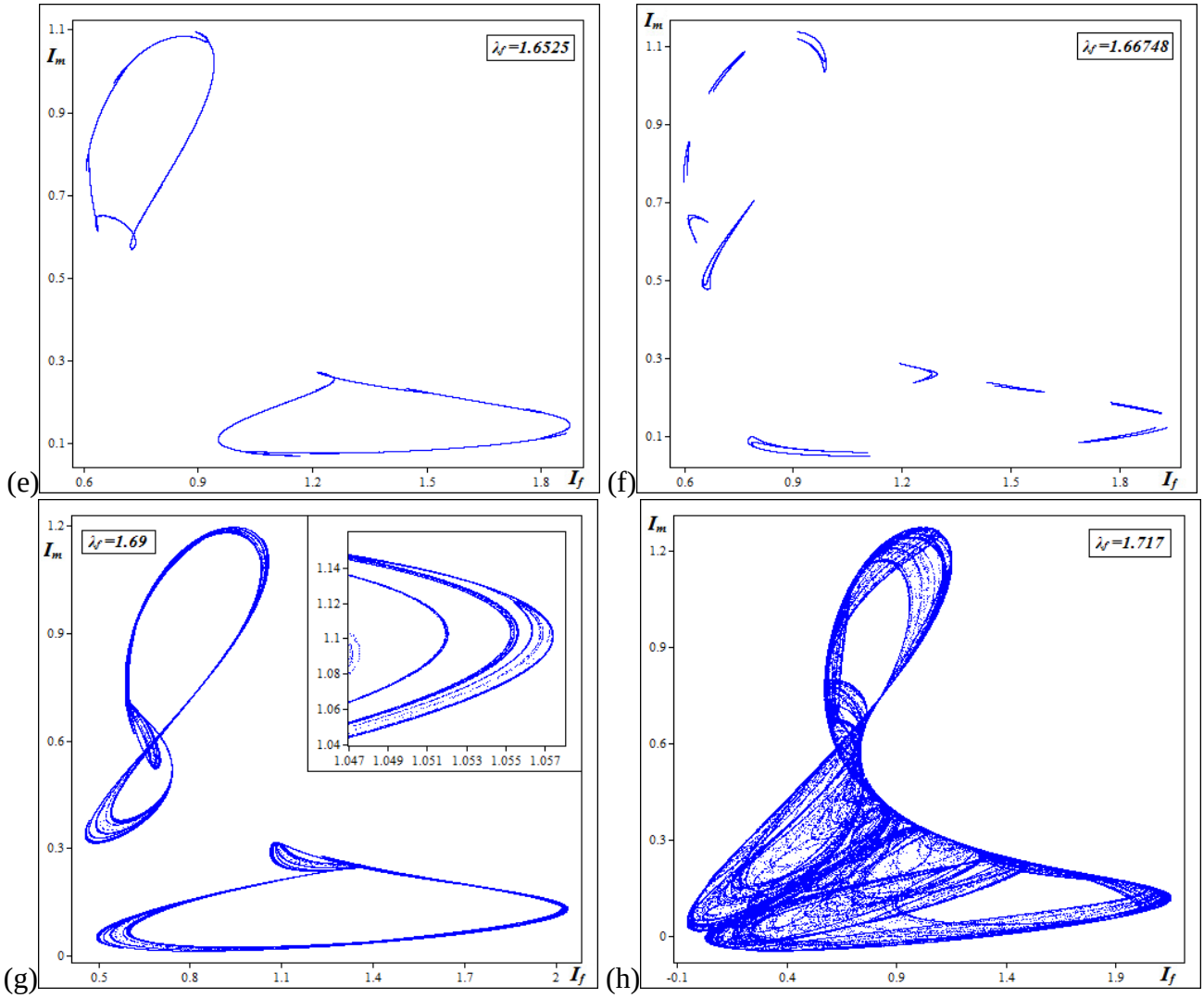

Figure 22 The phase plot (I_f , I_m) for δ = 2.65 as λ_f increases in the interval $\lambda_f \in$ [1.59, 1.72]. (a) Solutions converge to attracting 2-period cycle (λ_f = 1.5743), (b) The birth of two closed invariant curves (λ_f = 1.5916), (c) The invariant curves become kinked (λ_f = 1.6375), (d) The invariant curves split in a 64-period cycle (λ_f = 1.6446), (e) The invariant curves reappear slightly deformed (λ_f = 1.6525), (f) Invariant curves break into a 10-period motion (λ_f = 1.66748), (g) Invariant curves evolve into contiguous bands (λ_f = 1.69), (h) Solutions converge to a strange attractor (λ_f = 1.717).

- The kinked curves have a split, lock into a stable periodic orbit (Figure 22(d)) due to the first sequence of period-doubling occurring in the system $\left(32 \cdot 2^n\right)$ and reappear slightly deformed (Figure 22(e)). They have another split due to the second series of period-doubling $\left(10 \cdot 2^n\right)$ which gives rise to a motion of period 10 (Figure 22(f)).
- The motion of period 10 forms into two weakly chaotic contiguous bands (Figure 22(g)), while successive enlargements of the attractor can show its fine structure which looks identical in all scales (*i.e.* self-similarity). The chaotic contiguous bands become more and more complicated merging to form a *strange attractor* (Figure 22(h)) for a value of the varying parameter

$\left(\lambda_f \approx 1.717\right)$ in the chaotic domain (Figure 21). For higher values of the infection rate parameter the successive iterates diverge to infinity (*i.e.* both infected males and females become extinct through some kind of catastrophe) and the attractor disappears.

So we observe that the behavior of the discrete-time gonorrhea model (Equation (15)) differs significantly from its continuous counterpart (Equation (14)). Particularly, a time period $2 < \delta < 4$ days between successive clinical cases of gonorrhea and a sufficiently large infection rate of susceptible females allow for infinite sequences of period-doubling and chaotic behavior in the density of infected individuals.

3.1.6 Control of chaotic dynamics: Male latex condom

Nevertheless, chaos may be undesirable as the chaotic oscillations in the density of infected individuals can make the disease uncontrollable and, consequently, harmful to the people's health throughout the world. Therefore, the number of infected individuals needs to be under control. We use the method of controlling chaos proposed by Güémez and Matias (1993), known as the G.M. algorithm, which performs changes in the system variables allowing the stabilization of chaotic behavior. As mentioned above (Subsection 1.2.2), we apply the G.M. control algorithm to the discrete map (Equation (15)) by modifying the system variables I_n^f, I_n^m in the following form:

$$\begin{aligned} I_n^f &\to I_n^f\left(1+\gamma_1\right) \\ I_n^m &\to I_n^m\left(1+\gamma_2\right) \end{aligned} \tag{16}$$

Hence, our discrete-time gonorrhea model (Equation (15)) becomes:

$$\begin{cases} I_{n+1}^f = I_n^f\left(1+\gamma_1\right) + \delta\left(\dfrac{\lambda_f}{r}\left(1-I_n^f\left(1+\gamma_1\right)\right)I_n^m\left(1+\gamma_2\right) - \dfrac{I_n^f\left(1+\gamma_1\right)}{d_f}\right) \\ I_{n+1}^m = I_n^m\left(1+\gamma_2\right) + \delta\left(r\lambda_m\left(1-I_n^m\left(1+\gamma_2\right)\right)I_n^f\left(1+\gamma_1\right) - \dfrac{I_n^m\left(1+\gamma_2\right)}{d_m}\right) \end{cases} \tag{17}$$

γ_1, γ_2 represent the strength of the feedback for I_f, I_m.

For sexually active persons, male latex condoms are the most commonly used contraceptive method to prevent[47] sexually transmitted infections (Centers for Disease Control and Prevention, 2002). So

[47] In vitro studies indicate that latex condoms provide an effective mechanical barrier to passage of infectious agents comparable in size to or smaller than STI pathogens (Carey *et al.*, 1992; Carey *et al.*, 1999).

from a practical point of view, the modification in the system variables could be interpreted as the use of male latex condoms during each sexual intercourse. Hence, the new terms $\gamma_1 I_n^f, \gamma_2 I_n^m$ are associated with condom use during sexual intercourse protecting males and females from gonorrhea transmission and reducing the number of infected individuals $(-1 \le \gamma_1, \gamma_2 < 0)$, while the terms I_n^f, I_n^m are associated with sexual intercourse without condom use. Furthermore, for the sake of simplicity, we assume that the protection from gonorrhea transmission by condom use from female to male and vice versa is the same $(\gamma_1 = \gamma_2 = \gamma)$. The condition $\gamma = -1$ corresponds to an ideal situation where all sexually-active individuals use latex condoms during sexual intercourse consistently and correctly.

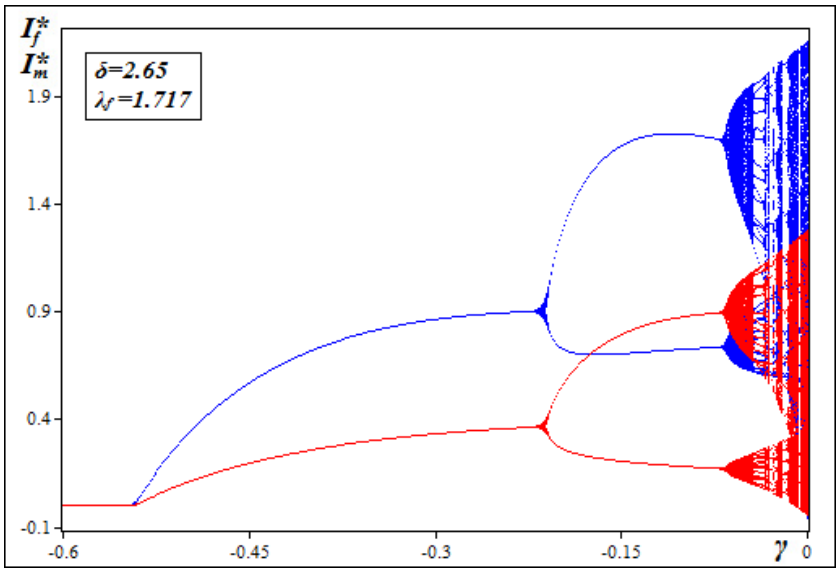

Figure 23 The bifurcation diagrams $(\gamma, I_f^*), (\gamma, I_m^*)$ as the varying parameter decreases in the interval $\gamma \in [-0.6, 0]$, for step size value $\delta = 2.65$ and infection rate of susceptible females $\lambda_f = 1.717$.

Thus, in order to see how the condom use affects the incidence of gonorrhea, we apply the G.M. method for the parameter values $\delta = 2.65$ and $\lambda_f = 1.717$ (the other parameters remain unchanged) for which the system's behavior is chaotic (Figure 22(h)) and let the control parameter (γ) vary. We illustrate the results by plotting the bifurcation diagram (Figure 23) along with the time series before $(\gamma = 0)$ and after $(\gamma < 0)$ the action of chaos control algorithm (Figure 24).

Without condom use during sexual intercourse $(\gamma = 0)$ the number of infective males and females appears irregular oscillations (Figure 24). As the intensity of pulses increases (*i.e.* condom use increases), the control parameter (γ) is taking smaller and smaller negative values, some part of I_f or I_m is injected from the map depending on the value of I_n^f or I_n^m at that moment and through

sequences of reverse period-doubling bifurcations the chaotic domains give rise to regular behavior (Figure 23) where the oscillations in the density of infected individuals become predictable. Particularly, near the value $\gamma \approx -0.066$ the behavior of solutions becomes periodic (cycle of period 2). In the parameter interval $-0.5432 < \gamma < -0.2091$ solutions converge to endemic equilibrium (Figure 24). Finally, the decline in the number of infective individuals leads to the end of the disease (gonorrhea-free equilibrium) for $-1 < \gamma < -0.5432$ (Figure 23).

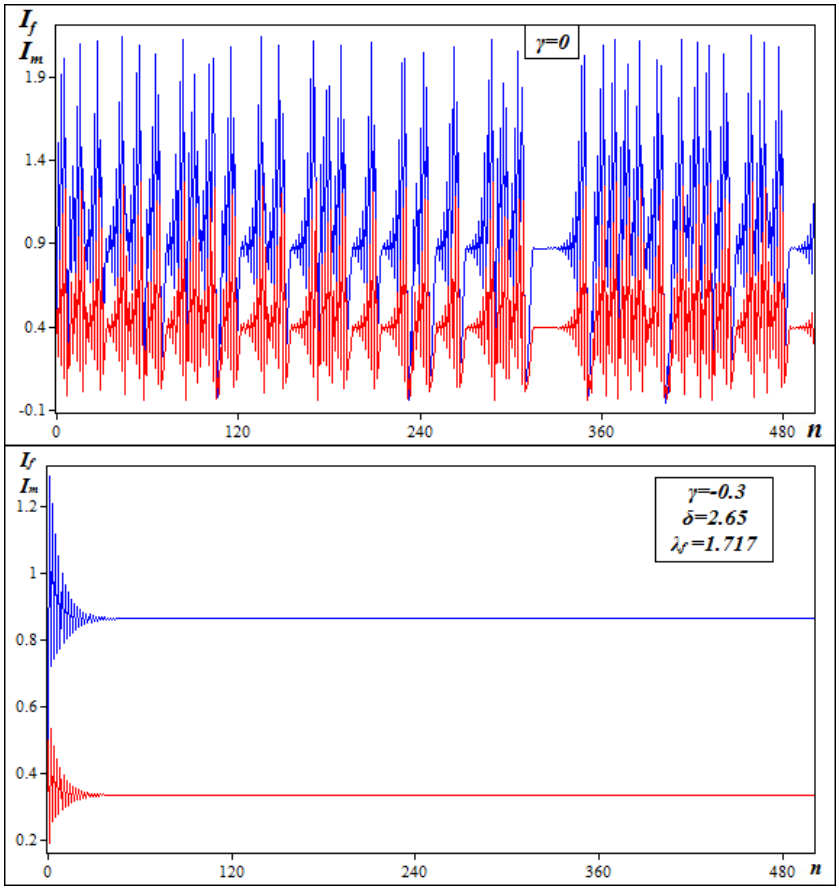

Figure 24 The time series[48] $(n, I_f), (n, I_m)$ for the parameter values $\gamma = 0$ (without control) and $\gamma = -0.3$ (with control), for step size value $\delta = 2.65$ and infection rate of susceptible females $\lambda_f = 1.717$.

Hence, for exceptionally high infection rate of susceptible females and time interval between clinical cases $2 < \delta < 4$ days, as the condom use during sexual intercourse increases slowly among individuals, the oscillations in the number of infective males and females decrease rapidly, leading to the reduction of gonorrhea incidence and the control of disease. So we observe that, condom use just by a fraction

[48] We plot the time series for the first $n \in [0, 500]$ iterations.

of the population 50% can reduce substantially the risk of gonorrhea transmission even for exceptionally high infection rates.

3.1.7 Gonorrhea outbreaks: Real-world fluctuations in gonorrhea cases and male latex condom

In this section we have discretize the gonorrhea model of Hethcote and Yorke (1984) and studied its dynamical characteristics using as a discrete-time step the interval between successive clinical cases (*i.e.* serial interval). We showed that the discrete-time model can result in a much richer set of patterns than the corresponding continuous-time model. The analytical stability analysis and the numerical simulation results showed that the discrete-time model undergoes: Fold, Flip bifurcations and the number of infective males and females can behave chaotically. In particular we showed that: (a) for low rate of infection of susceptible females gonorrhea remains endemic or dies out, while (b) for high rate of infection of susceptible females chaotic oscillations and gonorrhea outbreaks appear in the system.

The results of our study reflect the real-world large fluctuations which appear in the number of gonorrhea cases throughout the years. For instance, in Sweden from 2007 to 2011 the number of gonorrhea cases increased by 48% (from 642 to 951 cases) (Velicko and Unemo, 2012). The factors that might have been contributed to this increase in gonorrhea incidence seem to be: (a) the increased number of sexual partners over time, (b) the increased number of new casual sexual partners, and (c) the low level of condom use with casual sexual partners (Tikkanen *et al.*, 2011). Moreover, Alaska's outbreak of *Neisseria gonorrhoeae* infection (GC) began in 2008 and peaked in 2010 with a total 1,273 GC cases reported to Alaska Section of Epidemiology (State of Alaska Epidemiology, 2012). The 2009 case rate demonstrated a 69% increase from the 2008 rate, representing the greatest single-year increase in reported GC infection in Alaska since the 1970s; the rate increased in both sexes, among all races, in all age groups and in nearly all regions of the state (State of Alaska Epidemiology, 2010). Another example is the variations in the number of gonorrhea cases in the Onondaga County for the period 2006 – 2011. According to the Onondaga County Health Department (OCHD) annual reports, the number of gonorrhea cases each year for the period 2006 – 2011 are shown below.

Year	Gonorrhea cases	Year	Gonorrhea cases	Year	Gonorrhea cases
2006	670	2008	357	2010	395
2007	502	2009	377	2011	427

Source: Onondaga County Health Department (2009, 2011).

Moreover, according to the OCHD the number of cases of gonorrhea more than doubled in the county between 2011 and 2012. There were 602 cases in the first nine months up from 253 cases for the same period of 2011 (Syracuse, 2012). Hence, the proposed discrete-time model seems to be more effective in practice and gonorrhea, despite the fact that it is a non-fatal disease, is likely to have a strong negative effect on life history evolution. Moreover, the results of our study show that the time interval between successive clinical cases is important in case of gonorrhea emergency situations.

Finally, we have stabilized the unstable periodic orbits existing within the strange attractor and the unstable steady states (both endemic and disease-free) using a series of proportional feedbacks on the system's variables. The chaos control results could be definitely regarded as those which are obtained with male latex condom use during sexual intercourse. Our chaos control results show that condom use reduces the risk of gonorrhea transmission to a point where the number of infected individuals remains stable and is significantly small or zero. This reflects what many studies have shown, such as Barlow's study (1977) which showed that a 71% reduction in gonorrhea was associated with consistent and correct condom use. Which means that for every 100 cases of gonorrhea infection that would happen without condom use, only 29 would happen when condoms are used consistently.

However, one of the paradoxes in modeling infectious diseases is that, despite their quantitative nature, the best that we can often expect is qualitative insights (Garnett, 2002). Quantifying the relation between the number of condoms used and the incidence of gonorrhea is often difficult. For instance, Warner *et al.* (2006) reviewed studies published 1966 – 2004 to assess risk reduction for gonorrhea associated with male condom use. They found that, although most studies showed that condom use was associated with reduced risk for gonorrhea among men and women, however the exact magnitude of risk reduction is difficult to quantify because of limitations and variations in the methods and design of these studies.

Chapter 4

Solar Magnetic Activity

The Sun is a "second generation" star nearly 4.5 billion years old. It is a main-sequence star of spectral type GV2 composed of 92.1% hydrogen, 7.8% helium gas, and 0.1% of oxygen carbon, nitrogen, silicon, magnesium, neon, iron, sulfur, *etc*. The energy produced near the center of the Sun, creates a central temperature of about 15 million degrees Kelvin (°K) transported in the surface layers (*i.e.* photosphere) at 5780 °K. Dynamo processes (solar motions from rotation to turbulent convection) in the outer layers of the Sun, or convection zone, create a magnetic field (Hoyt and Schatten, 1997). The magnetic field of the Sun appears concentrated in flux tubes or ropes that appear on the surface of the photosphere as sunspots, pores, plages, and surface networks (Pustil'nik and Din, 2004). The generation of the magnetic field has a cyclical character; this cycle changes over periods varying from 8 to 17 years. The value of the best known parameter of the solar cycle – known as the *sunspot number* – varies during the cycle from 0 to 100 – 200 (Pustil'nik and Din, 2004).

Sunspots, by themselves, do not emit radiation or particles that could interact in some way with the Earth, but sunspots are markers of the Centres of Activity (de Jager, 2005). Hence, the variation of the sunspot number shows the activity level of the Sun. Sunspots are magnetized and normally occur in pairs (one corresponding to the North Pole and the other to the South Pole). During one cycle North spots lead and the South spots follow – the leading sunspots in the northern hemisphere will be magnetic north and those in the southern will be magnetic south; the polarity of the leading spot reverses in successive 11-year cycles – in the next cycle all the leading sunspots in the northern hemisphere will be magnetic south. (Kutner, 2003). In particular, the sunspots are transient features in the photosphere. They have vertically directed magnetic fields of the order of 1000 to about 4000 Gauss (de Jager, 2005). Some basic characteristics of the sunspots according to de Jager (2005) are the following:

1. At the location of the fields the convective motions are inhibited; hence less energy is carried upward than elsewhere in the photosphere. This results in the darker appearance of the spots. Yet the spots are not dark; their effective temperature is still as high as 4200°K.
2. The majority of the spots do not live longer than 2 days. The average lifetime is 6 days. Large spots may live for weeks and in rare cases even for months.

3. Typically spot diameters range from 2,000km to more than 40,000km. While motions are practically totally inhibited inside spots, there is a complicated velocity field under and around them.

The apothecary Schwabe (confirmed in 1851), after 17 years of sunspot observations, found that the solar activity, measured by the number of sunspots, varies in time and shows an 11-year periodicity (de Jager, 2005); this quasi-periodic 11-year cycle is known as the "Schwabe cycle" (Schwabe, 1844). The sunspot number (SSN) is one of the oldest measured indexes of solar activity forming a continuous record that covers more than 300 years. Predicting solar activity through the sunspot number began when the "Schwabe cycle" was first noticed. In the first two sections of this chapter we analyze the monthly and yearly sunspot-number data and we perform future monthly and yearly predictions trying to forecast the solar activity from July 2013 to June 2014 and from 2013 to 2102, respectively. The monthly and yearly SSN data were taken from the Solar Influences Data Analysis Center (SIDC: WDC-SILSO, Royal Observatory of Belgium, Brussels; Available at http://www.sidc.be/silso/versionarchive), in Belgium, which keeps the main database of sunspot numbers from a number of sources worldwide. The standard dataset provided by the SIDC is the International SSN known as the Zürich Sunspot Number [R_z] derived by Rudolf Wolf in the 19th century, based upon telescopic observation of sunspots. The Zürich Sunspot Number [R_z] is a very useful indicator of the level of solar activity defined by the following equation (Hoyt and Schatten, 1992):

$$R_Z = k\left(10g + n\right)$$

g is the number of sunspots groups; n is the number of individual sunspots; k is the constant correction factor which brings each observer to a common scale.

As a predictive tool we use the software package *GMDH Shell* (GS: Available at https://www.gmdhshell.com/). GS is a modeling tool that produces mathematical models and predictions. As a model-selection criterion we define the Root-Mean-Square Error, which selects models with the lowest difference between values predicted by a model and the values actually observed. We also select ranking variables according to their ability to predict testing data (variables ranking by error). A widely used technique in sunspot-number predictions is based on neural networks. Hence, as a core algorithm we define the polynomial neural networks. Neural-network forecasts are derived from nonlinear statistical algorithms that determine and model complex relationships between inputs and outputs to find patterns in the data that can be extrapolated (Pesnell, 2012). A core algorithm generates models from simple to complex ones until the testing accuracy increases. The GMDH-type

neural-network algorithm iteratively creates layers of neurons with two or more inputs. Every neuron in the network applies to a transfer function that allows exhaustive combinatorial search. Thus, the transfer function is suitably chosen that can predict testing data most accurately. We use two input variables and a linear transfer function for neurons.

Moreover, we are taking into account the Mean Absolute Error (MAE; *i.e.* the average over the verification sample of the absolute values of the differences between forecast and the corresponding observation) and the Root Mean Square Error (RMSE; *i.e.* the difference between forecast and corresponding observed values each squared and then averaged over the sample – the square root of the average is taken) obtained by comparing the predicted to the observed values in order to reduce the drop in the accuracy of our predictions. Finally, we perform several *post-facto* predictions comparing them with the actual sunspot-number values in order to evaluate the accuracy of our proposed predictive method.

4.1 Monthly Sunspot Numbers and Cycle-24 Future Predictions[49]

The solar cycles have been numbered since 1755 starting with Cycle 1 (1755 – 1766). The last recorded solar cycle lasted 12.6 years (1996 – 2008). In that order the current cycle that began with the 2008 solar minimum is Cycle 24. During the last few years, numerous studies have tried to predict the behavior of the present Cycle 24; some of them indicated that Cycle 24 is expected to be a quiet solar cycle. Badalyan *et al*. (2001) used cyclic variations of the coronal-green-line intensities to predict peak sunspot levels of 50. De Meyer (2003) used a semi-empirical transfer function model of solar cycles to predict the peak sunspot number for Cycle 24 of 95 – 125. Schatten (2003) used a solar dynamo amplitude method to predict a peak sunspot number of about 100 for Cycle 24. Svalgaard *et al*. (2005) used the strength of large-scale solar dynamo polar fields in Cycle 23 to predict Cycle 24 as 75 ± 8 at the peak.

In Figure 25 we visualize the plot of the monthly sunspot number (SSN) data for the last 24 sunspot cycles (January 1749 – June 2013). The 11-year periodicity rule is not strict; as we observe in Figure 25 there are short and long cycles, weak and strong ones. Moreover we observe that the most active SSN cycle since 1749 is the cycle 19; its maximum value deviates the most. Furthermore, we observe that the data trend supports Waldmeier (1961) hypothesis that lower activity cycles rise to peak latter

[49] This section is based on the publication "Sunspot numbers: data analysis, predictions and economic impacts" (Gkana, A., Zachilas, L.: 2015c, Sunspot numbers: data analysis, predictions and economic impacts, *Journal of Engineering Science and Technology Review* **8**(1), 79-85.).

in time. Observing the 10 prior cycles (14 – 23) the observed timelines fall into 2 categories (Ahluwalia and Jackiewicz, 2012): (i) the Cycles 14, 15, 17, 20 and 23 are slow risers like the cycle 24, (ii) the Cycles 16, 18, 19, 21 and 22 rise relatively steeply and exhibit above average activity.

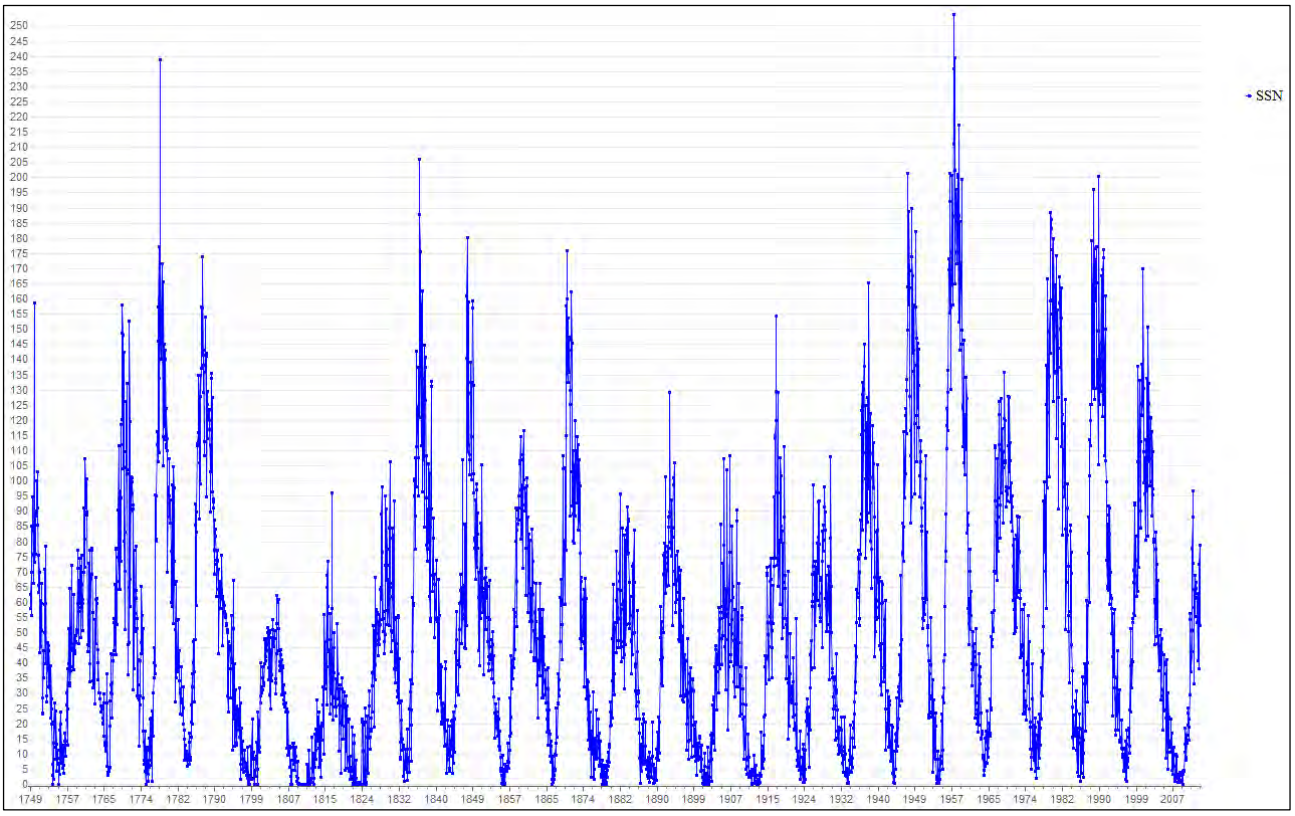

Figure 25 Time series plot of the monthly sunspot numbers for the last 24 solar cycles (January 1749 – June 2013).

Further, Gnevyshev and Ohl (1948) found that there exists good correlation between the properties of the even and the next following odd cycle, and not the preceding odd one. Beginning with Cycle 10, Gnevyshev and Ohl (1948) noted that there is a pattern such that even cycles of the even-odd pairing are less active; this pattern disappears after Cycle 21 (the even-odd symmetry in SSN cycles broke down with Cycle 22). The physical cause for this pattern is unknown. They might reappear in the future.

4.1.1 Data analysis of monthly R_Z numbers

The behavior of solar activity dynamics has been investigated by many researchers. The daily sunspot numbers, the monthly means and yearly means may be from a stochastic process (Siscoe, 1976) or from a deterministic chaotic process (Feynman and Gabriel, 1990). Morfill *et al.* (1991) analyzed the sunspot record over time scales of weeks or months. They consider a stochastic model, a heuristic model and a Lorenz model to represent the data. They showed that the deterministic chaos model

(Lorenz) provides the best fit of the data. Mundt *et al.* (1991) studied the variable solar activity over the time period from January 1749 to May 1990 using 2897 monthly sunspot numbers. They showed that the attractor does not fill the space and is a sheet much like the Rössler and Lorenz attractors with a dimension ≈ 2.3. The solar dynamo can be expressed with three differential equations identical to the Lorenz equations. Thus the solar cycle appears to be chaotic of low dimension and can only be predicted for a short term. Zhang (1996) performed a nonlinear analysis of the smoothed monthly sunspot numbers to obtain nonlinear parameters to predict the numbers. The analysis of the monthly smoothed numbers from January 1850 to May 1992 indicates the numbers are chaotic and of low dimension described by three to seven parameters.

Ostryakov and Usokin (1990) examined the structural character and inherent stochastic behavior of the monthly mean sunspot numbers. They calculated that the fractal dimension for the periods 1749 – 1771, 1792 – 1828 and 1848 – 1859 is 4.3, 3.0 and 4.0 respectively. Zhang (1994, 1995) calculated the fractal dimension $D = 2.8 \pm 0.1$ and the largest Lyapunov exponent $\lambda_{\max} = 0.023 \pm 0.004$ bits/month, for the monthly mean sunspot numbers for the period January 1850 to May 1992 using the methods given by Grassberger and Procaccia (1983b) and Wolf *et al.* (1985).

In this subsection we analyze the sunspot record over time scales of months using 3174 monthly sunspot numbers (January 1749 – June 2013). As mentioned above (Section 1.4), our data analysis is based on the method developed by Takens and Ruelle (1971) that shows how to reconstruct the phase space of a dynamical system from a single-variable observed times series. Thus, in order to investigate the dynamics of our system in a space defined by delayed vectors of dimension [*m*], we have to estimate the embedding parameters (*i.e.* the time delay and the embedding dimension).

Embedding parameters

In order to find the suitable time delay [τ] for the embedding, we use the Average Mutual Information suggested by Fraser and Swinney (1986) as a function of the time delay $I = I(T)$ (Figure 26). As mentioned above (Subsection 1.4.1), the lag at which the first minimum of the AMI function occurs is $T_m = 29$ and it is chosen as a delay time $\tau = 29$.

In order to find the suitable dimension [*m*], we use the False Nearest Neighbors method, which has been first introduced by Kennel *et al.* (1992) as a convenient method to determine the minimal sufficient embedding dimension (Subsection 1.4.1). Figure 27 illustrates the FNN as a function of the embedding dimension *m*. The suitable embedding dimension should not be smaller than the first dimension at which the number of false nearest neighbors drops to zero. Thus, the suitable embedding

dimension to unfold dynamics is estimated to be about $m = 7,8$ (*i.e.* at an embedding of 7 to 8 dimensions the attractor of the sunspot series is unfolded).

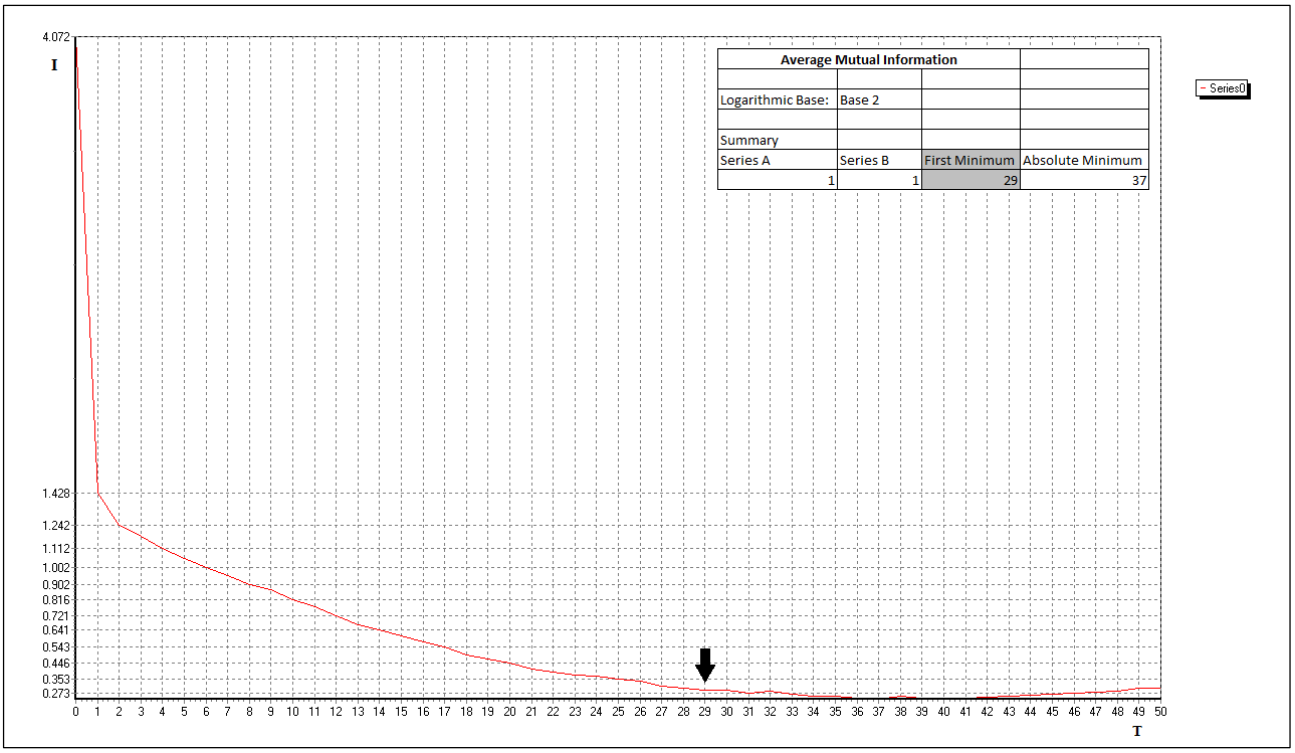

Figure 26 The Average Mutual Information as a function of the time delay $I = I(T)$ for $T = 0,1,...,50$.

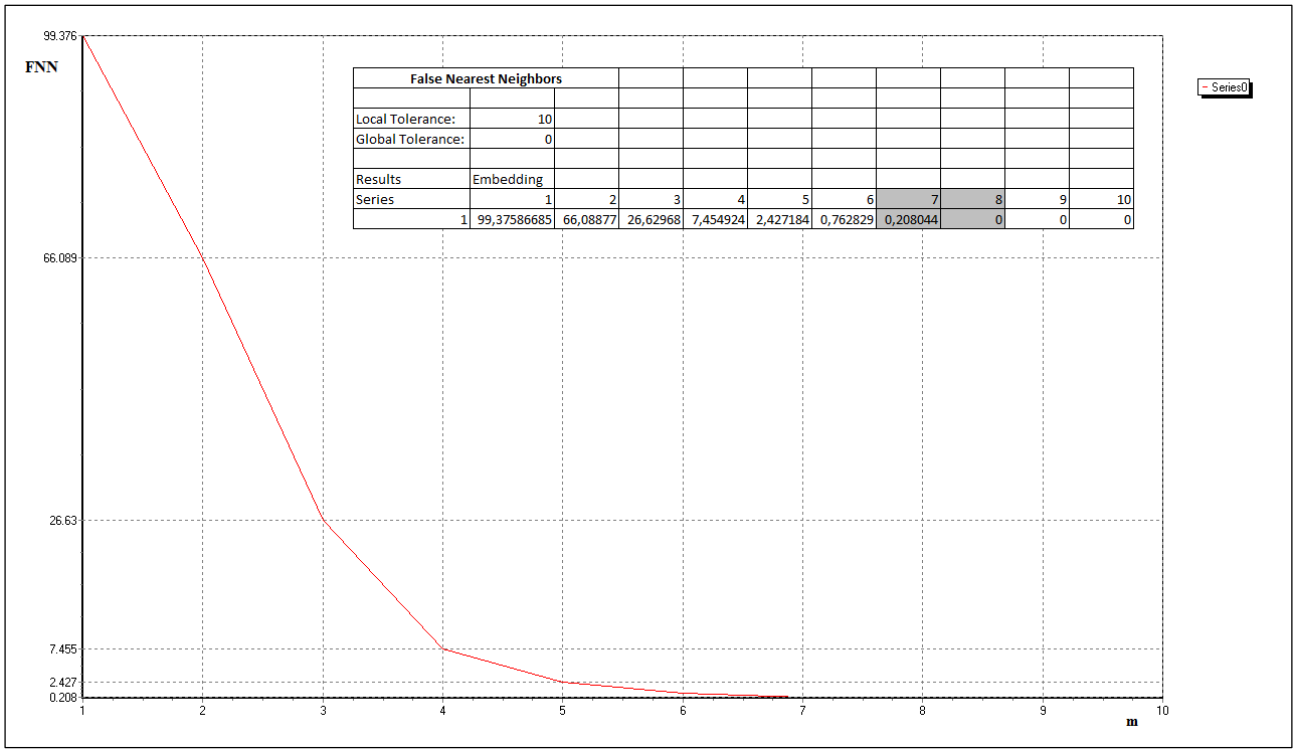

Figure 27 The False Nearest Neighbors as a function of the embedding dimension $FNN = FNN(m)$ for $m = 1,2,...,10$ embedding steps.

Dimension of the monthly SSN data attractor

As mentioned above (Subsection 1.4.2), the correlation dimension has been introduced by Grassberger and Procaccia (1983a, 1983b) as a fractal dimension measurement of an attractor. According to this method, we first calculate the logarithm of the correlation integral $\ln C^{(m)}(r)$ with increasing values of the logarithm of the distance in phase space ln *r* for various embedding dimensions [*m*] (Figure 28). By finding the slope of this graph we estimate the correlation dimension [$D_c(m)$] for every embedding dimension [*m*]. We calculate the correlation dimension as a function of the embedding dimension $D_c = D_c(m)$ in order to determine the fractal dimension of the attractor of the monthly sunspot numbers (Figure 29). By increasing *m*, the correlation dimension $D_c(m)$ will eventually converge to its true value $\nu \simeq D_c$.

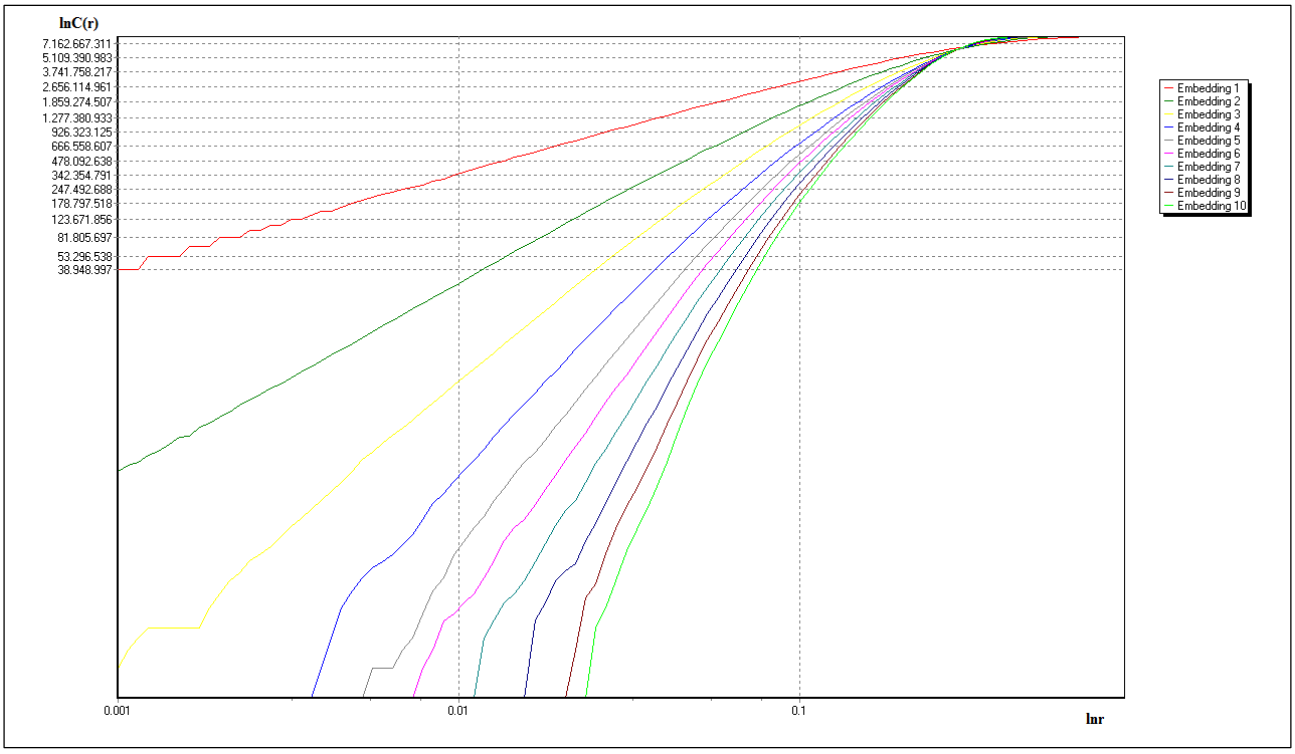

Figure 28 The graph of $\ln C^{(m)}(r)$ for increasing values of $\ln r$ for $m = 1, 2, ..., 10$ embedding dimensions.

In Figure 29, we observe that, when the embedding dimension exceeds $m_c \approx 7$ the correlation dimension converges to the value $D_c \approx 3.8$. The embedding dimension value at which the convergence begins is about twice the attractor dimension $m_c \approx 2D_c$. Thus, the dimension of the attractor is estimated to be about $D_c \approx 3.8$ (low dimensional). The attractor's dimension defines the number of

variables of the system. Therefore, the time series of the monthly sunspot numbers can be described by $v=4$ independent variables.

The convergence of the correlation dimension $D_c(m)$ with increasing values of the embedding dimension m to its true value D_c is an indication of chaotic behavior. A correlation dimension that does not converge corresponds to a white noise signal.

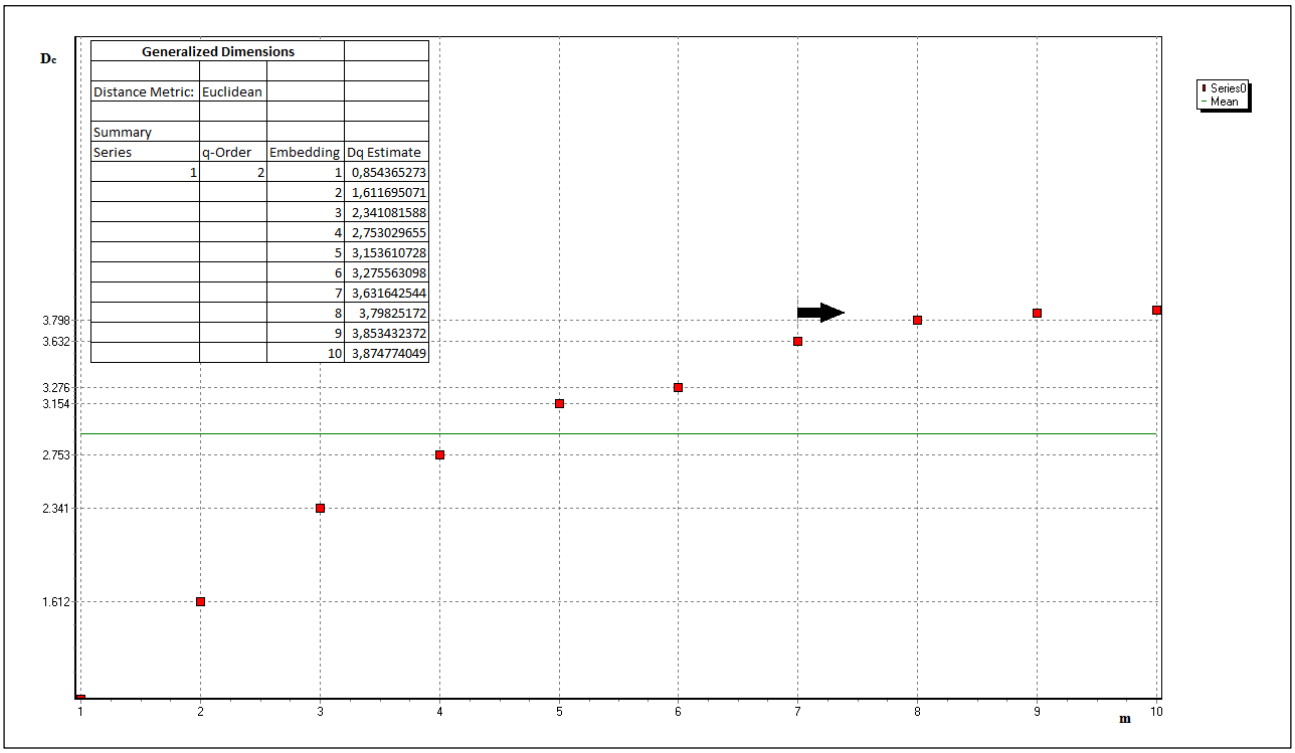

Figure 29 The Correlation dimension as a function of the embedding dimension $D_c = D_c(m)$ for $m=1,2,...,10$ embedding steps.

Predictive power

In order to determine the presence of a deterministic chaos in the time series, we calculate the largest Lyapunov exponent $(\lambda_{\max})$ by using the Kantz algorithm (Subsection 1.2.1). The largest Lyapunov exponent is $\lambda_{\max} \simeq 0.0195 > 0$; the positive value of the largest Lyapunov exponent indicates the presence of chaos in solar activity dynamics. In this case we have the so-called exponential instability where two arbitrary close trajectories will diverge apart exponentially; that is the hallmark of chaos (Bershadskii, 2009). The small largest Lyapunov exponent value indicates that the chaos for the monthly sunspot numbers is weak. Moreover, as mentioned above (Subsection 1.2.1), the predictive power can be estimated by $T_{\text{pr}} \approx 1/\lambda_{\max}$. So the upper limit of the theoretical time scale on which the monthly sunspot number can be used to make deterministic predictions is $T_{\text{pr}} \approx 1/\lambda_{\max} = 1/0.0195 \approx 51$

months. We observe that long-term predictions are not possible most likely due to the fact that the chaotic nature of the system results a high sensitive dependence on initial conditions for the monthly sunspot numbers.

Recurrence quantification analysis

We plot the RP (Figure 30) and use the RQA (Section 1.5) to study the recurrent patterns that exist within the time series of the monthly SSN data. Table 3 summarizes the RQA results. The high values of *DET*, $L_{\max}$ and *ENTR* indicate the deterministic chaotic behavior of our system. In particular, the high value of Determinism ($DET = 98.31\%$) indicates that most of the recurrent points are found in deterministic structures. The high value of the variable Maxline ($L_{\max}$ = 247) is consistent with the small value of the largest Lyapunov exponent ($\lambda_{\max} \simeq 0.0195$) indicating that the signal of the system's attractor is only slightly chaotic and the system is more stable. Moreover, the value of Trend (*TREND* = –1.99) does not deviate significantly from zero, indicating the system's stationarity. The large value of Entropy (*ENTR* = 4.8694) indicates the high complexity of the deterministic structure in the recurrence plot. Finally, the small value of Recurrence rate (*REC* = 21.76%) indicates that the monthly SSN data exhibit aperiodic dynamics.

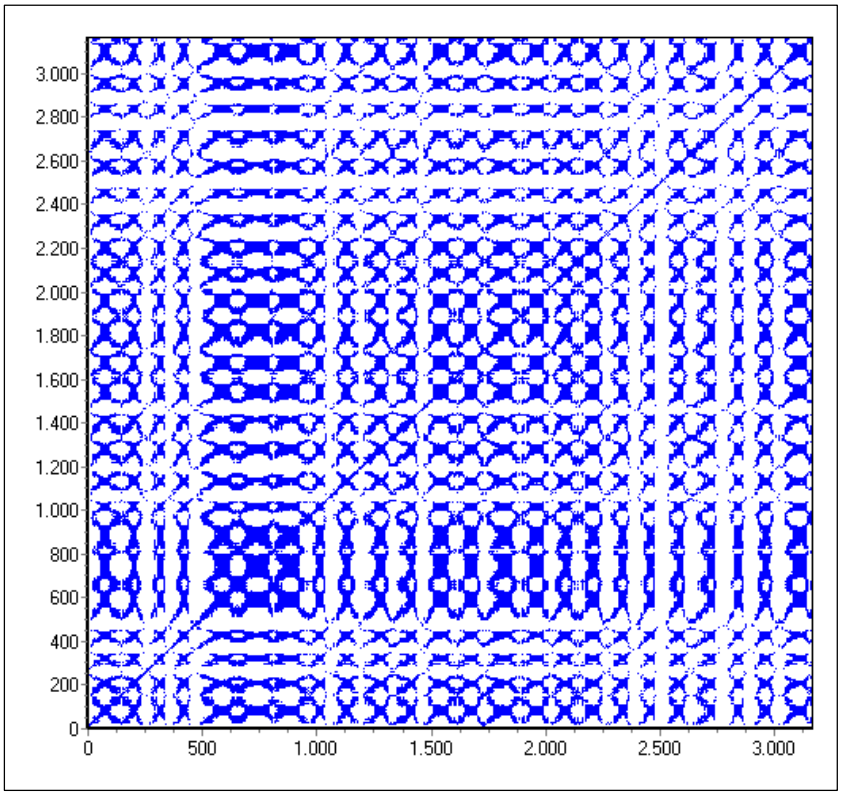

Figure 30 The Recurrence Plot for the monthly sunspot-number data (January 1749 – June 2013).

Table 3 Recurrence Quantitative Analysis results for the monthly sunspot-number data (January 1749 – June 2013).

Series	Epoch	*DIS*	*RR*	*DET*	*ENTR*	L_{max}	*TREND*
1	Entire Series	135.478656	0.217594	0.983094	4.869374	247	-1.990353

Thus the results of our data analysis indicate that the monthly sunspot numbers for the period January 1749 to June 2013 is a system of low dimensional deterministic chaos. Although chaotic systems are theoretically unpredictable in the long term, their underlying deterministic nature allows accurate short-term predictions (Mundt *et al.*, 1991).

4.1.2 Cycle-24 sunspot-number predictions

In this subsection we try to forecast the peak Cycle-24 activity. Zheng (1993) used the leap-step threshold autoregressive model and technique in nonlinear time series to obtain predictions from 1 month to 12 months ahead. De Meyer (2003) attempted to forecast the values of sunspot numbers [R_Z] on the basis of his model of the solar cycle consisting of a sequence of independent overlapping events. He predicted that the 24th cycle would start in 2007 to reach in 2011 a peak height in the range 95 – 125. Predicting solar activity is quite challenging, but there are indications that solar activity may decrease in coming decades. Clilverd *et al.* (2003) suggested a nearly constant level of solar activity till about 2050 and a slow decrease thereafter. However, this approach was criticized by Tobias *et al.* (2004): "*The future of such a chaotic system is intrinsically unpredictable*".

Ex-post sunspot-number predictions

We perform ex-post predictions of 6 steps (months) back in time (January 2013 – June 2013) and we compare them with the observed values (Figure 31) and the corresponding predictions given by the Solar Influences Data Analysis Center[50] (SIDC) (Figure 32). In Figure 31 we observe that the differences between the predicted and observed values (residuals) are quite small. So the ex-post predictions of the proposed neural network model fit the values of the actual data quite well. Moreover, in Figure 32 we observe that the values of MAE and RMSE for the post-processed predictions of the proposed neural network model (MAE = 11.22 and RMSE = 12.26) are consistent with those of the predictions published by SIDC (MAE = 11.5 and RMSE = 13.38).

[50] We are using the predictions of the monthly SSN published by the Solar Influences Data Analysis Center (SIDC) based on the Combined Method (CM); a regression technique combining a geomagnetic precursor (aa index) with a least-square fit to the actual profiles of the past 24 solar cycles (Available at: http://sidc.oma.be/sunspot-data/).

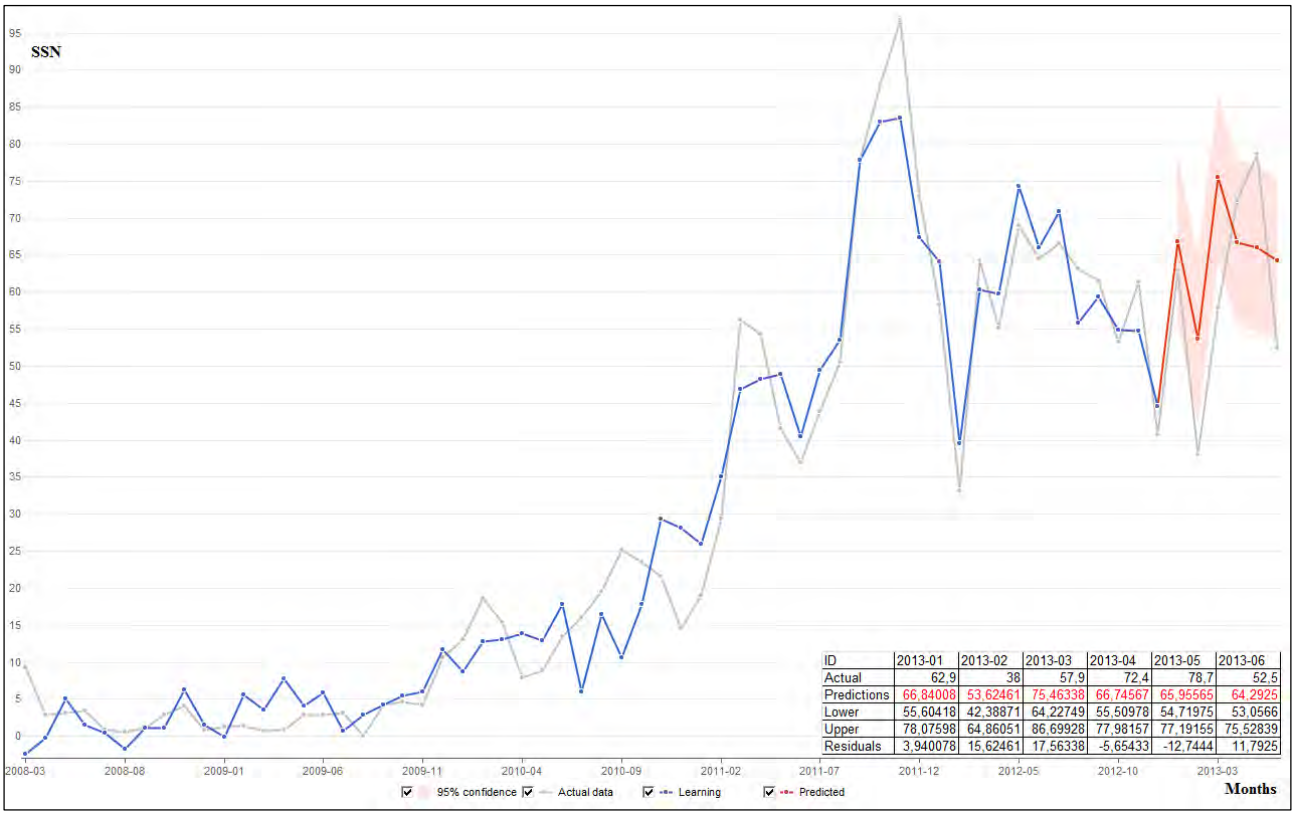

ID	2013-01	2013-02	2013-03	2013-04	2013-05	2013-06
Actual	62,9	38	57,9	72,4	78,7	52,5
Predictions	66,84008	53,62461	75,46338	66,74567	65,95565	64,2925
Lower	55,60418	42,38871	64,22749	55,50978	54,71975	53,0566
Upper	78,07598	64,86051	86,69928	77,98157	77,19155	75,52839
Residuals	3,940078	15,62461	17,56338	-5,65433	-12,7444	11,7925

Figure 31 Ex-post predictions of 6 steps (months) back in time (January 2013 – June 2013); the grey curve corresponds to the actual monthly sunspot-number data; the blue curve corresponds to the proposed neural network model; the red curve corresponds to the ex-post forecasts.

However, the oscillations in the observed SSN values seem to be predicted better by the proposed neural network model than the method used by SIDC (Figure 32); *i.e.* the time series of our neural network model predictions (red curve) fits better the actual sunspot data (blue curve) than the SIDC predictions (green curve). Furthermore, we observe that the maximum observed value from January 2013 to June 2013 was 78.7 in May 2013. Although the SIDC predicted maximum was in May 2013, the predicted value was 66.1, while the predicted maximum of our neural network model was 75.46 (much closer to the observed value 78.7) in March 2013. Thus our proposed neural network model seems to predict better the maximum SSN value (with a deviation of ±2 months) than the method used by SIDC.

Future sunspot-number predictions

Finally, we perform future predictions in order to forecast the maximum sunspot number value during the next 12 months. The predictions of 12 time steps (months) ahead, for the period from July 2013 to June 2014, are illustrated in Figure 33. The proposed neural network model of the 12-months-ahead prediction is:

$$
\begin{aligned}
R_Z(t) &= 3.03787 - 0.319168 \cdot R_Z(t-1428) + 1.3856 \cdot N[116] \\
N[116] &= -1.13723 + 0.613612 \cdot N[154] + 0.41996 \cdot N[264] \\
N[154] &= -4.40757 + 0.294369 \cdot R_Z(t-273) + 0.157676 \cdot R_Z(t-2098) \\
N[264] &= -1.11764 + 0.18513 \cdot R_Z(t-771) + 0.584038 \cdot R_Z(t-1154)
\end{aligned}
\tag{18}
$$

$R_Z(t)$ is the predicted value of the monthly sunspot numbers at time period t (for t = 3175, 3176, 3177,… in units of months); *e.g.* $R_Z(3175)$ refers to the predicted sunspot-number value in July 2013 (t = 3175 corresponds to July 2013). The terms $R_Z(t-1428)$, $R_Z(t-273)$, $R_Z(t-2098)$, $R_Z(t-771)$ and $R_Z(t-1154)$ are the observed values of the monthly sunspot numbers 1428, 273, 2098, 771 and 1154 steps (months) back in time, before the time period t, respectively (*e.g.* for the next period, t = 3175: July 2013, the $R_Z(t-1428) = R_Z(3175-1428) = R_Z(1747)$ corresponds to the actual monthly sunspot-number value recorded in July 1894).

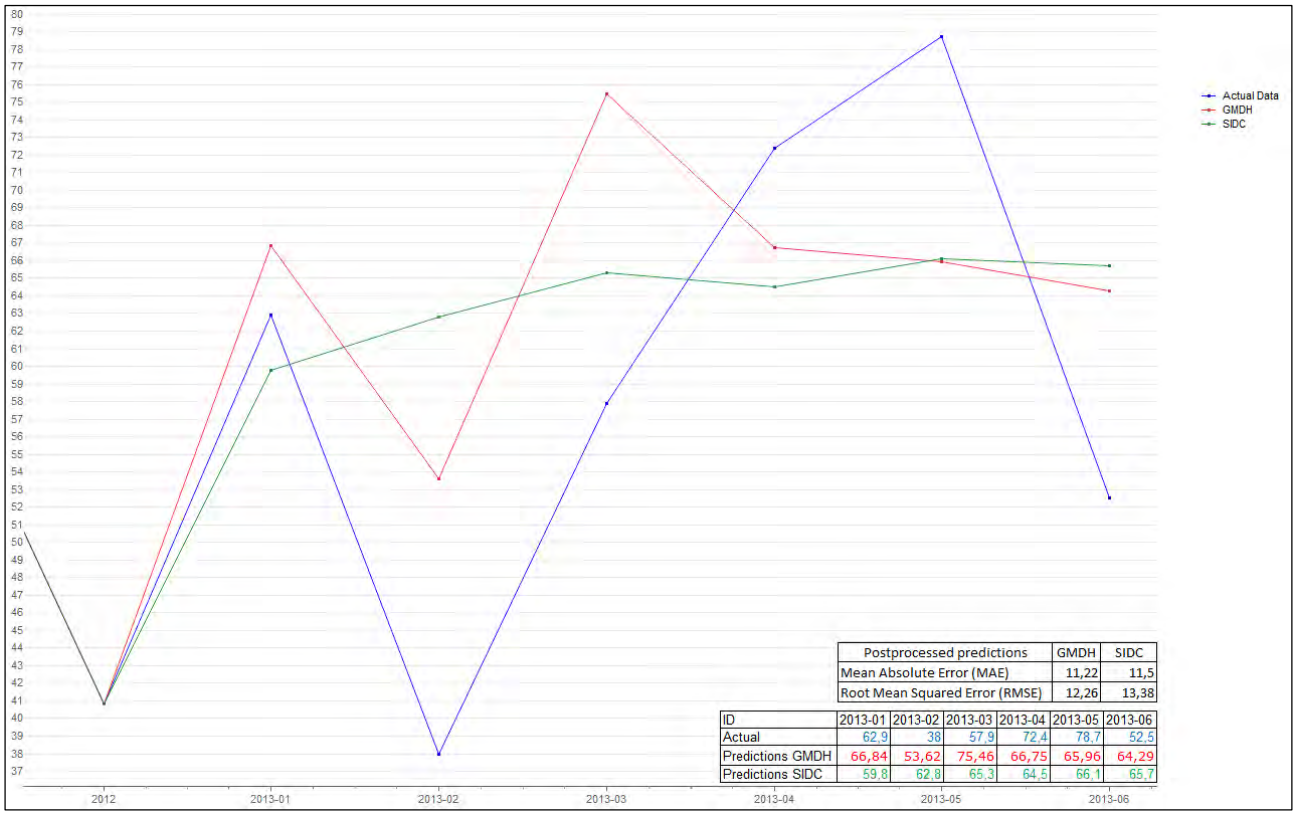

Postprocessed predictions	GMDH	SIDC
Mean Absolute Error (MAE)	11,22	11,5
Root Mean Squared Error (RMSE)	12,26	13,38

ID	2013-01	2013-02	2013-03	2013-04	2013-05	2013-06
Actual	62,9	38	57,9	72,4	78,7	52,5
Predictions GMDH	66,84	53,62	75,46	66,75	65,96	64,29
Predictions SIDC	59,8	62,8	65,3	64,5	66,1	65,7

Figure 32 Time series of the actual sunspot-number data (blue curve), predictions of the proposed neural network model (red curve) and predictions published by SIDC (green curve) from January 2013 to June 2013.

According to the predictions of the proposed neural network model (Equation (18)), the predicted maximum value of SSN for the next 12 months for Cycle 24 is expected to be 92.4 in November 2013 (± 2 months). Moreover, the MAE and the RMSE are relatively small (MAE = 4.898 and RMSE =

6.753) indicating the high predictive accuracy of our neural network model. Thus the sunspot number Cycle 24 is yet to peak.

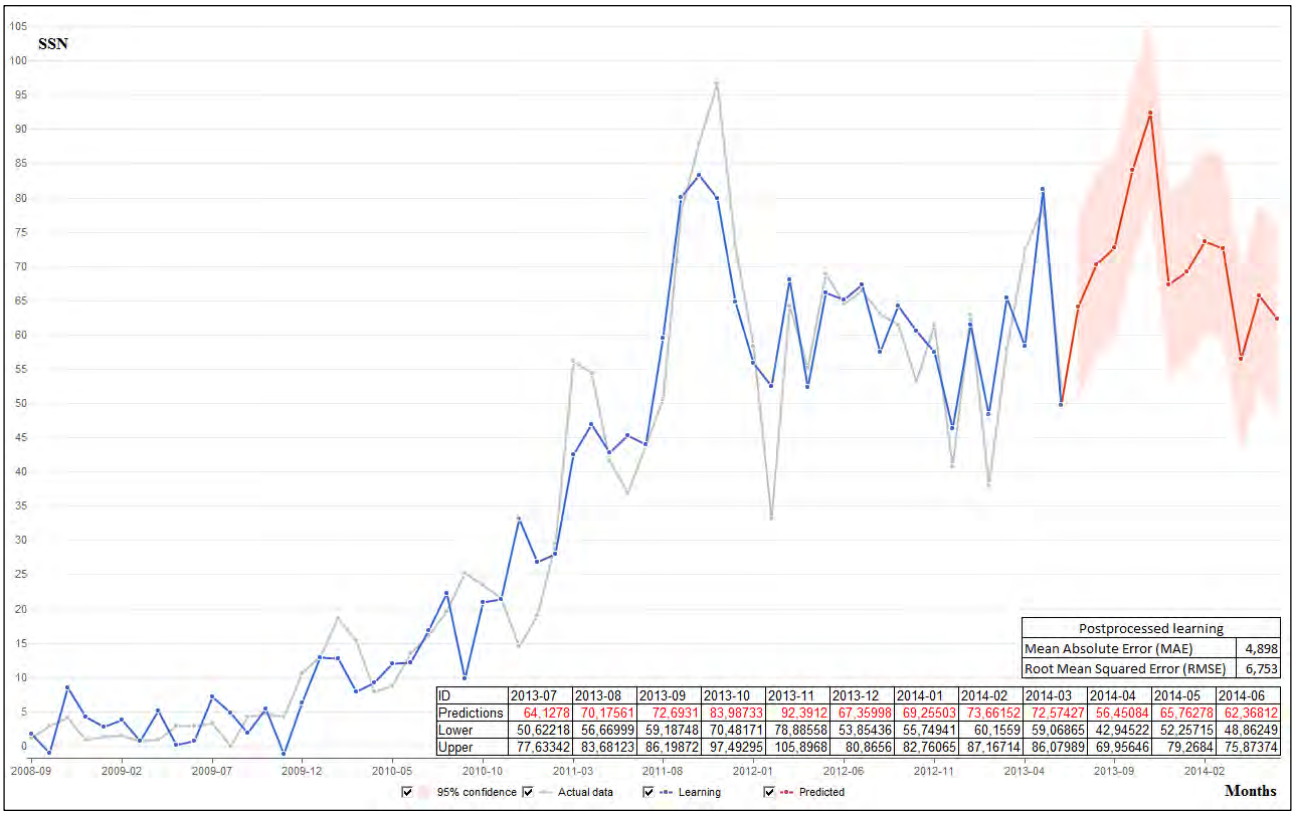

Figure 33 Future predictions of 12 time steps (months) ahead (July 2013 – June 2014); the grey curve corresponds to the actual monthly sunspot-number data; the blue curve corresponds to the proposed neural network model; the red curve corresponds to the future forecasts.

4.1.3 Maximum solar activity and Sun-Earth connection

In this section we analyzed the monthly sunspot-number data from January 1749 to June 2013 and performed solar activity predictions during the next few months (July 2013 – June 2014). The knowledge of the level of solar activity ahead in time is important to Earth. Edmund Halley, following the spectacular auroral display in Europe in March 1716, made the first step of understanding the Sun-Earth connection. He suggested that charged particles moving along the Earth's magnetic field lines are the cause of the aurora (Halley, 1692). The radiation environment of the Earth's atmosphere is very dynamic and consists of several components of ionizing radiation: galactic cosmic rays, solar energetic particles and radiation belt particles. Galactic cosmic rays reach their maximum intensity when the Sun is least active and are at a minimum intensity during solar maximum. In contrast, during maximum solar activity an increased number of Coronal Mass Ejections (CMEs) and solar flares produce high-energy solar particles (O'Sullivan, 2007). Beyond the protective shield of the Earth's atmosphere and

magnetosphere, there are sources of radiation that can be a serious hazard to humans and electronic equipment.

Space weather has severe impacts on satellites (Hastings and Garrett, 1996) and GPS/navigation (Wellenhof *et al.*, 2001). During solar events and geomagnetic storms the system may give navigators information that is inaccurate by as much as several km (Filjar, 2008). The problems of geomagnetically induced currents in power lines and flowing in high voltage transformers have been recognized at least since the early 1970s (Albertson *et al.*, 1974), but were brought into serious consideration by the widespread failure of the Hydro-Quebec power grid (Canada) resulting from severe geomagnetic storm on March 13-14, 1989 (Blais and Metsa, 1993).

The first observations of space weather effects on technological systems were made in telegraph equipment more than 150 years ago (Barlow, 1849). Many times since then, systems have suffered from peak overvoltages, interruptions in the operations and even fires caused by Geomagnetically Induced Currents (GICs) flowing through the equipment (Boteler *et al.*, 1998). During a magnetic storm in July 1982, such an effect made traffic lights turn red without any train coming, in Sweden (Wallerius, 1982). Submarine telephone cables lying on the ocean floors form a special category of systems affected by geomagnetic disturbances (Root, 1979).

Another consequence of space weather is its effect on humans and biological systems in space and on aircraft (Baker *et al.*, 2007). Solar proton events (SPEs) can knock electrons from cell molecules and damage them, especially from the skin, eye and blood-forming organs. These damaged cells are unrepairable (Crosby *et al.*, 2006). If DNA (deoxyribo nucleic acid) is damaged, then cell reproduction is hampered and even the effect could be passed to the next generations. Biological effects can also be in the form of severe burns, sterilization, cancer and damage to other organs.

These effects can have severe negative economic impacts on our society. Therefore, trying to predict the maximum of solar cycles becomes more and more of an urge, since it can minimize economic losses and help society save hundreds of millions of money each year.

4.2 Yearly Sunspot Numbers: Maunder Minimum Reconstruction and Future Predictions Up to 2100[51]

Long-term predictions of sunspot number can be quite challenging due to the chaotic nature of the system that produces them. However, several studies indicate that solar activity may decrease in coming decades. Clilverd *et al.* (2003) suggested that Cycle 24 would be similar to previous cycles in amplitude, with low activity levels not being reached until 2100. In particular, they suggested a nearly constant level of solar activity until about 2050 and a slow decrease thereafter. This was mainly because of a 420-year repetition of the low-activity conditions following the Maunder Minimum of 1700.

The Maunder Minimum is the well-known 70-year period of the prolonged sunspot minima from 1645 to 1715. This period has been recognized and confirmed by Spörer (1887), Maunder (1922), and Eddy (1976) as a period with exceedingly scarce sunspots. The entire records of those 70 years, combined together would scarcely supply sufficient observations of sunspots to equal one average year of an ordinary minimum (Maunder, 1922). Muscheler *et al*. (2004) drew attention to the four great activity minima of the last millennium, which are spaced at intervals of about 200 years. An easy way of forecasting would therefore be to use the De Vries period by extrapolating over the past five large minima (Oort, Wolf, Spörer, Maunder, Dalton). Thus one would "predict" another Maunder Minimum around 2050. In contrast, Usoskin *et al*. (2003) suggested that we are in a prolonged period of exceptionally high solar activity with little suggestion of lower activity levels to come.

Trying to predict the monthly sunspot numbers in the future as we did in the previous Section 4.1, can be very useful regarding the short-term oscillations in solar activity. Long-term sunspot-number predictions are exceptionally important as well; however, the monthly data are apparently not suitable for such predictions. The yearly sunspot-number data are likely more suitable for long-term predictions; they can give us insights about the possible minima of the solar activity in the future. Thus, in this section we use the yearly mean sunspot number to investigate the likely variation of solar activity in the next 90 years.

[51] This section is based on the publication "On the verge of a grand solar minimum: A second Maunder Minimum?" (Zachilas, L., Gkana, A.: 2015d, On the verge of a grand solar minimum: A second Maunder Minimum?, *Solar Physics* **290**(5),1457-1477.).

4.2.1 Data analysis of yearly R_Z numbers

In this subsection we analyze the yearly mean sunspot numbers (Figure 34) for the last 313 years (1700 – 2012). Once again, we investigate whether the yearly sunspot number come from a stochastic or a deterministic chaotic process, by analyzing the data using the method developed by Takens and Ruelle (1971) (Section 1.4). Thus, we first have to estimate the embedding parameters; *i.e.* the suitable time delay [τ] and the embedding dimension [m].

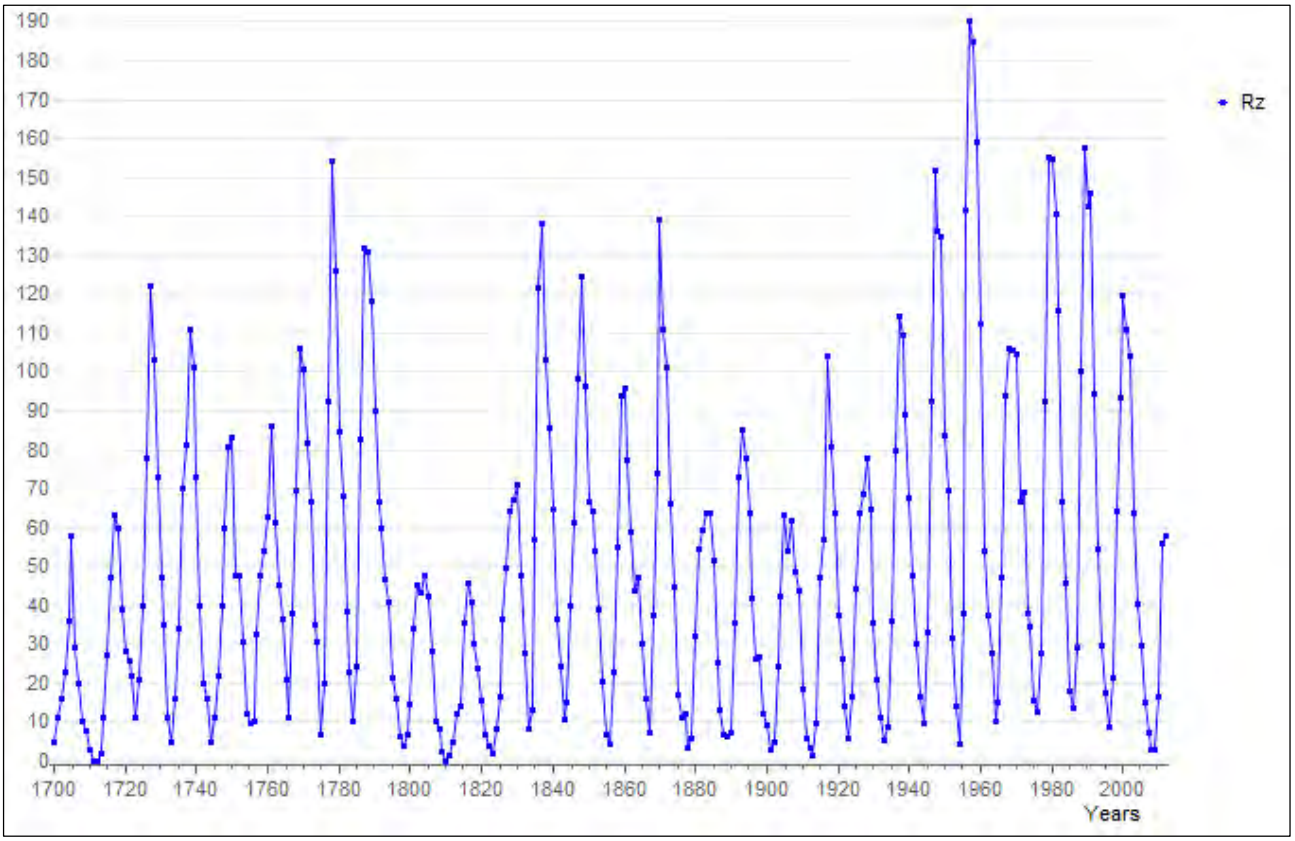

Figure 34 The time series of the yearly Zürich sunspot numbers [R_z] for the last 313 years (1700 – 2012).

Embedding parameters

Once again, in order to find the suitable time delay, we use the Average Mutual Information introduced by Fraser and Swinney (1986) as a method to determine a reasonable delay for nonlinear systems (Subsection 1.4.1). We calculate the AMI as a function of the time delay $I = I(T)$ for $T = 0, 1, \ldots, 20$ lags (Figure 35). We observe that by increasing the values of time delay, the lag at which the first minimum of the AMI function occurs, is $T_m = 4$. Hence, this value is chosen as the suitable time delay $\tau = 4$.

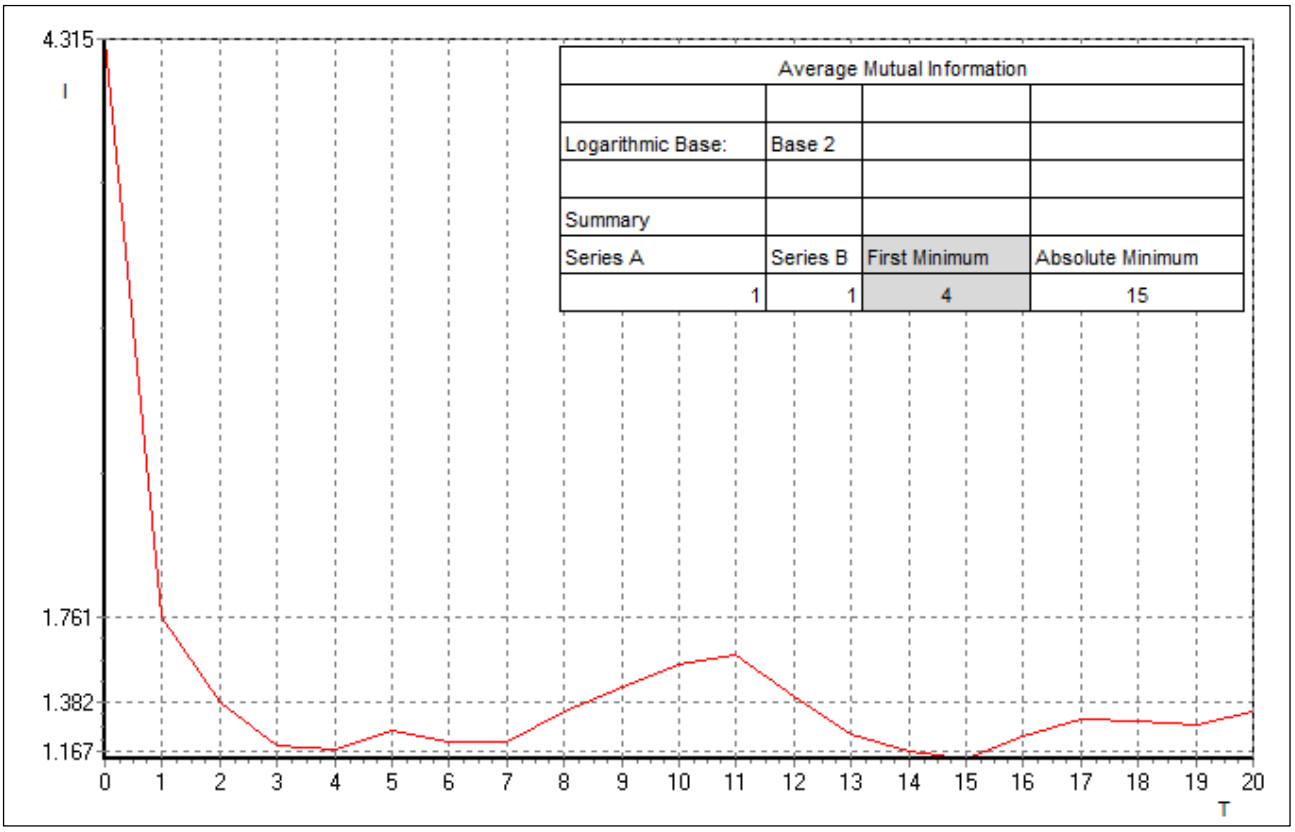

Figure 35 The AMI as a function of the time delay $I = I(T)$ for $T = 0, 1, \ldots, 20$.

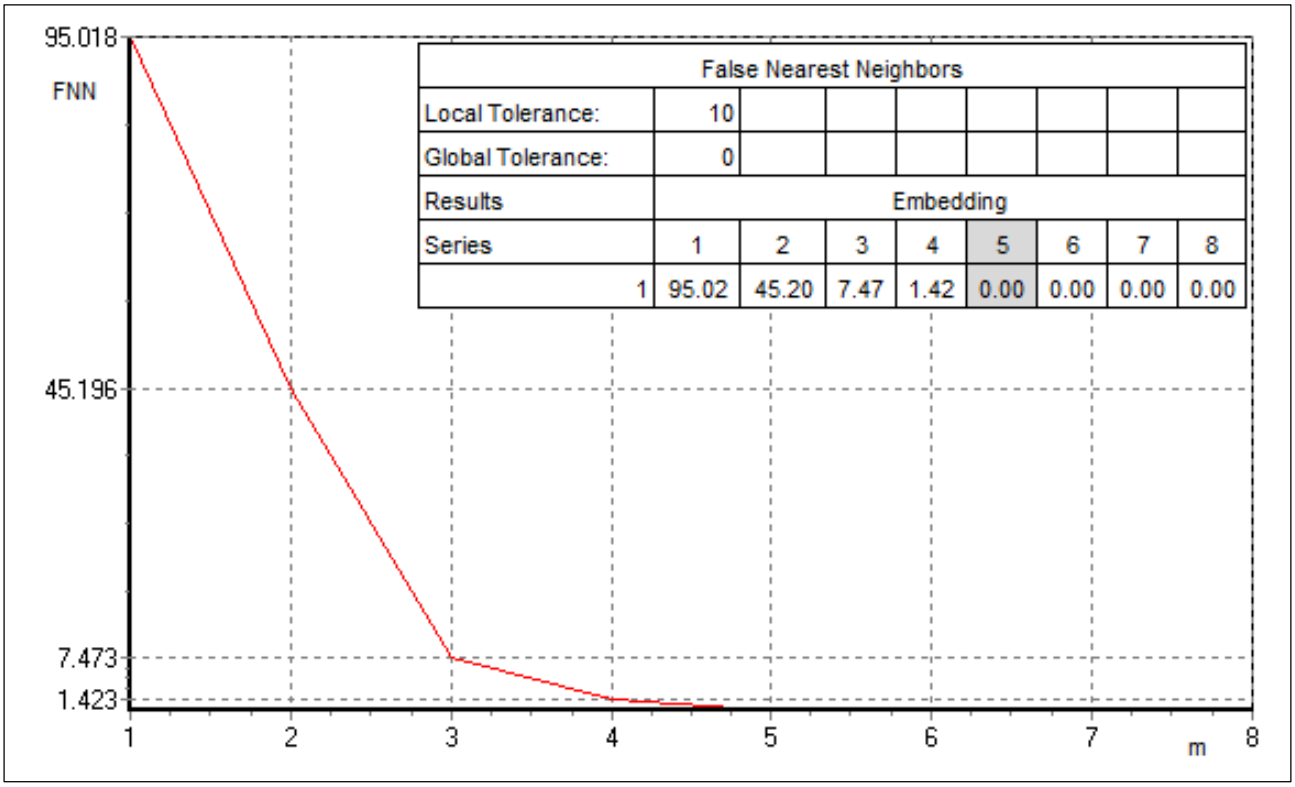

Figure 36 The FNN as a function of the embedding dimension FNN = FNN(m) for $m = 1, 2, \ldots, 8$.

In order to find the suitable embedding dimension, we use the False Nearest Neighbors, which has been introduced by Kennel *et al.* (1992) as a convenient method to determine the minimal sufficient embedding dimension (Subsection 1.4.1). We calculate the FNN as a function of the embedding dimension FNN = FNN(m) for m = 1, 2, …, 8 (Figure 36). We observe that by increasing the values of the embedding parameter, the first dimension, at which the number of FNN drops to zero, occurs around the value five. Taking into account that the suitable embedding dimension should not be smaller than this value, the embedding dimension is chosen to be $m \approx 5$. Moreover, the suitable embedding dimension indicates that at an embedding of five dimensions the attractor of the yearly SSN series is unfolded.

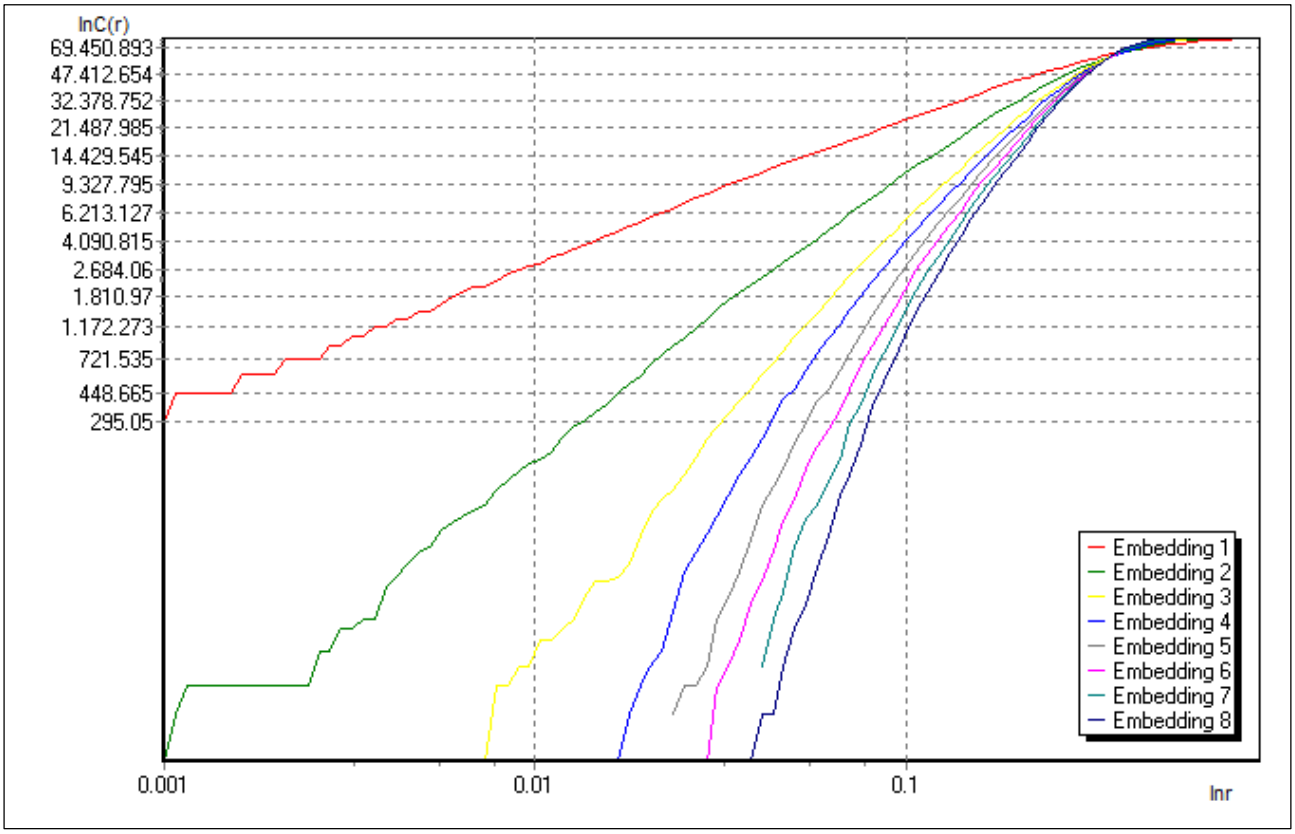

Figure 37 The graph of $\ln C^{(m)}(r)$ for increasing values of $\ln r$ for $m = 1, 2, ..., 8$ embedding dimensions.

Dimension of the yearly SSN data attractor

Once again, in order to find the dimension of the attractor of our system, we use the correlation dimension, which has been introduced by Grassberger and Procaccia (1983a, 1983b) as a suitable method to compute the fractal dimension of an attractor (Subsection 1.4.2). First we calculate the logarithm of the correlation integral $\ln C^{(m)}(r)$ with increasing values of the logarithm of the distance in phase space ln r for various embedding dimensions [m] (Figure 37). By finding the slope of this

graph we estimate the correlation dimension [D_c (m)] for every embedding dimension [m]. By calculating the correlation dimension as a function of the embedding dimension $D_c = D_c(m)$ for m = 1, 2, …, 8 embedding steps (Figure 38), we are able to determine the fractal dimension of the attractor of the yearly SSN data. For increasing values of the embedding parameter, we observe that once the embedding dimension exceeds the value $m_c \approx 5$ the correlation dimension $D_c(m)$ converges to the value $v = D_c \approx 2.87$. Moreover, the embedding dimension value, at which the convergence begins, is about twice the attractor dimension $m_c \approx 2D_c$. Hence, the dimension of our system's attractor is estimated to be $D_c \approx 2.87$; this value indicates that the attractor of the yearly SSN data is low dimensional, and the system can be described by $v = 3$ independent variables. Once again, the convergence of the correlation dimension as [m] increases to its true value $v = D_c$ is a strong indication of chaos, since a correlation dimension that does not converge, corresponds to a white noise signal.

Predictive power

Another way to investigate the presence of chaos in the yearly SSN data is by calculating the largest Lyapunov exponent [$\lambda_{\max}$]. As mentioned above (Subsection 1.2.1), Rosenstein *et al.* (1993) and Kantz (1994) developed two methods for calculating the largest Lyapunov exponent. Our yearly SSN time series is considered to be a small data set (313 observations). Thus, in this section we use the Rosenstein algorithm since it applies better to small data sets than the Kantz algorithm. By using the Rosenstein algorithm, the largest Lyapunov exponent is estimated to be $\lambda_{max} = 0.0207$. Its positive value indicates the presence of chaotic behavior in solar-activity dynamics, while its small value indicates that the presence of chaos is weak. Further, as already mentioned above (Subsection 1.2.1), by using the largest Lyapunov exponent we can estimate the upper limit on the period over which the yearly SSN data can be used to make deterministic predictions. This time limit is given by the inverse of the largest Lyapunov exponent and is estimated to be

$$T_{\text{pr}} \approx \frac{1}{\lambda_{\max}} = \frac{1}{0.0207} \approx 48 \text{ years}$$

The predictive maximum interval extent of the yearly mean SSN data is 48 years providing a reasonable basis for solar activity predictions of long range. Thus, considering the weak chaotic nature of our yearly mean sunspot-number data, we conclude that long-term predictions are quite possible due to the system's low sensitivity to initial conditions. In conclusion, the results of our analysis indicate that the yearly mean SSN data (1700 – 2012) is a low-dimensional deterministic chaotic system.

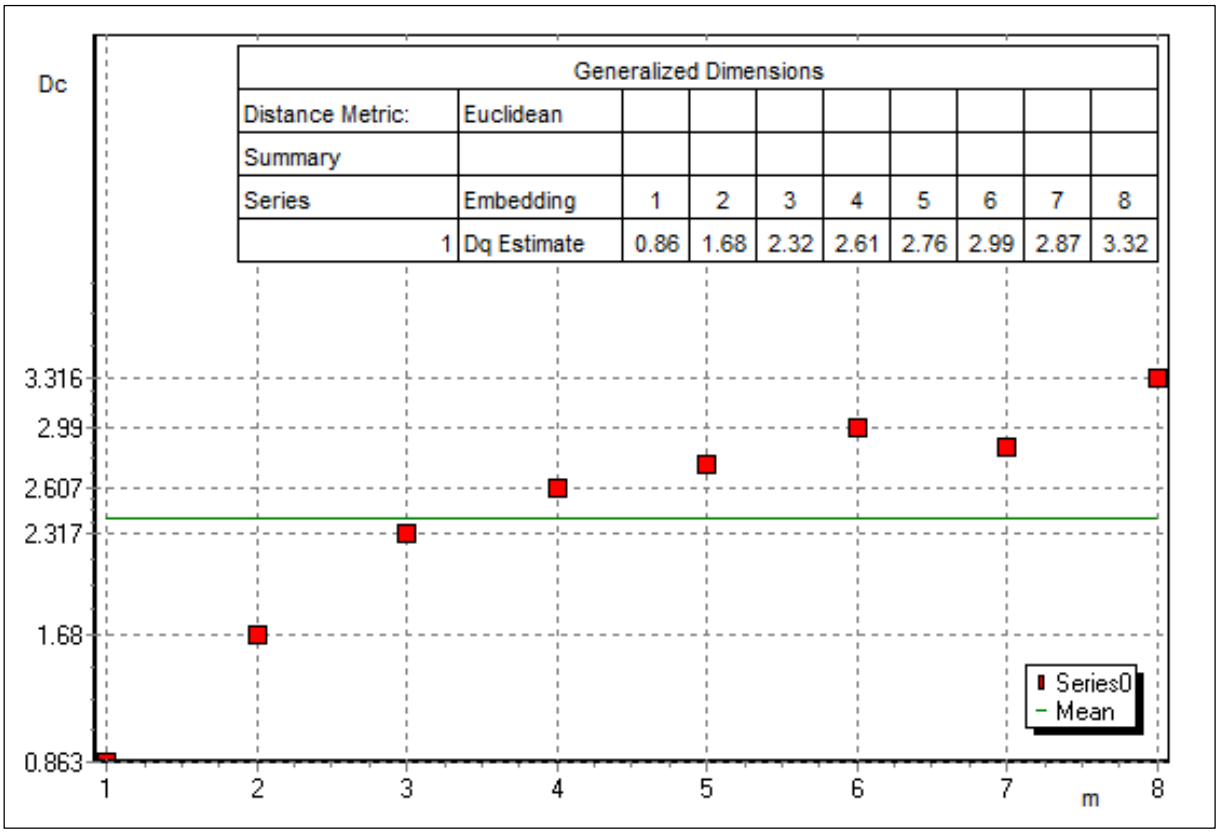

Figure 38 The correlation dimension as a function of the embedding dimension $D_c = D_c(m)$ for $m = 1, 2, \ldots, 8$ embedding steps.

4.2.2 *Post-facto* and future solar activity predictions

Considering the results of our data analysis, in this subsection we perform short-term and long-term predictions, trying to forecast the yearly mean sunspot numbers during the following years.

Short-term future sunspot-number predictions

We perform short-term future predictions in order to forecast the evolution of the present sunspot Cycle 24 during the next few years. In particular, we perform future predictions during the next five years, from 2013 to 2017. The proposed neural network model that predicts the testing data most accurately is the following:

$$
\begin{aligned}
&R_Z(t) = -0.9668 + 0.5253\{0.5704N[151] + 0.4378N[166]\} \\
&+0.4892\{-17.53 + 0.2948R_Z(t-259) + 1.104N[158]\} \\
&N[151] = 4.288 + 1.12R_Z(t-163) - 1.514R_Z(t-293) \\
&N[166] = 141.6 - 1.752R_Z(t-180) - 1.997R_Z(t-188) \\
&N[158] = -27.18 + 0.511R_z(t-32) + 0.6699R_z(t-213)
\end{aligned}
\qquad (19)
$$

$R_Z(t)$ is the predicted value of the yearly SSN at time period t (for $t = 314, 315, 316,\ldots$); $R_Z(t-163)$, $R_Z(t-293)$, $R_Z(t-180)$, $R_Z(t-188)$, $R_Z(t-259)$, $R_Z(t-32)$ and $R_Z(t-213)$ are the observed values of the yearly SSN at 163, 293, 180, 188, 259, 32, and 213 steps back in time, before the time period t (*e.g.* for the next period, $t = 314$, year 2013, the value $R_Z(t-163) = R_Z(314-163) = R_Z(151)$ corresponds to the observed yearly SSN value in 1850).

The five-years-ahead predictions of the proposed neural network model (Equation (19)) for the period 2013 – 2017 are illustrated in Figure 39. We observe that the MAE and the RMSE of the post-processed learning predictions are quite small, MAE = 1.333 and RMSE = 1.599, indicating the high predictive accuracy of our neural network model (Equation (19)). We predicted that the peak sunspot number for the present Cycle 24 would be significantly smaller than Cycle 23, with peak sunspot number of 54 in 2013, which is equivalent to the solar activity levels during the Dalton Minimum in 1804 (peak sunspot number of 47.5). Thus, the current Cycle 24 was expected to be a low-peak cycle; in fact, the weakest sunspots cycle over the last 100 years (the last small minimum in solar activity took place at the beginning of 1900s (Clilverd *et al.*, 2003)).

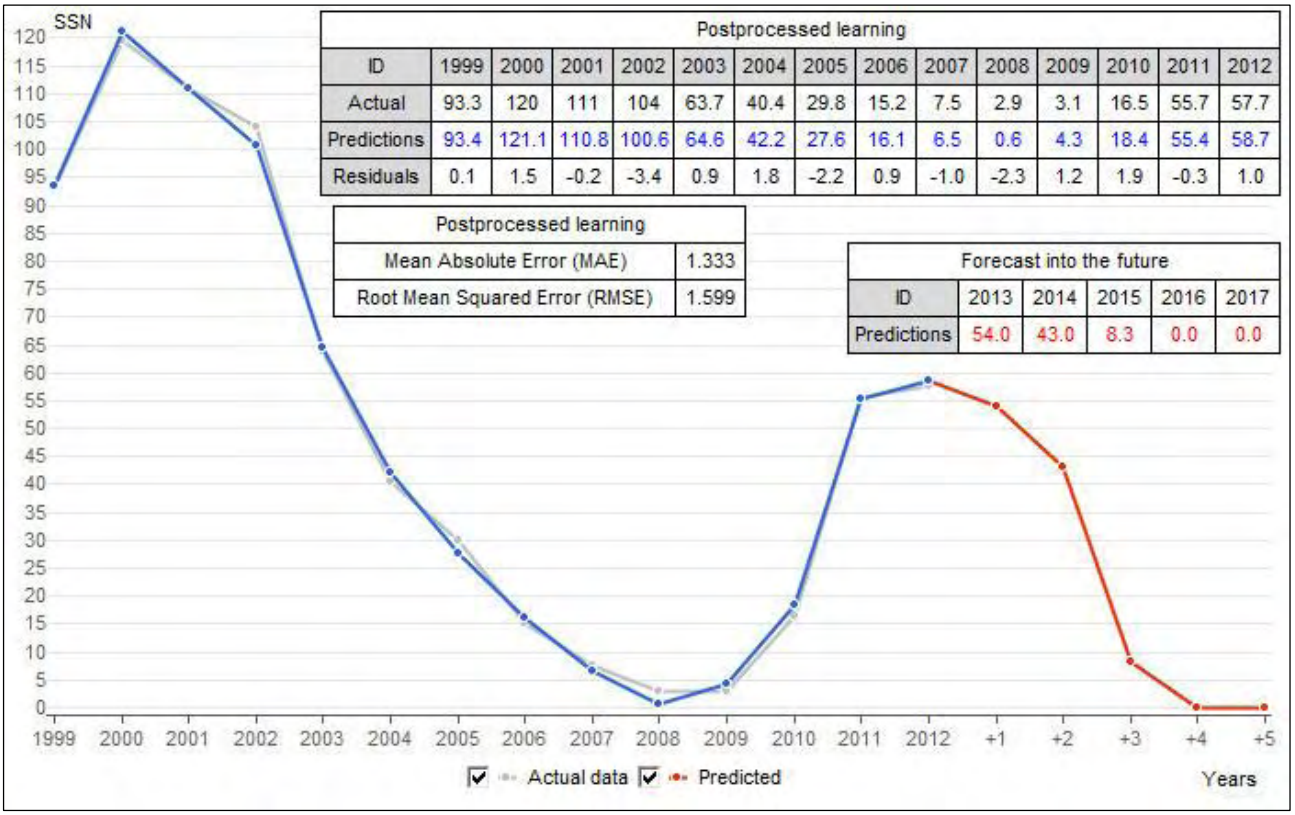

Figure 39 Future yearly sunspot-number predictions 5-steps-ahead (2013 – 2017). The grey curve corresponds to the actual sunspot-number data; the blue curve corresponds to the post-processed learning of the proposed neural network model; the red curve corresponds to the future predictions.

Further, we predict that the yearly mean SSN during the next 5 years will decrease continuously until 2016 – 2017, where it drops to zero. Thus, we expect that the solar activity during the present cycle is likely to resemble that in Dalton Minimum, rather than increasing, as has occurred during the previous 100 years. The expected peak sunspot number, which our model predicts (*i.e.* 54 for 2013) is quite close to the corresponding actual value 64.9 (the observed yearly mean SSN for the year 2013 has been announced by the Solar Influenced Data Analysis Center (SIDC) on 1 January 2014).

Testing predictive skill of the proposed method

In order to test the predictive skill of our proposed method we perform predictions of the sunspot number Cycles 19 – 23. We try to forecast each cycle separately (19, 20, 21, 22, 23) if only data up to the previous cycle were available (18, 19, 20, 21, 22 – respectively) and we compare them with the corresponding observed values. In particular, we conduct predictions of: the Cycle 19 (1955 – 1964) using the full database from 1700 up to Cycle 18 (1700 – 1954), the Cycle 20 (1965 – 1976) using the full database from 1700 up to Cycle 19 (1700 – 1964), *etc.* The predictions of each cycle are illustrated in Figure 40. We observe that the differences between the predicted and observed values (residuals) are quite small; the predictions of the proposed neural network model corresponding to each Cycle 19, 20, …, 23 fit the values of the actual data exceptionally well. Moreover, we observe that the values of the MAE and the RMSE of the post-processed learning predictions are quite small ($5.63 \leq$ MAE, RMSE ≤ 9.87), indicating the high predictive accuracy of each neural network model.

Furthermore, Waldmeier (1935) showed that there is an anti-correlation between the rise-time of a cycle and its peak sunspot number; *i.e.* strong cycles are expected to have shorter rise-time, while cycles with weaker peak rise more slowly. Ahluwalia (2003) using data for Cycles 17 – 23 concluded that the "Waldmeier effect" is still present; he showed that the active cycles evolved faster and the moderate cycles attained their maximum an average of five months later. We observe that our method seems to predict the peak sunspot number of each cycle remarkably well and its ascending phase (rise-time) as well; even for the case of the strongest Cycle 19 with a maximum observed value of 190, our method predicted a maximum of about 186.5. The only exception is the Cycle 21 with a predicted maximum sunspot number of about 111.8 (1982) three years after the observed value 155.4 (1979). The cause of this prediction error is unknown; however, it could be due to the limited ability of our method to describe precisely the nonlinear features of the SSN time series. Hence, despite this error, we conclude that our method predicts quite precisely the Cycles 19 – 23 despite the presence of the "Waldmeier effect".

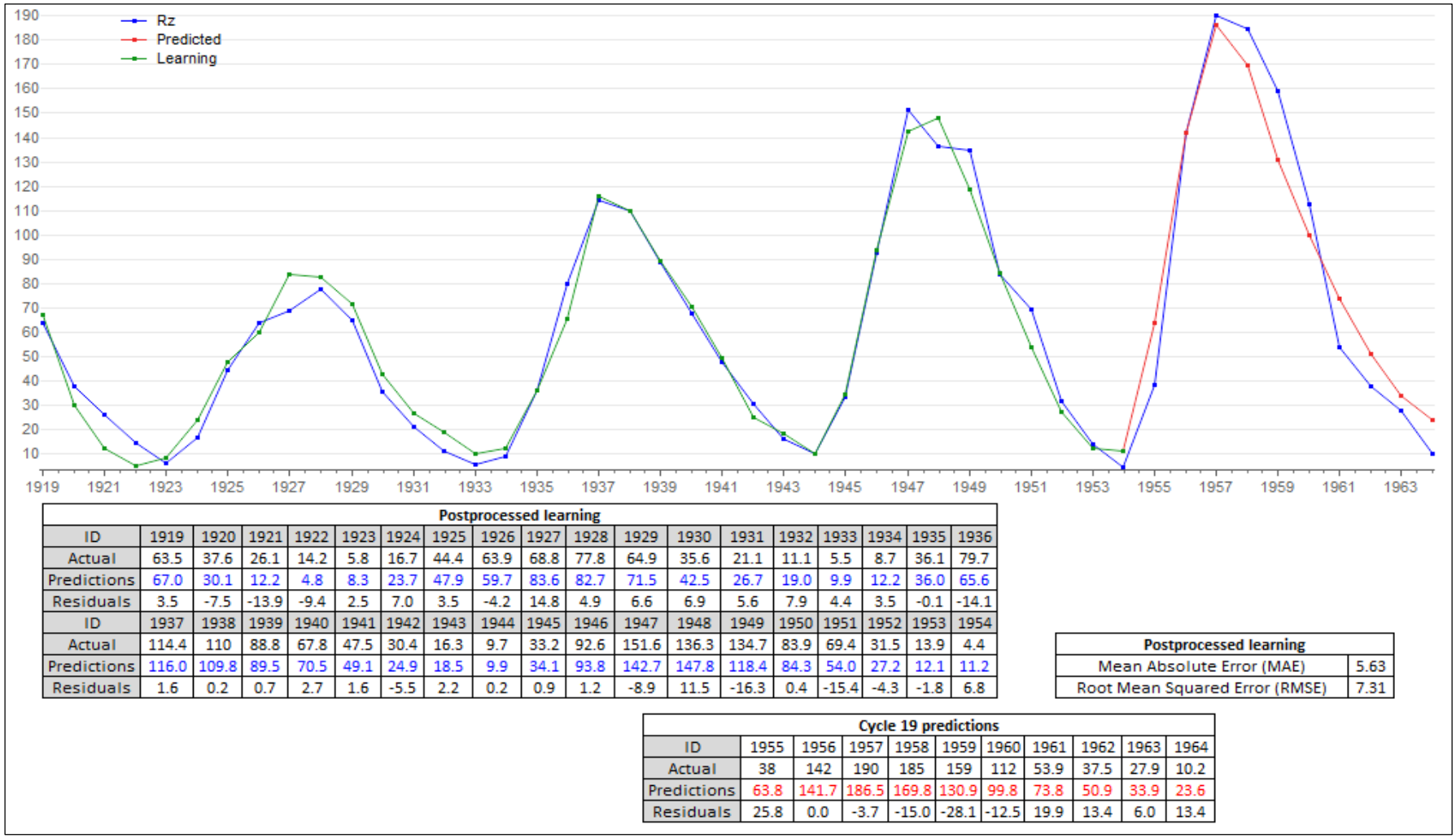

(a)

Postprocessed learning																			
ID	1919	1920	1921	1922	1923	1924	1925	1926	1927	1928	1929	1930	1931	1932	1933	1934	1935	1936
Actual	63.5	37.6	26.1	14.2	5.8	16.7	44.4	63.9	68.8	77.8	64.9	35.6	21.1	11.1	5.5	8.7	36.1	79.7
Predictions	67.0	30.1	12.2	4.8	8.3	23.7	47.9	59.7	83.6	82.7	71.5	42.5	26.7	19.0	9.9	12.2	36.0	65.6
Residuals	3.5	-7.5	-13.9	-9.4	2.5	7.0	3.5	-4.2	14.8	4.9	6.6	6.9	5.6	7.9	4.4	3.5	-0.1	-14.1
ID	1937	1938	1939	1940	1941	1942	1943	1944	1945	1946	1947	1948	1949	1950	1951	1952	1953	1954
Actual	114.4	110	88.8	67.8	47.5	30.4	16.3	9.7	33.2	92.6	151.6	136.3	134.7	83.9	69.4	31.5	13.9	4.4
Predictions	116.0	109.8	89.5	70.5	49.1	24.9	18.5	9.9	34.1	93.8	142.7	147.8	118.4	84.3	54.0	27.2	12.1	11.2
Residuals	1.6	0.2	0.7	2.7	1.6	-5.5	2.2	0.2	0.9	1.2	-8.9	11.5	-16.3	0.4	-15.4	-4.3	-1.8	6.8

Postprocessed learning	
Mean Absolute Error (MAE)	5.63
Root Mean Squared Error (RMSE)	7.31

Cycle 19 predictions										
ID	1955	1956	1957	1958	1959	1960	1961	1962	1963	1964
Actual	38	142	190	185	159	112	53.9	37.5	27.9	10.2
Predictions	63.8	141.7	186.5	169.8	130.9	99.8	73.8	50.9	33.9	23.6
Residuals	25.8	0.0	-3.7	-15.0	-28.1	-12.5	19.9	13.4	6.0	13.4

Figure 40 Yearly sunspot-number predictions of the Cycles 19-23. The blue curve corresponds to the actual sunspot-number data; the green curve corresponds to the post-processed learning of the proposed neural network model; the red curve corresponds to the cycle predictions. (a) Predictions of Cycle 19 (1955 – 1964) if only data up to Cycle 18 (1700 – 1954) were available. (b) Predictions of Cycle 20 (1965 – 1976) if only data up to Cycle 19 (1700 – 1964) were available. (c) Predictions of Cycle 21 (1977 – 1986) if only data up to Cycle 20 (1700 – 1976) were available. (d) Predictions of Cycle 22 (1987 – 1996) if only data up to Cycle 21 (1700 – 1986) were available. (e) Predictions of Cycle 23 (1997 – 2008) if only data up to Cycle 22 (1700 – 1996) were available.

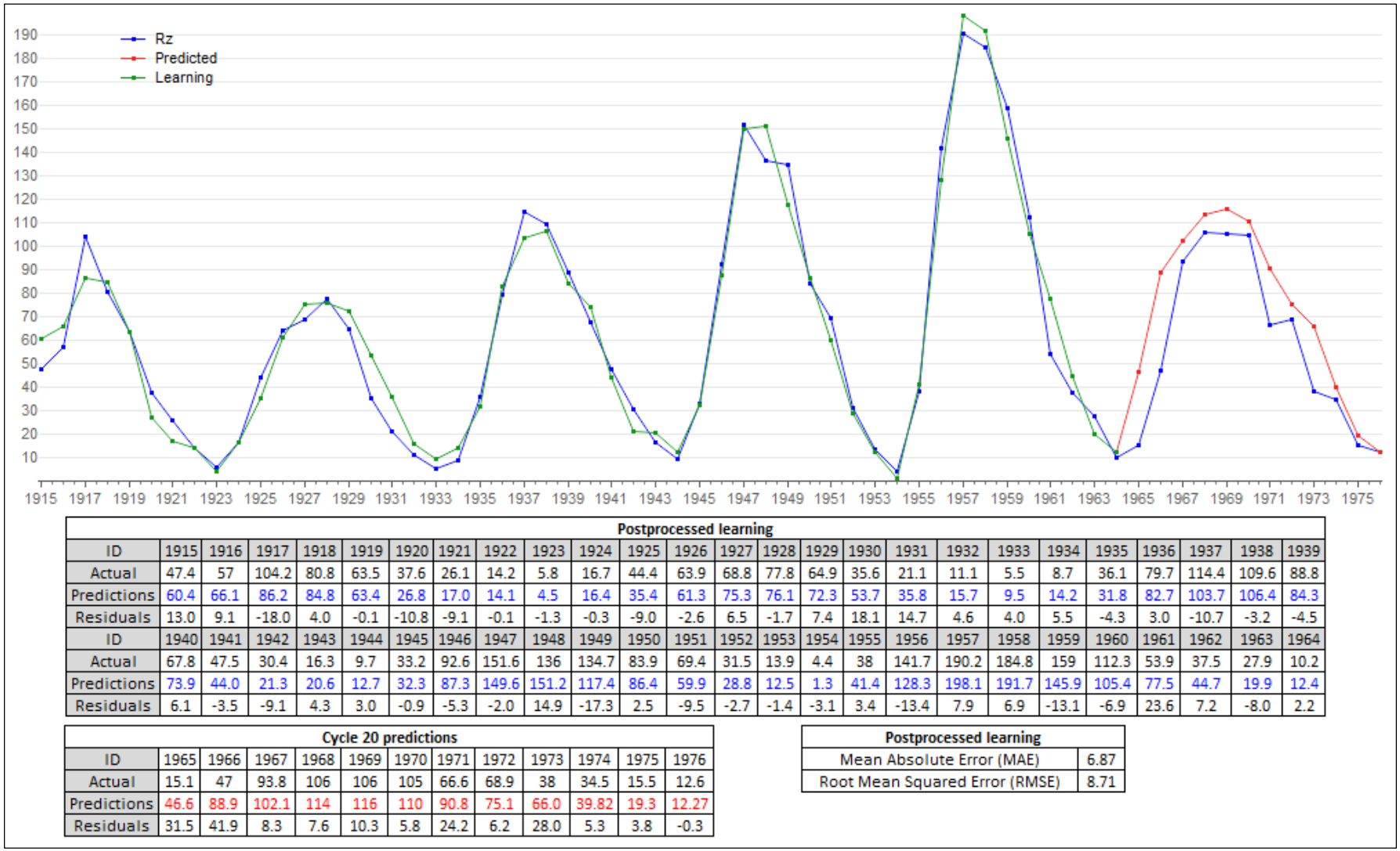

Postprocessed learning

ID	1915	1916	1917	1918	1919	1920	1921	1922	1923	1924	1925	1926	1927	1928	1929	1930	1931	1932	1933	1934	1935	1936	1937	1938	1939
Actual	47.4	57	104.2	80.8	63.5	37.6	26.1	14.2	5.8	16.7	44.4	63.9	68.8	77.8	64.9	35.6	21.1	11.1	5.5	8.7	36.1	79.7	114.4	109.6	88.8
Predictions	60.4	66.1	86.2	84.8	63.4	26.8	17.0	14.1	4.5	16.4	35.4	61.3	75.3	76.1	72.3	53.7	35.8	15.7	9.5	14.2	31.8	82.7	103.7	106.4	84.3
Residuals	13.0	9.1	-18.0	4.0	-0.1	-10.8	-9.1	-0.1	-1.3	-0.3	-9.0	-2.6	6.5	-1.7	7.4	18.1	14.7	4.6	4.0	5.5	-4.3	3.0	-10.7	-3.2	-4.5
ID	1940	1941	1942	1943	1944	1945	1946	1947	1948	1949	1950	1951	1952	1953	1954	1955	1956	1957	1958	1959	1960	1961	1962	1963	1964
Actual	67.8	47.5	30.4	16.3	9.7	33.2	92.6	151.6	136	134.7	83.9	69.4	31.5	13.9	4.4	38	141.7	190.2	184.8	159	112.3	53.9	37.5	27.9	10.2
Predictions	73.9	44.0	21.3	20.6	12.7	32.3	87.3	149.6	151.2	117.4	86.4	59.9	28.8	12.5	1.3	41.4	128.3	198.1	191.7	145.9	105.4	77.5	44.7	19.9	12.4
Residuals	6.1	-3.5	-9.1	4.3	3.0	-0.9	-5.3	-2.0	14.9	-17.3	2.5	-9.5	-2.7	-1.4	-3.1	3.4	-13.4	7.9	6.9	-13.1	-6.9	23.6	7.2	-8.0	2.2

Cycle 20 predictions

ID	1965	1966	1967	1968	1969	1970	1971	1972	1973	1974	1975	1976
Actual	15.1	47	93.8	106	106	105	66.6	68.9	38	34.5	15.5	12.6
Predictions	46.6	88.9	102.1	114	116	110	90.8	75.1	66.0	39.82	19.3	12.27
Residuals	31.5	41.9	8.3	7.6	10.3	5.8	24.2	6.2	28.0	5.3	3.8	-0.3

Postprocessed learning	
Mean Absolute Error (MAE)	6.87
Root Mean Squared Error (RMSE)	8.71

(b)

Figure 40 (*Continued*.)

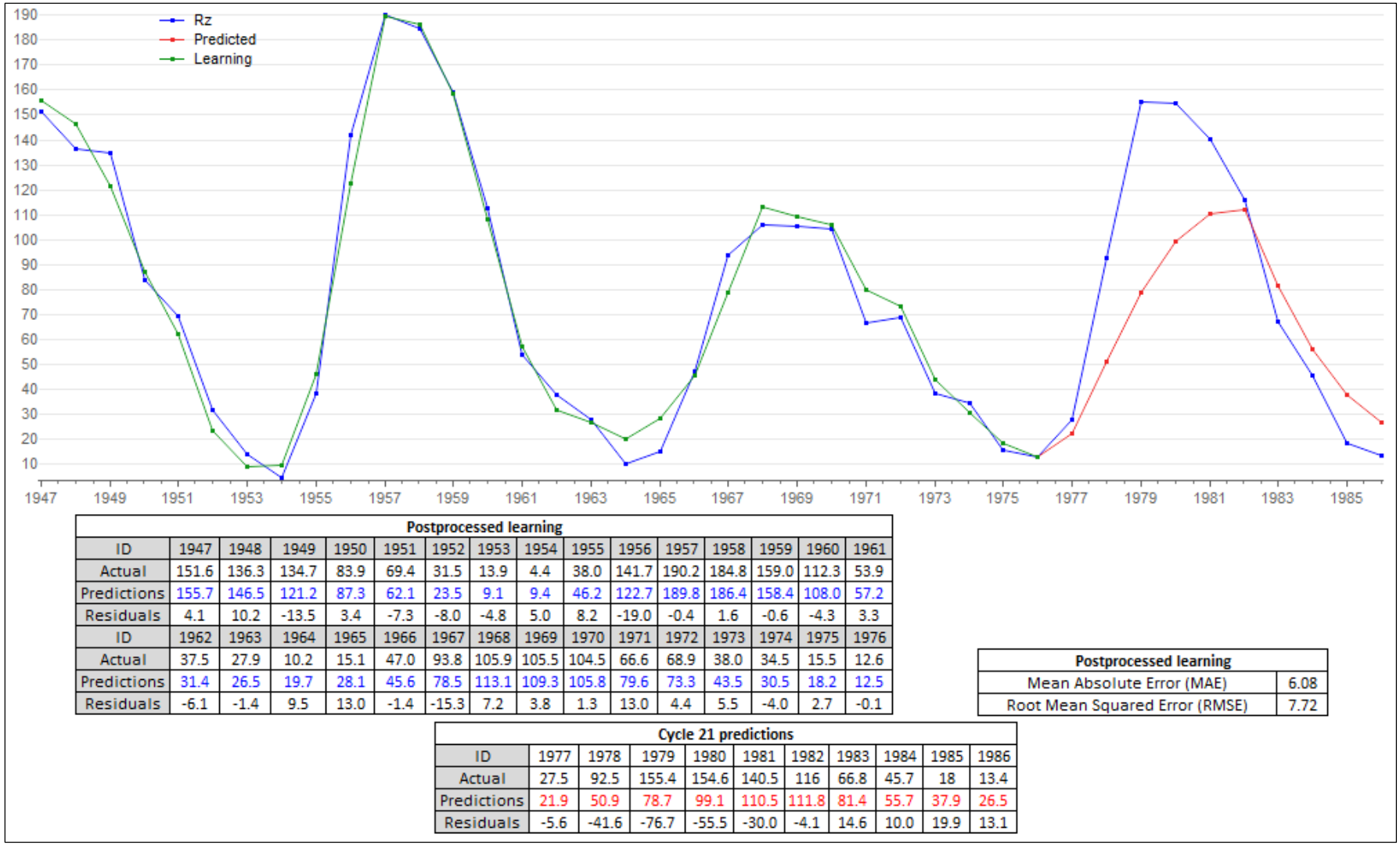

Postprocessed learning

ID	1947	1948	1949	1950	1951	1952	1953	1954	1955	1956	1957	1958	1959	1960	1961
Actual	151.6	136.3	134.7	83.9	69.4	31.5	13.9	4.4	38.0	141.7	190.2	184.8	159.0	112.3	53.9
Predictions	155.7	146.5	121.2	87.3	62.1	23.5	9.1	9.4	46.2	122.7	189.8	186.4	158.4	108.0	57.2
Residuals	4.1	10.2	-13.5	3.4	-7.3	-8.0	-4.8	5.0	8.2	-19.0	-0.4	1.6	-0.6	-4.3	3.3
ID	1962	1963	1964	1965	1966	1967	1968	1969	1970	1971	1972	1973	1974	1975	1976
Actual	37.5	27.9	10.2	15.1	47.0	93.8	105.9	105.5	104.5	66.6	68.9	38.0	34.5	15.5	12.6
Predictions	31.4	26.5	19.7	28.1	45.6	78.5	113.1	109.3	105.8	79.6	73.3	43.5	30.5	18.2	12.5
Residuals	-6.1	-1.4	9.5	13.0	-1.4	-15.3	7.2	3.8	1.3	13.0	4.4	5.5	-4.0	2.7	-0.1

Postprocessed learning	
Mean Absolute Error (MAE)	6.08
Root Mean Squared Error (RMSE)	7.72

Cycle 21 predictions

ID	1977	1978	1979	1980	1981	1982	1983	1984	1985	1986
Actual	27.5	92.5	155.4	154.6	140.5	116	66.8	45.7	18	13.4
Predictions	21.9	50.9	78.7	99.1	110.5	111.8	81.4	55.7	37.9	26.5
Residuals	-5.6	-41.6	-76.7	-55.5	-30.0	-4.1	14.6	10.0	19.9	13.1

(c)

Figure 40 (*Continued*.)

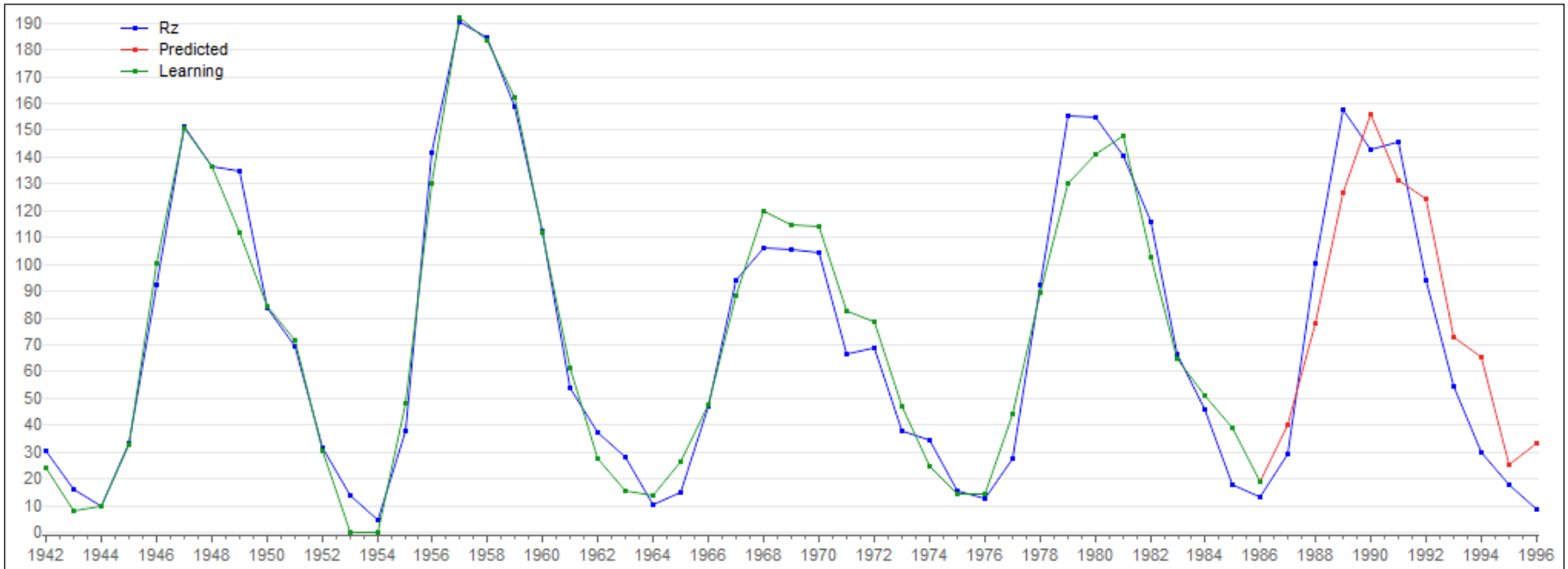

Postprocessed learning

ID	1942	1943	1944	1945	1946	1947	1948	1949	1950	1951	1952	1953	1954	1955	1956	1957	1958	1959	1960	1961	1962	1963	1964
Actual	30.4	16.3	9.7	33.2	92.6	151.6	136.3	134.7	83.9	69.4	31.5	13.9	4.4	38.0	141.7	190.2	184.8	159.0	112.3	53.9	37.5	27.9	10.2
Predictions	24.3	8.1	9.7	32.6	100.5	150.9	136.7	111.8	84.4	71.8	30.7	0.0	0.0	48.2	130.3	192.1	183.4	162.2	111.6	61.6	27.7	15.6	14.0
Residuals	-6.1	-8.2	0.0	-0.6	7.9	-0.7	0.4	-22.9	0.5	2.4	-0.8	-13.9	-4.4	10.2	-11.4	1.9	-1.4	3.2	-0.7	7.7	-9.8	-12.3	3.8
ID	1965	1966	1967	1968	1969	1970	1971	1972	1973	1974	1975	1976	1977	1978	1979	1980	1981	1982	1983	1984	1985	1986	
Actual	15.1	47.0	93.8	105.9	105.5	104.5	66.6	68.9	38.0	34.5	15.5	12.6	27.5	92.5	155.4	154.6	140.5	115.9	66.8	45.7	18.0	13.4	
Predictions	26.3	47.4	88.3	119.7	115.0	114.3	82.6	78.7	47.1	24.7	14.1	14.4	44.3	89.4	130.3	141.3	147.7	102.9	65.0	51.3	39.1	18.9	
Residuals	11.2	0.4	-5.5	13.8	9.5	9.8	16.0	9.8	9.1	-9.8	-1.4	1.8	16.8	-3.1	-25.1	-13.3	7.2	-13.0	-1.8	5.6	21.1	5.5	

Cycle 22 predictions

ID	1987	1988	1989	1990	1991	1992	1993	1994	1995	1996
Actual	29.4	100	158	143	146	94.3	54.6	29.9	17.5	8.6
Predictions	40.0	77.9	126.5	156.0	131.3	124.5	72.7	65.2	25.1	33.3
Residuals	10.6	-22.3	-31.1	13.4	-14.4	30.2	18.1	35.3	7.6	24.7

Postprocessed learning

Mean Absolute Error (MAE)	7.6
Root Mean Squared Error (RMSE)	9.87

(d)

Figure 40 (*Continued*.)

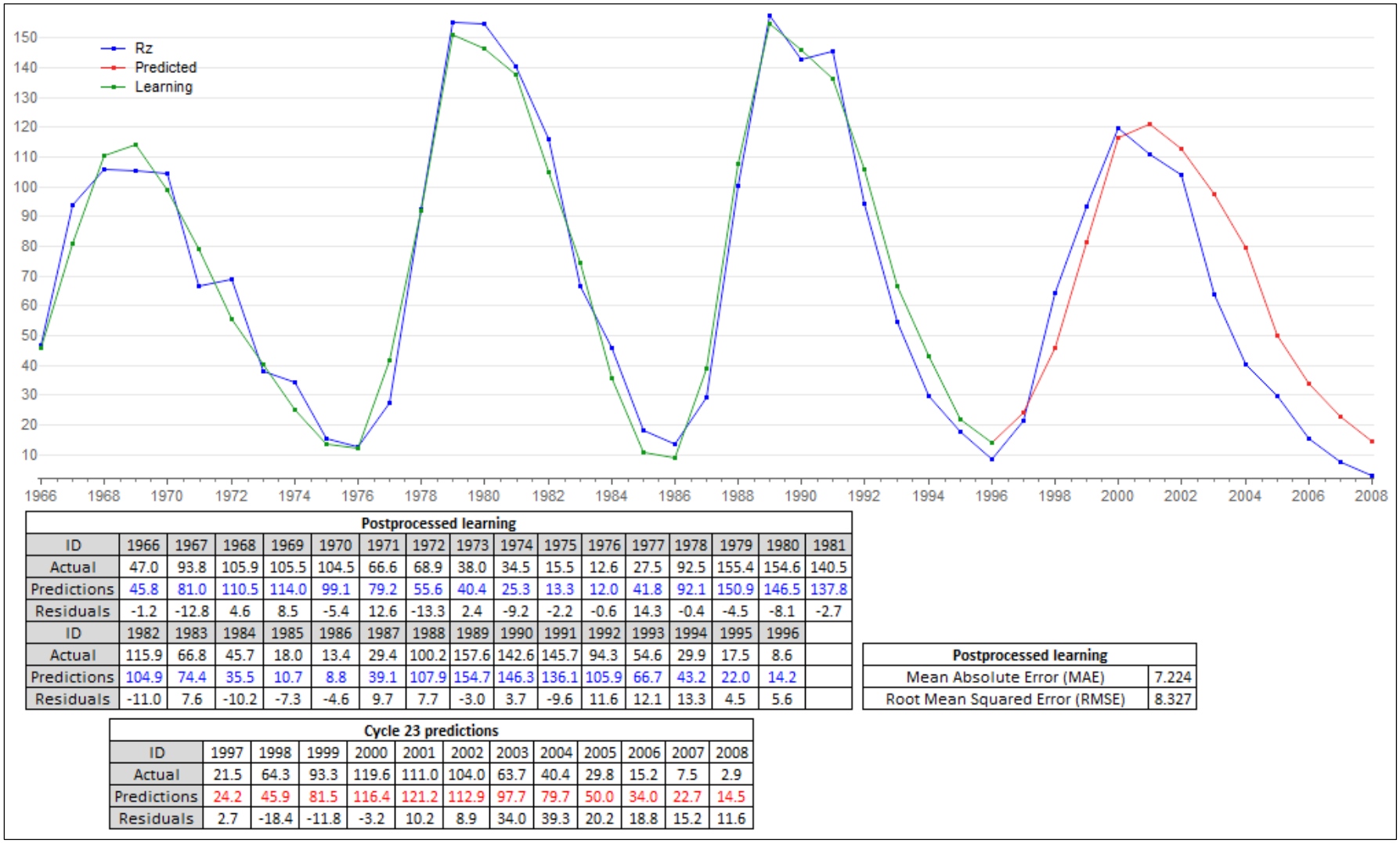

Postprocessed learning

ID	1966	1967	1968	1969	1970	1971	1972	1973	1974	1975	1976	1977	1978	1979	1980	1981
Actual	47.0	93.8	105.9	105.5	104.5	66.6	68.9	38.0	34.5	15.5	12.6	27.5	92.5	155.4	154.6	140.5
Predictions	45.8	81.0	110.5	114.0	99.1	79.2	55.6	40.4	25.3	13.3	12.0	41.8	92.1	150.9	146.5	137.8
Residuals	-1.2	-12.8	4.6	8.5	-5.4	12.6	-13.3	2.4	-9.2	-2.2	-0.6	14.3	-0.4	-4.5	-8.1	-2.7
ID	1982	1983	1984	1985	1986	1987	1988	1989	1990	1991	1992	1993	1994	1995	1996	
Actual	115.9	66.8	45.7	18.0	13.4	29.4	100.2	157.6	142.6	145.7	94.3	54.6	29.9	17.5	8.6	
Predictions	104.9	74.4	35.5	10.7	8.8	39.1	107.9	154.7	146.3	136.1	105.9	66.7	43.2	22.0	14.2	
Residuals	-11.0	7.6	-10.2	-7.3	-4.6	9.7	7.7	-3.0	3.7	-9.6	11.6	12.1	13.3	4.5	5.6	

Postprocessed learning	
Mean Absolute Error (MAE)	7.224
Root Mean Squared Error (RMSE)	8.327

Cycle 23 predictions

ID	1997	1998	1999	2000	2001	2002	2003	2004	2005	2006	2007	2008
Actual	21.5	64.3	93.3	119.6	111.0	104.0	63.7	40.4	29.8	15.2	7.5	2.9
Predictions	24.2	45.9	81.5	116.4	121.2	112.9	97.7	79.7	50.0	34.0	22.7	14.5
Residuals	2.7	-18.4	-11.8	-3.2	10.2	8.9	34.0	39.3	20.2	18.8	15.2	11.6

(e)

Figure 40 (*Continued*.)

Long-term *post-facto* predictions

We perform long-term past reconstruction of 90 steps (years) back in time (1610 – 1699) in order to see whether our neural network model (Equation (19)) is able to predict the Maunder Minimum period (1615 – 1715). The Zürich SSN data (R_Z numbers) define the solar activity from 1700 onwards including only the Dalton Minimum period (1790 – 1830); Wolf missed some observers, such as Hevelius's observations from 1642 to 1684 and Flamsteed's observations from 1676 to 1719 which provide a good coverage of the Maunder Minimum period, and had incorrect tabulations of several observers (Hoyt and Schatten, 1995a; 1995b). Thus, in order to compare our *post-facto* predictions with the actual sunspot-number data before the year 1700, we further need to include the actual SSN series for the period of the Maunder Minimum. The Group Sunspot Number [R_G] series appears to be the best choice, since it includes observation sunspot-number values during the last grand minimum – the Maunder Minimum era (Hoyt and Schatten, 1998). Therefore, just for the sake of comparison, we use the solar-activity reconstruction (R_G time series) made by Hoyt and Schatten (1998) for the time period 1610 – 1699 as the actual sunspot-number observations during the Maunder Minimum period.

The solar activity reconstruction made by Hoyt and Schatten (1998) uses the Sunspot Group Number [R_G], rather than the Zürich Sunspot Number [R_Z]. The Sunspot Group Number [R_G] is much easier to reconstruct from early observations. It is defined as

$$R_G = \frac{12.08}{N} \sum k_i' G_i$$

G_i is the number of sunspot groups recorded by the i^{th} observer, k_i' is the i^{th} observer's correction factor, N is the number of observers used to form the daily value, and 12.08 is a normalization factor chosen to make the mean of the R_Gs identical with the mean of the R_Z for 1874 through 1976.

Faria *et al.* (2004) compared the characteristics of the R_G and R_Z time series concluding that the well-known periodicities (the Gleissberg cycle ≈ 90 – 100 years, the Schwabe cycle ≈ 11 years, and the second solar harmonic ≈ 5 years) and the main spectral characteristics of both indices are very similar.

The differences between the sunspot number during the Maunder Minimum and our *post-facto* predictions are shown in Figure 41, where we compare our *post-facto* predictions with the Sunspot Group Number for the time period 1610 – 1699. We observe that a few years before the Maunder Minimum the difference between the predicted and observed sunspot number is somewhat large (>50); particularly, our model underestimates the solar activity during the years 1610 – 1614 where the predicted SSN values are 0, 0, 0, 0, and 11.3 respectively, while the corresponding actual SSN values are 72, 54.7, 92.1, 92.3 and 109.7 respectively. This also occurs during the years 1638 and 1639 where

the predicted values are 11 and 13.2 respectively, while the actual values are 69.2 and 76.7 respectively. Despite these seven somewhat large differences among the predicted and observed SSN values, during the remaining 25 years before Maunder Minimum (1615 – 1637 and 1640 – 1644), we observe only small overestimates and underestimates in general.

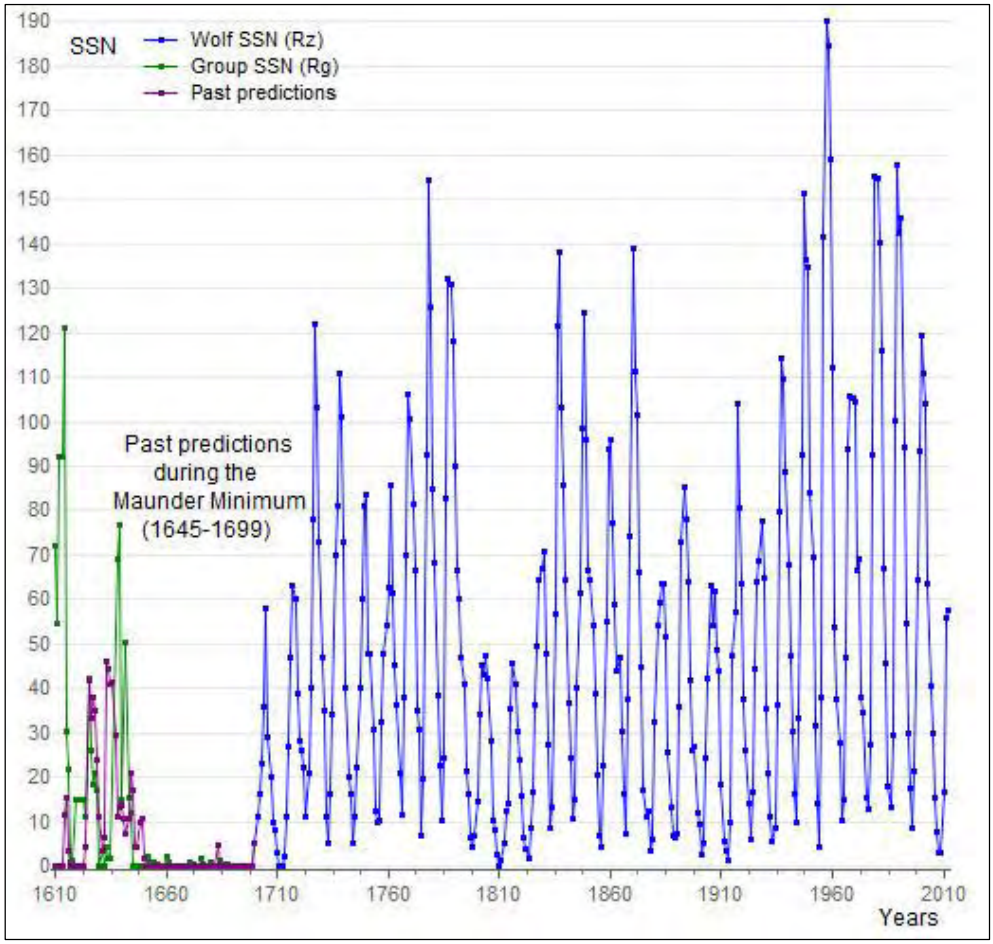

Figure 41 *Post-facto* yearly sunspot-number predictions of 90 steps back in time (1610 – 1699). The blue curve corresponds to the actual yearly mean sunspot-number data (1700 – 2012) of the Wolf's reconstruction [R_Z]; the purple curve corresponds to the *post-facto* predictions of our neural network model; the green curve corresponds to the actual yearly mean sunspot-number data (1610 – 1699) of the Hoyt and Schatten's reconstruction [R_G].

Concerning the Maunder Minimum, we observe something impressive. Our *post-facto* predictions fit the actual sunspot-number data during the Maunder Minimum period (1645 – 1669) almost perfectly (Table 4); extremely long intervals without sunspots occurred, while the average difference between the observed and the predicted SSN values is only ± 0.7. Thus, despite the fact that long-term predictions are almost never quite accurate, our neural network model seems to predict the Maunder Minimum period remarkably well. In conclusion, our neural network model is exceptionally successful

in predicting the solar activity 90 years back in time (from 1610 to 1699). These *post-facto* predictions encouraged us to use our model in order to try to predict the solar activity 90 years in the future.

Table 4 Comparison of the yearly mean sunspot number between our *post-facto* predictions and the R_G-numbers during the Maunder Minimum period (1644 – 1699).

Year	*Post-facto* predictions[a]	R_G[b]	Year	*Post-facto* predictions[a]	R_G[b]	Year	*Post-facto* predictions[a]	R_G[b]
1644	21.1	12	1663	0	0	1682	0	0
1645	17	0	1664	0	0	1683	4.7	0
1646	4.1	0	1665	0	0	1684	0	1.4
1647	4.3	0	1666	0	0	1685	0	0
1648	9.7	0	1667	0	0	1686	0	0.6
1649	10.7	0	1668	0	0	1687	0	0.1
1650	1.7	0	1669	0	0	1688	0	0.5
1651	0	0	1670	0	0	1689	0	0.2
1652	0	2	1671	0	1	1690	0	0
1653	0	0.8	1672	0	0.4	1691	0	0
1654	0	0.7	1673	0	0	1692	0	0
1655	0	0.5	1674	0	0.2	1693	0	0
1656	0	0.5	1675	0	0	1694	0	0
1657	0	0.2	1676	0	1.7	1695	0	0.1
1658	0	0	1677	0	0.3	1696	0	0
1659	0	0	1678	0	0.2	1697	0	0
1660	0	2	1679	0	0	1698	0	0
1661	0	0.8	1680	0	0.8	1699	0	0
1662	0	0	1681	0	0			

[a] *Post-facto* predictions = the yearly mean sunspot number of our long-term past predictions using our neural network model.

[b] R_G = the yearly mean Sunspot Group Number of Hoyt and Schatten solar activity reconstruction.

Long-term future predictions

We perform long-term future predictions in order to investigate the likely variation of solar activity in future cycles. In particular, we try to forecast the yearly mean sunspot numbers during the next 90

years from 2013 to 2102 (Figure 42). The predicted yearly mean sunspot numbers indicates that the future cycles up to 2102 are expected to be smaller than the Dalton Minimum in 1805. In particular, according to our predictions (Table 5), we observe that the peak sunspot numbers of Cycles 25, 26, 27, 28, and 29 are expected to continuously decrease; *i.e.* peak sunspot numbers are predicted to be 39, 29.8, 22, 17, and 12.8 respectively. However, our model predicts a recovery to higher levels during the following Cycles 30, 31, and 32; *i.e.* peak sunspot numbers are predicted to be 22.2, 31.4, and 40.3 respectively. Moreover, we expect exceptionally extended periods of minima with unusually low solar activity among the cycles; *i.e.* long periods without sunspots lasting from five to ten years are expected to occur as minima between the cycles. Thus, we predict that solar activity will not increase in the same way as it has in the last 100 years. Our predictions suggest that we are heading into an extended period with significant decrease in solar activity lasting up to the year ≈ 2100.

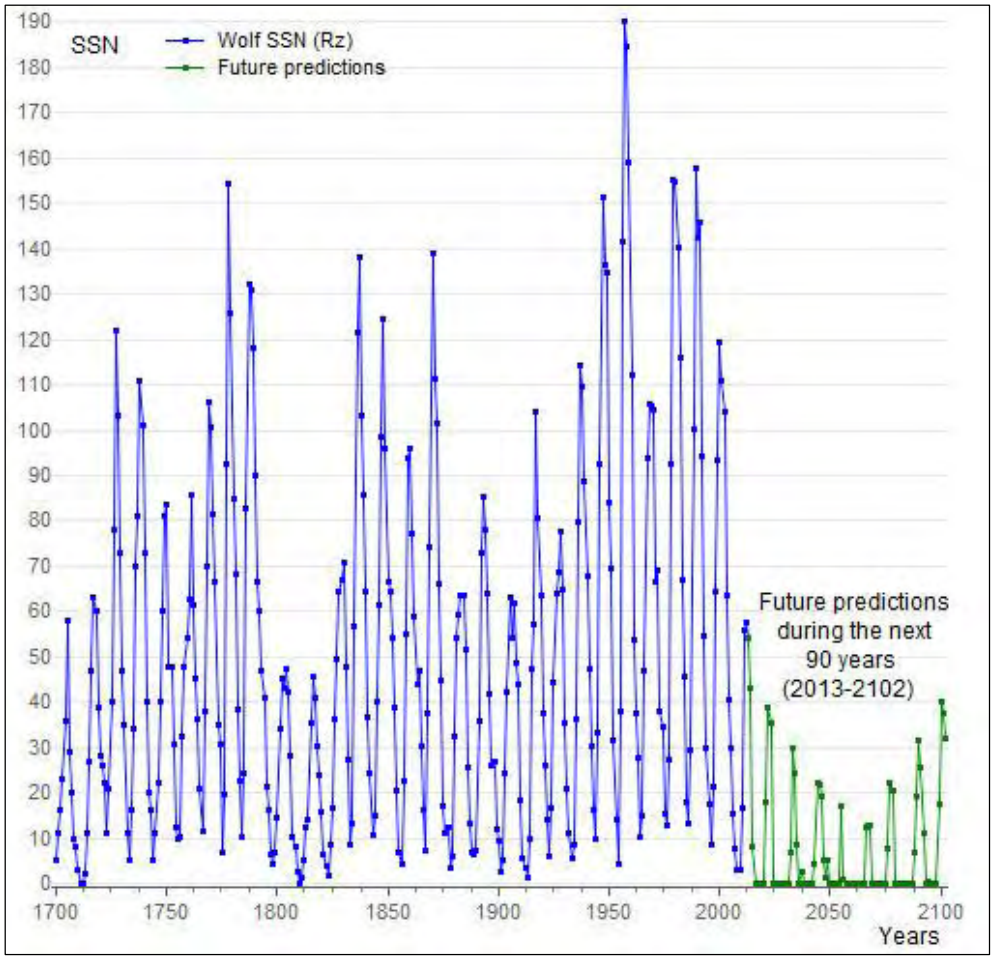

Figure 42 Future yearly sunspot-number predictions 90 steps ahead (2013 – 2102). The blue curve corresponds to the actual yearly mean sunspot-number data (1700 – 2012) of Wolf's reconstruction [R_Z numbers]; the green curve corresponds to the future predictions of our neural network model.

Table 5 Future yearly mean sunspot-number predictions of 90 steps ahead (2013 – 2102).

Year	Future forecast[a]	Year	Future forecast[a]	Year	Future forecast[a]	Year	Future forecast[a]	Year	Future forecast[a]
2013	54	2031	0	2049	5.2	2067	12.8	2085	0
2014	43.1	2032	6.7	2050	0	2068	13	2086	0
2015	8.3	2033	29.8	2051	0	2069	0	2087	0
2016	0	2034	24.4	2052	0	2070	0	2088	7
2017	0	2035	8.5	2053	0	2071	0	2089	19.2
2018	0	2036	0	2054	0	2072	0	2090	31.4
2019	0	2037	2.6	2055	17	2073	0	2091	25.6
2020	0	2038	0	2056	0.7	2074	0	2092	10.9
2021	17.9	2039	0	2057	0	2075	0	2093	0
2022	39	2040	0	2058	0	2076	7.8	2094	0.4
2023	35.5	2041	0	2059	0	2077	22.2	2095	0
2024	0	2042	0	2060	0	2078	20.4	2096	0
2025	0	2043	4.3	2061	0	2079	0	2097	0
2026	0	2044	22	2062	0	2080	0	2098	0
2027	0	2045	22	2063	0	2081	0	2099	17.5
2028	0	2046	19.3	2064	0	2082	0	2100	40.3
2029	0	2047	5.3	2065	0	2083	0	2101	37.5
2030	0	2048	1.1	2066	12.5	2084	0	2102	31.9

[a] Future forecast = the yearly mean sunspot number of our long-term predictions using our neural network model.

Furthermore, we observe that our predicted picture of low solar activity up to 2102 somewhat resembles the solar activity during the last prolonged sunspot minimum, that is, the Maunder Minimum (1645 – 1715); *i.e.* exceptionally low number of sunspots and long intervals without sunspots at all are expected to occur between the cycles, while even the peak sunspot number will be smaller than the Dalton Minimum period (Figure 43). Thus, the likely expected minimum by 2102 represents the quietest solar-activity conditions during the last 400 years. Predicting a small minimum about 400 years after the Maunder Minimum is also consistent with the fundamental 420-year oscillatory mode of the Sun's convective zone (Stuiver and Braziunas, 1989). Our prediction lends some support to the

prediction of low solar activity in 2100 made by Clilverd *et al.* (2003). Rigozo *et al.* (2010) obtained a prevision of ten year average sunspot-number time series by using a sum of sine waves derived from applying spectral analysis to the sunspot-number data; they found four solar activity minimum and one maximum epochs during the next 1000 years.

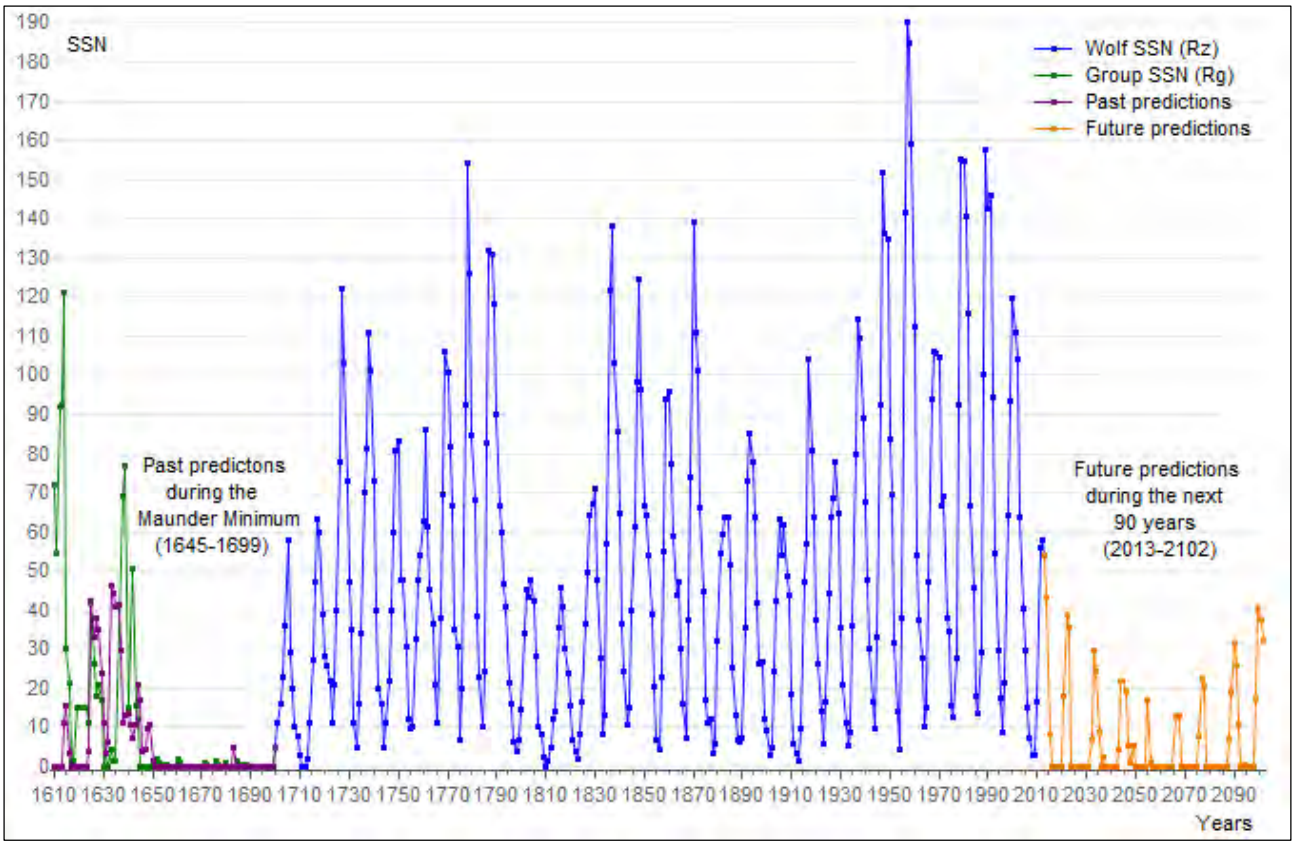

Figure 43 Time series of our *post-facto* yearly sunspot-number predictions from 1610 to 1699 (purple curve) along with our future predictions from 2013 to 2102 (orange curve). The blue curve corresponds to the actual yearly mean sunspot-number data (R_Z numbers); the green curve corresponds to the actual yearly mean sunspot-number data (1610 – 1699) of the Hoyt and Schatten's reconstruction (R_G numbers).

They showed that the next solar minimum epoch (2076 – 2146) is expected to be similar to the Dalton Minimum; they found that it presents solar wind parameters identical to that of the Dalton Minimum (Table 6). Our predictions seem to be consistent with the next solar minimum they found (2076 – 2146); *i.e.* a period of low solar activity but not as low as the Maunder Minimum. In particular, the Dalton-like next solar minimum they predicted coincides with the period of solar activity recovery to higher levels (Solar Cycles 30, 31, and 32) that we predicted (Table 6). However, they found that the next Maunder-like minimum epoch is expected to occur from 2306 to 2366. On the contrary, according to our predictions, periods of minima without sunspots lasting from five to ten years are expected to

occur between the Cycles 25 – 32, resembling the solar activity during the Maunder minimum (Table 6).

Table 6 Comparison of the next solar minima between our long-term future predictions (2013 – 2102) using the technique of neural networks and Rigozo *et al.* (2010) predictions (1016 – 3006) using wavelet analysis.

Predictive method	Next solar-activity minimum
Wavelet analysis (Rigozo *et al.*, 2010)	2076 – 2146 and 2306 – 2366: Weak solar minimum; Dalton-like minimum solar wind parameters. 2416 – 2636 and 2646 – 2746: Great solar minimum – Maunder-like minimum solar wind parameters.
Neural networks[a]	2013 – 2102: Cycles 25, 26, 27, 28 and 29 – continuously reduced solar activity; Cycles 30, 31 and 32 – recovery of solar activity to higher levels; intervals among the cycles – periods of minima without sunspots lasting from five to ten years.

[a] Neural networks = our predictive method.

4.2.3 Concluding remarks

In conclusion, we analyzed the yearly mean SSN data (1700 – 2012), indicating that it is a low-dimensional deterministic chaotic system. We have performed future predictions trying to forecast the solar activity during the next five years (2013 – 2017). We tested and proved that our model is able to predict the Maunder Minimum period (1645 – 1715), performing long-term *post-facto* predictions and comparing them with the observed SSN values. Finally, we performed long-term future predictions trying to forecast the solar activity up to 2102. We predicted that the level of solar activity is likely to be reduced significantly during the next decades leading us to another prolonged sunspot minimum (since the era of Maunder Minimum) lasting up to the year ≈ 2100. We observe that the picture of our predicted prolonged sunspot minimum up to the year ≈ 2100 seems to be consistent with the conditions during the Maunder Minimum.

4.3 Sunspot Number Version 2.0: Re-evaluation of the Proposed Predictive Models in Light of New Data[52]

On 1 July 2015 after a 4-year study, the original version of the sunspot number – the only direct record of the evolution of solar activity – has been revised, for the first time since its creation in 1849, by an entirely new series. Since 2011 a group of 40 solar astronomers – led by Ed Cliver (National Solar Observatory, USA), Frédéric Clette, Director of the World Data Centre (WDC-SILSO, Royal Observatory of Belgium) and Leif Svalgaard (Stanford University, USA) – undertook a full revision of the two available solar activity indices: the Zürich Sunspot Number, [R_Z], initiated by Rudolf Wolf in 1849 and the Group Sunspot Number, [R_G], constructed by Hoyt and Schatten (1998). They tried to eliminate the discrepancies hinting at strong inhomogeneities between the two historical records; the two series indicated significantly different levels of solar activity in 1880 – 1915 for the Group Sunspot Number and in 1947 and 1980 – 2014 for the Zürich Sunspot Number (Clette *et al.*, 2014).

The new corrected series, called the Sunspot Number Version 2.0 [V2.0] provide a homogenous record of solar activity over the last 400 years. The most notable correction is that the new record [V2.0] has no significant rising trend in solar activity after the Maunder Minimum, as was previously indicated (Sunspot Number Version 1.0 [V1.0]); by the mid-18th century, solar activity had already returned to levels equivalent to those observed in recent solar cycles in the 20th century (Clette *et al.*, 2014). Hence, solar activity appears to have remained relatively stable over the past few centuries without any significant upward trend since the 1700s.

In the two previous Sections 4.1 and 4.2 we proposed two neural network models that predict the solar activity using the original monthly and yearly mean Zürich Sunspot Number [V1.0] as input data. Given the revised record of solar activity [V2.0] existing solar activity models need to be re-evaluated. Hence, the purpose of this study is to re-evaluate the performance of our previously proposed models for predicting solar activity in the light of the new sunspot-number data. We perform new predictions using the Zürich Sunspot Number Version 2.0[53] as input data and we compare them with our original predictions (using the V1.0 series as input data). We compare the residuals and the values of the Mean Absolute Error and Root Mean Squared Error for the two different input-data cases (V1.0 and V2.0 series). We quantify the differences between our original and new predictions by measuring the relative

[52] This section is based on the publication "Sunspot Number Version 2.0: Re-evaluation of the Proposed Predictive Solar Activity Models in Light of New Data" (Gkana, A., Zachilas, L.: 2016, Re-evaluation of Predictive Models in Light of New Data: Sunspot Number Version 2.0, *Solar Physics* **291**(8), 2457-2472.).

[53] The monthly and yearly V2.0 data are taken from the Solar Influences Data Analysis Center (SIDC: WDC-SILSO, Royal Observatory of Belgium, Brussels, and are available at http://www.sidc.be/silso/datafiles).

changes in the predictive errors, calculating the percentage errors of our predictions, and comparing the distributions of the percentage errors based on the mean and the standard deviations. In order to evaluate the predictive accuracy of our previously proposed models, we compare the percentage errors with the corresponding standard errors of the actual sunspot-number data.

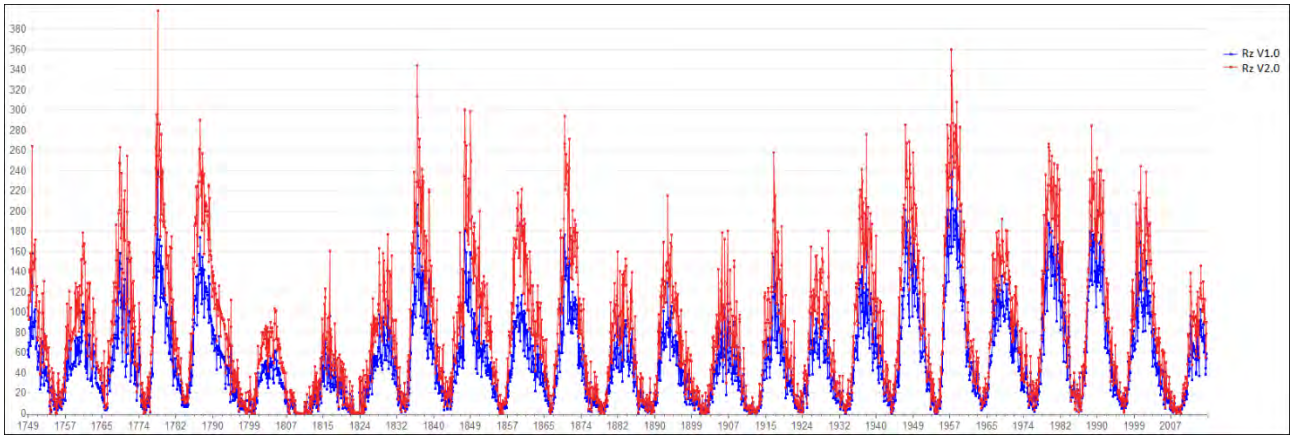

Figure 44 The time series of the monthly mean total Zürich [R_Z] Sunspot Number Version 1.0 (blue curve) and Version 2.0 (red curve) for the last 24 sunspot cycles (January 1749 – August 2015).

4.3.1 Re-evaluation of the monthly solar activity predictive model

Figure 44 demonstrates the original and the revised monthly mean total sunspot-number data (*i.e.* V1.0 and V2.0) from January 1749 to August 2015. As mentioned above (Subsection 1.2.1), an important factor in performing accurate predictions is the upper limit of predictability. In Section 4.1 we showed that the upper limit of predictability for the monthly sunspot numbers V1.0 is $T_{\text{pr}} \approx 51$ months. Following the same technique for the V2.0 series, we calculate the largest Lyapunov exponent using the Kantz algorithm which is estimated to be $\lambda_{\max} \approx 0.02$.

Thus, the upper limit of predictability for the V2.0 series is $T_{\text{pr}} = 1/\lambda_{\max} \approx 50$ months; *i.e.* the maximum time length on which predictions are effective is 50 months. Hence, we perform monthly predictions of 26 steps (months) ahead in time (*i.e.* within the predictability time $T_{\text{pr}} \approx 50$) from July 2013 to August 2015 (Figure 45) using our previously proposed model (Equation (18)). As input data we use: (i) the monthly Sunspot Number Version 1.0 and (ii) the revised series V2.0 ($T = 3174$ records – from January 1749 to June 2013). In fact, regarding the predictions using the V1.0 series as input data, we extend our original 12-months-ahead monthly predictions (July 2013 – June 2014) from our previous work, 14 months into the future.

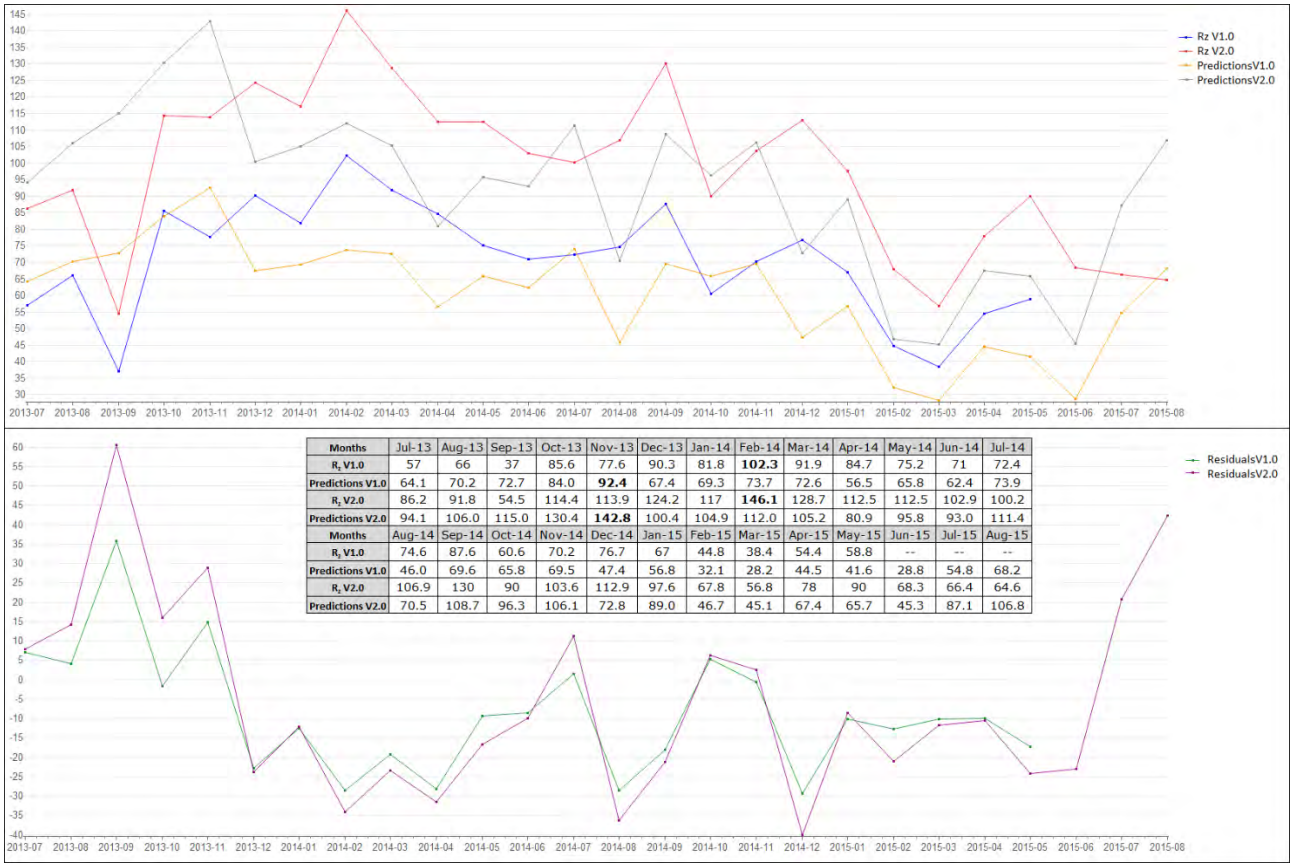

Months	Jul-13	Aug-13	Sep-13	Oct-13	Nov-13	Dec-13	Jan-14	Feb-14	Mar-14	Apr-14	May-14	Jun-14	Jul-14
R_z V1.0	57	66	37	85.6	77.6	90.3	81.8	**102.3**	91.9	84.7	75.2	71	72.4
Predictions V1.0	64.1	70.2	72.7	84.0	**92.4**	67.4	69.3	73.7	72.6	56.5	65.8	62.4	73.9
R_z V2.0	86.2	91.8	54.5	114.4	113.9	124.2	117	**146.1**	128.7	112.5	112.5	102.9	100.2
Predictions V2.0	94.1	106.0	115.0	130.4	**142.8**	100.4	104.9	112.0	105.2	80.9	95.8	93.0	111.4
Months	Aug-14	Sep-14	Oct-14	Nov-14	Dec-14	Jan-15	Feb-15	Mar-15	Apr-15	May-15	Jun-15	Jul-15	Aug-15
R_z V1.0	74.6	87.6	60.6	70.2	76.7	67	44.8	38.4	54.4	58.8	--	--	--
Predictions V1.0	46.0	69.6	65.8	69.5	47.4	56.8	32.1	28.2	44.5	41.6	28.8	54.8	68.2
R_z V2.0	106.9	130	90	103.6	112.9	97.6	67.8	56.8	78	90	68.3	66.4	64.6
Predictions V2.0	70.5	108.7	96.3	106.1	72.8	89.0	46.7	45.1	67.4	65.7	45.3	87.1	106.8

Figure 45 The future monthly sunspot-number predictions of 26 steps ahead (July 2013 – August 2015). In the upper part of the diagram, the blue curve corresponds to the actual sunspot-number V1.0 series; the red curve corresponds to the actual sunspot-number V2.0 series; the orange curve corresponds to our predictions using the V1.0 series as input data; the grey curve corresponds to our predictions using the V2.0 series as input data. In the lower part of the diagram, the green curve indicates the difference between the actual V1.0 series and the corresponding predictions, while the purple curve indicates the difference between the actual V2.0 series and the corresponding predictions.

As expected, the sunspot revision yields to predictions with higher counts (Figure 45). However, using the V2.0 series as input data produces predictions with predictive errors different from those of our original predictions. The MAE and RMSE values of our original and new predictions are $MAE_{V1.0} = 14.64$, $RMSE_{V1.0} = 17.69$ and $MAE_{V2.0} = 20.59$, $RMSE_{V2.0} = 24.45$, respectively. In order to quantify the change in these errors we use the percentage change[54] which measures the relative change in a variable by calculating the difference between the old value and the new value. The percentage change for the MAE values is 40.6%, while for the RMSE values is 38.2%. We observe that the predictive errors using the V2.0 series as input data have increased by 40 percent.

[54] The percentage change is calculated by $\%\text{Change} = \left(\left(x_2 - x_1\right)/x_1\right) \times 100$, where x_2 is the new value of the variable x and x_1 is the original value of the variable x.

In order to investigate the difference between our original and new predictions in more detail, we calculate and compare the distributions of the percentage errors[55] [%Error] based on the mean and the standard deviations (Tables 7 and 8).

Table 7 Comparison between the percentage errors of our monthly predictions and the corresponding standard errors of the actual monthly sunspot numbers Version 2.0 for the time period (July 2013 – August 2015).

Month	$R_Z^{V2.0}$ *	σ §	N †	SE ‡	$\hat{R}_Z^{V2.0}$ ₴	% *Error* ±
Jul-13	86.2	6.7	575	**0.279**	94.1	**0.091**
Aug-13	91.8	6.6	563	**0.278**	106.0	**0.155**
Sep-13	54.5	5.3	446	0.251	115.0	1.111
Oct-13	114.4	8.2	421	**0.400**	130.4	**0.140**
Nov-13	113.9	8.2	321	**0.458**	142.8	**0.254**
Dec-13	124.2	9.1	402	**0.454**	100.4	**-0.192**
Jan-14	117	8.2	398	**0.411**	104.9	**-0.103**
Feb-14	146.1	10.7	384	**0.546**	112.0	**-0.233**
Mar-14	128.7	8.6	493	**0.387**	105.2	**-0.183**
Apr-14	112.5	6.9	486	**0.313**	80.9	**-0.281**
May-14	112.5	7.5	493	**0.338**	95.8	**-0.149**
Jun-14	102.9	7.7	469	**0.356**	93.0	**-0.096**
Jul-14	100.2	7.4	477	**0.339**	111.4	**0.111**
Aug-14	106.9	7.6	486	**0.345**	70.5	**-0.341**
Sep-14	130	8.7	419	**0.425**	108.7	**-0.164**
Oct-14	90	6.9	440	**0.329**	96.3	**0.070**
Nov-14	103.6	8.5	397	**0.427**	106.1	**0.024**
Dec-14	112.9	7.4	331	**0.407**	72.8	**-0.355**
Jan-15	93	7.5	546	**0.321**	89.0	**-0.044**
Feb-15	66.7	5.3	442	0.252	46.7	-0.300
Mar-15	54.5	4.8	628	**0.192**	45.1	**-0.173**

[55] The percentage errors were calculated as follows: $\%\text{Error} = (\hat{R}_Z - R_Z)/R_Z \times 100$, where R_Z is the actual sunspot-number value and $\hat{R}_Z$ is the corresponding predicted sunspot-number value.

Apr-15	75.3	8.2	847	**0.282**	67.4	**-0.105**
May-15	88.8	8.6	895	**0.287**	65.7	**-0.260**
Jun-15	66.5	6.3	826	0.219	45.3	-0.319
Jul-15	65.8	5.7	977	0.182	87.1	0.324
Aug-15	64.4	5.2	892	0.174	106.8	0.659

* The monthly mean total Zürich [R_Z] Sunspot Number Version 2.0.

§ The monthly mean standard deviation of the input sunspot numbers from individual stations.

† Number of observations used to compute the monthly mean total sunspot number.

‡ The standard error on the monthly mean values computed by $SE = \sigma/\sqrt{\mathrm{N}}$.

ƨ Our monthly sunspot-number predictions using the V2.0 series as input data.

± The percentage error calculated by $\%\mathrm{Error} = \left(\hat{R}_Z^{V2.0} - R_Z^{V2.0}\right)/R_Z^{V2.0}\times 100$.

A negative (positive) %Error indicates that the predicted sunspot-number value $\hat{R}_Z$ is smaller (larger) than the corresponding actual value R_Z. Concerning the %Error of our original predictions shown in Table 8, the mean and the standard deviation of the percentage errors are $\bar{x} = -0.111$ and $s = 0.278$, respectively. The percentage errors range from –0.567 to +0.965 with 7 overestimations and 19 underestimations of the actual sunspot numbers; 23 percentage errors (88.5%) lie within 1 standard deviation of the mean value $\bar{x} \pm s : [-0.389, 0.167]$, 25 values (96.2%) lie within 2 standard deviations of the mean $\bar{x} \pm 2s : [-0.667, 0.445]$, and 1 outlier – the percentage error 0.965 – lies within 4 standard deviations of the mean $\bar{x} \pm 4s : [-1.223, 1.001]$.

Table 8 Comparison between the percentage errors of our original and new monthly predictions for the time period (July 2013 – August 2015).

Month	$R_Z^{V1.0}$ *	$\hat{R}_Z^{V1.0}$ §	*V1.0 %Error* ±	*V2.0 % Error* †
Jul-13	57	64.1	0.125	**0.091**
Aug-13	66	70.2	0.063	0.155
Sep-13	37	72.7	0.965	1.111
Oct-13	85.6	84.0	-0.019	0.140
Nov-13	77.6	92.4	0.191	0.254
Dec-13	90.3	67.4	-0.254	**-0.192**
Jan-14	81.8	69.3	-0.153	**-0.103**
Feb-14	102.3	73.7	-0.280	**-0.233**

Mar-14	91.9	72.6	-0.210	**-0.183**
Apr-14	84.7	56.5	-0.334	**-0.281**
May-14	75.2	65.8	-0.125	**-0.149**
Jun-14	71	62.4	-0.122	**-0.096**
Jul-14	72.4	73.9	0.021	0.111
Aug-14	74.6	46.0	-0.384	**-0.341**
Sep-14	87.6	69.6	-0.206	**-0.164**
Oct-14	60.6	65.8	0.086	**0.070**
Nov-14	70.2	69.5	-0.009	0.024
Dec-14	76.7	47.4	-0.382	**-0.355**
Jan-15	67	56.8	-0.152	**-0.044**
Feb-15	44.8	32.1	-0.284	**-0.300**
Mar-15	38.4	28.2	-0.265	**-0.173**
Apr-15	54.4	44.5	-0.182	**-0.105**
May-15	58.8	41.6	-0.293	**-0.260**
Jun-15	66.5	28.8	-0.567	**-0.319**
Jul-15	65.8	54.8	-0.168	0.324
Aug-15	64.4	68.2	0.059	0.659

* The monthly mean total Zürich [R_Z] Sunspot Number Version 1.0.

§ Our monthly sunspot-number predictions using the V1.0 series as input data.

± The percentage errors of our original predictions (using the monthly sunspot numbers Version 1 as input data).

† The percentage errors of our new predictions (using the monthly sunspot numbers Version 2 as input data).

Regarding the percentage errors of our new predictions (Table 8), the mean and the standard deviation are $\bar{x} = -0.014$ and $s = 0.323$, respectively. The percentage errors range from –0.355 to +1.111 with 10 overestimations and 16 underestimations of the actual sunspot numbers; 21 percentage errors (80.8%) lie within 1 standard deviation of the mean value $\bar{x} \pm s : [-0.337, 0.309]$, 24 values (92.3%) lie within 2 standard deviations of the mean $\bar{x} \pm 2s : [-0.66, 0.632]$, and 2 outliers – the percentage errors 0.659 and 1.111 – lie within 3 and 4 standard deviations of the mean ($\bar{x} \pm 3s : [-0.983, 0.955]$ and $\bar{x} \pm 4s : [-1.306, 1.278]$, respectively). Overall, these results indicate that the percentage errors of

our new predictions are close to those of our original predictions. In particular, for 18 out of 26 months the percentage errors of our new predictions are smaller than those of our original predictions (Table 7); the mean percentage error of our new predictions (–0.014) is smaller than the mean percentage error of our original predictions (–0.111).

Further, by dividing the listed standard deviation [σ] with the square root of the total number of observations in the month [N] we calculate the standard error (SE) of the actual monthly sunspot numbers V2.0 (Table 7). The standard error determines the uncertainty of the actual monthly mean sunspot-number estimation; hence, the percentage errors of our new predictions should be roughly the size of the corresponding standard errors. As shown in Table 7, 21 out of 26 percentage errors (in absolute values) are smaller than the corresponding standard errors; only the percentage errors for Sep-13, Feb-15, Jun-15, Jul-15, and Aug-15 are larger than the corresponding standard errors (*i.e.* $\%\text{Error}_{Sep-13} = 1.111 > SE_{Sep-13} = 0.251$, $\left|\%\text{Error}_{Feb-15}\right| = 0.300 > SE_{Feb-15} = 0.252$, $\left|\%\text{Error}_{Jun-15}\right| = 0.319 > SE_{Jun-15} = 0.219$, $\%\text{Error}_{Jul-15} = 0.324 > SE_{Jul-15} = 0.182$, $\%\text{Error}_{Aug-15} = 0.659 > SE_{Aug-15} = 0.174$). The mean percentage error –0.014 or –1.4% is significantly smaller in absolute value than the mean standard error 0.333 or 33.3%.

Finally, our model predicts the second peak of the present cycle; that is, the maximum of Cycle 24 (*i.e.* the Cycle 24 had a double peak with the second peak higher than the first). The actual sunspot-number maximum for the current 11-year solar cycle was $R_{\text{Z max}}^{V1.0} = 102.3$ in February 2014, while according to our original predictions the maximum was expected to be 92.4 in November 2013 (± 2 months) with percentage error of about – 0.097. Our model (Equation (18)) now predicts a higher maximum sunspot number V2.0. Our predicted peak leaped up to 142.8 in the same month (November 2013); it is still quite close to the new actual maximum of about $R_{\text{Z max}}^{V2.0} = 146.1$ in February 2014. The percentage error of our new predicted maximum is $\%Error_{\hat{R}_{Z_{\max}}=142.8}^{V2.0} = -0.022$; it is smaller in absolute value than the standard error of the new actual maximum $SE_{Feb-14} = 0.546$ (Table 7) and close to the percentage error of our original predictions $\%Error_{\hat{R}_{Z_{\max}}=92.4}^{V1.0} = -0.097$.

Overall, with a mean percentage error close to zero, 21 out of 26 percentage errors lie within 1 standard deviation of the mean, and 88.5% of the percentage errors are smaller than the corresponding standard errors, our model (Equation (18)) using the monthly sunspot numbers V2.0 as input data seems to produce unbiased predictions, despite the full revision of the monthly R_Z record. Hence, we extend our new monthly predictions (using V2.0 as input data) 50 steps (months) ahead in future – the maximum

temporal extent for performing deterministic predictions – from September 2015 to October 2019 (Figure 46).

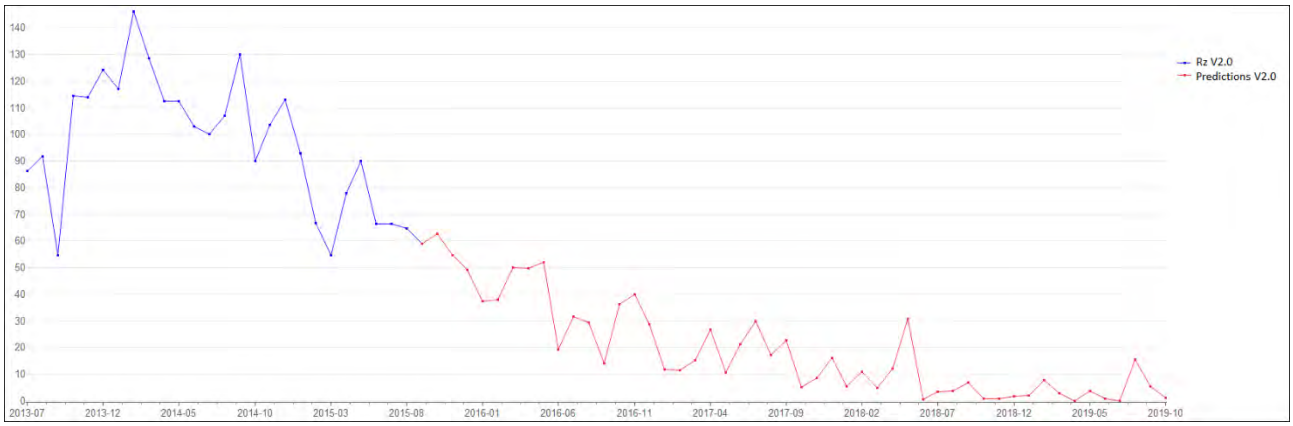

Figure 46 Extension of our monthly sunspot-number V2.0 predictions 50 steps ahead (September 2015 – October 2019). The blue curve corresponds to the actual sunspot-number V2.0 series; the red curve corresponds to our predictions using the V2.0 series as input data.

We are currently nearly 7 years into Cycle 24 (the present solar cycle began in September 2009) and according to our predictions we are 4 years away from the minimum; we estimate that the significant decrease in sunspot numbers (less than 40 sunspots per month) will start during 2016 (June 2016) peaking to as low as zero sunspots in July 2019 (the same as the previous Cycle 23, which ended in August 2009 with the sunspot numbers going through a minimum of zero). Solar Cycle 24 is predicted to have a length of about 119 months, which is considered to be a short-period cycle; Wilson (1987) estimated that short-period cycles average about 122 ± 4 months and long-period cycles average about 140 ± 5 months. Kane (2008) showed that the total length of a cycle and the next cycle's peak seems to be anti-correlated; hence, we expect that the solar maximum during the next Cycle 25 will be larger than the peak of present cycle.

However, this is not consistent with our yearly sunspot-number predictions (Subsection 4.2.2) according to which the yearly mean sunspot-number peak for Cycle 25 is expected to be lower ($R_{Z\max}^{V1.0} = 39$) than the peak of the present Cycle 24 ($R_{Z\max}^{V1.0} = 54$). But this inconsistency has also been observed in the long-period Cycle 20 (144 months – from August 1964 to July 1976) followed by Cycle 21 with maximum sunspot number $R_{Z\max}^{V1.0} = 188.4$ in September 1979 – one of the largest on record. Hence, according to our forecasts, the exceptionally low solar maximum of the present Cycle 24 – despite its expected short total length (which could be just another outlier such as the long-period Cycle 20) – indicates the possibility that we are heading into a period of dramatic low solar activity.

4.3.2 Re-evaluation of the yearly solar activity predictive model

Figure 47 demonstrates the original and the revised yearly mean total sunspot-number records (*i.e.* Sunspot Number Versions 1.0 and 2.0) from 1700 to 2012. In the previous Section 4.2 we performed *post-facto* predictions using the Zürich Sunspot Number V1.0 as input data in order to reconstruct the solar activity 90 years back in time (before the year 1700) during the Maunder Minimum (1610 – 1715). We compared our predictions with the Group Sunspot Numbers Version 1.0 (Hoyt and Schatten, 1998) for the time period 1610 – 1699 and showed that our proposed neural network model (Equation (19)) is successful in reconstructing the Maunder Minimum period. In order to re-evaluate the performance of our previous model (Equation (19)) we perform *post-facto* predictions from 1610 to 1699 using the Zürich V2.0 series as input data (Figure 48).

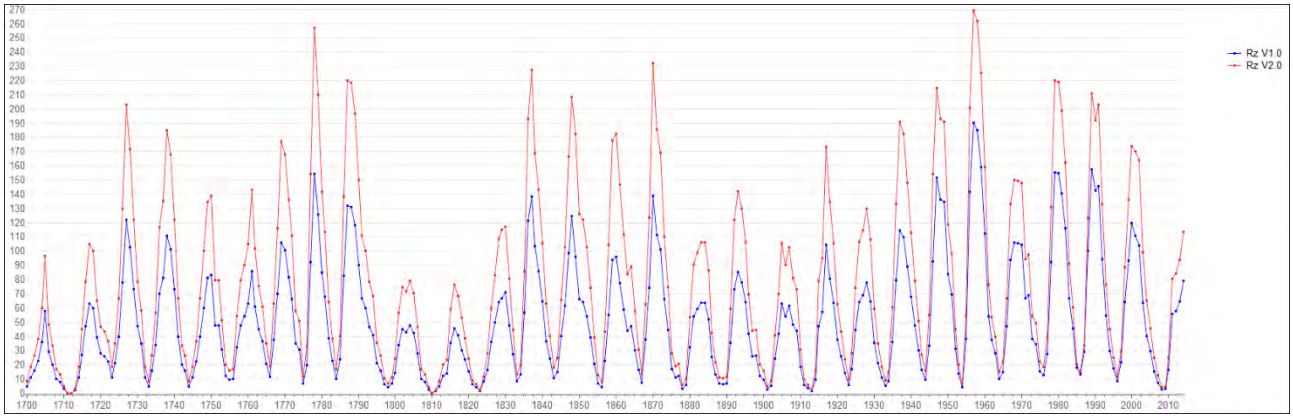

Figure 47 The time series of the yearly mean total Zürich [R_Z] Sunspot Number Version 1.0 (blue curve) and Version 2.0 (red curve) for the past 313 years (1700 – 2014).

However, in this section we do not use the revised version of the Group Sunspot Numbers [V2.0] to compare our new *post-facto* predictions with the actual sunspot numbers from 1610 to 1699, because the new numbers [V2.0] are scaled to raw group counts without any normalization factor. The Group Sunspot Number [R_G] in order to be comparable with the Zürich Sunspot Number [R_Z] needs to be scaled by a suitable scale factor. The original Group Sunspot Number [V1.0] was defined by Hoyt and Schatten (1998), using the constant 12.08 as a normalization factor to bring the R_G series to the same scale as the R_Z series. Therefore, we use the original R_G time series [V1.0] reported by Hoyt and Schatten (1998) for the time period 1610 – 1699 as the actual sunspot-number observations during the Maunder Minimum period.

Our two *post-facto* yearly sunspot-number reconstructions disagree slightly before the Maunder Minimum; the two series present different levels of solar activity mainly from about 1624 to 1650 (Figure 48).

Figure 48 The *post-facto* yearly sunspot-number reconstruction of 90 steps back in time (1610 – 1699). In the upper part of the diagram, the grey curve corresponds to our *post-facto* predictions using the V2.0 series as input data; the purple curve corresponds to our *post-facto* predictions using the V1.0 series as input data; the green curve corresponds to the original actual yearly mean sunspot-number data (1610 – 1699) of the Hoyt and Schatten reconstruction [R_G] Version 1.0. In the lower part of the diagram, the blue curve indicates the residuals corresponding to the predictions using the V1.0 series as input data, while the red curve indicates the residuals corresponding to the predictions using the V2.0 series as input data.

During the following nineteen years: 1616, 1624 – 1631, 1633 – 1635, 1642 and 1644 – 1649, the differences between our new *post-facto* predictions (using the V2.0 series as input data) and the actual values are larger than those of our original predictions (using the V1.0 series as input data). In particular, the differences between the predicted and actual yearly sunspot-number values have increased on average by 4.3 sunspots ranging from 0.6 to 9.1 sunspots, except for the years 1625 – 1628 and 1633 – 1635 where the differences have increased on average by 19.2 sunspots ranging from 16.4 to 22.1 sunspots (Figure 48, lower diagram). However, during the following nine years: 1614, 1615, 1632, 1638 – 1640, 1643, 1650 and 1683, the residuals are smaller comparing to those of our original reconstruction; *i.e.* the differences between the predicted and actual sunspot numbers have decreased on average by 2.7 sunspots ranging from 0.8 to 5.3 sunspots (Figure 48, lower diagram). Regarding the remaining fifty-nine years: 1610 – 1613, 1617 – 1623, 1651 – 1682 and 1684 – 1699,

there are no differences at all between our original and new *post-facto* reconstruction. Finally, the MAE and the RMSE of our new *post-facto* reconstruction ($MAE_{V2.0} = 13.92$, $RMSE_{V2.0} = 27.95$) are quite similar to these of our original reconstruction ($MAE_{V1.0} = 11.72$, $RMSE_{V1.0} = 25.28$). The percentage change for the MAE values is 18.8%, while for the RMSE values it is 10.6%; *i.e.* the predictive errors using the V2.0 series as input data have increased by less than 20 percent.

Overall, from 1610 to 1699 we observe the following: (i) for 12 years the differences between our original and new *post-facto* reconstruction are less than 10 sunspot-number counts, (ii) for 59 years there are no differences at all, (iii) for 9 years our new *post-facto* predictions are closer to the actual sunspot-number values than our original *post-facto* predictions, (iv) for 7 years the differences between the two *post-facto* reconstructions are somewhat larger (up to 22.1 sunspot-number counts), and (v) the relative change in the predictive errors is small (increased by less than 20%). These results indicate that our model (Equation (19)) is able to reconstruct remarkably well the solar activity 90 time-steps (years) back in time before the year 1700 despite the revision of the yearly R_Z series. This suggests that our previously proposed model is still able to produce accurate long-range future solar-activity predictions. Hence, we further perform long-term future predictions trying to forecast the solar activity up to 2102 using the V2.0 series as input data and we compare them with the original predictions (using the V1.0 series as input data) from the previous Section 4.2.

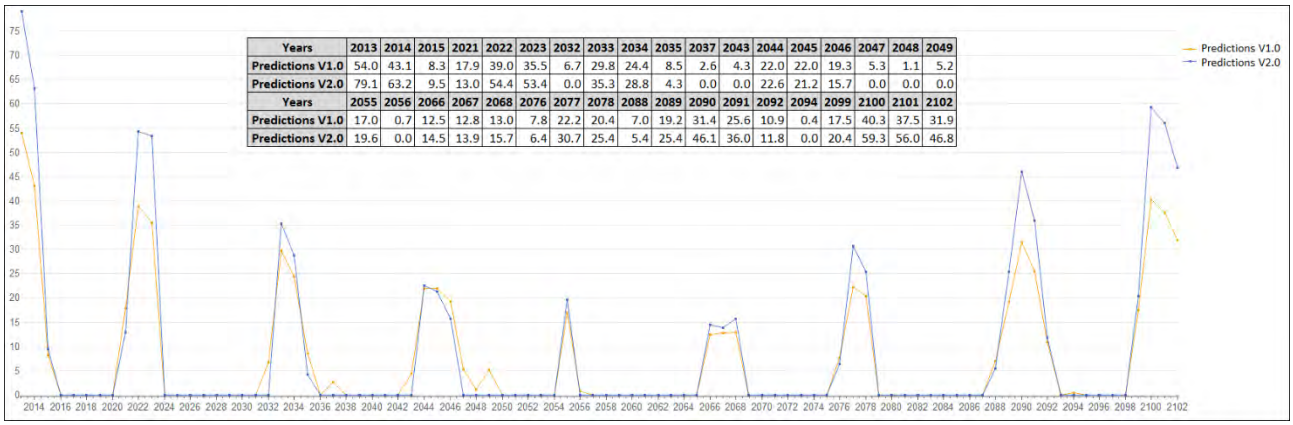

Years	2013	2014	2015	2021	2022	2023	2032	2033	2034	2035	2037	2043	2044	2045	2046	2047	2048	2049
Predictions V1.0	54.0	43.1	8.3	17.9	39.0	35.5	6.7	29.8	24.4	8.5	2.6	4.3	22.0	22.0	19.3	5.3	1.1	5.2
Predictions V2.0	79.1	63.2	9.5	13.0	54.4	53.4	0.0	35.3	28.8	4.3	0.0	0.0	22.6	21.2	15.7	0.0	0.0	0.0
Years	2055	2056	2066	2067	2068	2076	2077	2078	2088	2089	2090	2091	2092	2094	2099	2100	2101	2102
Predictions V1.0	17.0	0.7	12.5	12.8	13.0	7.8	22.2	20.4	7.0	19.2	31.4	25.6	10.9	0.4	17.5	40.3	37.5	31.9
Predictions V2.0	19.6	0.0	14.5	13.9	15.7	6.4	30.7	25.4	5.4	25.4	46.1	36.0	11.8	0.0	20.4	59.3	56.0	46.8

Figure 49 The future yearly sunspot-number predictions of 90 steps ahead (2013 – 2102). The light blue curve corresponds to our future predictions using the V2.0 series as input data; the orange curve corresponds to our future predictions using the V1.0 series as input data.

Figure 49 illustrates the level of disagreement between our original and new long-term future predictions using the V1.0 and V2.0 time series as input data, respectively. The present Cycle 24 is still expected to be the first entering into a period of successive weak solar cycles with exceptionally low sunspot maximums; in all cycles from 25 to 29 covering the period 2020 – 2075 each cycle's peak will be lower than the preceding one. However, our model (Equation (19)) using the V2.0 series as

input data predicts that the peaks of the nine following cycles will be higher than that of our original predictions. The solar activity is predicted to decrease further during the Cycle 25, which is predicted to peak in 2022 with a maximum of about 54.4. All future cycles (25 – 32) are expected to be double peaked with the first peak in sunspot number larger than the second, except for the single peaked Cycle 28 with a maximum of about 19.6 in 2055 and the Cycle 29 in which the second peak (15.7 in 2068) will be slightly larger than the first (14.5 in 2066). The recovery of solar activity to higher levels during the following cycles covering the period 2075 – 2102, will be stronger according to our new predictions; the Cycles 30, 31, and 32 are predicted to have higher maximums of about 30.7, 46.1, and 59.3 in 2077, 2090, and 2100, respectively.

Hence, the most obvious change is that the sunspot counts have increased across the next 90-year sunspot timeline. In particular, during the years 2015, 2021, 2032 – 2035, 2037, 2043 – 2049, 2055 – 2056, 2066 – 2068, 2076 – 2078, 2088 – 2089, 2092, 2094, and 2099 the differences between our original and new long-term yearly predictions have increased on average by 3.2 sunspots ranging from 0.4 to 8.4 sunspots, while for the years 2013 – 2014, 2022 – 2023, 2090 – 2091, and 2100 – 2102 the differences have increased on average by 17.3 sunspots ranging from 10.4 to 25.1 sunspots (Figure 49). Besides having higher sunspot counts during these years, there is no difference between the two predictions for the remaining years. Each cycle is still followed by extended periods of calm (zero sunspot counts); between the cycles (2016 – 2020, 2024 – 2032, 2036 – 2043, 2047 – 2054, 2056 – 2065, 2069 – 2075, 2079 – 2087, 2093 – 2098) solar activity will fall significantly to levels last seen during the Maunder Minimum. The lengths of the minima between the cycles are still the same. Hence, we observe that despite the full revision of the Zürich Sunspot Numbers, our new future long-term predictions endorse our previous claim that a prolonged solar activity minimum is expected to occur lasting up to the year ≈ 2100. Finally, the differences between our original and new predictions 90 years ahead in time are consistent with the differences between our original and new *post-facto* reconstruction 90 years back in time; *i.e.* the differences between our original and new long-term yearly predictions are less than 10 sunspot-number counts, except for 9 years only where there are differences of up to 25.1 sunspot-number counts.

4.3.3 Concluding remarks

In this section we re-evaluated our previous models for predicting solar activity in the light of the revised sunspot-number dataset [V2.0]. In order to monitor each model's accuracy and performance over time, we performed predictions using the revised records of the monthly and the yearly sunspot numbers as input data. We compared our models' predictions using the old [V1.0] and the new [V2.0]

datasets, and found that there is no significant degradation in the performance of our models. We observe that despite the full revision of the Zürich Sunspot Number, the new data [V2.0] fit well to our models' original training; *i.e.* our proposed models produce unbiased predictions using the monthly and yearly V2.0 series as input data despite the full revision of the sunspot numbers. Hence, it is unnecessary to retrain our models to meet the new data; that is, we do not have to propose new models for performing monthly and yearly sunspot-number predictions.

Chapter 5

Solar-Terrestrial Phenomena

In this chapter we investigate the possible existence of solar activity impacts on Earth. In particular, this last part connects all the topics studied in the previous chapters; we start with a literature review on the relationship between solar activity and population dynamics with emphasis on the prey populations (pest insects) studied in this thesis. We continue with a summary of the existing literature on the solar activity link with economy ending this chapter with a study on the solar-agricultural connection.

The impacts of solar activity on climate is still under discussion; however, several studies show that the sunspot cycles seem to be correlated with the global temperature variation (Lean and Rind, 2008; Mann *et al.*, 2009; de Jager and Usoskin, 2006). Eddy (1976) described the relationship between the Sun and terrestrial climate considering the coincidence of Maunder's prolonged solar minimum with the coldest excursion of the Little Ice Age; he pointed out that long term relations between solar activity and global climate might be caused by changes in the solar irradiance. Reid (1987) showed that the time series of the globally averaged sea-surface temperature and the Zürich sunspot number, although not identical, had several features in common. Friis-Christensen and Lassen (1991) presented a set of data supporting the idea that long-term variations in Earth's temperature are closely associated with variations in the solar-cycle length. Hence, an exceptional extended period of unusually low solar activity over the next 90 years or so (that we predicted in Chapter 4), could lead to a significant decrease in solar radiation and activity having most likely wide impacts on our planet's climate.

5.1 Heliobiology and Helioeconomy

5.1.1 Pest outbreaks, vector-borne diseases and solar activity

Early studies have suggested that pest population outbreaks are related somehow with solar activity. Insect populations are sensitive to climate change; *i.e.* insects can tolerate only narrow ranges of temperature or precipitation. If meteorological variables alter that range, a new species of insect will replace the old. Insects occupy one of the lower levels of the food chain. Hence, fluctuations in their population may cause corresponding fluctuations in their predators (*e.g.* birds or spiders) (Hoyt and

Schatten, 1997). Hence, studying the relationship between insect-population dynamics and solar activity could help in the identification of pest population outbreaks.

MacLagen (1940) made one of the most thorough studies on the relation between solar activity and insect populations. Using accounts in newspapers, agricultural tracts, and almanacs of outbreaks of mosquitoes, antler moths, diamond back moths, leather-jackets, flea-beetles, and cutworms in Britain from the 1600s to the 1900s, found an 11-year cycle. He found that insect population outbreaks tend to occur a few years before sunspot maximum, speculating that these population outbreaks are caused by two factors: (i) increased warmth and precipitation, and (ii) increased ultraviolet radiation. The results of his study were consistent with other previous studies (Hahn, 1877; Archibald, 1878; Criddle, 1932). Hahn (1877) observed that locusts appear in temperate regions only during unusually hot and dry years suggesting that solar activity influences locust populations. He showed that European locusts appear mostly between the years of sunspot minimums up to the next sunspot maximum, an average of about 4 years. For the 7 years from the sunspot maximum to the next sunspot minimum, locusts are scarcer. Archibald (1878) showed that locusts appeared in Europe in 1613, 1690, and 1748 – 1749; these dates occur 1 to 3 years after a sunspot minimum. Later, Criddle (1932) with additional information of grasshoppers reported that in Manitoba they followed an 11-year cycle. Swinton (1883) submitted inconclusive evidence that grasshopper outbreaks tend to occur during periods of sunspot minima. Similarly, DeLury (1930) found correlations of grasshopper and grouse maxima with the sunspot minima.

Riley *et al*. (1880) calculated that the interval from the years of the great locust invasions reported for central Europe (1333, 1650, 1693, 1748, and 1825), Spain (1495, 1542, 1619, and 1682), Algiers and adjoining regions (1799, 1845, 1866, and 1878), and America (1820, 1855, 1866, and 1874 – 1876) in each case was approximately a multiple of 11 years. Pasquier (1942) studied locust plagues from 98 years of observations at Algiers; during this span there were eight periods of presence and eight of absence of locusts. The cycles of abundance and scarcity varied between 9 and 15 years in length, whereas the sunspot cycle was 9 – 14 years. Moreover, between 1843 and 1942 there were 9 solar cycles and 9 locust cycles in North Africa, with the latter almost always beginning near the minimum of a sunspot-number period and with a zero to five year lapse after North-West India locust outbreaks (Spinage, 2012). In contrast to these studies, Eidmann (1931) studied population outbreaks of forest insects and concluded that they are correlated with sunspot maxima.

Several studies have examined how the climate-biological relationships affect the transmission of vector-borne diseases. In particular, there is evidence indicating that epidemics of vector-borne

diseases are associated with temperature, rainfall, humidity, *etc*. Descloux *et al*. (2012) analyzed the epidemiology of dengue in Noumea (New Caledonia) from 1971 to 2010 and its relationships with local and remote climate conditions; they showed that the occurrence of outbreaks in Noumea was strongly influenced by climate (temperature) during the last forty years. Hales *et al*. (2002) studied the potential effects of global climate change (rainfall) on the transmission of dengue fever; with population and climate change projections for 2085, they estimated that about 5 – 6 billion people would be at risk of dengue transmission, compared with 3.5 billion people, if climate change did not happen. Chakravarti and Kumaria (2005) studied the relationship of dengue infection with climatic factors such as rainfall, temperature and relative humidity during the dengue fever epidemic in the year 2003. They found that dengue outbreaks coincided mainly with the post monsoon period of subnormal rainfall.

Further, studies on the impact of solar activity on infectious diseases have suggested that epidemics of mosquito-borne diseases also show strong correspondence with the variations of solar cycle. Dutroulau (1868) found that epidemics of malaria in the Lesser Antilles (Caribbean) exhibited a periodicity of either 6 or 10 years. In particular, malaria epidemics appeared to occur at times of minimum solar activity; Gill (1936) showed that malaria pandemics since 1800 were associated with variations of the sunspot cycle occurring at periods of sunspot minima (major epidemics occurred during sunspot minima, while minor epidemics occurred during sunspot maxima). Similarly, the epidemics of yellow fever that occurred in Africa since 1800 coincided with periods of sunspot minima; *i.e.* from 1825 to 1935 eight out of a total eleven sunspot minima have been associated with yellow fever outbreaks in the Gambia (West Africa) (Findlay and Davey, 1936).

These studies provide evidence for the existence of an interrelationship between solar activity and pest population outbreaks. However, further research is required to see whether or not locust outbreaks and the epidemics of vector-borne diseases are interconnected with the variations of solar cycles. Revealing such a correlation could help significantly in the prediction, prevention and control outbreaks of pest and vector-borne diseases in future.

5.1.2 Economy and solar activity fluctuations

Studies over the years have tried to answer whether solar activity has any direct or indirect economic effects. Herschel (1801) was first considered that solar activity may be related with the economy. His studies covered six periods (1650 – 1670, 1676 – 1684, 1686 – 1688, 1695 – 1700, 1710 – 1713, 1714 – 1717) showing a relationship between sunspot activity and the wheat price; he found that the wheat prices were higher when sunspots were scarce. Carrington (1863) charted the variations in frequency

of sunspots and the imperial average wheat-price from 1750 to 1860. Comparing the two curves he noted the general but imperfect correspondence among them but warned that this correspondence was insufficient upon which to base any conclusions. However, he noted that they powerfully stimulate further inquiry with a view of ascertaining whether the discrepancy may admit of future explanation.

Gloyne (1973) found an 11-year cycle in the length of the growing season in Scandinavia, while Currie (1988) found a 10.0-year cycle in Iowa crop yields, a 9.5-year cycle in Arkansas, and a 10.9-year cycle in Illinois; moreover, both the crop yields and the mammalian populations in Iowa and Arkansas exhibited 9.5-year and 10.0-year cycles. These results are consistent with Jevons's (1875) study in 1875. He also found a correlation between the length of the sunspot cycle – 11.11 years – and the fluctuation in the price of oats, wheat, barley, peas, beans, vetches, and rye (by arranging them as nearly as possible in 11.11 year arrays) for the time period 1259 – 1400; for each grain and for all grains combined he found maxima in the same year of his arbitrary arrangement. Later, Jevons (1879) identified 14 commercial crises in England with a well-marked 10.44-year periodicity. However, 7 of the 14 commercial crises occurred during years of minimum solar activity, 4 occurred during years of maximum solar activity, and 3 of them were not clearly associated with solar maxima or minima. Jevons claimed that if a solar-commercial cycle exists it is not a straightforward one.

One of the most thorough studies on the terrestrial and extraterrestrial relationships was carried out in 1915 by Tchijevsky (1971) who observed that important mass historical events correlated to sunspot cycles. In particular, he presented an Index of *Mass Human Excitability* (500 B.C. – A.D. 1922) showing a consistent pattern of 9 waves of excitability per century over the entire span of 2422 years. This index was compiled from detailed statistical researches in the histories of 72 countries of the world. Studying the social movements on these countries he noted that his index was characterized by 11.1-year cycles and that the maxima of mass activity of all humanity (*i.e.* pandemics, revolutions, insurrections, expeditions, migrations, *etc.*) tended to correlate to the middle points of sunspot cycles. In particular, he found that the number of important mass historical events increases during the sunspot maximum; *i.e.* 80% of the most important events occurred during periods of maximum solar activity. The research showed that the Revolutions in Austria (1848 – 1849), the American Civil War occurred during 1858 – 1861, the World War I (1914 – 1918) along with the Russian Revolution of February and October 1917 and the Revolutions in Germany (1918 – 1919), and the peak of the Vietnam War occurred during 1967 – 1969 followed an exceptionally powerful rising of sunspots (Figure 50). For instance, in the middle of June 1915 a large group of sunspots crossed the central meridian of the sun, the aurora borealis were exceedingly powerful in North America and Northern Europe, and magnetic storms were exceptionally strong and interfered with telegraph work. At the time of these phenomena,

the hardest and bloodiest fights of the war were being fought by Germans, Russians, Austrians, Serbians, French, and English. In contrary, the number of important human military-political events decreased during periods of minimum solar activity giving way to creative activity in the sphere of state organizations, international relations, science and art, with a pronounced tendency towards absolutism in the governing powers and a disintegration of the masses.

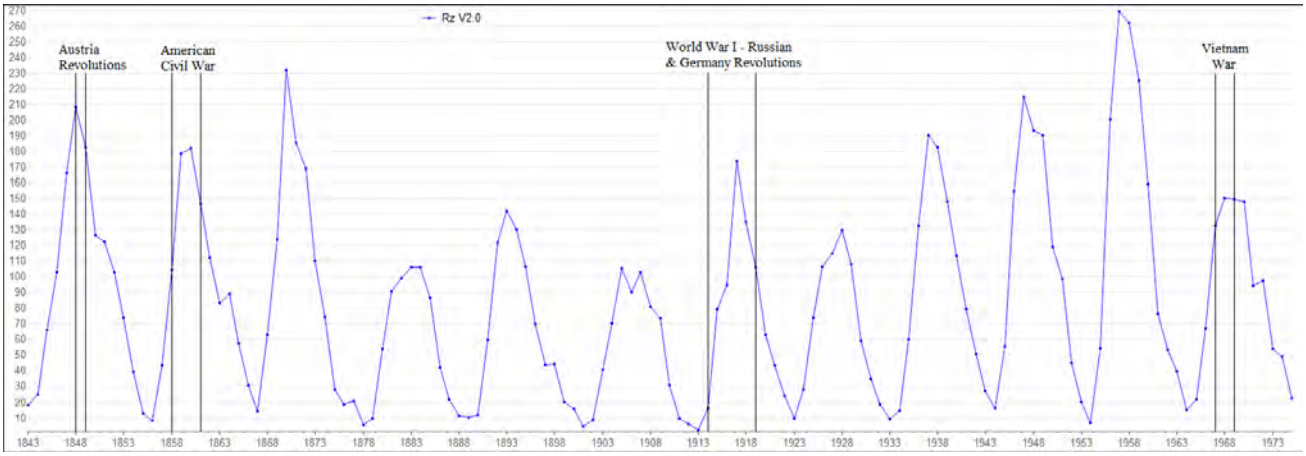

Figure 50 Comparison between the solar activity and the important peaks of mass historical events from 1843 to 1975. The blue curve corresponds to the yearly sunspot numbers Version 2.0.

Huntington (1920) advanced the idea that variations in solar radiation had an effect upon human beings and thus in turn upon business conditions, instead of affecting business first and then human beings as was commonly believed. Garcia-Mata and Shaffner (1934) tried to prove that the idea of solar-economic relationships was completely untenable. However, they found a very close correlation, indeed. In particular, they found a solar-manufactures correlation during the time period 1875 – 1931; *i.e.* manufacturing and production fluctuated with an 11-year cycle. However the peaks and troughs of the solar cycles came after the peaks and troughs of manufacturing and of total production. Not being able to explain this they only suggested that changes in psychological factors, caused by changes in the global electric field, may lead to long-term shifts in optimism and pessimism that show up in the manufacturing economy. Moreover they found little or no correlation with crops. In 1936, Andrews (1936) called attention to the apparent correlation over the preceding years between sunspot activity and wars, international crises, and economic distress. He conjectured that the cause of these and other solar-terrestrial correlations might be due to two solar phenomena associated with sunspot activity; either to the intensity of solar radiation or to emanations of ultraviolet light. Concerning the economic and sociological correlations he suggested that the variations in the ultraviolet light was the more reasonable of the two possible explanations.

Dewey (1960) made an investigation in depth of Tchijevsky's work using dates of sunspot maxima derived by Shove (1956) from old Chinese manuscripts and other sources which were not available to Tchijevsky. He found that comparing all values of Tchijevsky's Index of *Mass Human Excitability* with the years of sunspot maxima, the crests of the sunspot cycles follow the crests of the Index by about a year, on the average. He concluded that there is probably some response on the part of human beings to the sunspot cycle. However, this response would seem to be the cycle, not to the spots themselves, for the maximum of mass human excitability precedes the maximum number of spots.

5.2 Investigation of Solar-Agricultural Connection: Sunspot Numbers and Wheat Prices in London and Southern England

In the past, agricultural peaks and troughs could lead to poverty the entire economy. Moreover, low solar activity has been linked with poor crop production leading to famines; *e.g.* famines in India during 1870s came at periods without sunspots – in 18 out of 22 world observatories of the world it had been shown that the minimum rainfall occured at times when there were no spots on the Sun (Hoyt and Schatten, 1997). We showed that a lot of research has been done on the relationship between solar activity and agricultural prices. However, the Maunder Minimum period (1645 – 1715) has not been included in any of these studies due to the rare and sporadic appearance of sunspots. Consequently, it is difficult to determine if solar cycles with any kind of periodicity were presented during this period. However, a number of studies have shown that the 11-year cycle may be presented during the Maunder Minimum (Waldmeier, 1961; Hoyt and Schatten, 1998; Usoskin *et al.*, 2000, Beer *et al.*, 1998); *i.e.* the years of solar-activity maxima obtained in these studies are quite close to each other and demonstrate an 11-year periodicity. Hence, in this section we examine the relationship between solar activity and crop prices from 1610 throughout the Maunder Minimum (1645 – 1715) and the Dalton Minimum (1790 – 1830) until 1914.

In particular, we investigate the impacts of solar activity on wheat market by using the yearly mean sunspot numbers[56] and the London & Southern England wheat prices. We use the wheat prices in Early Modern Britain as source data for economic comparison since England was largely self-sufficient in food from 1500 to 1750; English agriculture produced only food for humans by the 1860s, when this was at least 90% of English agricultural output (Clark, 2002). The wheat-price data are available from

[56] The sunspot number series is likely the most suitable solar index to study the solar-agricultural oscillations since it is the longest direct series of solar activity; *i.e.* a 400-year-long series which depicts the dramatic contrast between the (almost spotless) Maunder minimum and the modern period of very high activity (Usoskin, 2013).

1259 till 1914; we compare the wheat prices with the sunspot numbers over the same span of time – from 1610 to 1914 – for which both datasets are available. The yearly wheat-price series (Figure 51, lower diagram) up to 1702 are taken from Rogers (1866 – 1892) and after 1703 are taken from Mitchell and Deane (1971). The original wheat-price data are given in two columns in shillings and pence; considering that until 1971 the pound was divided into 20 shillings or 240 pennies (Wood, 2002) we converted the wheat-price data in pounds. Concerning the yearly sunspot-number dataset (Figure 51, upper diagram), we use the R_Z numbers (V2.0) from 1700 to 1914 and the R_G numbers (V1.0) from 1610 to 1699 – since the R_Z numbers (V2.0) do not cover the Maunder Minimum period (1645 – 1715), as noted above (Subsection 4.3.2).

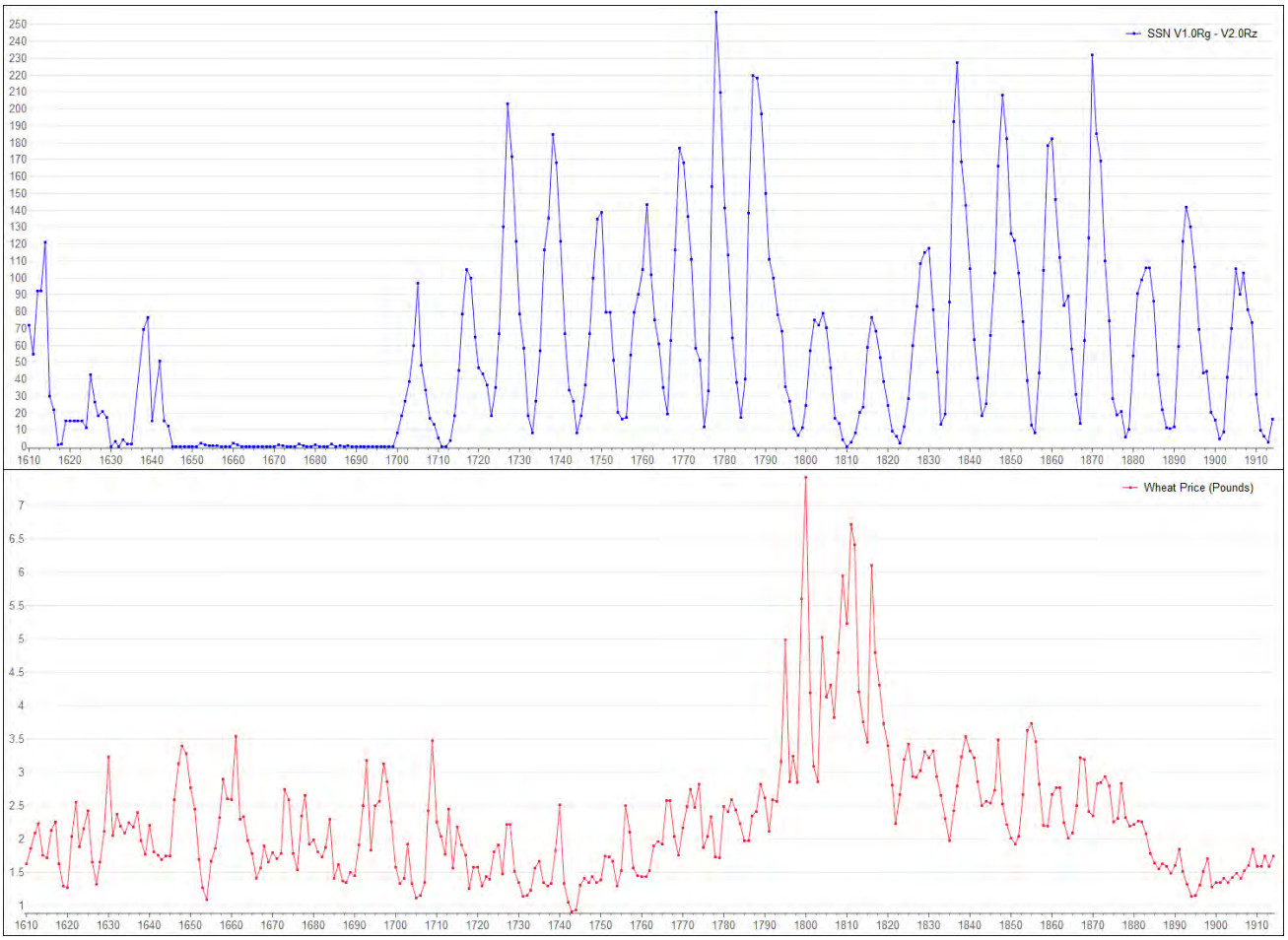

Figure 51 The yearly mean sunspot numbers (upper diagram) and the yearly wheat prices (lower diagram) during the period 1610 – 1914.

5.2.1 Wheat prices and sunspot numbers over the course of 305 years

The sunspot-number and wheat-price data are measured on different scales; therefore, in order to illustrate the similarities and differences between price and solar activity oscillations, such as corresponding periods, peaks and troughs, time lags between minima and maxima, *etc.*, we use unity-

based normalization to scale both time series in the range [0,1] (Figure 52). The sunspot-number cycles from 1610 to 1914 peak at 1614, 1625, 1639, 1652, 1660, 1676, 1684, 1695, 1705, 1717, 1727, 1738, 1750, 1761, 1769, 1778, 1787, 1804, 1816, 1830, 1837, 1848, 1860, 1871, 1883, 1893, and 1905. The cycles have ranged in length from 9 to 14 years with an average duration of about 11.27 years long.

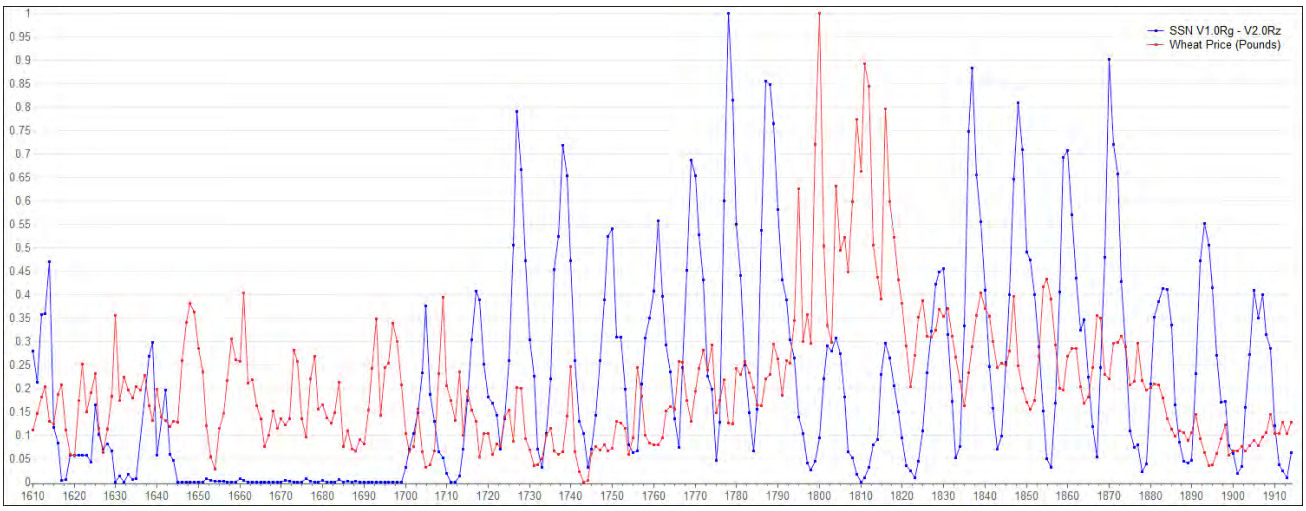

Figure 52 Normalized sunspot-number and wheat-price data between 0 and 1 from 1610 to 1914.

Regarding the wheat prices, we observe that the series also fluctuate in cycles; there is an 11.15 periodic cycle that is almost identical to the average length of the sunspot cycle. However, the length of the wheat-price cycles varies from 5 to 16 years. Moreover, the maxima and minima of the wheat-price cycles mostly come before the maxima and minima of the corresponding sunspot cycles; hence, the sunspot and wheat-price cycles are not identical. In particular, the 27 cycles found in wheat prices from 1610 to 1914 peak at 1617, 1622, 1630, 1648, 1661, 1673, 1678, 1693, 1697, 1709, 1727, 1740, 1751, 1756, 1766, 1774, 1789, 1800, 1811, 1816, 1825, 1839, 1855, 1867, 1877, 1891, and 1909, respectively. We observe that, the wheat-price maxima occured on average 3 ¾ years before the correspondent sunspot-number peaks (*i.e.* the lags between the wheat-price maxima and the nearest sunspot-number maxima are +3, -3, -9, -4, +1, -3, -6, -2, -8, -8, 0, +2, +1, -5, -3, -4, +2, -4, -5, -14, -12, -9, -5, -4, -6, -2, +4), and the wheat-price minima occured on average 4 years before the correspondent sunspot-number minima (*i.e.* the lags between the wheat-price minima and the nearest sunspot-number minima are +3, -3, -2, -4, -2, -3, -2, -5, -6, -5, -2, -1, -1, -5, -6, -5, -7, -7, -8, -11, -8, -5, -3, -3, 0, -7, -3).

Further, the wheat prices around (± 2 years) each sunspot minimum were higher than the prices during maximum solar activity (Figure 53) – indicating a possible interrelationship between solar activity and wheat market. In particular, this occurs almost for all – in 25 out of 27 – sunspot minima during the period 1610 – 1914, except for those occurred in 1668 and 1823 where the correspondent wheat prices

were lower (*i.e.* P^{1668} = £ 1.89, P^{1825} = £ 3.43) than those during the sunspot maxima which occurred in 1660 and 1816 (*i.e.* P^{1662} = £ 2.29, P^{1815} = £ 3.45), respectively (Table 9).

Table 9 Comparison between the yearly mean sunspot-number maxima and minima with the correspondent (plus/minus two years) London and Southern England wheat prices during the period (1610 – 1914).

Year	SSN Maxima	Year	Wheat Price (in £)	Year	SSN Minima	Year	Wheat Price (in £)
1614	121	1615	**1.71**	1617	0.8	1617	**2.25**
1625	42.4	1627	**1.32**	1630	0	1630	**3.23**
1639	76.7	1639	**1.76**	1645	0	1647	**3.13**
1652	2	1654	**1.08**	1658	0	1658	**2.89**
1660	2	1662	**2.29**	1668	0	1668	**1.89**
1676	1.7	1676	**1.54**	1679	0	1678	**2.65**
1684	1.4	1685	**1.41**	1690	0	1692	**2.49**
1695	0.1	1694	**1.83**	1699	0	1697	**3.12**
1705	96.7	1705	**1.11**	1711	0	1709	**3.48**
1717	105	1718	**1.25**	1723	18.3	1725	**1.90**
1727	203.3	1726	**1.48**	1733	8.3	1735	**1.66**
1738	185	1737	**1.30**	1744	8.3	1746	**1.40**
1750	139	1749	**1.34**	1755	16	1756	**2.50**
1761	143.2	1761	**1.43**	1766	19	1766	**2.58**
1769	176.8	1769	**1.75**	1775	11.7	1774	**2.82**
1778	257.3	1779	**1.72**	1784	17	1782	**2.59**
1787	220	1786	**1.97**	1798	6.8	1800	**7.43**
1804	79.2	1803	**2.85**	1810	0	1811	**6.73**
1816	76.3	1815	**3.45**	1823	2.2	1825	**3.43**
1830	117.4	1828	**3.02**	1833	13.4	1831	**3.32**
1837	227.3	1835	**1.97**	1843	18.1	1841	**3.22**
1848	208.3	1850	**2.01**	1856	8.2	1855	**3.73**
1860	182.2	1859	**2.19**	1867	13.9	1867	**3.22**
1871	185.3	1870	**2.35**	1878	5.7	1877	**2.84**
1883	106.1	1885	**1.64**	1889	10.4	1891	**1.85**
1893	142	1894	**1.14**	1901	4.6	1902	**1.40**
1905	105.5	1903	**1.34**	1913	2.4	1914	**1.75**

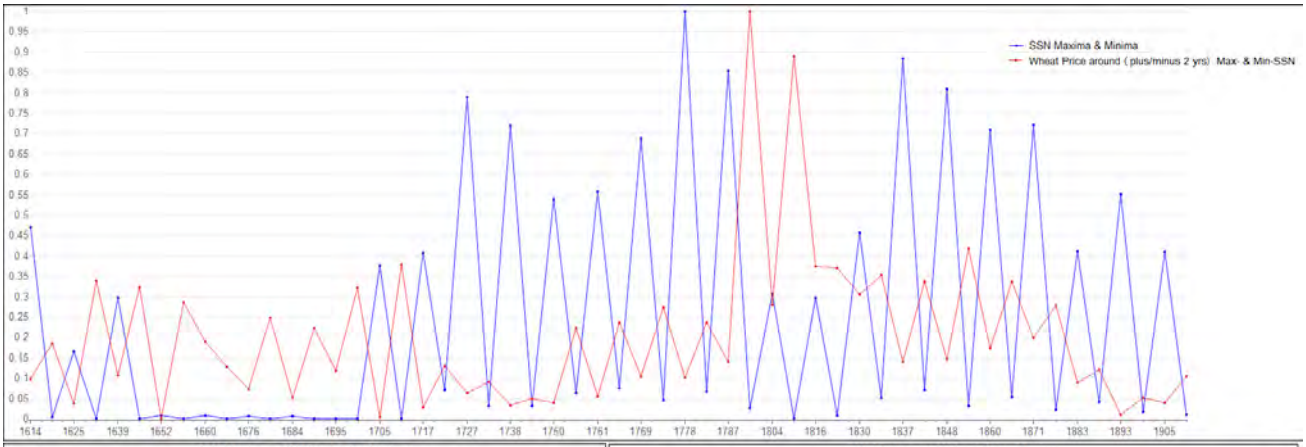

SSN Maxima and Wheat Price Minima													
Year	1625	1652	1676	1695	1705	1717	1761	1769	1778	1804	1816	1837	1893
SSN Maxima	42.4	2	1.7	0.1	96.7	105	143	177	257	79.2	76.3	227	142
Year	1627	1654	1676	1694	1705	1718	1761	1769	1779	1803	1815	1835	1894
Wheat Price Minima	1.32	1.08	1.54	1.83	1.11	1.25	1.43	1.75	1.72	2.85	3.45	1.97	1.14

SSN Minima and Wheat Price Maxima															
Year	1617	1630	1679	1699	1711	1755	1766	1775	1798	1810	1823	1856	1867	1878	1889
SSN Minima	0.8	0	0	0	0	16	19	11.7	6.8	0	2.2	8.2	13.9	5.7	10.4
Year	1617	1630	1678	1697	1709	1756	1766	1774	1800	1811	1825	1855	1867	1877	1891
Wheat Price Maxima	2.25	3.23	2.65	3.12	3.48	2.50	2.58	2.82	7.43	6.73	3.43	3.73	3.22	2.84	1.85

Figure 53 Normalized data of the sunspot-number maxima and minima and the correspondent (±2 years) London wheat prices during the time period 1610 – 1914. The tables below the time series plot indicate the sunspot-number maxima and minima for which the correspondent wheat price reaches its minimum and maximum value respectively.

Moreover, we observe a coincidence between solar-activity peaks and wheat-price troughs. As shown in Figure 53, for 13 different wheat-price cycles the minima occurred ±2 years around the closest sunspot-number maxima – on average 2 years after the corresponding sunspot-number maxima (*i.e.* the lags between the wheat-price minima and the closest sunspot-number maxima are +6, +2, +4, +2, +6, 0, +4, -1, 0, +1, +4, +5, +4, 0, 0, +1, +4, -1, -1, -8, -2, +3, +4, +4, +6, +1, +5). In particular, during the cycles 1617 – 1629, 1645 – 1657, 1668 – 1678, 1690 – 1698, 1699 – 1710, 1711 – 1722, 1755 – 1765, 1766 – 1744, 1775 – 1783, 1798 – 1809, 1810 – 1822, 1833 – 1842, and 1889 – 1900 as soon as the sunspot cycle reaches its peak value the wheat price falls to its minimum. On the contrary, over the course of 15 cycles (*i.e.* 1617 – 1629, 1630 – 1644, 1679 – 1689, 1699 – 1710, 1711 – 1722, 1755 – 1765, 1766 – 1744, 1775 – 1783, 1798 – 1809, 1810 – 1822, 1823 – 1832, 1856 – 1866, 1867 – 1877, 1878 – 1888, 1889 – 1900) once the sunspot cycle falls to the minimum the wheat price reaches its maximum value (Figure 53).

Harrison (1976) studied the hypothesis that various crop yields including wheat might be related with the sunspot-number cycle. Using data from 1866 to 1973 he showed that wheat yields were influenced by solar activity; *i.e.* lower than average yields were associated with low sunspot activity and higher than average yields were associated with high sunspot activity. Moreover, Pustil'nik and Din (2004) suggested that a possible effect of solar activity on wheat-prices behavior can be multiplied by nonlinear links in the causal chain: *solar activity – climate – wheat production – market prices*. Hence, the coincidence we observe between sunspot-number maxima and wheat-price minima could possibly

be explained as follows: on periods with high solar activity (sunspot-number maxima) the wheat production increases due to climate change leading to lower wheat prices.

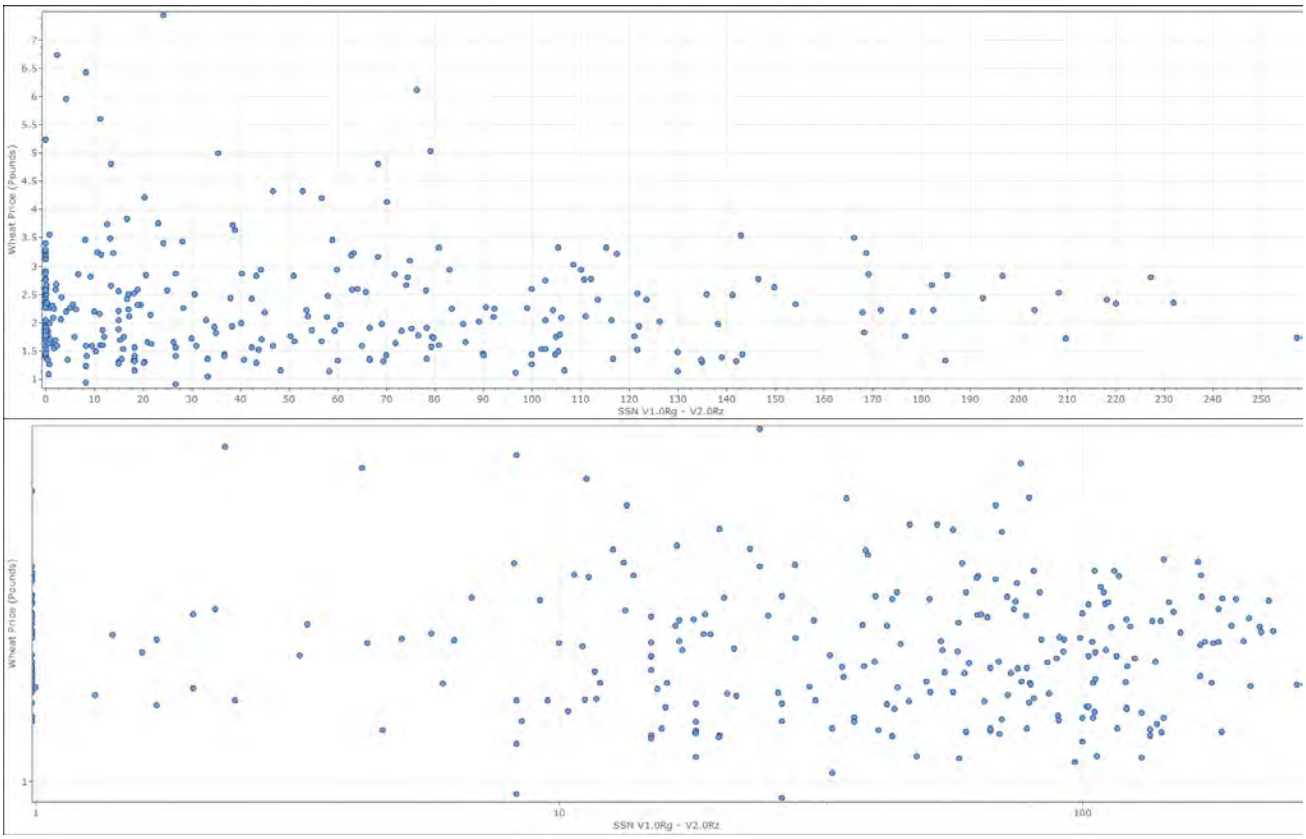

Figure 54 Scatterplot of sunspot numbers (horizontal axis) versus wheat prices (vertical axis) during the period 1610 – 1914 in linear scale (upper diagram) and in logarithmic scale (lower diagram).

Figure 54 illustrates the scatter plot of the sunspot numbers against the wheat prices. The upper diagram illustrates the data in linear scale while the lower diagram in logarithmic scale – for a better visualization since the data vary over several magnitudes. We observe that the pattern is neither rising nor falling indicating no correlation between the sunspot numbers and wheat prices. Moreover, the *Pearson correlation coefficient*[57] of the sunspot numbers with the wheat prices from 1610 to 1914 is estimated to be $r = -0.04$; that is, negative $(r < 0)$ and far from –1.0 $(r \to 0)$. This indicates that the strength[58] of the relationship between the sunspot numbers and wheat prices seems to be very weak and a negative one (*i.e.* when the sunspot numbers increase the wheat price decreases, and vice versa), making it difficult to support the existence of an interrelationship between the two series. However,

[57] The Pearson correlation coefficient is a measure of strength of the association between two variables taking values in the range $-1 \le r \le +1$; $r = +1$ indicates a perfect positive correlation, $r = -1$ indicates a perfect negative correlation, and $r = 0$ indicates no overall correlation (Myers *et al.*, 2010).

[58] Evans (1996) suggested guidelines about the sizes of correlation according to which the absolute value of correlation coefficient of 0.00 – 0.19, 0.20 – 0.39, 0.40 – 0.59, 0.60 – 0.79, and 0.80 – 1.00 correspond to very weak, weak, moderate, strong, and very strong correlation between two variables, respectively.

the correlation coefficient only measures the strength of linear relationships; it provides no information about the existence of nonlinear relationships. Therefore, finding a correlation coefficient *r* close to zero or even zero does not necessarily imply that the variables are unrelated (Myers *et al.*, 2010). Hence, it is possible that the relationship between the sunspot numbers and wheat prices is a strong nonlinear one.

5.2.2 Wheat prices during Maunder and Dalton minima

Earlier in this thesis, our long-term future yearly sunspot-number predictions suggested that the solar-activity level is likely to be reduced significantly during the next decades leading us to another prolonged sunspot minimum (since the era of Maunder Minimum) lasting up to the year ≈ 2100. Considering that we are heading into a period with sunspot-number peaks lower than those during the Dalton Minimum but not as low as those during the Maunder Minimum, it would be interesting to study in more detail the wheat-price variations during the Maunder Minimum (1645 – 1715) and Dalton Minimum (1790 – 1830).

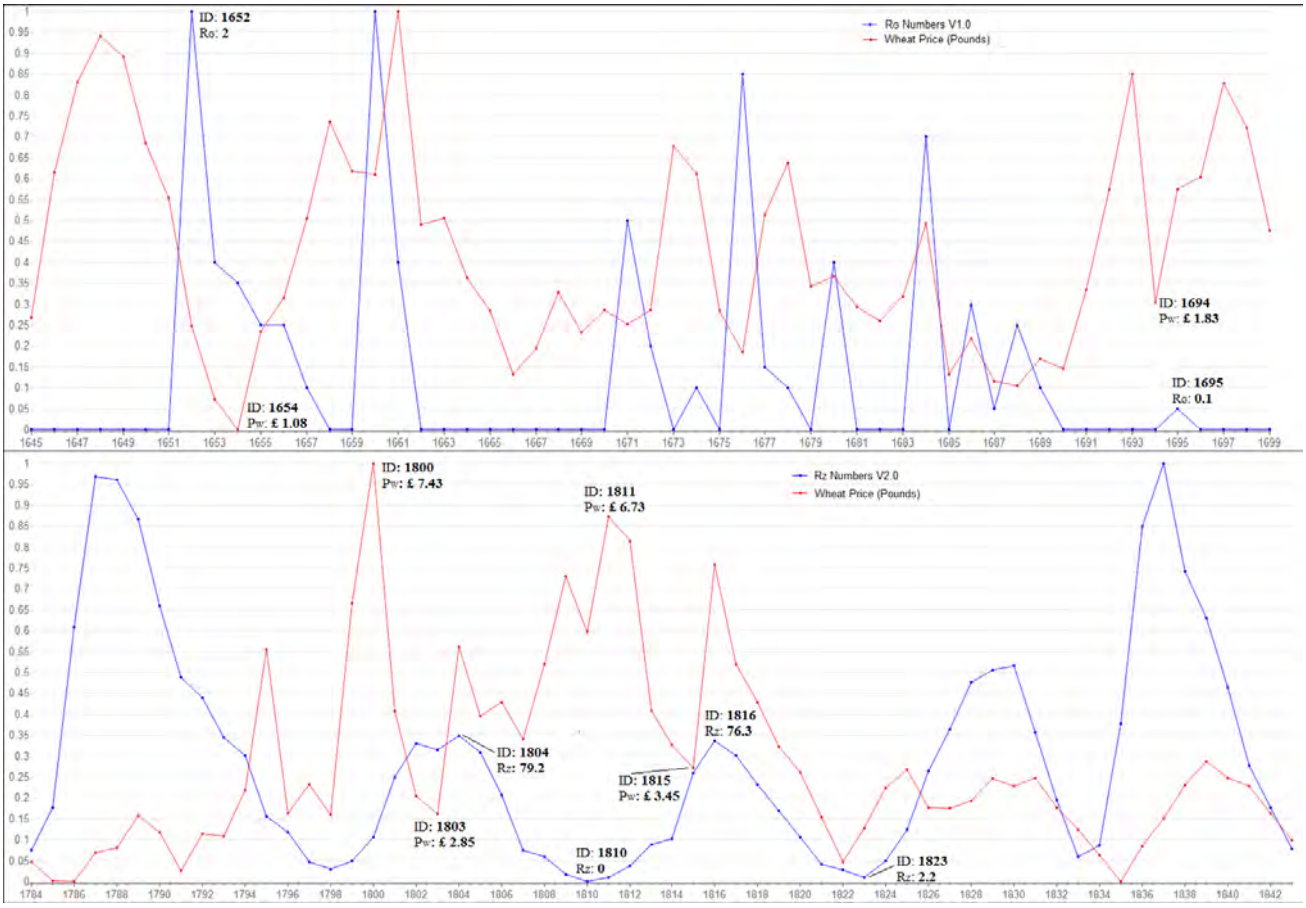

Figure 55 Normalized yearly mean sunspot-number and wheat-price data between 0 and 1 during the periods 1645 – 1699 (upper diagram) and 1784 – 1843 (lower diagram). Comparison between the smallest and largest wheat-price and sunspot-number maxima and minima.

As shown in Figure 55, during the Maunder Minimum, the wheat-price cycles with the smallest and largest price minima (*i.e.* the cycles 1643 – 1653 and 1688 – 1693 with minima £ 1.08 and £ 1.83, respectively) have coincided with sunspot-number cycles with the largest and smallest maxima (*i.e.* the cycles 1645 – 1657 and 1690 – 1698 with maxima 2 and 0.1, respectively), respectively. Moreover (Figure 55, Table 10), during the Dalton Minimum (1790 – 1830), the sunspot-number cycles with the smallest maxima and minima (*i.e.* the cycles 1798 – 1809, 1810 – 1822 with maxima 79.2, 76.3 and minima 0, 2.2, respectively) have coincided with wheat-price cycles with the largest maxima and minima (*i.e.* the cycles 1791 – 1802, 1803 – 1814 with maxima £ 7.43, £ 6.73 and minima £ 2.85, £ 3.45, respectively). Finally, the wheat-price maximum £ 7.43 – the largest wheat-price peak reached at 1800 – coincided with the smallest sunspot-number minimum 0 occurred at 1810.

Table 10 The average sunspot-number counts (per solar cycle) and the correspondent percent wheat-price decline (per wheat-price cycle) along with the sunspot-number and wheat-price maxima and minima (per cycle) from 1699 to 1914.

Solar Cycles	Maximum SSN	Minimum SSN	Average SSN	Wheat-Price Cycles	Maximum Price (£)	Minimum Price (£)	Percent Price Decline
1699 – 1710	96.7	0	**30.41**	1694 – 1704	3.12	1.11	**64.3%**
1711 – 1722	105	18.3	**45.13**	1705 – 1717	3.48	1.25	**64.0%**
1723 – 1732	203.3	8.3	90.16	1718 – 1730	2.22	1.14	48.7%
1733 – 1743	185	8.3	85.92	1731 – 1742	2.51	0.91	63.9%
1744 – 1754	139	16	66.77	1743 – 1753	1.75	1.30	25.7%
1755 – 1765	143.2	19	70.64	1754 – 1760	2.50	1.43	42.7%
1766 – 1774	176.8	11.7	99.88	1761 – 1768	2.58	1.75	32.2%
1775 – 1783	257.3	17	113.67	1769 – 1778	2.82	1.72	39.0%
1784 – 1797	220	6.8	100.76	1779 – 1790	2.82	2.11	25.2%
1798 – 1809	**79.2**	**0**	**39.72**	1791 – 1802	**7.43**	**2.85**	**61.6%**
1810 – 1822	**76.3**	**2.2**	**29.91**	1803 – 1814	**6.73**	**3.45**	48.7%
1823 – 1832	117.4	13.4	65.09	1815 – 1821	6.10	2.23	**63.5%**
1833 – 1842	227.3	18.1	105.95	1822 – 1834	3.43	1.97	42.6%
1843 – 1855	208.3	8.2	95.82	1835 – 1850	3.53	1.93	45.5%
1856 – 1866	182.2	13.9	94.22	1851 – 1863	3.73	2.01	46.2%
1867 – 1877	185.3	5.7	94.48	1864 – 1874	3.22	2.26	29.9%
1878 – 1888	106.1	10.4	57.8	1875 – 1888	2.84	1.49	47.6%
1889 – 1900	142	4.6	64.63	1889 – 1893	1.85	1.14	38.3%
1901 – 1912	105.5	2.4	51.91	1894 – 1909	1.85	1.58	14.2%

However, the wheat prices during the period 1645 – 1699 (*i.e.* the deepest phase of the Maunder Minimum when sunspots were scarce) were not significantly higher than the prices over the following years (when sunspots were significantly more abundant) taken as a whole (Figure 52). Moreover, as shown in Table 10, during the years after the Maunder Minimum (1700 – 1914) the wheat-price cycles with the largest percentage decline (*i.e.* the cycles 1694 – 1704, 1705 – 1717, 1791 – 1802, and 1815 – 1821 with 64%, 64%, 62%, and 63% decline, respectively) have coincided with or followed the weakest sunspot-number cycles; that is, cycles with the smallest average yearly sunspot numbers – the average counts have not exceeded fifty – (*i.e.* the cycles 1699 – 1710, 1711 – 1722, 1798 – 1809, and 1810 – 1822 with 30.41, 45.13, 39.72, and 29.91, respectively).

But the solar cycles with the smallest average sunspot-number counts during the period 1700 – 1914 were significantly stronger than the cycles during the Maunder Minimum when the average sunspot-number counts were close to zero (*i.e.* the cycles 1645 – 1657, 1658 – 1667, 1668 – 1678, 1679 – 1689, and 1690 – 1698 with 0.63, 0.28, 0.35, 0.33, and 0.01, respectively); hence, we would expect that the percentage wheat-price declines of the correspondent cycles during the Maunder Minimum would be the largest ones. However, we observe that the percentage wheat-price declines during the Maunder Minimum were not only no larger but even smaller (*i.e.* the cycles 1643 – 1653, 1654 – 1665, 1666 – 1675, 1676 – 1687, and 1688 – 1693 with 68%, 60%, 44%, 49%,and 42% decline, respectively) than those corresponding to the weakest solar cycles during the years 1700 – 1914 (*i.e.* 64%, 64%, 62%, and 63% decline, respectively).

These two results are not consistent with each other; we would expect that the exceptionally low solar activity during Maunder Minimum would be associated with lower grain yields leading to even higher prices than those over the following years. This inconsistency could be due to the uncertainties in the observations during this period; the exact number of sunspots observed on a single day of the Maunder Minimum is not very reliable since the number of observers (with imprecise instrumentation) was small (Usoskin *et al.*, 2000). However, Hoyt and Schatten (1996) made a thorough study of how well sunspots were observed during the Maunder Minimum supporting that this prolonged solar-activity minimum existed and was not an artifact of few observations; they estimated that 248 days[59] per year were observed suggesting that the existence of the Maunder Minimum would not be threatened by the discovery of a few more sunspots in future research.

[59] Of 358 days per year, 192 days per year were directly observed, 93 days per year were in gaps between observations lasting 6 days or less (it is unlikely that many sunspots were created and destroyed within these gaps), 72 days per year are covered by general statements, and 7 days per year were unobserved (Hoyt and Schatten, 1996).

But the Maunder Minimum coincided with the coldest phase of the Little Ice Age; radical climate change with a series of extremely dry and cold winters, weather extremes, changes in the average trends of temperature (lower than average temperatures) and precipitation along with recurrent long lasting and strong advection of continental air from the northeast towards western Russia and Europe (White, 2013; Luterbacher *et al.*, 2001; Wanner *et al.*, 1995; Pfister, 1994). During this period, agriculture in England faced abnormally severe winters and insufficient solar radiance during the grain growth period[60] (Pustil'nik and Din, 2004). Moreover, the English Agricultural Revolution also took place during this period – the agricultural output increased; *i.e.* grain output did not increase significantly before 1650 (until 1640), while rapid technological change in the form of cropping innovations[61] took place in the century after 1650 (Jones, 1974). Yield growth in Southern England from the early fourteenth to the late fifteenth centuries was significantly low[62]; while the period from 1640 to 1740 is known as a long "agrarian depression" not because of the lack of wheat, but rather the opposite – the low price paid for grains in England by the middle of 17th century until the mid-18th century became a problem (Tello *et al.*, 2015). Tello *et al.* (2015) suggested that the English farming innovations could have: (i) counteracted the effect of colder temperatures on agricultural yields through the decreasing N mineralization rate during the period 1645 – 1695[63], and (ii) reinforced the effect of temperature rise during the period 1696 – 1730[64].

In conclusion, although the cause of the English Agricultural Revolution remains unclear, the rapid transformation in techniques that were taken during the Maunder Minimum leading to grain-output increase, could be a response to the radical climate change of the time (coldest phase of the Little Ice Age). Hence, this could be an explanation for the inconsistency we observe in the wheat prices between the Maunder and Dalton Minima. However, more research is needed on the causes of the increased grain output in England during the Maunder Minimum.

[60] The length of the growing season was shortened lessening yields and jeopardizing the ability of certain grains to withstand this cooling period (Jones, 1965).
[61] A rise in the fertility of the soil through turnips and clover and their associated crop rotations led to increases in grain output per acre (Overton, 1986).
[62] The yields estimated net output per acre for Southern England in 1300-49 was the equivalent of 4.1 bushels per acre (Clark, 1991); the yields estimated net output per acre for 1500-39 was the equivalent of 3.5 bushels of wheat per acre (Clark, 2002).
[63] During the first Maunder Minimum period (1645 – 1695) the yearly average temperatures of Central and Southern England kept falling leading to reduced soil bacterial activity and N mineralization; the new farming practices that were also taken during this period were good enough to withstand the harsh climatic conditions (Tello *et al.*, 2015).
[64] With rising temperature (after 1695 up to 1730) in Central and Southern England, bacterial activity increased fostering in turn N mineralization in the soil, and along with the farming investments made in the earlier period, a growing reward on yields followed (Tello *et al.*, 2015).

5.2.3 Concluding remarks

In this section we investigated the solar-agricultural connection by comparing the yearly mean sunspot numbers with the London and Southern England wheat prices during the period 1610 – 1914. We showed that the wheat-price oscillations present a cyclic behavior with almost the same period as the solar-activity oscillations; since the wheat-price minimum in 1610 the average lengths of the cycles have been 11.15 years for the wheat prices and 11.27 years for the sunspot numbers. Moreover, the wheat-price minima and the closest sunspot-number maxima were within 2 years of each other. However, the wheat-price cycle appears to be slightly more variable in length than the sunspot-number cycle. Further, by calculating the correlation coefficient between the two series we observe that if there is a relationship between the sunspot numbers and wheat prices, it is a very weak one. This alone indicates that the two series cannot be correlated. However, if the association between the two series is nonlinear, then it is even possible the relationship between the sunspot numbers and wheat prices to be a strong nonlinear one.

Finally, an inconsistency is presented in the wheat prices between the Maunder and Dalton Minima; *i.e.* the wheat prices during the Maunder Minimum (scarce sunspots) were not higher than the prices during the Dalton Minimum (abundant sunspots comparing to Maunder Minimum). Regarding this inconsistency, we suggested that the rapid transformation in farming techniques that were taken during the Maunder Minimum leading to grain-output increase, could be a response to the radical climate change of the coldest phase of the Little Ice Age. Overall, the results of our study are consistent with the existing literature results, suggesting that there is connection between solar activity and wheat prices. However, this link might be coincidental. Further investigation is required to see if both time series are significantly related to each other.

Chapter 6

Conclusions

In this thesis we studied the complex population dynamics of predator-prey interactions, epidemics of infectious diseases and sunspot activity. In Section 2.1 we studied a predator-prey model with Holling type I functional response by incorporating prey refuge in the system. The stability properties of the fixed points were investigated through analytical stability analysis, while numerical simulation tools were used to study further the complex dynamics of our system. We showed that refuge does not always stabilize the predator-prey interactions; prey refuge in some cases produces even more chaotic, random-like dynamics than without refuge and prey population outbreaks appear. Following (Section 2.2), we investigated the prey refuge effect on predator-prey interactions by using a predator-prey model suitable for species having no overlap between successive generations. We showed that our modified model exhibits a wider array of dynamics than its continuous counterpart. Adding an average refuge destabilizes the predator-prey interactions via a supercritical Neimark-Sacker bifurcation and several period-doubling bifurcations. The addition of a large refuge exhibits random-like dynamics leading to outbreaks in the prey population density. The findings of this study suggest that the reproduction in certain intervals should be taken into account since it could help in the identification of pest outbreaks. In Section 2.3 the economic impacts of the outbreaks and infectious disease epidemics corresponding to the prey populations studied in Sections 2.1 – 2.2 (locust plagues and vector-borne diseases) were examined as well.

In Section 3.1 we investigated the spread of gonorrhea by taking into account the interval between successive clinical cases using a deterministic epidemic model; our analytical and numerical simulation results show a wider array of dynamics. We verified that there are phenomena of Fold and Flip bifurcations and we found some new qualitative dynamics. We came across the phenomenon "intermittency route to chaos", while as the density of infected individuals goes through quasi-periodicity, a strange attractor appears in the system. Moreover, we obtained chaos control in order to see how the male latex condom use during sexual intercourse affects the incidence of gonorrhea. Our results reflect what many studies on male latex condoms have shown; we showed that the male latex condom use stabilizes the chaotic vibrations of the system to a point where the number of infected individuals remains stable and is significantly small or zero, leading to the control of disease.

In Sections 4.1 – 4.2 we investigated the solar magnetic activity using the sunspot numbers. We analyzed the monthly and yearly sunspot-number data showing that they are both low-dimensional deterministic chaotic systems. In Section 4.1 we performed *post-facto* and future monthly solar activity predictions by using a neural network-type core algorithm and the actual monthly mean sunspot numbers from January 1749 to June 2013 as input data. We compared our *post-facto* predictions with the actual sunspot numbers and the predictions published by the Solar Influences Data Analysis Center showing that our technique is a better candidate for the prediction of the maximum monthly sunspot-number value. We also performed future predictions from July 2013 to June 2014 showing that the present Cycle 24 was yet to peak; our future mean monthly SSN predictions are coming true so far. We achieved rather good predictions on the Cycle 24 activity. We predicted that the maximum monthly SSN for the present Cycle 24 was expected to be 92.4 in November 2013 (±2 months), while the actual peak SSN was 102.8 in February 2014 (announced by the Solar Influences Data Analysis Center on 1 March 2014).

Following (Section 4.2), we performed future predictions trying to forecast the solar activity during the next five years (2013 – 2017) by using the actual yearly mean sunspot numbers from 1700 to 2012 as input data. We provided evidence that the yearly sunspot-number data can be used for long-term predictions. Moreover, in order to test and prove that our model is able to predict the Maunder Minimum period (1645 – 1715), we performed long-term *post-facto* predictions comparing them with the observed sunspot-number values. We also performed long-term future predictions trying to forecast the solar activity up to 2102. We achieved accurate predictions on the Cycle 24 activity; our predictions indicate that the present Cycle 24 is expected to be a low-peak-cycle. Regarding our long-term yearly forecasts, we predicted that the level of solar activity is likely to be reduced significantly during the next decades (90 years) leading to another prolonged sunspot minimum comparable to the Maunder Minimum.

However, testing the predictive skill of our proposed models (Sections 4.1 and 4.2) is an ongoing process; we constantly monitor the accuracy of our models' performance over time. Hence, in Section 4.3, we re-evaluated the performance of our proposed models for predicting solar activity in the light of the recently revised data (Sunspot Number Version 2.0). We performed new monthly and yearly predictions using the Sunspot Number Version 2.0 as input data and we compared them with our original predictions (using the Sunspot Number Version 1.0 series as input data). We showed that our proposed models are still able to produce quite accurate solar-activity predictions despite the full revision of the Zürich Sunspot Number, indicating that there is no significant degradation in their performance. Extending our new monthly predictions (July 2013 – August 2015) by 50 steps ahead in

time (from September 2015 to October 2019) we provided evidence that we are heading into a period of dramatic low solar activity. Our new future long-term predictions endorse our previous claim (Section 4.2) that a prolonged solar activity minimum is expected to occur lasting up to the year ≈ 2100.

In Section 5.1 all the topics studied in this thesis were connected. We provided some background review of the existing literature and empirical results on terrestrial and extraterrestrial relationships; *i.e.* possible connection between solar activity, biological (pest population outbreaks and epidemics of vector-borne diseases) and economic phenomena. In Section 5.2, we attempted to find a correlation between solar activity and agricultural economy by studying the wheat prices in Early Modern Britain for 305 consecutive years for which both sunspot-number and wheat-price data are available. The results of our study suggested the existence of a link between solar activity and wheat market. A cyclic correspondence was found between the oscillations of the two series; a periodic cycle was found in wheat prices sufficiently close in length to the 11-year cycle of sunspot numbers. Several of the wheat-price minima occurred close to the sunspot number maxima providing evidence of an association between the two series.

As far as our long-term yearly sunspot-number predictions, we also examined the wheat-price variations during the Maunder Minimum and Dalton Minimum; an inconsistency was presented in the wheat prices between the two minima (*i.e.* the wheat prices and the percentage wheat-price declines during the Maunder Minimum were smaller than those during the Dalton Minimum). Regarding this inconsistency, we suggested that the rapid transformation in farming techniques that were taken during the Maunder Minimum leading to grain-output increase, could be a response to the radical climate change of the coldest phase of the Little Ice Age, resulting to low prices paid for wheat. The results of our study suggest that there is a connection between the wheat-price and sunspot-number fluctuations. However, they provide little evidences in support of the solar-agricultural connection. Further investigation is required to see if both time series are significantly related to each other.

In conclusion, this thesis has gone some way towards enhancing our understanding of the complex population dynamics as follows:

Predator-Prey Interactions and Gonorrhea Transmission

1. The findings of the predator-prey studies have important implications for the identification of pest population outbreaks. They suggest that our modified proposed models under the new assumptions of prey refuge and non-overlapping generations, can be applied to dangerous pests like mosquitoes and desert locusts, which often show population outbreaks in real world. Clearly, our proposed

models have some limitations. Nevertheless, they seem to be more appropriate for describing the real world pest population outbreaks (such as locust plagues and mosquito outbreaks) than the original predator-prey models.

2. Further, our modified epidemic model seems to be more effective in practice reflecting the real-world fluctuations in gonorrhea cases. The findings of this study suggest that the time interval between successive clinical cases is important for policy makers and public health authorities and should be taken into account, since it could help in the identification of gonorrhea emergency situations. However, little is known about the clinical onset serial intervals of gonorrhea. Therefore, collected data on serial intervals of gonorrhea could provide some useful public health information to guide any public health action.

Taken together the findings of these studies provide further evidence that the dynamical systems have the potential to describe the real-world population outbreaks and therefore can be used for their identification, prediction and control in order to reduce their disastrous effects on public health, food security and global economy.

Solar Magnetic Activity, Heliobiology and Helioeconomy

Turning now to the solar activity studies, our proposed model for predicting solar activity using the monthly mean sunspot numbers have been very promising so far. Moreover, our future long-term solar activity predictions are in good agreement with other studies supporting the concept of another expected prolonged sunspot minimum (since the era of Maunder Minimum) over the following decades, having most likely wide impacts on our planet's climate. There is a rapidly growing literature focusing on the existence of terrestrial and extraterrestrial relationships. However, the arena of research on the impact of solar activity on biological and economic phenomena is still limited.

1. Relatively few studies investigate the solar-agricultural connection, ignoring the solar activity during the Maunder Minimum (1645 – 1715). The last part of this thesis offers an innovative study on the possible link between solar activity and crop prices, by investigating the relationship between the yearly mean sunspot numbers and the London & Southern England wheat prices from 1610 throughout the Maunder Minimum (1645 – 1715) and the Dalton Minimum (1790 – 1830) until 1914, as a way to stimulate research in the area of helioeconomy. Returning to the question posed at the beginning of this study, our findings do suggest that there is a connection between solar activity and wheat prices. However, considering the limitations of the methodology chosen for this investigation, the results need to be interpreted with caution since this link might be

coincidental. Thus, further investigation is required to see if both time series are significantly related to each other.

2. Moreover, this study has raised many questions in need of further investigation. In particular, it provides the framework for a new way to predict the real-world pest population outbreaks. As stated in the literature review for the existence of an interrelationship between solar activity and pest outbreaks, revealing such a correlation could contribute significantly to the prevention and control of outbreaks of pest populations and vector-borne diseases in future. In such a case, our proposed models for predicting solar activity could be further used to predict outbreaks of dangerous pests like desert locusts and mosquitoes, in order to ensure global food security and reduce the considerable health burden and devastating socioeconomic breakdowns they inflict.

The prospect of being able to predict biological and economic phenomena via solar activity variations, serves as a continuous stimulus for future research. Future studies on this topic are therefore required in order to verify the existence of solar-terrestrial interrelationships.

Appendix

Local Stability of the Endemic Fixed Point (Subsection 3.1.4)

Using the three stability conditions (Equation (3)) we let:

$$\left(\lambda_m d_m r+1\right)\cdot\left(\sqrt{\begin{array}{l}\lambda_m d_m \delta r\left(\lambda_m d_m \delta\left(\delta-2d_f\right)^2 r+2\left(\delta^3+4d_f\left(d_m+d_f\right)\delta-8d_f^2 d_m\right)\right)\\ +\delta^4+4d_f\left(\delta^3+\left(d_f-2d_m\right)\delta^2+4D\left(d_m-\delta\right)\right)\end{array}}\right)$$

$$F_3=\frac{+\lambda_m^2 d_m^2\delta\left(2d_f-\delta\right)r^2+4\lambda_m d_m\left(\left(d_m+d_f\right)\delta-D\right)Dr+\delta^2+2d_f\delta-4D}{2\lambda_m D\delta\left(\lambda_m d_m\delta r+\delta-2d_m\right)}$$

$$F_4=-\frac{-\lambda_m d_m^2\left(Ld_f^2+1\right)r^2-2LD\left(d_m+d_f\right)r-\lambda_f d_f^2\left(d_m LD+1\right)}{\left(\lambda_m d_m r^2+\lambda_f d_f\right)\cdot\left(LD-1\right)+\left(LD^2-1\right)r}$$

$$\sqrt{\begin{array}{l}\lambda_m^2 d_m^3\left(LD\left(Ld_f^2-2\right)d_f+d_m+4d_f\right)r^4+4\lambda_m d_f d_m^2\left(LD\left(1-Ld_f^2\right)d_m+LD\left(Ld_f^2+1\right)+2\right)r^3\\ +2D\left(L^2 d_f d_m^3\left(3-Ld_f^2\right)-2LD^2+LD\left(3Ld_f^2+7\right)+2\right)r^2\\ +4\lambda_f d_f^2 d_m\left(L^2 d_f d_m^3-LD^2+LD+\left(Ld_f^2+2\right)\right)r+\lambda_f^2 d_f^3\left(L^2 d_f d_m^4-2d_m LD+4d_m+d_f\right)\end{array}}$$

$$F_5=\frac{+\lambda_m d_m^2\left(Ld_f^2+1\right)r^2+2LD\left(d_m+d_f\right)r+\lambda_f d_f^2\left(d_m LD+1\right)}{\left(\lambda_m d_m r^2+\lambda_f d_f\right)\cdot\left(LD-1\right)+\left(LD^2-1\right)r}$$

where, $LD=\lambda_f\lambda_m d_f d_m$, $L=\lambda_f\lambda_m$ and $D=d_f d_m$

References

Agliari, A., Bischi, G.I., Gardini, L., Sushko, I.: 2009, Introduction to Discrete Nonlinear Dynamical Systems, University of Trento. Available at: http://citeseerx.ist.psu.edu/viewdoc/download?doi=10.1.1.602.5941&rep=rep1&type=pdf

Ahluwalia, H.S.: 2003, Meandering Path to Solar Activity Forecast for Cycle 23, In: Velli, M., Bruno, R., Malara, F. (eds.), *AIP Conference Proceedings* **CP679**, Pisa, Italy, 176-179. doi:10.1063/1.1618570

Ahluwalia, H.S., Jackiewicz, J.: 2012, Sunspot cycle 23 descent to an unusual minimum and forecasts for cycle 24 activity, *Advances in Space Research* **50**(6), 662-668. doi:10.1016/j.asr.2011.04.023

Aittokallio, T., Gyllenberg, M., Hietarinta, J., Kuusela, T., Multamäki, T.: 1999, Improving the false nearest neighbors method with graphical analysis, *Physical Review E* **60**(1), 416-421. doi:10.1103/physreve.60.416

Albertson, V.D., Thorson, J.M., Miske, S.A.: 1974, The effects of geomagnetic storms on electrical power systems, *IEEE Transactions on Power Apparatus and Systems* **PAS-93**(4), 1031-1044. doi: 10.1109/TPAS.1974.294047

Allen, L.J.S.: 1994, Some discrete-time SI, SIR, SIS epidemic models, *Mathematical Biosciences* **124**(1), 83-105. doi:10.1016/0025-5564(94)90025-6

Allen, L.J.S., Jones, M.A., Martin, C.F.: 1991, A discrete-time model with vaccination for a measles epidemic, *Mathematical Biosciences* **105**(1), 111-131. doi:10.1016/0025-5564(91)90051-J

Allen, L.J.S., Kirupaharan, N., Wilson, S.M.: 2004, SIS Epidemic Models with Multiple Pathogen Strains, *Journal of Difference Equations and Applications* **10**(1) 53-75. doi:10.1080/10236190310001603680

Alligood, K.T., Sauer, T.D., Yorke, J.A.: 1996, *Chaos: An Introduction to Dynamical Systems*, Springer-Verlag, New York. doi:10.1007/b97589

Al-Shameri, W.F.H.: 2012, Correlation dimension of an attractor generated by an orbit of general two-dimensional iterated quadratic map, *International Journal of Contemporary Mathematical Sciences* **7**(9-12), 413-424. Available at: http://www.m-hikari.com/ijcms/ijcms-2012/9-12-2012/alshameriIJCMS9-12-2012.pdf

Anderson, J.F.: 1970, Metabolic rates of spiders, *Comparative Biochemistry and Physiology* **33**(1), 51-72. doi:10.1016/0010-406X(70)90483-4

Anderson, J.F.: 1974, Responses to starvation in the spiders *Lycosa lenta Hentz* and *Filistate hibernalis* (*Hentz*), *Ecology* **55**(3), 576-585. doi:10.2307/1935148

Anderson, J.F., Prestwich, K.N.: 1975, The fluid pressure pumps of spiders (*Chelicerata*, *Araneae*), *Zeitschrift für Morphologie der Tiere* **81**(4), 257-277. doi:10.1007/BF00298488

Anderson, J.F., Prestwich, K.N.: 1982, Respiratory gas exchange in spiders, *Physiological Zoology* **55**(1), 72-90. Available at: http://www.jstor.org/stable/30158445

Andrews, L.B.: 1936, The earth, the sun, and sunspots, *Smithsonian Institution Publication* **3418**, 137-177.

Aparicio, T., Pozo, E.F., Saura, D.: 2008, Detecting determinism using recurrence quantification analysis: Three test procedures, *Journal of Economic Behavior & Organization* **65**(3-4), 768-787. doi:10.1016/j.jebo.2006.03.005

Archibald, E.D.: 1878, Locusts and Sun-Spots, *Nature* **19**, 145-146. doi:10.1038/019145c0

Aronson, D.G., Chory, M.A., Hall G.R., McGehee, R.P.: 1982, Bifurcations from an invariant circle for two-parameter families of maps on the plane: A computer-assisted study, *Communications in Mathematical Physics* **83**(3), 303-354. doi:10.1007/BF01213607

Aronsson, G., Mellander, I.: 1980, A deterministic model in biomathematics: asymptotic behavior and threshold conditions, *Mathematical Biosciences* **49**(3-4), 207-222. doi:10.1016/0025-5564(80)90079-6

Asante, F.A., Asenso-Okyere, K.: 2003, Economic Burden of Malaria in Ghana, A Technical Report Submitted to the World Health Organisation, African Regional Office. Available at: http://www.who.int/countries/gha/publications/Economic_Burden_of_Malaria_in_Ghana_Final_Report_Nov03.pdf

Badalyan, O.G., Obridko, V.N., Sykora, J.: 2001, Brightness of the Coronal Green Line and Prediction for Activity Cycles 23 and 24, *Solar Physics* **199**(2), 421-435. doi:10.1023/A:1010343520424

Bailey, N.T.J.: 1975, *The Mathematical Theory of Infectious Diseases*, Hafner Press, 2nd edition, New York.

Baker, D.N., Barby, L.A., Curtis, S., Jokipii, J.R., Lewis, W.S., Miller, J., Schimmerling, W., Singer, H.J., Townsend, L.W., Turner, R.E., Zurbuchen, T.H.: 2007, Space Radiation Hazards and the Vision for Space Exploration: A Report on the October 2005 Wintergreen Conference, *Space Weather* **5**(2), 1-4. doi:10.1029/2007sw000313.

Barlow, D.: 1977, The condom and gonorrhoea, *The Lancet* **310**(8042), 811-813. doi:10.1016/S0140-6736(77)90737-1

Barlow, W.H.: 1849, On the spontaneous electrical currents observed in wires of the electrical telegraph, *Philosophical Transactions of the Royal Society of London* **139**(1849), 61-72. doi:10.1098/rstl.1849.0006

Barnett, W.A., Serletis, A., Serletis, D.: 2006, Nonlinear and Complex Dynamics in Real Systems, *International Journal of Nonlinear Sciences and Numerical Simulation* **7**(2), 191-196. doi:10.1515/IJNSNS.2006.7.2.191

Barrientos, L.L.: 1995, The Present State of the Locust and Grasshopper Problem in Brazil, *Journal of Orthoptera Research* **4**, 61-64. doi:10.2307/3503459

Beer, J., Tobias, S., Weiss, N.: 1998, An Active Sun Throughout the Maunder Minimum, *Solar Physics* **181**(1), 237-249. doi:10.1023/a:1005026001784

Begon, M., Townsend, C.R., Harper, J.L.: 2006, *Ecology: From Individuals to Ecosystems*, 4th Edition, Blackwell Publishing, CPI Bath Press, United Kingdom.

Belaire-Franch, J., Contreras, D., Tordera-Lledo, L.: 2002, Assessing nonlinear structures in real exchange rates using recurrence plot strategies, *Physica D: Nonlinear Phenomena* **171**(4), 249-264. doi:10.1016/s0167-2789(02)00625-5

Bell, M.: 2005, The 2004 desert locust outbreak, *Bulletin of the American Meteorological Society* **86**, S60.

Berger, R.E., Alexander, E.R., Harnisch, J.P., Paulsen, C.A., Monda, G.D., Ansell, J., Holmes, K.K.: 1979, Etiology, manifestations and therapy of acute epididymitis: prospective study of 50 cases, *Journal of Urology* **121**(6), 750-754. doi:10.1016/S0196-0644(80)80036-9

Bershadskii, A.: 2009, Chaotic mean wind in turbulent thermal convection and long-term correlations in solar activity, arXiv:0908.4008v4 [astro-ph.SR].

Bhatt, S., Gething, P.W., Brady, O.J., Messina, J.P., Farlow, A.W., Moyes, C.L., Drake, J.M., Brownstein, J.S., Hoen, A.G., Sankoh, O., Myers, M.F., George, D.B., Jaenisch, T., Wint, G.R., Simmons, C.P., Scott, T.W., Farrar, J.J., Hay, S.I.: 2013, The global distribution and burden of dengue, *Nature* **496**(7446), 504-507. doi:10.1038/nature12060

Bhavsar, A.T., Shepard, D.S., Suaya, J.A., Mafowosofo, M., Hurley, C.L.: 2010, A private hospital-based study assessing knowledge, attitudes, practices and costs associated with dengue illness in Surat, India, WHO Regional Office for South-East Asia, Dengue Bulletin, Volume 34. Available at: http://apps.who.int/iris/bitstream/10665/170975/1/db2010v34p54.pdf

Blais, G., Metsa, P.: 1993, Operating the hydro-Quebec grid under magnetic storm conditions since the storm of 13 March 1989, In: IV Solar-Terrestrial Predictions Workshop Proceedings held May 18-20, 1992, at Ottawa, Canada, *National Oceanic and Atmospheric Administration* **1,** Environmental Research Laboratories, Boulder, CO USA, 108-130.

Blanchard, P., Devaney, L.R., Hall, R.G.: 2006, *Differential equations*, Thomson Brooks/Cole, Belmont, CA, USA.

Boccara, N.: 2010, *Modeling Complex Systems*, 2nd Edition, Springer-Verlag, New York. doi:10.1007/978-1-4419-6562-2

Boteler, D.H., Pirjola, R.J., Nevanlinna, H.: 1998: The effects of geomagnetic disturbances on electrical systems at the earth's surface, *Advances in Space Research* **22**(1), 17-27. doi:10.1016/S0273-1177(97)01096-X

Brady, O.J., Gething, P.W., Bhatt, S., Messina, J.P., Brownstein, J.S., Hoen, A.G., Moyes, C.L., Farlow, A.W., Scott, T.W., Hay, S.I.: 2012, Refining the Global Spatial Limits of Dengue Virus Transmission by Evidence-Based Consensus, *PLoS Neglected Tropical Diseases* **6**(8), e1760. doi:10.1371/journal.pntd.0001760

Carey, R.F., Herman, W.A., Retta, S.M., Rinaldi, J.E., Herman, B.A., Athey, T.W.: 1992, Effectiveness of latex condoms as a barrier to human immunodeficiency virus-sized particles under conditions of simulated use, *Sexually Transmitted Diseases* **19**(4), 230-234. doi:10.1097/00007435-199207000-00009

Carey, R.F., Lytle, C.D., Cyr, W.H.: 1999, Implications of laboratory tests of condom integrity, *Sexually Transmitted Diseases* **26**(4), 216-220. doi:10.1097/00007435-199904000-00006

Carrasco, L.R., Lee, L.K., Lee, V.J., Ooi, E.E., Shepard, D.S., Thein, T.L., Gan, V., Cook, A.R., Lye, D., Ng, L.C., Leo, Y.S.: 2011, Economic Impact of Dengue Illness and the Cost-Effectiveness of Future Vaccination Programs in Singapore, *PLoS Neglected Tropical Diseases* **5**(12), e1426. doi:10.1371/journal.pntd.0001426

Carrington, C.V.F., Auguste, A.J.: 2013, Evolutionary and ecological factors underlying the tempo and distribution of yellow fever virus activity, *Infection, Genetics and Evolution* **13**, 198-210. doi:10.1016/j.meegid.2012.08.015

Carrington, R.C.: 1863, *Observations of the Spots on the Sun, from November 9th 1853 to March 24th 1861*, Made at Redhill, Williams and Norgate, London. Available at: http://parhelio.com/biblioteca/libros/Richard%20Carrington_Observations%20of%20the%20spots%20on%20the%20sun_1863.pdf

Castillo-Chavez, C., Yakubu, A-A.: 2001, Discrete-time S-I-S models with complex dynamics, *Nonlinear Analysis, Theory, Methods and Applications* **47**(7), 4753-4762. doi:10.1016/S0362-546X(01)00587-9

Centers for Disease Control and Prevention: 2000, Tracking the Hidden Epidemic: Trends in STDs in the United States 2000, Department of Health and Human Services, USA. Available at: http://www.cdc.gov/std/trends2000/trends2000.pdf

Centers for Disease Control and Prevention: 2002, Sexually transmitted diseases treatment guidelines 2002, *Morbidity and Mortality Weekly Report Recommendations and Reports* **51**(RR-6), 1-78. Available at: http://www.cdc.gov/std/treatment/rr5106.pdf

Chakravarti, A., Kumaria, R.: 2005, Eco-epidemiological analysis of dengue infection during an outbreak of dengue fever, India, *Virology Journal* **2**(32), 1-7. doi:10.1186/1743-422X-2-32

Chen, J.P., Zhang, H.D.: 1986, The qualitative analysis of two species predator-prey model with Holling's type III functional response, *Applied Mathematics and Mechanics* **7**(1), 77-86. doi:10.1007/BF01896254

Clark, G.: 1991, Labour Productivity in English Agriculture, 1300-1860, In: Campbell, B.M.S., Overton, M., *Land, Labour, and Livestock: Historical Studies in European Agricultural Productivity*, Manchester, Manchester University Press, 211-235.

Clark, G.: 2002, The Agricultural Revolution and the Industrial Revolution: England, 1500-1912, University of California, Davis. Available at: http://www.econ.ucdavis.edu/faculty/gclark/papers/prod2002.pdf

Clette, F., Svalgaard, L., Vaquero, J.M., Cliver, E.W.: 2014, Revisiting the Sunspot Number: A 400-Year Perspective on the Solar Cycle, *Space Science Reviews* **186**(1-4), 35-103. doi:10.1007/s11214-014-0074-2

Clilverd, M.A., Clarke, E., Rishbeth, H., Clark, T.D.G., Ulich, T.: 2003, Solar activity levels in 2100, *Astronomy & Geophysics* **44**(5), 5.20-5.22. doi:10.1046/j.1468-4004.2003.44520.x

Codreanu, S., Danca, M.: 1997a, Control of Chaos in a Nonlinear Prey-Predator Model, *Polish Journal of Environmental Studies* **6**(1), 21-24. Available at: http://danca.rist.ro/doc/codreanu%20si%20danca.pdf

Codreanu, S., Danca, M.: 1997b, Suppression of Chaos in a One-dimensional Mapping, *Journal of Biological Physics* **23**(1), 1-9. doi:10.1023/A:1004910118920

Cooke, K.L., Yorke, J.A.: 1973, Some equations modelling growth processes and gonorrhea epidemics, *Mathematical Biosciences* **16**(1-2), 75-101. doi:10.1016/0025-5564(73)90046-1

Criddle, N.: 1932, The correlation of the sunspot periodicity with grasshopper fluctuations in Manitoba, *Canadian Field Naturalist* **46**, 195-199.

Cropper, M.L., Haile, M., Lampietti, J.A., Poulos, C., Whittington, D.: 2000, The value of preventing malaria in Tembien, Ethiopia, *Policy Research Working Papers*, The World Bank, Washington DC. doi:10.1596/1813-9450-2273

Crosby, N.B., Rycroft, M.J., Tulunay, Y.: 2006, Overview of a graduate course delivered in Turkey, emphasizing solar-terrestrial physics and space weather, *Surveys in Geophysics* **27**(3), 319-364. doi:10.1007/s10712-005-6204-3

Currie, R.G.: 1988, Lunar tides and the wealth of nations, *New Scientist* **120**(1627), 52-55.

Danca, M., Codreanu, S., Bako, B.: 1997, Detailed Analysis of a Nonlinear Prey-Predator Model, *Journal of Biological Physics* **23**(1), 11-20. doi:10.1023/A:1004918920121

De Jager, C.: 2005, Solar Forcing of Climate 1: Solar Variability, *Space Science Reviews* **120**(3-4), 197-241. doi:10.1007/s11214-005-7046-5

De Jager, C., Usoskin, I.: 2006, On possible drivers of Sun-induced climate changes, *Journal of Atmospheric and Solar-Terrestrial Physics* **68**(18), 2053-2060. doi:10.1016/j.jastp.2006.05.019

De Lury, R.E.: 1930, Sunspots in relation to fluctuations in grasshoppers and grouse at Aweme, Manitoba, *The Canadian field-naturalist*, **44**(5), 120.

De Meyer, F.: 2003, A Transfer Function Model for the Sunspot Cycle, *Solar Physics* **217**(2), 349-366. doi:10.1023/B:SOLA-0000006856-85960-2e

Descloux, E., Mangeas, M., Menkes, C.E., Lengaigne, M., Leroy, A., Tehei, T., Guillaumot, L., Teurlai, M., Gourinat, A.C., Benzler, J., Pfannstiel, A., Grangeon, J.P., Degallier, N., De Lamballerie, X.: 2012, Climate-Based Models for Understanding and Forecasting Dengue Epidemics, *PLoS Neglected Tropical Diseases* **6**(2), e1470. doi:10.1371/journal.pntd.0001470

Desert Locust Control Organization-Eastern Africa, "Activities of DCLO-EA". Available at: http://www.dlcoea.org.et/index.php/dlcoactivities

Despland, E.: 2005, Diet Breadth and Anti-Predator Strategies in Desert Locusts and Other Orthopterans, *Journal of Orthoptera Research* **14**(2), 227-233. doi:10.1665/1082-6467(2005)14[227:DBAASI]2.0.CO;2

Dewey, E.R.: 1960, Correspondence between Tchijevsky's Index of Mass Human Excitability and Sunspot Maxima 500 B.C. – A.D. 1922, *Journal of Cycle Research* **9**(1).

Diks, C., Hommes, C., Panchenko, V., Van der Weide, R.: 2008, E&F Chaos: A user-friendly software package for nonlinear economic dynamics, *Computational Economics* **32**(1-2), 221-244. doi:10.1007/s10614-008-9130-x

Ditto, W.L., Rauseo, S.N., Spano, M.L.: 1990, Experimental control of chaos, *Physical Review Letters* **65**(26), 3211-3214. doi:10.1103/PhysRevLett.65.3211

Dutroulau, A.F.: 1868, *Traité des Maladies des Européens dans les Pays Chauds (Régions tropicales)*, 2nd Edition, Paris: J.B. Bailliére et Fils.

Eckmann, J.P., Kamphorst, S.O., Ruelle, D.: 1987, Recurrence plots of dynamical systems, *Europhysics Letters* **4**(9), 973-977. doi:10.1209/0295-5075/4/9/004

Eckmann, J.P., Ruelle, D.: 1985, Ergodic theory of chaos and strange attractors, *Reviews of Modern Physics* **57**(3), 617-656. doi:10.1103/revmodphys.57.617

Eddy, J.A.: 1976, The Maunder Minimum, *Science* **192**(4245), 1189-1202. doi:10.1126/science.192.4245.1189

Edgar, W.D.: 1969, Prey and predators of wolf spider *Lycosa lugubris*, *Journal of Zoology* **159**(4), 405-411. doi:10.1111/j.1469-7998.1969.tb03897.x

Edgar, W.D.: 1971, Aspects of the ecological energetic of the wolf spider *Pardosa* (*Lycosa*) *lugubris* (*Walckenaer*), *Oecologia* **7**(2), 136-154. doi:10.1007/BF00346356

Eidmann, H.: 1931, Zur Kenntnis der Periodizitat der Insekten-Epidemien, *Zeitschrift für Angewandte Entomologie*, **18**(3), 537-567. doi:10.1111/j.1439-0418.1931.tb00223.x

Elaydi, S.N.: 2005, *An Introduction to Difference Equations*, 3rd Edition, Springer Science + Business Media, Inc., New York, USA. doi:10.1007/0-387-27602-5

Enatsu, Y., Nakata, Y., Muroya, Y.: 2012, Global stability for a discrete SIS epidemic model with immigration of infectives, *Journal of Difference Equations and Applications* **18**(11), 1913-1924. doi:10.1080/10236198.2011.602973

Evans, J.D.: 1996, *Straightforward statistics for the behavioral sciences*, Pacific Grove, CA: Brooks/Cole Publishing.

Fabretti, A., Ausloos, M.: 2005, Recurrence Plot and Recurrence Quantification Analysis Techniques for Detecting a Critical Regime. Examples from Financial Market Indices, *International Journal of Modern Physics C*, **16**(5), 671-706. doi:10.1142/S0129183105007492

Faria, H.H., Echer, E., Rigozo, R., Vieira, L.E.A., Nordemann, D.J.R., Prestes, A.: 2004, A comparison of the spectral characteristics of the Wolf Sunspot Number (R_Z) and Group Sunspot Number (R_G), *Solar Physics* **223**(1), 305-318. doi:10.1007/s11207-004-5318-y

Feynman, J., Gabriel, S.B.: 1990, Period and phase of the 88-year solar cycle and the Maunder minimum: Evidence for a chaotic sun, *Solar Physics* **127**(2), 393-403. doi:10.1007/BF00152176

Filjar, R.: 2008, A study of direct severe space weather effects on GPS ionospheric delay, *Journal of Navigation* **61**(1), 115-128. doi:10.1017/S0373463307004420

Findlay, G.M., Davey, T.H.: 1936, Yellow fever in the gambia. I. Historical, *Transactions of the Royal Society of Tropical Medicine and Hygiene* **29**(6), 667-678. doi:10.1016/s0035-9203(36)90044-5

Fine, P.E.M.: 2003, The interval between successive cases of an infectious disease, *American Journal of Epidemiology* **158**(11), 1039-1047. doi:10.1093/aje/kwg251

Fleming, D.T., Wasserheit, J.N.: 1999, From epidemiological synergy to public health policy and practice: the contribution of other sexually transmitted diseases to sexual transmission of HIV infection, *Sexually Transmitted Infections* **75**(1), 3-17. doi:10.1136/sti.75.1.3

Ford, M.J.: 1977, Energy costs of the predation strategy of the web-spinning spider *Lepthyphantes zimmermanni Bertkau* (*Linyphiidae*), *Oecologia* **28**(4), 341-349. doi:10.1007/BF00345989

Fraser, A.M., Swinney, H.L.: 1986, Independent coordinates for strange attractors from mutual information, *Physical Review A* **33**(2), 1134-1140. doi:10.1103/PhysRevA.33.1134

Friis-Christensen, E., Lassen, K.: 1991, Length of the Solar Cycle: An Indicator of Solar Activity Closely Associated with Climate, *Science* **254**(5032), 698-700. doi:10.1126/science.254.5032.698

Futami, K., Sonye, G., Akweywa, P., Kaneko, S., Minakawa, N.: 2008, Diving Behavior in *Anopheles gambiae* (Diptera: *Culicidae*): Avoidance of a Predacious Wolf Spider (Araneae: *Lycosidae*) in Relation to Life Stage and Water Depth, *Journal of Medical Entomology* **45**(6), 1050-1056. doi:10.1093/jmedent/45.6.1050

Gallup, J.L., Sachs, J.D.: 2001, The Economic Burden of Malaria, *American Journal of Tropical Medicine and Hygiene* **64**(1,2)S, 85-96. Available at: http://www.ajtmh.org/content/64/1_suppl/85.full.pdf

Garcia-Mata, C., Shaffner, F.I.: 1934, Solar and Economic Relationships: A Preliminary Report, *Quarterly Journal of Economics* **49**(1), 1-51. doi:10.2307/1883875

Garnett, G.P.: 2002, An introduction to mathematical models in sexually transmitted disease epidemiology, *Sexually Transmitted Infections* **78**(1), 7-12. doi:10.1136/sti.78.1.7

Garske, T., Van Kerkhove, M.D., Yactayo, S., Ronveaux, O., Lewis, R.F., Staples, J.E., Perea, W., Ferguson, N.M.: 2014, Yellow Fever in Africa: Estimating the Burden of Disease and Impact of Mass Vaccination from Outbreak and Serological Data, *PLoS Medicine* **11**(5), e1001638. doi:10.1371/journal.pmed.1001638

Gerbase, A.C., Rowley, J.T., Heymann, D.H., Berkley, S.F., Piot, P.: 1998, Global prevalence and incidence estimates of selected curable STDs, *Sexually Transmitted Infections* **74**(1), S12-S16. Available at: http://cedoc.cies.edu.ni/general/2nd_Generation%20(D)/Methods%20for%20estimation/STI%201998%20paper.PDF

Getz, W.M., Lloyd-Smith, J.O.: 2006, Basic Methods for Modeling the Invasion and Spread of Contagious Diseases. In: Feng, Z., Dieckmann, U., Levin, S.A. (eds.), *Disease Evolution: Models, Concepts and Data Analyses*, AMS/DIMACS, DIMACS Series in Discrete Mathematics and Theoretical Computer Science American Mathematical Society, Volume 71, 87-109. Available at: http://nature.berkeley.edu/~getz/Reprints05/Getz1.pdf

Gill, C.A.: 1936, Some points in the epidemiology of malaria arising out of the study of the malaria epidemic in Ceylon in 1934-1935, *Transactions of the Royal Society of Tropical Medicine and Hygiene* **29**(5), 427-480. doi:10.1016/S0035-9203(36)90001-9

Gilmore, C.G.: 1993, A new test for chaos, *Journal of Economic Behavior & Organization* **22**(2), 209-237. doi:10.1016/0167-2681(93)90064-v

Gkana, A., Zachilas, L.: 2013, Incorporating prey refuge in a prey-predator model with Holling type I functional response: Random dynamics and population outbreaks, *Journal of Biological Physics* **39**(4), 587-606. doi:10.1007/s10867-013-9319-7

Gkana, A., Zachilas, L.: 2015a, Non-overlapping Generation Species: Complex Prey-Predator Interactions, *International Journal of Nonlinear Sciences and Numerical Simulation* **16**(5), 207-219. doi:10.1515/ijnsns-2014-0121

Gkana, A., Zachilas, L.: 2015b, Bifurcations and chaos in discrete-time gonorrhea model, *Chaotic Modeling and Simulation* **1**, 51-64. Available at: http://www.cmsim.eu/papers_pdf/january_2015_papers/4_CMSIM_Journal_Gkana-Zachilas_2015_1_51-64.pdf

Gkana, A., Zachilas, L.: 2015c, Sunspot numbers: data analysis, predictions and economic impacts, *Journal of Engineering Science and Technology Review* **8**(1), 79-85. Available at: http://www.jestr.org/downloads/Volume8Issue1/fulltext148115.pdf

Gkana, A., Zachilas, L.: 2016, Re-evaluation of Predictive Models in Light of New Data: Sunspot Number Version 2.0, *Solar Physics* **291**(8), 2457-2472. doi:10.1007/s11207-016-0965-3

Gloyne, R.W.: 1973, The "growing season" at Eskdalemuir observatory, Dumfriesshire, *Meteorological Magazine* **102**, 174-178.

Gnevyshev, M.N., Ohl, A.I.: 1948, On the 22-year cycle of solar activity, *Astronomicheskii Zhurnal* **25**(1), 18-20.

Government of New Brunswick: 2010, Public Information Fact Sheet Gonorrhea. Available at: http://www2.gnb.ca/content/dam/gnb/Departments/h-s/pdf/en/CDC/FactSheets/gonorrhea-e.pdf

Grassberger, P., Procaccia, I.: 1983a, Characterization of Strange Attractors, *Physical Review Letters* **50**(5), 346-349. doi:10.1103/PhysRevLett.50.346

Grassberger, P., Procaccia, I.: 1983b, Measuring the strangeness of strange attractors, *Physica D* **9**(1-2), 189-208. doi:10.1016/0167-2789(83)90298-1

Grebogi, C., Ott, E., Yorke, J.A.: 1988, Unstable periodic orbits and the dimensions of multifractal chaotic attractors, *Physical Review A* **37**(5), 1711-1724. doi:10.1103/PhysRevA.37.1711

Güémez, J., Matias, M.A.: 1993, Control of chaos in unidimensional maps, *Physics Letters A* **181**(1), 29-32. doi:10.1016/0375-9601(93)91119-P

Guzman, A., Istúriz, R.E.: 2010, Update on the global spread of dengue, *International Journal of Antimicrobial Agents* **36**(1), S40-S42. doi:10.1016/j.ijantimicag.2010.06.018

Hadeler, K.P., Gerstmann, I.: 1990, The discrete Rosenzweig model, *Mathematical Biosciences* **98**(1) 49-72. doi:10.1016/0025-5564(90)90011-M

Hahn, F.G.: 1877, *Uber die Beziehungen der Sonnenfleckenperiode zu meteorologischen Erscheinungen*, Leipzig.

Halasa, Y.A., Shepard, D.S., Zeng, W.: 2012, Economic Cost of Dengue in Puerto Rico, *American Journal of Tropical Medicine and Hygiene* **86**(5), 745-752. doi:10.4269/ajtmh.2012.11-0784

Hales, S., de Wet, N., Maindonald, J., Woodward, A.: 2002, Potential effect of population and climate changes on global distribution of dengue fever: an empirical model, *The Lancet* **360**(9336), 830-834. doi:10.1016/S0140-6736(02)09964-6

Halley, E.: 1692, An account of the cause of the change of the variation of the magnetical needle with an hypothesis of the structure of the internal parts of the Earth, *Philosophical Transactions of Royal Society of London* **16**(179-191) 563-578. doi:10.1098/rstl.1686.0107

Harrison, V.L.: 1976, Do sunspot cycles affect crop yields?, Economic Research Service, U.S. Department of Agriculture, Agricultural Economic Report, No. 327, Washington D.C. Available at: http://naldc.nal.usda.gov/naldc/download.xhtml?id=CAT76674961&

Hassel, M.P.: 1978, *The Dynamics of arthropod predator-prey Systems*, Princeton University Press, Princeton.

Hastings, D., Garrett, H.: 1996, *Spacecraft-environment interactions*, Cambridge University Press, Cambridge. doi:10.1017/cbo9780511525032

He, Z., Lai, X.: 2011, Bifurcation and chaotic behavior of a discrete-time predator-prey system, *Nonlinear Analysis: Real World Applications* **12**(1), 403-417. doi:10.1016/j.nonrwa.2010.06.026

Herschel, W.: 1801, Observations Tending to Investigate the Nature of the Sun, in Order to Find the Causes or Symptoms of Its Variable Emission of Light and Heat; With Remarks on the Use That May Possibly Be Drawn from Solar Observations, *Philosophical Transactions of the Royal Society of London* **91**(0), 265-318. doi:10.1098/rstl.1801.0015

Hethcote, H.W.: 1976, Qualitative analyses of communicable disease models, *Mathematical Biosciences* **28**(3-4), 335-356. doi:10.1016/0025-5564(76)90132-2

Hethcote, H.W., Yorke, J.A.: 1984, *Gonorrhea Transmission Dynamics and Control*, Lecture Notes in Biomathematics, Springer-Verlag, Berlin, Heidelberg. doi:10.1007/978-3-662-07544-9

Hirsch, M.W.: 1984, The differential equations approach to dynamical systems, *Bulletin of the American Mathematical Society* **11**(1), 1-64. Available at: http://projecteuclid.org/euclid.bams/1183551833

Hirsch, M.W., Smale, S., Devaney, R.L.: 2004, *Differential Equations, Dynamical Systems, and An Introduction to Chaos*, 2nd Edition, Academic Press, Elsevier Science & Technology Books, USA.

Holling, C.S.: 1959, The components of predation as revealed by a study of small-mammal predation of the European pine sawfly, *The Canadian Entomologist* **91**(5), 293-320. doi:10.4039/Ent91293-5

Holling, C.S.: 1965, The functional response of predators to prey density and its role in mimicry and population regulation, *Memoirs of the Entomological Society of Canada* **97**(S45), 5-60. doi:10.4039/entm9745fv

Holmes, K.K., Counts, G.W., Beaty, H.N: 1971, Disseminated gonococcal infection, *Annals of Internal Medicine* **74**(6), 979-993. doi:10.7326/0003-4819-74-6-979

Hoyt, D.V., Schatten, K.H.: 1992, A new look at wolf sunspot numbers in the late 1700's, *Solar Physics* **138**(2), 387-397. doi:10.1007/BF00151922

Hoyt, D.V., Schatten, K.H.: 1995a, Overlooked Sunspot Observations by Hevelius in the Early Maunder Minimum, 1653 – 1684, *Solar Physics* **160**(2), 371-378. doi:10.1007/BF00732815

Hoyt, D.V., Schatten, K.H.: 1995b, Observations of Sunspots by Flamsteed during the Maunder Minimum, *Solar Physics* **160**(2), 379-385. doi:10.1007/BF00732816

Hoyt, D.V., Schatten, K.H.: 1996, How well was the Sun observed during the Maunder Minimum?, *Solar Physics* **165**(1), 181-192. doi:10.1007/bf00149097

Hoyt, D.V., Schatten, K.H.: 1997, *The Role of the Sun in Climate Change*, Oxford University Press, Oxford New York. Available at: http://library.uniteddiversity.coop/Climate_Change/The_Role_of_the_Sun_in_Climate_Change.pdf

Hoyt, D.V., Schatten, K.H.: 1998, Group Sunspot Numbers: A New Solar Activity Reconstruction, *Solar Physics* **179**(1), 189-219. doi:10.1023/A:1005007527816

Huang, Y., Chen, F., Zhong, L.: 2006, Stability analysis of a prey-predator model with Holling type III response function incorporating a prey refuge, *Applied Mathematics and Computation* **182**(1), 672-683. doi:10.1016/j.amc.2006.04.030

Huntington, E.: 1920, *World-Power and Evolution*, New Haven, Yale University Press, London. doi:10.5962/bhl.title.25519

Huo, H.F., Li, W.T.: 2004, Stable periodic solution of the discrete periodic Leslie-newer predator-prey model, *Mathematical and Computer Modelling* **40**(3-4), 261-269. doi:10.1016/j.mcm.2004.02.026

Jevons, W.S.: 1875, The Solar Period and the Price of Corn, In: *Investigations in Currency and Finance*, MacMillan, London, 1884.

Jevons, W.S.: 1879, Sun-Spots and Commercial Crises, *Nature* **19**(495), 588-590. doi:10.1038/019588a0

Jones, E.L.: 1965, Agriculture and Economic Growth in England, 1660-1750: Agricultural Change, *The Journal of Economic History* **25**(1), 1-18. doi:10.1017/s0022050700061362

Jones, E.L.: 1974, *Agriculture and the industrial revolution*, Oxford: Basil Blackwell.

Jury, E.I.: 1974, *Inners and Stability of Dynamic Systems*, Wiley, New York.

Kane, R.P.: 2008, Prediction of solar cycle maximum using solar cycle lengths, *Solar Physics* **248**(1), 203-209. doi:10.1007/s11207-008-9125-8

Kantz, H.: 1994, A robust method to estimate the maximal Lyapunov exponent of a time series, *Physics Letters A* **185**(1), 77-87. doi:10.1016/0375-9601(94)90991-1

Kar, T.K.: 2005, Stability analysis of a prey-predator model incorporating a prey refuge, *Communications in Nonlinear Science and Numerical Simulation* **10**(6), 681-691. doi:10.1016/j.cnsns.2003.08.006

Kennedy, J.S.: 1951, The Migration of the Desert Locust (*Schistocerca gregaria Forsk*.). I. The Behaviour of Swarms. II. A Theory of Long-Range Migrations. *Philosophical Transactions of the Royal Society B: Biological Sciences*, **235**(625), 163-290. doi:10.1098/rstb.1951.0003

Kennel, M.B., Brown, R., Abarbanel, H.D.I.: 1992, Determining embedding dimension for phase-space reconstruction using a geometrical construction, *Physical Review A* **45**(6), 3403-3411. doi:10.1103/PhysRevA.45.3403

Kermack, W.O., McKendrick, A.G.: 1927, A contribution to the Mathematical Theory of Epidemics, *Proceedings of the Royal Society A* **115**(772), 700-721. doi:10.1098/rspa.1927.0118

Kotiaho, J.S., Alatalo, R.V., Mappes, J., Nielsen, M.G., Parri, S., Rivero, A.: 1998, Energetic costs of size and sexual signaling in a wolf spider, *Proceedings of the Royal Society B* **265**(1411), 2203-2209. doi:10.1098/rspb.1998.0560

Kutner, M.L.: 2003, *Astronomy: A Physical Perspective*, 2nd Edition, Cambridge University Press, United Kingdom. doi:10.1017/cbo9780511802195

Kyrtsou, C., Malliaris, A.G., Serletis, A.: 2009, Energy sector pricing: On the role of neglected nonlinearity, *Energy Economics* **31**(3), 492-502. doi:10.1016/j.eneco.2008.12.009

Lajmanovich, A., Yorke, J.A.: 1976, A deterministic model for gonorrhea in a nonhomogeneous population, *Mathematical Bioscience* **28**(3-4), 221-236. doi:10.1016/0025-5564(76)90125-5

Last, J.M.: 2001, *A Dictionary of Epidemiology*, 4th Edition, Oxford University Press, New York, United States of America.

Lean, J.L., Rind, D.H.: 2008, How natural and anthropogenic influences alter global and regional surface temperatures: 1889 to 2006, *Geophysical Research Letters* **35**(18), L18701. doi:10.1029/2008GL034864

Lecoq, M.: 2005, Desert Locust Management: From Ecology to Anthropology, *Journal of Orthoptera Research*, **14**(2), 179-186. doi:10.1665/1082-6467(2005)14[179:DLMFET]2.0.CO;2

Lehrer, S.: 2010, Anopheles mosquito transmission of brain tumor, *Medical Hypotheses* **74**(1), 167-168. doi:10.1016/j.mehy.2009.07.005

Leslie, P.H.: 1948, Some further notes on the use of matrices in population mathematics, *Biometrika* **35**(3-4) 213-245. doi:10.1093/biomet/35.3-4.213

Leslie, P.H.: 1958, A stochastic model for studying the properties of certain biological systems by numerical methods, *Biometrika* **45**(1-2), 16-31. doi:10.1093/biomet/45.1-2.16

Li, J., Lou, J., Lou, M.: 2008, Some discrete SI and SIS epidemic models, *Applied Mathematics and Mechanics* **29**(1), 113-119. doi:10.1016/0025-5564(94)90025-6

Li, L., Sun, G., Jin, Z.: 2010, Bifurcation and chaos in an epidemic model with nonlinear incidence rates, *Applied Mathematics and Computation* **216**(4), 1226-1234. doi:10.1016/j.amc.2010.02.014

Library of Congress: 1915, "The Locust Plague of 1915 Photograph Album", American Colony in Jerusalem, 1870 – 2006. Available at: https://www.loc.gov/collections/american-colony-in-jerusalem/articles-and-essays/the-locust-plague-of-1915-photograph-album/

Liu, X., Xiao, D.: 2007, Complex dynamic behaviors of a discrete-time predator-prey system, *Chaos, Solitons and Fractals* **32**(1), 80-94. doi:10.1016/j.chaos.2005.10.081

Lotka, A.J.: 1925, *Elements of Physical Biology*, Williams and Wilkins Company, Baltimore Md., United States of America. Available at: https://archive.org/details/elementsofphysic017171mbp

Love, G., Riwoe, D.: 2005, Economic Costs and Benefits of Locust Control in Eastern Australia, ABARE *e*Report 05.14, Prepared for Australian Plague Locust Commission, Canberra, November 2005. Available at: http://www.agriculture.gov.au/SiteCollectionDocuments/animal-plant/aplc/locust/reports/ABARE_report.pdf

Luterbacher, J., Rickli, R., Xoplaki, E., Tinguely, C., Beck, C., Pfister, C., Wanner, H.: 2001, The Late Maunder Minimum (1675 – 1715) – A Key Period for Studying Decadal Scale Climatic Change in Europe, *Climatic Change* **49**(4), 441-446. doi:10.1023/A:1010667524422

Macek, W.M., Strumik, M.: 2006, Testing for nonlinearity and low-dimensional dynamics in the slow solar wind, *Advances in Space Research* **37**(8), 1544-1549. doi:10.1016/j.asr.2005.07.038

MacLagen, D.S.: 1940, Sunspots and insect outbreaks: An epidemic-logical study, *Proceedings of the University of Durham Philosophical Society* **10**, 173-190.

Mann, M.E., Zhang, Z., Rutherford, S., Bradley, R.S., Hughes, M.K., Shindell, D., Ammann, C., Faluvegi, G., Ni, F.: 2009, Global Signatures and Dynamical Origins of the Little Ice Age and Medieval Climate Anomaly, *Science* **326**(5957), 1256-1260. doi:10.1126/science.1177303

Manneville, P., Pomeau, Y.: 1980, Different ways to turbulence in dissipative systems, *Physica D: Nonlinear Phenomena* **1**(2), 219-226. doi:10.1016/0167-2789(80)90013-5

Marine Medical Systems: 1997, "Health Advisories For Travelers: Their Impact On Developing Countries", January 1997. Available at: http://www.marinemedical.com/health

Marrazzo, J.M., Handsfield, H.H., Sparling, P.F.: 2010, Neisseria gonorrhoeae, In: Mandell, G.L., Bennett, J.E., Dolin, R. (eds.), *Mandell, Douglas, and Bennett's principles and practice of infectious diseases*, 7th edition, Philadelphia: Chuchill Livingstone, 2753-2770. doi:10.1016/b978-0-443-06839-3.00212-5

Marwan, N., Kurths, J.: 2005, Line structures in recurrence plots, *Physics Letters A* **336**(4-5), 349-357. doi:10.1016/j.physleta.2004.12.056

Marwan, N., Romano, M.C., Thiel, M., Kurths, J.: 2007, Recurrence plots for the analysis of complex systems, *Physics Reports*, **438**(5-6), 237-329. doi:10.1016/j.physrep.2006.11.001

Matías, M.A., Güémez, J.: 1994, Stabilization of chaos by proportional pulses in the system variables, *Physical Review Letters* **72**(10), 1455-1458. doi:10.1103/physrevlett.72.1455

Maunder, E.W.: 1922, The prolonged sunspot minimum 1675 – 1715, *Journal of the British Astronomical Association* **32**(4), 140-145.

May, R.M.: 1976, Simple Mathematical Models with Very Complicated Dynamics, *Nature* **261** 459-467. doi:10.1038/261459a0

McCarthy, M.: 2016, WHO sets out $ 56m Zika virus response plan, *British Medical Journal* **352**, i1042. doi:10.1136/bmj.i1042

McCue, L.S., Troesch, A.W.: 2011, Use of Lyapunov Exponents to Predict Chaotic Vessel Motions, In: Neves, M.A.S. *et al.* (eds.), *Contemporary Ideas on Ship Stability and Capsizing in Waves*, Springer Netherlands, Dordrecht, 415-432. doi:10.1007/978-94-007-1482-3_23

McKane, A.: 2007, Non-Linear Dynamics, University of Manchester. Available at: http://www.jpoffline.com/physics_docs/y3s5/nlp_lecture_notes.pdf

Méndez, V., Fort, J.: 2000, Dynamical evolution of discrete epidemic models, *Physica A: Statistical Mechanics and its Applications* **284**(1-4), 309-317. doi:10.1016/S0378-4371(00)00210-7

Ministry of Health: 2014, "The Uganda Malaria Reduction Strategic Plan 2014 – 2020", May 2014. Available at: http://library.health.go.ug/download/file/fid/580890

Mitchell, B.R., Deane, P.: 1971, *Abstract of British Historical Statistics*, Cambridge University Press, Cambridge.

Morfill, G.E., Scheingraber, H., Voges, W., Sonett, C.P.: 1991, Sunspot number variations: stochastic or chaotic, In: Sonett, C.P., Giampapa, M.S., Mathews, M.S. (eds.), *The Sun in Time*, University of Arizona Press, Tucson.

Mundt, M.D., Maguire, W.B.II, Chase, R.R.P.: 1991, Chaos in the sunspot cycle – Analysis and prediction, *Journal of Geophysical Research* **96**(2), 1705-1716. doi:10.1029/90JA02150

Murray, J.D.: 1993, *Mathematical Biology*, Springer-Verlag, 2nd edition, Berlin. doi:10.1007/978-3-662-08542-4

Muscheler, R., Beer, J., Kubik, P.W.: 2004, Long-Term Solar Variability and Climate Change Based on Radionuclide Data from Ice Cores, In: Pap, J.M., Fox, P., Frohlich, C., Hudson, H.S., Kuhn, J., McCormack, J., *et al.* (eds.), *Solar Variability and Its Effects on Climate*, Washington, D.C.. doi:10.1029/141GM16

Mushayabasa, S.: 2012, The epidemiological consequences of Chlamydia and gonorrhea co-infection: Insights from a mathematical model, *International Journal of Applied Mathematics and Computation* **4**(3), 295-306. doi:10.0000/ijamc.2012.4.3.335

Myers, J.L., Well, A., Lorch, R.F.: 2010, *Research design and statistical analysis*, 3rd Edition, Routledge, Great Britain. doi:10.4324/9780203726631

Nallaswamy, R., Shukla, J.B.: 1982, Effects of dispersal on the stability of a gonorrhea endemic model, *Mathematical Biosciences* **61**(1), 63-72. doi:10.1016/0025-5564(82)90096-7

National Institute of Allergy and Infectious Diseases: 1980, *Sexually transmitted diseases: 1980 status report*, NIH Publication, No. 81-2213.

Nesis, A., Hammer, R., Roth, M., Schleicher, H.: 2001, Dynamics of the solar granulation. VII. A nonlinear approach, *Astronomy and Astrophysics* **373**(1), 307-317. doi:10.1051/0004-6361:20010494

New York Times: 1915a, Distress in Jerusalem: Many Deaths from Starvation Reported, Special Cable to the New York Times, 23 April 1915. Available at: http://query.nytimes.com/mem/archive-free/pdf?res=9D06E4DE1338E633A25750C2A9629C946496D6CF

New York Times: 1915b, Remarkable details from American consul on Palestine locust plague, The New York Times, 21 November 1915. Available at: http://query.nytimes.com/mem/archive-free/pdf?res=9F05E4DB153BE233A25752C2A9679D946496D6CF

Nyffeler, M., Breene, R.G.: 1990, Evidence of low daily food consumption by wolf spiders in meadowland and comparison with other cursorial hunters, *Journal of Applied Entomology* **110**(1-5), 73-81. doi:10.1111/j.1439-0418.1990.tb00097.x

O'Sullivan, D.: 2007, Exposure to galactic cosmic radiation and solar energetic particles, *Radiation Protection Dosimetry*, **125**(1-4), 407-411. doi:10.1093/rpd/ncm317

Oldstone, M.B.A.: 1998, *Viruses, Plagues, & History: Past, Present, and Future*, Oxford University Press, 1st Edition, USA.

Onondaga County Health Department: 2009, 2009 Annual Report. Available at: http://www.ongov.net/health/documents/2009OCHDAnnualReport.pdf

Onondaga County Health Department: 2011, "2011 Annual Report". Available at: http://www.ongov.net/health/documents/2011OCHDAnnualReport.pdf

Ostryakov, V.M., Usoskin, I.G.: 1990, On the dimension of solar attractor, *Solar Physics* **127**(2), 405-412. doi:10.1007/BF00152177

Ott, E., Grebogi, C., Yorke, J.A.: 1990, Controlling chaos, *Physical Review Letters* **64**(11), 1196-1199. doi:10.1103/PhysRevLett.64.1196

Overton, M.: 1986, Agricultural Revolution? England, 1540 – 1850, *ReFRESH* 3, In: Digby, A., Feinstein, C.: 1989, *New Directions in Economic and Social History*, Palgrave Macmillan UK, London, 9-21. doi:10.1007/978-1-349-20315-4_2

Packard, N.H., Crutcheld, J.P., Farmer, J.D., Shaw, R.S.: 1980, Geometry from a Time Series, *Physical Review Letters* **45**(9), 712-716. doi:10.1103/PhysRevLett.45.712

Pandey, A.: 2016, Economic Cost of Zika Virus, Indian Council of World Affairs Viewpoint, 16 March 2016. Available at: http://www.icwa.in/pdfs/VP/2014/EconomicCostofZikaVirusvp16032016.pdf

Pasquier, R.: 1942, Prévision et Périodicité des Invasions de la Sauterelle Pèlerine en Afrique du Nord, *Bulletin de la Société d'Agriculture d'Algérie* **85**, 51-70.

Pérez-Guerra, C.L., Halasa, Y.A., Rivera, R., Peña, M., Ramírez, V., Cano, M.P., Shepard, D.S.: 2010, Economic cost of dengue public prevention activities in Puerto Rico, World Health Organization (WHO) Regional Office for South-East Asia, Dengue Bulletin, Volume 34. Available at: http://apps.who.int/iris/bitstream/10665/170983/1/db2010v34p13.pdf

Perkins, T.A., Siraj, A.S., Ruktanonchai, C.W., Kraemer, M.U.G., Tatem, A.J.: 2016, Model-based projections of Zika virus infections in childbearing women in the Americas, *Nature Microbiology* **1**(9), 16126. doi:10.1038/nmicrobiol.2016.126

Pesnell, W.D.: 2012, Solar Cycle Predictions (Invited Review), *Solar Physics* **281**(1), 507-532. doi:10.1007/s11207-012-9997-5

Pfister, C.: 1994, Spatial Patterns of Climatic Change in Europe 1675 – 1715, In: Frenzel, B., Pfister, C., Glaeser, B. (eds.), *Climatic Trends and Anomalies in Europe 1675 – 1715*, Fischer, Stuttgart.

Pikovsky, A., Politi, A.: 2016, *Lyapunov Exponents: A Tool to Explore Complex Dynamics*, Cambridge University Press. doi:10.1017/CBO9781139343473

Pikovsky, A., Rosenblum, M., Kurths, J: 2001, *Synchronization: A Universal Concept in Nonlinear Sciences*, Cambridge University Press. doi:10.1017/CBO9780511755743

Plapp, B.P., Hubler, A.W.: 1990, Nonlinear Resonances and Suppression of Chaos in the Rf-Biased Josephson Junction, *Physical Review Letters* **65**(18), 2302-2305. doi:10.1103/PhysRevLett.65.2302

Poincaré, H.: 1890, Sur la probleme des trois corps et les équations de la dynamique, *Acta Mathematica* **13**, 1-270.

Pollock, S.T.: 1993, *Ecology*, Eyewitness Science, Volume 10, Dorling Kindersley, London.

Pomeau, Y., Manneville, P.: 1980, Intermittent Transition to Turbulence in Dissipative Dynamical Systems, *Communications in Mathematical Physics* **74**(2), 189-197. doi:10.1007/BF01197757

Prestwich, K.N.: 1977, The energetics of web-building in spiders, *Comparative Biochemistry and Physiology Part A: Physiology* **57**(3), 321-326. doi:10.1016/0300-9629(77)90199-2

Pustil'nik, L.A., Din, G.Y.: 2004, Influence of solar activity on the state of the wheat market in medieval England, *Solar Physics* **223**(1-2), 335-356. doi:10.1007/s11207-004-5356-5

Ramani, A., Carstea, A.S., Willox, R., Grammaticos, B.: 2004, Oscillating epidemics: a discrete-time model, *Physica A: Statistical Mechanics and its Applications* **333**, 278-292. doi:10.1016/j.physa.2003.10.051

Reid, G.C.: 1987, Influence of solar variability on global sea surface temperatures, *Nature* **329**, 142-143. doi:10.1038/329142a0

Reid, N.: 2006, Birds on New England wool properties – A woolgrower guide, Land, Water & Wool Northern Tablelands Property Fact Sheet, Australian Government-Land and Water Australia. Available at: http://snelcc.org.au/landwaterwool/FS1_Birds.pdf

Reynolds, G.H., Chan, Y.K.: 1974, A control model for gonorrhea, *Bulletin of the International Statistics Institute* **46**(2), 264-279.

Rigozo, N.R., Nordemann, D.J.R., Echer, E., Echer, M.P.S., Silva, H.E.: 2010, Prediction of solar minimum and maximum epochs on the basis of spectral characteristics for the next millennium, *Planetary and Space Science* **58**(14-15), 1971-1976. doi:10.1016/j.pss.2010.09.020

Riley, C.V., Packard, A.S., Thomas, C.: 1880, Second Report of the United States Commission for the Years 1878 and 1879, relating to the Rocky Mountain Locust and Western Cricket, Washington, Government Printing Office.

Rodríguez-Prieto, I., Fernández-Juricic, E., Martín, J.: 2006, Anti-Predator Behavioral Responses of Mosquito Pupae to Aerial Predation Risk, *Journal of Insect Behavior* **19**(3), 373-381. doi:10.1007/s10905-006-9033-4

Rogers, J.E.T.: 1866 – 1892, *A History of Agriculture and Prices in England*, Volumes 7, Oxford.

Root, H.G.: 1979, Earth-current effects on communication-cable power subsystems, *IEEE Transactions on Electromagnetic Capability* **EMC-21**(2), 87-92. doi:10.1109/TEMC.1979.303750

Rosenstein, M.T., Collins, J.J., De Luca, C.J.: 1993, A practical method for calculating largest Lyapunov exponents from small data sets, *Physica D* **65**(1-2), 117-134. doi:10.1016/0167-2789(93)90009-P

Rosenzweig, M.L., MacArthur, R.H.: 1963, Graphical representation and stability conditions of predator-prey interactions, *The American Naturalist* **97**(895), 209-223. doi:10.1086/282272

Ruelle, D.: 1980, Strange attractors, *The Mathematical Intelligencer* **2**(3), 126-137. doi:10.1007/bf03023053

Ruelle, D., Takens, F.: 1971, On the nature of turbulence, *Communications in Mathematical Physics* **20**(3), 167-192. doi:10.1007/BF01646553

Ruppert, E.E., Fox, R.S., Barnes, R.B.: 2004, *Invertebrate Zoology: A Functional Evolutionary Approach*, 7th Edition, Brooks Cole Thomson, Belmont, California.

Scalia, T.G., Svensson, A., Asikainen, T., Giesecke, J.: 2010, Some model based considerations on observing generation times for communicable diseases, *Mathematical Biosciences* **223**(1), 24-31. doi:10.1016/j.mbs.2009.10.004

Schatten, K.H.: 2003, Solar activity and the solar cycle, *Advances in Space Research* **32**(4), 451-460. doi:10.1016/S0273-1177(03)00328-4

Schwabe, A.N.: 1844, Sonnen-Beobachtungen im Jahre 1843, *Astronomische Nachrichten* **21**(15), 234-235. doi:10.1002/asna.18440211505

Shepard, D.S., Coudeville, L., Halasa, Y.A., Zambrano, B., Dayan, G.H.: 2011, Economic Impact of Dengue Illness in the Americas, *American Journal of Tropical Medicine and Hygiene* **84**(2), 200-207. doi:10.4269/ajtmh.2011.10-0503

Shepard, D.S., Undurraga, E.A., Halasa, Y.A.: 2013, Economic and Disease Burden of Dengue in Southeast Asia, *PLoS Neglected Tropical Diseases* **7**(2), e2055. doi:10.1371/journal.pntd.0002055

Shil, P., Gurav, Y.K., Chadha, M.S., Mishra, A.C.: 2011, Transmission dynamics of novel influenza A/H1N1 2009 outbreak in a residential school in India, *Current Science* **100**(8), 1177-1183. Available at: http://repository.ias.ac.in/73624/1/73624.pdf

Shove, D.J.: 1956, Sunspot Maxima since 649 B.C., *Journal of the British Astronomical Association* **66**(2), 59-61.

Singer, J., Wang, Y.Z., Bau, H.H.: 1991, Controlling a chaotic system, *Physical Review Letters* **66**(9), 1123-1125. doi:10.1103/PhysRevLett.66.1123

Siscoe, G.L.: 1976, On the statistics of the largest sunspot numbers per solar cycle, *Journal of Geophysical Research*, **81**(34), 6224-6226. doi:10.1029/JA081i034p06224

Smith, J.M.: 1968, *Mathematical Ideas in Biology*, Cambridge University Press, Cambridge. doi:10.1017/cbo9780511565144

Smith, J.M.: 1974, *Models in ecology*, Cambridge University Press, London.

Smith, W.: 2010, What I Didn't Know About Sexual Health: Reflections From a New Perch, National Coalition of STD Directors (NCSD), RH Reality Check, April 15, 2010. Available at: http://www.ncsddc.org/printpdf/2362

Spinage, C.A.: 2012, *African Ecology: Benchmarks and Historical Perspectives*, Springer Geography, Springer-Verlag Berlin Heidelberg. doi:10.1007/978-3-642-22872-8

Spörer, F.W.G.: 1887, Über die Periodizität der Sonnenflecken seit dem Jahre 1618, *Vierteljahrsschr Astronomische Gesellschaft (Leipzig)* **22**, 323-329.

State of Alaska Epidemiology: 2012, Gonococcal Infection – Alaska, 2011, *Bulletin*, No. 11, June 21. Available at: http://www.epi.hss.state.ak.us/bulletins/docs/b2012_11.pdf

State of Alaska Epidemiology: 2010, Statewide Increase in Gonococcal Infection – Alaska, 2009, *Bulletin*, No. 6, March 9. Available at: http://www.epi.alaska.gov/bulletins/docs/b2010_06.pdf

Strogatz, S.H.: 1994, *Nonlinear Dynamics and Chaos: With Applications to Physics, Biology, Chemistry, and Engineering*, Studies in Nonlinearity, Westview Press, Perseus Books, United States of America. Available at: http://users.uoa.gr/~pjioannou/nonlin/Strogatz,%20S.%20H.%20-%20Nonlinear%20Dynamics%20And%20Chaos.pdf

Stuiver, M., Braziunas, T.F.: 1989, Atmospheric ^{14}C and century-scale solar oscillations, *Nature* **338**(6214), 405-408. doi:10.1038/338405a0

Suaya, J.A., Chantha, N., Huy, R., Sah, B.K., Moh-Seng, C., Socheat, D., Buchy, P., Vantha, T., Sivuth, O., Haileselassie, E., Shepard, D.S.: 2010, Clinical characterization, diagnosis and socioeconomic impact of hospitalized dengue in Cambodia, World Health Organization (WHO) Regional Office for South-East Asia, Dengue Bulletin, Volume 34. Available at: http://apps.who.int/iris/bitstream/10665/170966/1/db2010v34p89.pdf

Suaya, J.A., Shepard, D.S., Siqueira, J.B., Martelli, C.T., Lum, L.C., Tan, L.H., Kongsin, S., Jiamton, S., Garrido, F., Montoya, R., Armien, B., Huy, R., Castillo, L., Caram, M., Sah, B.K., Sughayyar, R., Tyo, K.R., Halstead, S.B.: 2009, Cost of Dengue Cases in Eight Countries in the Americas and Asia: A Prospective Study, *The American Journal of Tropical Medicine and Hygiene* **80**(5), 846-855. Available at: http://www.ajtmh.org/cgi/pmidlookup?view=long&pmid=19407136

Svalgaard, L., Cliver, E.W., Kamide, Y.: 2005, Sunspot cycle 24: Smallest cycle in 100 years?, *Geophysical Research Letters* **32**(1), L01104. doi:10.1029/2004GL021664

Swinton, A.H., 1883, Data Obtained from solar physics and earthquake commotions applied to elucidate locust multiplication and migration, Third Report of the United States Entomological Commission, Washington, 65-85. Available at: http://ufdc.ufl.edu/AA00018861/00001

Symmons, P.M., Cressman, K.: 2001, Desert Locust Guidelines: Biology and behavior, Food and Agriculture Organization of the United Nations, Rome. Available at: https://www.google.gr/url?sa=t&rct=j&q=&esrc=s&source=web&cd=1&cad=rja&uact=8&ved=0ahUKEwiZpPnzsYXTAhULkSwKHd4QD5QQFggkMAA&url=http%3A%2F%2Fwww.fao.org%2Fag%2Flocusts%2Fcommon%2Fecg%2F347_en_DLG1e.pdf&usg=AFQjCNFYqL_MQS1qTpdTW6P0aQJx6Uq_YA&bvm=bv.151325232,d.bGg

Syracuse, N.Y.: 2012, "Onondaga County sees big outbreak of gonorrhea, Public health officials are investigating a sharp increase in gonorrhea in Onondaga County", November 29, 2012. Available at: http://www.syracuse.com/news/index.ssf/2012/11/onondaga_county_sees_big_outbr.html

Takens, F.: 1981, Detecting strange attractors in turbulence, In: Rand, D.A., Young, L.S. (Eds.), *Dynamical Systems and Turbulence, Warwick 1980*, Springer-Verlag, Berlin, 366-381. doi:10.1007/bfb0091924

Takens, F.: 1993, Detecting nonlinearities in stationary time series, *International Journal of Bifurcation and Chaos* **3**(2), 241-256. doi:10.1142/S0218127493000192

Takens, F., Ruelle, D.: 1971, On the nature of turbulence, *Communications in Mathematical Physics* **20**(3), 167-192. doi:10.1007/BF01646553

Tavernise, S.: 2016, "U.S. Funding for Fighting Zika Virus Is Nearly Spent, C.D.C. Says", The New York Times, August 30, 2016. Available at: http://www.nytimes.com/2016/08/31/health/us-funding-for-fighting-zika-virus-is-nearly-spent-cdc-says.html

Taylor, R.J.: 1984, *Predation*, Springer Netherlands, Chapman & Hall, New York. doi:10.1007/978-94-009-5554-7

Tchijevsky, A.L.: 1971, Physical Factors of the Historical Process, *Cycles* **22**, 11-27. Available at: http://cyclesresearchinstitute.org/pdf/cycles-history/chizhevsky1.pdf

Tello, E., Martinez, J.L., Jover, G., Olarieta, J.R., Garcia-Ruiz, R., Gonzalez de Molina, M., Badia-Miro, M., Winiwarter, V., Koepke, N.: 2015, Building on Allen's Nitrogen Hypothesis: The English Agricultural Revolution during the Maunder Minimum in the Little Ice Age (1645-1715), Working paper, University of Barcelona. Available at: http://estructuraehistoria.unizar.es/personal/vpinilla/documents/TelloETAL.pdf

Thieme, H.R.: 1982, Global asymptotic stability in epidemic models, In: *Equadiff 82*, Proceedings of the international conference held in Würzburg, FRG, August 23-28, 608-615, Springer Berlin Heidelberg, Springer-Verlag. doi:10.1007/BFb0103284

Thomas, M., Klass, J., Blanford, S.: 2000, The year of the locust, *Pesticide Outlook* **11**(5), 192-195. doi:10.1039/b008010l

Thompson, J.N.: 1982, *Interaction and Coevolution*, University of Chicago Press, Wiley, New York. doi:10.7208/chicago/9780226127323.001.0001

Tikkanen, R.H., Abelsson, J., Forsberg, M.: 2011, *UngKAB09 - Kunskap, attityder och sexuella handlingar bland unga [UngKAB09 - Knowledge, attitudes and sexual practices among young people]*, Gothenburg: Gothenburg University, Swedish.

Tobias, S.M., Weiss, N.O., Beer, J.: 2004, Long-term prediction of solar activity, *Astronomy & Geophysics*, **45**(2), 2.06. doi:10.1046/j.1468-4004.2003.45206_1.x

Topaz, C.M., Bernoff, A.J., Logan, S., Toolson, W.: 2008, A model for rolling swarms of locusts, *The European Physical Journal Special Topics* **157**(1), 93-109. doi:10.1140/epjst/e2008-00633-y

Topaz, C.M., D'Orsogna, M.R., Edelstein-Keshet, L., Bernoff, A.J.: 2012, Locust Dynamics: Behavioral Phase Change and Swarming, *PLoS Computational Biology* **8**(8), e1002642. doi:10.1371/journal.pcbi.1002642

Trottier, H., Philippe, P.: 2000, Deterministic Modeling of Infectious Diseases: Theory and Methods, *The Internet Journal of Infectious Diseases* **1**(2), 1-6. Available at: http://print.ispub.com/api/0/ispub-article/12783

Trulla, L.L., Giuliani, A., Zbilut, J.P., Webber, C.L.Jr.: 1996, Recurrence quantification analysis of the logistic equation with transients, *Physics Letters A* **223**(4), 255-260. doi:10.1016/S0375-9601(96)00741-4

University of Utah: 2012, "Climate change threatens tropical birds: Global warming, extreme weather aggravate habitat loss", University of Utah News, Science and Technology, 16 February 2012. Available at: http://archive.unews.utah.edu/news_releases/climate-change-threatens-tropical-birds/

Usoskin, I.G.: 2013, A History of Solar Activity over Millennia, *Living Reviews in Solar Physics* **10**, 1-94. doi:10.12942/lrsp-2013-1

Usoskin, I.G., Mursula, K., Kovaltsov, G.A.: 2000, Cyclic behaviour of sunspot activity during the Maunder minimum, *Astronomy and Astrophysics* **354**, L33-L36. Available at: http://adsabs.harvard.edu/full/2000A%26A...354L..33U

Usoskin, I.G., Solanki, S.K., Schüssler, M.: 2003, Millennium scale sunspot number reconstruction: Evidence for an unusually active Sun since the 1940s, *Physical Review Letters* **91**(21), 211101. doi:10.1103/PhysRevLett.91.211101

Uvarov, B.P.: 1977, *Grasshoppers and Locusts: A Handbook of General Acridology*, Volume 2, Centre for Overseas Pest Research, Cambridge University Press, London, UK.

Velicko, I., Unemo, M.: 2012, Recent trends in gonorrhoea and syphilis epidemiology in Sweden: 2007 to 2011, *Eurosurveillance* **17**(29), 20223. Available at: http://www.eurosurveillance.org/images/dynamic/EE/V17N29/art20223.pdf

Verhulst, P.F.: 1838, Notice sur la loi que la population suit dans son accroissement, *Correspondance mathématique et physique* **10**, 113-121.

Viète, F.: 1646, *Opera mathematica: in unum volumen congesta, ac recognita*, van Schouten, F. (ed.), Leiden: Elzeviriorum.

Vine, M.J.: 1948, The Anti-malaria Campaign in Greece (1946), *Bulletin of the World Health Organization* **1**(1), 197-204. Available at: https://www.ncbi.nlm.nih.gov/pmc/articles/pmid/20603913/

Volterra, V.: 1926, Fluctuations in the Abundance of a Species considered Mathematically, *Nature* **118**(2972), 558-560. doi:10.1038/118558a0

Waldmeier, M.: 1935, Neue Eigenschaften der Sonnenfleckenkurve, *Astronomische Mitteilungen der Eidgenössischen Sternwarte Zürich* **14**, 105-136. Available at: http://adsabs.harvard.edu/abs/1935MiZur..14..105W

Waldmeier, M.: 1961, *The Sunspot Activity in the Years 1610-1960*, Verlag Schulthess & Co. AG, Zürich.

Wallerius, A.: 1982, Solen gav Sverige en strömstöt (The Sun gave Sweden a "current shock"), *Ny-Teknik Teknisk Tidskrift* **29**, 3.

Wanner, H., Pfister, C., Brázdil, R., Frich, P., Frydendahl, K., Jónsson, T., Kington, J., Rosenørn, S., Wishman, E.: 1995, Wintertime European Circulation Patterns during the Late Maunder Minimum Cooling Period (1675-1704), *Theoretical and Applied Climatology* **51**(3), 167-175. doi:10.1007/bf00867443

Warner, L., Stone, K.M., Macaluso, M., Buehler, J.W., Austin, H.D.: 2006, Condom Use and Risk of Gonorrhea and Chlamydia: A Systematic Review of Design and Measurement Factors Assessed in Epidemiologic Studies, *Sexually Transmitted Diseases* **33**(1), 36-51. doi:10.1097/01.olq.0000187908.42622.fd

Webber, C.L. Jr., Zbilut, J.P.: 1994, Dynamical assessment of physiological systems and states using recurrence plot strategies, *Journal of Applied Physiology* **76**(2), 965-973. Available at: http://jap.physiology.org/cgi/pmidlookup?view=long&pmid=8175612

Weinstock, H., Berman, S., Cates, W.: 2004, Sexually transmitted diseases among American youth: Incidence and prevalence estimates, 2000, *Perspectives on Sexual and Reproductive Health* **36**(1), 6-10. doi:10.1111/j.1931-2393.2004.tb00002.x

Wellenhof, B.H., Lichtenegger, H., Collins, J.: 2001, *Global Positioning System: Theory and practice*, 5th Edition, Springer-Verlag Wien, New York. doi:10.1007/978-3-7091-6199-9

White, S.: 2013, The Real Little Ice Age, *Journal of Interdisciplinary History* **44**(3), 327-352. doi:10.1162/jinh_a_00574

Wiesner, P.J., Thompson III, S.E.: 1980, Gonococcal diseases, *Disease-a-Month* **27**(5), 1-44. doi:10.1016/S0011-5029(80)80002-2

Wilson, R.M.: 1987, On the Distribution of Sunspot Cycle Periods, *Journal of Geophysical Research* **92**(A9), 10101-10104. doi:10.1029/JA092iA09p10101

Wisconsin Division of Public Health: 2015, Gonorrhea (Neisseria gonorrhoeae), Disease Fact Sheet Series, Department of Health Services, October 8, 2015. Available at: http://www.dhs.wisconsin.gov/publications/p4/p42048.pdf

Wolf, A.: 1986, Quantifying Chaos with Lyapunov Exponents, In: Holden, A.V. (eds.) *Nonlinear Science: Theory and Applications*, Princeton University Press. doi:10.1515/9781400858156.273

Wolf, A., Swift, J., Swinney, H., Vastano, J.: 1985, Determining Lyapunov exponents from a time series, *Physica D: Nonlinear Phenomena*, **16**(3), 285-317. doi:10.1016/0167-2789(85)90011-9

Wood, D.: 2002, *Medieval Economic Thought*, Cambridge University Press, Cambridge. doi:10.1017/cbo9780511811043

World Bank Group: 2016, The short-term economic costs of Zika in Latin America and the Caribbean (LCR), Washington, DC: World Bank, February 18, 2016. Available at: http://pubdocs.worldbank.org/en/410321455758564708/The-short-term-economic-costs-of-Zika-in-LCR-final-doc-autores-feb-18.pdf

World Health Organization: 2001, Global Prevalence and Incidence of Selected Curable Sexually Transmitted Infections: Overview and Estimates, Geneva, WHO/HIV_AIDS/2001.02. Available at: http://www.who.int/hiv/pub/sti/en/who_hiv_aids_2001.02.pdf

World Health Organization: 2010, Yellow Fever Initiative: Providing an opportunity of a lifetime. Available at: http://www.who.int/entity/csr/disease/yellowfev/YFIbrochure.pdf

World Health Organization: 2012, "Urgent action needed to prevent the spread of untreatable gonorrhoea", Media Centre, June 6, 2012. Available at: http://www.who.int/mediacentre/news/notes/2012/gonorrhoea_20120606/en/index.html

World Health Organization: 2014, A global brief on vector-borne diseases, March 2014. Available at: http://apps.who.int/iris/bitstream/10665/111008/1/WHO_DCO_WHD_2014.1_eng.pdf

World Health Organization: 2015, World Malaria Report 2015, WHO Global Malaria Programme. Available at: http://apps.who.int/iris/bitstream/10665/200018/1/9789241565158_eng.pdf

World Health Organization: 2016a, "Dengue and severe dengue", Fact Sheet, July 2016. Available at: http://www.who.int/mediacentre/factsheets/fs117/en/

World Health Organization: 2016b, Yellow Fever Strategic Response Plan: June – August 2016, July. Available at: http://apps.who.int/iris/bitstream/10665/246103/1/WHO-YF-ENB-16.2-eng.pdf

World Health Organization: 2016c, Yellow Fever: Update and Funding Request, 30 August 2016. Available at: http://www.who.int/entity/emergencies/yellow-fever/yf-donor-update.pdf

World Health Organization: 2016d, Zika Virus: Technical Report, Interim Risk Assessment, Regional Office for World Health Organization (WHO) European Region, May 2016. Available at: http://www.euro.who.int/__data/assets/pdf_file/0003/309981/Zika-Virus-Technical-report.pdf?ua=1

World Health Organization: 2016e, Strategic Response Plan – Quarterly Update: July – September 2016, 25 October 2016. Available at: http://apps.who.int/iris/bitstream/10665/250626/1/WHO-ZIKV-SRF-16.4-eng.pdf

World Health Organization: 2016f, Zika Situation Report: Zika and Potential Complications, 12 February 2016. Available at: http://www.who.int/emergencies/zika-virus/situation-report/who-zika-situation-report-12-02-2016.pdf

Yu, G., Shen, H., Liu, J.: 2009, Impacts of climate change on historical locust outbreaks in China, *Journal of Geophysical Research* **114**, D18104. doi:10.1029/2009JD011833

Zachilas, L., Gkana, A.: 2015, On the verge of a grand solar minimum: A second Maunder Minimum?, *Solar Physics* **290**(5), 1457-1477. doi:10.1007/s11207-015-0684-1

Zbilut, J.P., Webber, C.L. Jr.: 1992, Embeddings and delays as derived from quantification of recurrence plots, *Physics Letters A* **171**(3-4), 199-203. doi:10.1016/0375-9601(92)90426-M

Zhang, Q.: 1994, Research on Fractal Dimension for Sunspot Relative Number, *Acta Astronomica Sinica* **35**(1), 27.

Zhang, Q.: 1995, Predictability of the long term variations of monthly mean sunspot numbers, *Acta Astrophysica Sinica* **15**(1), 84-89.

Zhang, Q.: 1996, A nonlinear prediction of the smoothed monthly sunspot numbers, *Astronomy and Astrophysics* **310**, 646-650. Available at: http://adsabs.harvard.edu/abs/1996A%26A...310..646Z

Zheng, D.: 1993, Preliminary study on application of LSTAR model to prediction of relative sunspot numbers, *Annals of the Shanghai Observatory* **14**, 164-169.

Zhuang, K., Wen, Z.: 2011, Dynamical behaviors in a discrete predator-prey model with a prey refuge, *International Journal of Mathematical, Computational, Physical, Electrical and Computer Engineering* **5**(8), 1149-1151. Available at: http://waset.org/publications/8300/dynamical-behaviors-in-a-discrete-predator-prey-model-with-a-prey-refuge

Zou, Y., Pazó, D., Romano, M.C., Thiel, M., Kurths, J.: 2007a, Distinguishing quasiperiodic dynamics from chaos in short-time series, *Physical Review E* **76**(1). doi:10.1103/physreve.76.016210

Zou, Y., Thiel, M., Romano, M.C., Kurths, J.: 2007b, Characterization of stickiness by means of recurrence, *Chaos: An Interdisciplinary Journal of Nonlinear Science* **17**(4), 043101. doi:10.1063/1.2785159